Dissertation

Alternative materials for crystalline silicon solar cells

Risks and implications

zur Erlangung des akademischen Grades des
Doktors der Naturwissenschaften (Dr. rer. nat.)

an der Universität Konstanz
Fakultät für Physik

angefertigt am Fraunhofer Institut für Solare Energiesysteme
Freiburg im Breisgau

vorgelegt von

Wolfram Kwapil

Tag der mündlichen Prüfung: 16.12.2010

Referenten: Prof. Dr. Gerhard Willeke

Prof. Dr. Thomas Dekorsy

Zusammenfassung in deutscher Sprache

Die vorliegende Arbeit betrachtet aus verschiedenen Blickwinkeln die Verwendung alternativer Siliciummaterialien für die Photovoltaik – häufig „upgraded metallurgical grade" (UMG)-Silicium genannt –und bewertet seine Auswirkungen auf die Wafer- und Solarzelleigenschaften an ausgewählten Punkten entlang der Prozesskette bis hin zum Modul.

Die Eigenschaften der hier untersuchten Siliciummaterialien werden hauptsächlich durch die hohe Konzentration sowohl an Bor als auch an Phosphor (beide etwa $>2x10^{16}$ at/cm^3) bestimmt. Dies hat fundamentale Auswirkungen u.a. auf die Basiswiderstandsverteilung durch elektrische Kompensation, die Ladungsträgermobilität und die lichtinduzierte Degradation.

Wegen der Verwendung von Mobilitätsmodellen in vielen Analysetechniken und Simulationen ist es von großer Bedeutung, die Ladungsträgermobilität auch in kompensierten Materialien modellieren zu können. Daher wurden in dieser Arbeit umfangreiche Messungen der Majoritätenleitfähigkeitsbeweglichkeit und Hall-Beweglichkeit in Siliciumwafern mit unterschiedlichen B- und P-Konzentrationen durchgeführt: In kompensiertem Si verringert sich die Ladungsträgermobilität deutlich sowohl mit zunehmender Summe beider Dotierstoffe (N_A+N_D), also mit wachsender Streuzentrendichte, als auch mit abnehmender Nettodotierkonzentration p_0=(N_A-N_D), was auf eine abnehmende Coulomb-Abschirmung ionisierter Streuzentren zurückgeführt wird. Unsere Messungen weisen darauf hin, dass das für kompensiertes Si am ehesten geeignete Mobilitätsmodell von Klaassen die Coulomb-Abschirmung nicht korrekt beschreibt. Im Moment kann es daher die Ladungsträgermobilität nur in einem eingeschränkten Bereich von N_A- und N_D-Werten treffend vorhersagen.

Eine sorgfältige Analyse der lichtinduzierten Degradation in kompensiertem und UMG Czochralski-Silicium ergab, dass die normalisierte Cz-Defektkonzentration nicht, wie bisher angenommen, in allen Dotierbereichen linear von der Nettodotierkonzentration abhängt, sondern vielmehr eine Funktion der Kompensation R_C ist. Dies gilt sowohl für p- als auch für n-Typ-Silicium, welches in kompensiertem Si ebenfalls unter Lichteinfluss degradiert. Für die in der Praxis relevanten Nettodotierkonzentrationen reicht das lineare Modell jedoch aus. Um die lichtinduzierte Degradation in sauerstoffreichem UMG-Si zu minimieren, sollten die B- und P-Konzentrationen gleichermaßen verringert werden.

Obwohl die Konzentration der Übergangsmetalle in UMG-Si geringer ist als ursprünglich angenommen, wurden die Konzepte des „Defect Engineering", die eine Materialverbesserung durch intrinsisches Gettern zum Ziel haben (theoretisch verbessert durch Ko-Präzipitation mit beweglichen Verunreinigungen wie z.B. Cu), unter die Lupe genommen. Es wurde gezeigt, dass die Kristallqualität unter einer Wechselwirkung zwischen metallischen Verunreinigungen und der Kristallisation leidet; die Stärke der Wechselwirkung hängt von der Zusammensetzung und Konzentration der Verunreinigungselemente ab. Dies wird auf einen erhöhten Einbau von Metallen in Kristalldefekt-reichen Gebieten zurückgeführt: In sorgfältigen Messungen der Verunreinigungskonzentration in Abhängigkeit der Versetzungsdichte konnte ein (super-)linearer Zusammenhang nachgewiesen werden, weshalb die absichtliche Zugabe schnell diffundierender Metalle für das „Defect Engineering" über Ko-Präzipitation keinen Vorteil bringen dürfte.

Die optimale Ausgestaltung von Hochtemperaturschritten für das intrinsische Gettern von Metallen hängt von der dominierenden Verunreinigung ab. Während mittelschnell diffundierende Metalle (Fe, Cr,…) re-präzipitieren, wenn nach einem Hochtemperaturprozess ein Temperschritt bei 600°C durchgeführt wird, verursacht die gleiche Temperaturführung eine Auflösung der großen Präzipitate von schnell diffundieren, hoch löslichen Metallen wie Ni. Wie Synchrotronmessungen belegen, verteilen sich diese Atome anschließend entlang der Korngrenzen und Versetzungen und bieten daher eine größere, rekombinationsaktive Grenzfläche als zuvor. Um für Ni ein intrinsisches Gettern zu bewirken, werden niedrigere Temperaturen (ca. 500°C-550°C) über eine längere Zeit (12 h) benötigt.

In vergleichenden Messungen der Verunreinigungskonzentration in hoch-versetzten Gebieten von Nachbarwafern, wovon die Hälfte einer Phosphordiffusion (externes Gettern) unterzogen wurden, konnte jedoch gezeigt werden, dass die schnell diffundierenden Elemente Ni und Cu, teilweise auch Co, trotz hoher Versetzungsdichte äußerst effektiv gegettert werden. Die mittelschnell diffundierenden Elemente Fe und Cr hingegen werden hier so gut wie nicht entfernt, weshalb sich für diese Spezies das Gettern auf Gebiete geringerer Kristalldefektdichte beschränkt.

Zusammengenommen bedeuten diese Ergebnisse, dass das Zusammenspiel zwischen externem und intrinsischem Gettern für die spezielle Elementgruppe der mittelschnell diffundierenden Metalle optimiert werden kann, da leicht bewegliche Elemente gegettert werden, während sich die langsam diffundierenden Metalle im relevanten Temperatur- und Zeitbereich kaum bewegen.

Berichte über schlechtere Sperreigenschaften der Solarzellen aus UMG-Si, welche möglicherweise zur Entstehung sogenannter „Hot Spots“ im Modul beitragen können, haben eine Reihe detaillierter Untersuchungen der Rückwärtseigenschaften von multikristallinen Si-Solarzellen im Allgemeinen ausgelöst. Im Rahmen dieser Arbeit wurde erstmals gezeigt, dass der Diodendurchbruch in mc-Si in drei Klassen („früh“, „weich“ und „hart“) unterteilt werden kann. Sie lassen sich anhand ihrer Durchbruchspannung und ihrer Kennlinie in Sperrrichtung unterscheiden und können durch drei verschiedene physikalische Vorgänge beschrieben werden.

Alle drei Klassen haben gemeinsam, dass der Durchbruch in zahlreichen, mikrometergroßen Bereichen stattfindet, welche daraufhin weißes Licht aussenden. Dies deutet auf die Anwesenheit „heißer“ Elektronen und damit auf Elektronenmultiplikation durch einen Avalanche-Vorgang hin.

Der „frühe” Durchbruch beginnt bei -4 bis -5 V und wird wahrscheinlich durch eine beschädigte Solarzellenoberfläche verursacht, wozu eingefeuerte Pastenpartikel der Vorder- und Rückseitenmetallisierung gehören als auch kleine Risse und Löcher. Diese Beschädigungen verändern die lokalen Eigenschaften des Emitters; infolgedessen werden vermutlich hohe elektrische Felder in der Raumladungszone induziert, die zu einem Durchbruch führen. Da der frühe Durchbruch stets auf eine sehr kleine Fläche beschränkt ist und bereits bei einer relativ niedrigen Sperrspannung einsetzt, kann es zu einer großen Hitzeentwicklung kommen. In den meisten beobachteten Fällen blieb die Erwärmung jedoch unkritisch.

„Weicher“ Durchbruch findet ausschließlich an rekombinationsaktiven Kristalldefekten statt. Wie Synchrotronuntersuchungen zeigen, wird er mit hoher Wahrscheinlichkeit durch Metallpräzipitate in der Raumladungszone verursacht. Dabei beeinflussen mehrere

Faktoren die Durchbruchspannung: In Wafern mit einer hohe Metallverunreinigungskonzentration oder einer hohen Dotierkonzentration (d.h. mit einem niedrigen Basiswiderstand) setzt der weiche Durchbruch bei niedrigeren Spannungen ein. Ebenfalls reduziert wird die Durchbruchspannung durch eine tiefe Anätzung der Waferoberfläche bevorzugt an Korngrenzen und Versetzungen, z.B. durch die Texturierung. Daher variiert der Beginn des weichen Durchbruchs je nach Solarzelleigenschaften zwischen -8 und -14 V. Weil rekombinationsaktive Defekte im Allgemeinen über ein großes Gebiet verteilt sind und weil der weiche Durchbruch eine weiche Rückwärtskennlinie besitzt, wird davon ausgegangen, dass die Wärmeentwicklung stets ungefährlich für ein Modul bleibt.

Um die Entstehung des weichen Durchbruchs erklären zu können, wurde ein Metallpräzipitat, welches sich in der Raumladungszone befindet, mittels eines internen Schottky-Übergangs beschrieben und die Verteilung des elektrischen Feldes numerisch berechnet. Es zeigte sich, dass das Feld schon bei geringen Sperrspannungen große Werte erreichen kann, welche gewöhnlich mit der Entstehung von Lawinenmultiplikation in Verbindung gebracht werden.

Der “harte” Durchbruch setzt erst bei etwa -14 bis -16 V an tief geätzten Versetzungen ein, an welche sich keine Verunreinigungen angelagert haben. Wegen der starken Zunahme des Sperrstroms innerhalb eines relativ kleinen Spannungsintervalls und weil er sich häufig auf ein kleines Gebiet konzentriert, kann der harte Durchbruch für das Modul gefährlich werden, wenn die erforderlichen Sperrspannungen erreicht werden.

Indem die allgemeinen Mechanismen des Diodendurchbruchs in multikristallinen Si-Solarzellen weitestgehend aufgeklärt werden konnten, konnte auch die Ursache der relativ hohen Sperrströme in UMG-Si Solarzellen ermittelt werden: die verhältnismäßig hohe Nettodotierkonzentration in der Waferbasis. Da es sich hier um den weichen Durchbruchtyp handelt, kann man davon ausgehen, dass durch die Verwendung von UMG-Si Solarzellen im Modul nicht das Risiko von Hot Spot-Entstehung steigt.

Wie in der vorliegenden Arbeit gezeigt wird, werden wichtige Eigenschaften der UMG-Si Wafer vorwiegend durch hohe Bor- und Phosphorkonzentrationen bestimmt. Indem der Gehalt an beiden Dotierstoffen im Feedstock reduziert wird, was bereits gegenwärtig recht erfolgreich bei einigen Herstellern erfolgt, bietet UMG-Silicium in naher Zukunft eine interessante, kosteneffektive Alternative zu herkömmlichen Materialien. Ob dies jedoch so bleiben wird, hängt entscheidend davon ab, ob UMG-Si Solarzellen mit zukünftigen Wirkungsgradverbesserungen mithalten können.

Index of contents

List of symbols

Symbol	Unit	Signification
α	cm^{-1}	absorption coefficient
α_{FC}	cm^{-1}	free carrier absorption coefficient
α_{Si}	cm^{-1}	coefficient describing absorption due to the silicon lattice
α_{Def}	cm^{-1}	coefficient describing absorption due to defects
A	cm^2	solar cell area
$A(p_0,\lambda)$	--	absorbance depending on net doping conc. and wavelength
$A(i,t)$	s^{-1}	term relating growth and dissolution rates in the Fokker-Planck mechanism
A_e^*, A_h^*	$Acm^{-2}K^{-2}$	effective electron and hole Richardson constants, respectively
A_i	--	factor describing the geometry of the photoluminescence measurement setup
B	cm^3s^{-1}	material constant of the radiative recombination
$\vec{B}$	T	magnetic field vector
$B(i,t)$	s^{-1}	term relating growth and dissolution rates in the Fokker-Planck mechanism
$C_{0,Me}$	cm^{-3}	prefactor of the temperature-dependent solubility of metal Me in Si
C_e	cm^6s^{-1}	electron Auger recombination coefficient
C_{eq}(el)	cm^{-3}	equilibrium concentration of element (el)
c_{FCA}	$m^2V^{-1}s^{-1}$	constant in the determination of the free carrier absorption
C_h	cm^6s^{-1}	hole Auger recombination coefficient
$C_{Me}(T)$	cm^{-3}	temperature-dependent solubility of metal Me in Si
$C_{solid}(el)$	cm^{-3}	concentration of element (el) in the solid silicon
d	cm	sample thickness
$d(i,t)$	s^{-1}	precipitate dissolution rate in the Fokker-Planck mechanism
$D_{0,Me}$	cm^2s^{-1}	prefactor of the temperature-dependent diffusivity of metal Me in Si
D_e	cm^2s^{-1}	electron diffusion coefficient
DL	cm^{-2}	dislocation density
$D_{Me}(T)$	cm^2s^{-1}	temperature-dependent diffusivity of metal Me in Si
ε	Fm^{-1}	permittivity

Symbol	Unit	Signification
E	eV	energy
$\vec{E}$	Vcm^{-1}	electric field vector
$\vec{E}_m$	Vcm^{-1}	maximum electric field vector in the space charge region
E_a	eV	activation energy
E_C	eV	conduction band edge energy
$E_{DL,C}$, $E_{DL,V}$	eV	dislocation level energies beneath the conduction band edge and above the valence band edge, respectively
E_F	eV	Fermi energy
$E_{F,e}$	eV	electron quasi-Fermi energy
$E_{F,h}$	eV	hole quasi-Fermi energy
$E_{F,m}$	eV	quasi-Fermi energy in metal
E_G	eV	band gap energy
E_t	eV	trap level energy
E_{top}	eV	energy at the top of the conduction band
E_V	eV	valence band edge energy
f	--	solidified ingot fraction
f_{abs}	--	surface-dependent correction factor for the photon absorption
$f(E)$	--	Fermi-Dirac distribution
$F(i,t)$	cm^{-3}	density of precipitation sites containing i atoms at time t
G_n	$cm^{-3}s^{-1}$	total electron generation rate
G_p	$cm^{-3}s^{-1}$	total hole generation rate
g_{eeh}, g_{ehh}	--	Auger recombination correction factors
$g(i,t)$	s^{-1}	precipitate growth rate in the Fokker-Planck mechanism
$h = 2\pi\hbar$	eVs	Planck's constant
$H_{C,Me}$	eV	solution enthalpy of metal Me in Si
$H_{D,Me}$	eV	migration enthalpy of metal Me in Si
i	--	number of atoms in a metallic precipitate
I	A	current
J_μ	Acm^{-2}	current density in the microplasma channel
$\vec{J}_n$	Acm^{-2}	electron current density

Symbol	Unit	Signification
$\vec{J}_p$	Acm^{-2}	hole current density
J_{ph}	$cm^{-2}s^{-1}$	photon current density
$J_{rev1,2}$	Acm^{-2}	saturation current densities
J_{SC}	Acm^{-2}	short circuit current density
$k_{0\,phase1}^{phase2}(\mathrm{el})$	--	equilibrium segregation coefficient between phases 1 and 2 of element (el)
k_B	eVK^{-1}	Boltzmann constant
$k_{eff\,phase1}^{phase2}(\mathrm{el})$	--	effective segregation coefficient between phases 1 and 2 of element (el)
λ	nm	wavelength
L_e	µm	electron diffusion length
$\mu_{C,e}$	$cm^2V^{-1}s^{-1}$	electron conductivity mobility
$\mu_{C,h}$	$cm^2V^{-1}s^{-1}$	hole conductivity mobility
$\mu_{H,e}$	$cm^2V^{-1}s^{-1}$	electron Hall mobility
$\mu_{H,h}$	$cm^2V^{-1}s^{-1}$	hole Hall mobility
M	$sK^{-1}cm^{-3}$	constant in the determination of the iron-boron pairing time
m_e^*	kg	effective electron mass
m_h^*	kg	effective hole mass
n	cm^{-3}	electron density
Δn	cm^{-3}	excess electron density
n_0	cm^{-3}	electron density in thermodynamic equilibrium
n_1	cm^{-3}	Shockley-Read-Hall density of electrons
N_A	cm^{-3}	acceptor concentration
N_C	cm^{-3}	effective electron density of states
N_D	cm^{-3}	donor concentration
$N(E)$	cm^{-3}	electron density of states at energy E
n_i	cm^{-3}	intrinsic carrier density
N_{min}	cm^{-3}	doping concentration on the lower doped side of a pn-junction
N_{ph}^{1sun}	s^{-1}	photon flux at the intensity of 1 sun

Symbol	Unit	Signification
N_t	cm^{-3}	density of defect levels in the band gap
N_t^*	μs^{-1}	normalized Cz-defect density
N_V	cm^{-3}	effective hole density of states
Φ_B	V	Schottky barrier potential
Φ_e	V	electron quasi-Fermi potential
Φ_h	V	hole quasi-Fermi potential
Φ_m	V	metal work function potential
Ψ	V	electrostatic potential
Ψ_s	V	electrostatic potential at the precipitate surface
Δp	cm^{-3}	excess hole density
p_0	cm^{-3}	hole density in thermodynamic equilibrium / effective net doping concentration in compensated p-type silicon
p_1	cm^{-3}	Shockley-Read-Hall density of holes
q	V	elementary charge
ρ	Ωcm	resistivity
r	--	Hall scattering factor
$R(\lambda)$	--	reflectance depending on wavelength
r_C	nm	average capture radius
r_{prec}	nm	precipitate radius
R_C	--	compensation ratio
R_H	m^3C^{-1}	Hall coefficient
R_n	$cm^{-3}s^{-1}$	total electron recombination rate
R_p	$cm^{-3}s^{-1}$	total hole recombination rate
R_{rad}	$cm^{-3}s^{-1}$	total radiative recombination rate
σ_e	$\Omega^{-1}cm^{-1}$	electron conductivity
σ_h	$\Omega^{-1}cm^{-1}$	hole conductivity
$\Delta\sigma$	$\Omega^{-1}cm^{-1}$	difference in the conductivity
$\sigma_{e,t}$	cm^2	defect level capture cross section for electrons
$\sigma_{h,t}$	cm^2	defect level capture cross section for holes

Symbol	Unit	Signification
$\vec{s}$	--	surface normal
S_{av}	Wm^{-2}	average light intensity
τ_0	µs	minority carrier lifetime of Cz samples in the annealed state
τ_{Cz}	µs	minority carrier lifetime limited by recombination due to the Cz-defect
τ_d	µs	minority carrier lifetime of Cz samples in the degraded state
τ_e	µs	electron lifetime
τ_{eff}	µs	effective carrier lifetime
$\tau_{e,surf}$	µs	electron lifetime limited by recombination at the sample surface
τ_h	µs	hole lifetime
t	s	time
T	K	temperature
$T(p_0,\lambda)$	--	transmittance depending on net doping conc. and wavelength
U	$cm^{-3}s^{-1}$	total net recombination rate
U_{Aug}	$cm^{-3}s^{-1}$	Auger net recombination rate
U_{rad}	$cm^{-3}s^{-1}$	net radiative recombination rate
U_{SRH}	$cm^{-3}s^{-1}$	Shockley-Read-Hall net recombination rate
V_a	V	external bias
V_B	V	breakdown voltage
V_{bi}	V	built-in voltage
V_H	V	Hall voltage
V_{OC}	V	open circuit voltage
v_s	cms^{-1}	saturation velocity of free charge carriers
V_t	V	thermal voltage
v_{th}	cms^{-1}	thermal velocity of free charge carriers
ω	s^{-1}	photon frequency
W	µm	space charge region width
χ	eV	electron affinity
z	µm	wafer depth

1 Introduction

Alarmed by the "Stern Review Report on the Economics of Climate Change" in 2006 [1], followed by the "Fourth Assessment Report" of the Intergovernmental Panel on Climate Change (IPCC) in 2007 [2], the media have brought the detrimental impact of the conventional energy production and consumption by fossil fuels to everyone's attention. Both reports added authority to the long-known relation between the emission of green-house gases and the fundamental climate change by quantifying its negative impact on the lives of billions of people and, last but not least, on the global economy. As a consequence, in 2008, scientists and politicians proclaimed the aim to restrict the global warming to +2 °C in average, compared to the global temperature in the pre-industrial era. Although no final agreement was reached during the 2009 United Nations Climate Change Conference in Copenhagen, most governments meanwhile are in accordance with the goal to significantly decrease the global carbon dioxide emission in the near future.

An important contribution is expected to come from the reconstruction of the energy sector constituting one of the largest emission sources so far. In several countries, incentives have been set up in order to increase the employment of renewable energy sources; one of the first programs was installed in Germany in 1991. As a result, the energy production in Germany has been subject to a fundamental change [3]: While renewable energy provided for 37 TWh of the electrical power generation in the year 2000 (6.4% of the respective total electrical energy consumption), it accounted for 94.7 TWh (16.1%) in 2009. During this time span, the power generation of photovoltaic systems grew by a factor 100, from 64 GWh to 6.6 TWh; besides geothermic energy technologies, photovoltaic power generation has thus been the fastest growing sector. Although the PV energy only corresponds to 1.1% of today's total electrical energy consumption in Germany, its future potential is estimated to be huge [3]: Photovoltaic systems installed on suitable roofs and façades could supply around 115 TWh of electrical power per year. It is reckoned that renewable energies in Germany could account for in total 700 TWh/a, which is 120% of the electrical power consumption in 2009.

An essential step on this way consists in reaching "grid parity", the point in time when the generated PV power can profitably be offered at the same price as conventionally produced energy. Two factors influence this development: Firstly, it is expected that the cost of conventional energy production will increase significantly in the near future due to the decreasing supply of fossil fuels. Secondly, the cost of photovoltaic power production has been decreasing significantly during the last decade, mainly as a result of large-scale solar cell and module manufacturing accompanied by an increase of the system efficiency. To obtain grid parity as early as possible, further cost reductions in the PV module manufacturing are however necessary.

In order to assess the cost reduction potential in the solar module manufacturing chain based on crystalline silicon, it is instructive to visualize the contributions of the individual process steps to the total module cost. Most recently, a complex cost analysis was performed in the frame of the CrystalClear project published in 2009/10 (for detailed information, see references [4, 5]) taking different solar cell process scenarios into account. For the graph shown in *Figure 1.1*, the calculations included cost structure data from different solar cell manufacturers, regarding crystalline silicon wafers of 180 µm thickness

and an encapsulated solar cell efficiency of 15.8% in a large-scale production plant. Roughly, the module cost (in this case estimated to sum up to 1.15 €/W_p) can be divided into three segments: While about half of the total cost can be attributed to the expense on material and labor of the final module assembly, a quarter is ascribed to the cost of the solar cell processing and another quarter to the expense on the wafer production. About 9% of the total cost can be traced back to the feedstock material and approx. 6% to the crystallization process.

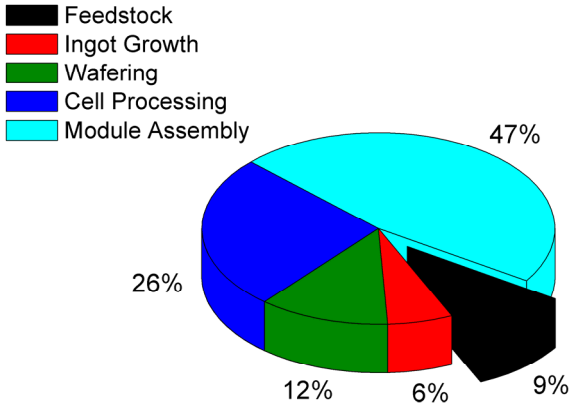

Figure 1.1: Relative contributions of individual process steps to the total production cost of a solar module. This calculation is based on the standard industrial screen printing technology (p-type wafers, front- and rear-contacts, Al-BSF) with an averaged encapsulated solar cell efficiency of 15.8% on 180 µm thick silicon wafers, adding up to a total cost of 1.15 €/W_p (after del Coso et al. [4, 5]).

Although its contribution to the total cost is comparatively small, nevertheless a reduced feedstock cost could in principle account for a total cost cutting below the important threshold of 1 €/W_p in this scenario. However, in this calculation the impact of the feedstock quality on the solar cell efficiency and yield have to be considered as well. Therefore, in the above scenario, del Coso et al. computed the correlation between the feedstock cost and the solar cell efficiency shown in *Figure 1.2*, which allows to estimate the impact on the total module cost brought about by a change of either factor. For example, starting with a module cost of around 1.2 €/W_p and a feedstock cost of around 20 €/kg, the total cost could be reduced to 1.0 €/W_p if the expense for the feedstock material decreased to about 2 €/kg, at the same time keeping the solar cell efficiency at the same level; alternatively, the same goal could be achieved by increasing the efficiency by about 11% relative (in this scenario from 15.8% to around 17.5% abs.). More realistically, this significant cost reduction could be realized by a combination of both factors. From another point of view, by halving the feedstock cost to 10 €/W_p, one could afford to lose about 5% relative in efficiency (from 15.8% to 15.0% abs.) without changing the total module cost. Any lower efficiency loss would contribute to a module cost reduction.

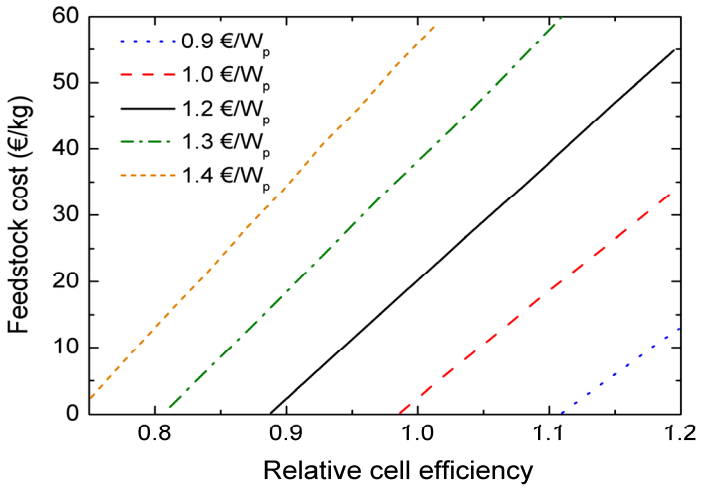

Figure 1.2: Assuming different total module costs (colored lines), this graph shows iso-cost curves of the scenario presented in Figure 1.1 relating the feedstock cost to the relative solar cell efficiency. For example, starting with a feedstock at 20 €/kg and a relative cell efficiency of 1.0, the module cost would stay constant if a new, cheaper material (10 €/kg) involved a relative efficiency decrease of about 5% relative. Taken from del Coso et al. [4, 5].

The search for a way to produce raw material more inexpensively was intensified in the year 2006, when it became clear that the traditional silicon feedstock supply for the growing photovoltaic industry, consisting to this date mainly of the left-overs from the integrated circuits industry, would no longer cover the increasing demand. Suddenly, the fast production of silicon in alternative routes – for which the term "upgraded metallurgical grade silicon" (UMG-Si) was coined – became attractive due to the lower capital investment and the shorter ramping-up time of the factories compared to standard silicon feedstock production. Moreover, the research on the role and behavior of the transition metals in multicrystalline silicon wafers, which were mainly made responsible for the reduced solar cell efficiency in less expensive, alternative material, led to the understanding that by adaptive processing their distribution, and thus their harmfulness, could be mitigated. This approach was termed "defect engineering" and was enthusiastically propagated as the promising way to "dramatically enhance the solar cell performance even of very dirty silicon" [6].

Another strong argument for the development of alternative silicon feedstock production routes has been the reduced energy consumption during the production compared to standard processes (see e.g. reference [7]), translating into a lower carbon dioxide emission in the entire process cycle.

Hence, there are several excellent reasons for the use of UMG-Si in solar cell fabrication. The cell performance achieved in laboratory and industrial processes have been encouraging. However, since UMG-Si has been extensively used only for a relatively short time, the understanding of the risks and implications coming along with its employment are still limited.

This thesis therefore sheds light on various aspects of the crystal growth of alternative silicon material, the electrical properties of the resulting wafers and solar cells and their behavior in solar modules. Since many different approaches exist for the alternative production of silicon feedstock, resulting in a large variety of materials, these considerations are extended to selected model materials possessing individual UMG-Si properties where necessary for their investigation.

Chapter 2 starts off with a concise description of the silicon feedstock production via conventional and alternative routes, followed by a short account of the crystallization processes for mono- and multicrystalline ingot growth. In the course of this chapter, several typical features of alternative silicon material are established, which have been investigated in this thesis.

Before the results are presented, *Chapter 3* summarizes some important fundamentals of the physics of semiconductors which are needed for the understanding of the following chapters.

In *Chapter 4* typical properties of UMG silicon are analyzed, concluding that the high concentration of both dopant species, phosphorus and boron, exerts a significant influence on the electrical properties. While the correlations between the dopant concentration and the important semiconductor parameters are well known if the silicon contains only one dopant species, the electrical compensation in the presence of both species leads to significant modifications, which have only recently begun to elicit research efforts. In particular, the high dopant concentration reduces the carrier mobility and, in combination with a high oxygen density, leads to the formation of highly recombination active boron-oxygen pairs.

Having assessed the properties of typical UMG silicon materials by putting emphasis on the impact of dopants in the preceding chapter, in *Chapter 5* the concept of "defect engineering" of transition metals in multicrystalline silicon wafers and solar cells is critically reviewed. Beginning with the investigation of the interaction between the transition metals and the silicon crystals during and after ingot growth, the behavior of different metal elements during high-temperature processing is analyzed, concluding with an evaluation of the feasibility and utility of the concepts of defect engineering.

Inspired by common suspicions that the long-term performance of UMG-Si solar cells in solar modules may be reduced, possibly related to an inferior diode breakdown behavior, in *Chapter 6*, the multicrystalline silicon solar cell behavior in reverse bias is studied. Due to the lack of knowledge in the scientific community about diode breakdown in solar cells in general, these investigations were extended to different kinds of multicrystalline material. Thus, it was possible to decipher the many influences on the solar cell reverse characteristics which led to a detailed understanding of UMG-Si related issues. As a result, one factor of the long-term UMG-Si cell performance could be assessed.

Finally, *Chapter 7* summarizes the results obtained in the course of this thesis.

2 Fabrication of “alternative” silicon material

Since the 1950’s, a huge industry has evolved around the processing of semiconductors due to their importance for the manufacturing of integrated circuits. Silicon being one of the most abundant elements on earth with especially suitable properties, it has become one of the most prominent representatives for this class of material. Therefore, a lot of experience has been gathered to obtain pure silicon from the minerals found in the earth’s crust. The cleaning procedures have been refined to such a degree that the silicon feedstock in the electronic industry contains only trace impurity levels measured in the ppb or even ppt-range.

However, the production of high-purity silicon is always associated with large efforts and huge capital investments, a high energy consumption and hence, high cost. The search for less expensive cleaning and fabrication methods has been going on for decades. Especially in the case of solar cells made from silicon, the exploration of alternatives was re-fueled by a shortage of raw material due to the boom in solar cell fabrication at the beginning of the new millenium, the silicon consumption of the large-area devices exceeding by far the demand of the integrated circuit industry.

In the process chain up to silicon wafers, two factors determine the overall labor and cost and thus present starting points for alternative fabrication routes: The synthesis and purification of the raw material in order to obtain silicon feedstock material (the cleaning procedure) and the crystallization of the silicon.

In this chapter, at first the reference techniques for the feedstock fabrication and crystallization are presented. Then, viable alternatives to the conventional routes are shown which have been developed and investigated by various companies in recent years. These descriptions are confined to the materials used in the course of this thesis, which are listed in the last section of the present chapter in order to facilitate the placement of the different experiments.

2.1 The silicon feedstock

Silicon is found in various minerals, one of which is simple silica or, in its pure state, quartz sand (SiO_2). Highly pure quartz is used as the starting material for the silicon production [8]. By adding coal and coke to an electrode arc furnace, at around 2000°C the following reaction takes place [9]:

$$SiO_2(s) + 2C(s) \rightarrow Si(l) + 2CO(g) \qquad (2\text{-}1).$$

The product is called metallurgical grade silicon (MG-Si) and contains about 1-2% impurities after a first refinement. The composition of the contaminants depends on many factors, e.g on the raw silica, the components used for the silica reduction and the actual processes. A typical list of impurity concentrations is displayed in Table 2.1 (taken from reference [8]).

Table 2.1: Representative impurity concentrations in metallurgical grade (MG) silicon [8]. Lower (first row) and upper bounds (second row) for the impurity content are given in ppma.

Al	B	C	Ca	Cr	Cu	Fe	Mg	Mn	Mo	Ni	O	P	Ti
300	5	50	20	5	5	300	5	10	1	10	100	5	100
5000	70	1500	2000	150	100	25000	200	300	10	100	5000	100	1000

The further purification of the MG-Si is mostly done in the Siemens process. Since the Siemens refinement is energetically expensive, at this point alternative cleaning cycles have a large potential to reduce production costs.

2.1.1 The standard: Silicon from the Siemens process

In the Siemens process, the metallurgical grade silicon is transferred into the gaseous phase by reaction with anhydrous hydrogen chloride in a fluidized bed reactor according to the simplified expression [8]

$$Si(s) + 3HCl(g) \rightarrow SiHCl_3(g) + H_2(g) \qquad (2\text{-}2).$$

After the reaction, most of the silicon is bound in trichlorosilane (TCS), with a small percentage forming chlorides such as $SiCl_4$.

TCS can easily be purified by fractional distillation (making use of differences in boiling points of the other chlorides) as well as by passing it through several filters.

Afterwards, the gaseous TCS is directed towards pure monocrystalline silicon seed rods which are heated to temperatures above 1100°C [8]. In fact, during the deposition, about 90% of the heating energy are lost to the surroundings, making the process extremely energy consumptive and inefficient [8]. At the silicon surface, the TCS is reduced by hydrogen following the reaction

$$SiHCl_3(g) + H_2(g) \rightarrow Si(s) + 3HCl(g) \qquad (2\text{-}3).$$

The resulting polysilicon rods are crushed and used as highly pure silicon feedstock. In general, the impurity content is lower than $1x10^{-10}$ %.

2.1.2 Alternative feedstock fabrication: The upgraded metallurgical grade route

In the search for more inexpensive ways to refine metallurgical grade silicon, a large variety of possibilities to remove contaminants have been investigated. Since these techniques avoid the transition into the gaseous phase and rely on less elaborate processes for the silicon refinement, they have sometimes been dubbed "upgraded metallurgical grade" (UMG) silicon. To avoid the depreciatory word "metallurgical", in industry often the

term "solar grade" (SoG) silicon is also used for the same range of material. Neither expression has been given a clear definition. Throughout this thesis, "upgraded metallurgical grade" silicon, or simply UMG-Si, will mean a material which was not purified by transformation into the gaseous phase.

At this point, it is important to note that the contaminants exemplified by Table 2.1 can be classified according to their different properties in silicon:

1) Some impurities have no significant influence on the silicon properties in the usual concentrations present after crystal growth. In particular, in these concentrations they do not diminish the minority carrier lifetime (section 3.2.3) or induce shunts in the solar cell harming their performance. Therefore, their removal from the MG-Si is not in the focus of the refinement efforts. To these belong e.g. Ca, K, Mg and Na. Their concentrations are often reduced as a side-effect of existing purification techniques.

2) There are many elements that decrease the minority carrier lifetime in silicon and thus the achievable solar cell efficiency. Hence, their removal is a major aim during refinement. The main culprits are transition metals such as Fe, Cu, Ni etc. Fortunately, transition metals tend to stay in the silicon melt during crystallization (section 2.2.1) and can thus be removed by one or several unidirectional solidifications (UDS) to a very high degree [8].

3) Oxygen, nitrogen and carbon tend to develop macroscopic clusters when they are present in silicon in a high concentration. Oxygen additionally forms a highly recombination active complex with boron, seriously decreasing the minority carrier lifetime (section 4.3.3). Silicon nitride (Si_3N_4) and silicon carbide (SiC) pervade the silicon crystals in the shape of, often electrically conducting, filaments, then producing shunts and thus decreasing the fill factor of the solar cells [10]. As integral parts of the crystallization facility, the three contaminants enter the silicon melt mainly during the crystallization process, the silicon feedstock playing only a minor role. Keeping the O, N and C concentration below a critical level is of high importance during solidification.

4) Elements from the elemental groups IIIA and VA in the periodic table act as dopants in Si. In silicon semiconductor technology, mostly phosphorus and boron are used. The high dopant concentrations originally present in the feedstock have to be reduced to the intended doping of the target material. Unfortunately, neither P nor B can be effectively removed from the silicon crystal by UDS. Therefore, the main efforts in UMG-Si production are aimed at an effective process to lower the P and B content.

Variations of the laboratory UMG-Si refining processes have entered the silicon industry [11], where the details of the procedures are proprietary and therefore not known to the public. An overview over the basic physico-chemical processes in MG-Si refinement is given by Lynch [12] and is shortly summarized here.

A) Removal of phosphorus

Viable ways to remove phosphorus are volatilization [13] combined with vacuum treatment, slagging or acid treatment [14].

Volatilization, performed with the help of different heating methods including plasma [15] or electron beam processes [13, 16], aims to transfer the phosphorus into the gaseous phase, from where it can be drawn by gas exchange. However, volatilization is limited by the low vapor pressures of volatile P. Therefore, large amounts of gas and long process times are required, making the approach ineffective.

An alleged 90% of phosphorus can be removed from MG-Si by an acid treatment called Silgrain process patented by Elkem [14], which seems to have initially been intended to remove transition metals from the silicon. In the Silgrain process, Ca is added to the silicon smelt in a high concentration (several %), resulting in $CaSi_2$ formation along the grain boundaries in the solidified silicon. After rough crunching, the Ca silicide causes the silicon lumps to crack along the grain boundaries in a first leaching step with $FeCl_3$+HCl, exposing the surfaces where most of the metal silicides tend to have formed during crystallization. They can be effectively removed by a second HCl-leaching step. Lynch assumes [12] that the phosphorus concentration is reduced during this process by forming phosphides with Ca and the transition metals, as SiP and $CaSi_2$ are less stable than CaP. The phosphides are then removed during the leaching or the final water rinsing.

B) Removal of boron

For the reduction of the boron concentration, proposed techniques involve volatilization and slagging.

Volatilization occurs from molten silicon in the presence of HO_2 and H_2 [17]. The gaseous boron compound probably consists of HBO [12]. During this process, however, a significant amount of silicon is lost due to the formation of SiO(g), which decomposes to SiO_2 on cool surfaces. Therefore, this process is hard to control.

Slagging processes use oxides or nitrides of various compositions (all have in common that they melt at higher temperatures than silicon) which are likely to undergo reactions with B or P. However, since they already contain significant quantities of B and P from the start, their capability to absorb additional boron from the silicon smelt are limited. A promising approach to resolve this problem was patented by Elkem [18]: Silicon slag containing usual amounts of P are added to a ferrosilicon melt with Fe concentrations of 65% or higher. Since the phosphorus solubility in ferrosilicon is higher than in silicon slags, P is drawn from the slags into the ferrosilicon. The obtained unsaturated slag is then added to the MG-Si smelt with an increased capability to absorb boron as well as phosphorus.

One possible process chain for the refinement of UMG silicon is pictured in *Figure 2.1*, showing the approach propagated by Elkem, one of the major suppliers of UMG-Si.

As the unidirectional solidification (whatever crystallization technique is used) plays a major role in the distribution of dopants and impurities in the final ingot, with the possibility to employ it for the purification of the silicon, the next section gives a short overview over the different crystallization techniques.

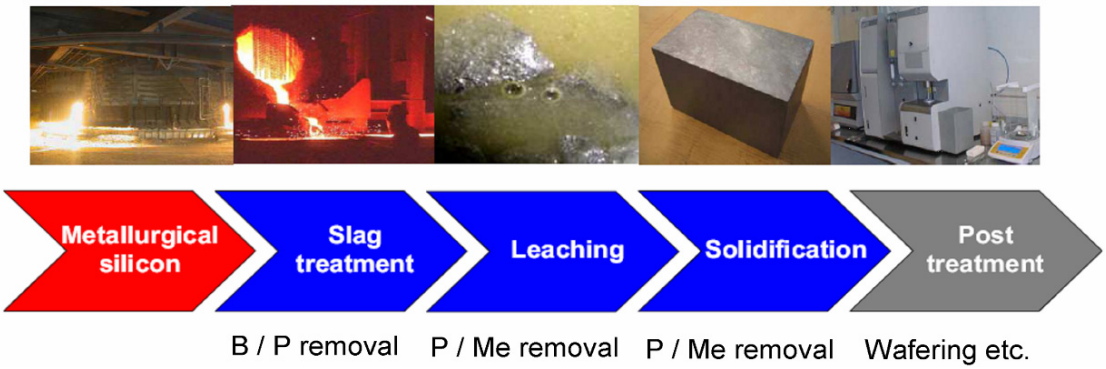

Figure 2.1: Elkem's process chain for the refinement of MG silicon (taken from [19]). Below, the intention of each process step is highlighted.

2.2 The crystallization techniques

The outcome of the silicon solidification can be divided into two material classes according to their crystal structure, which are mono- or multicrystalline silicon. For both, several crystallization techniques exist differing in their cost and quality of the product. While for the industrial production of monocrystalline wafers, the Cz-pulling is usually chosen, the industrial fabrication of multicrystalline blocks often uses the Bridgman and the heat exchange (HEM) method [20].

Monocrystalline wafers investigated in the course of this thesis were mainly produced with the help of the Czochralski (Cz)- method, while multicrystalline material was obtained via the block-casting technique, which slightly differs from the above mentioned industrial methods.

In the following, the multicrystalline block-casting and the monocrystalline Cz-pulling are introduced. In addition, an alternative to the block-casting is presented, providing relatively low-priced multicrystalline material which was also investigated in the course of this thesis. Finally, the segregation of impurity elements to the liquid phase, inherent to all crystallization techniques, is described in detail.

2.2.1 Multicrystalline silicon made in the block-casting method

Probably one of the simplest crystallization techniques is the block-casting of multicrystalline silicon. The process is visualized in *Figure 2.2*.

The silicon feedstock is first melted via inductive heating; next, the liquid silicon is poured into a silica crucible. The walls of the crucible are usually lined with silicon nitride powder, Si_3N_4, preventing the silicon from sticking to the silica. The silicon crystallizes starting from the bottom of the crucible, solidifying towards the top of the block. It is the aim to achieve a planar liquid / solid interface and thus unidirectional growth, reducing stress within the silicon and therefore minimizing the appearance of crystal defects which are potentially harmful – in the worst case, they can lead to major cracks and thus to the splitting of the block.

Since at the beginning of the solidification, many individual crystal grains develop, the resulting material is multicrystalline, with a preferential direction of the grain boundaries at a right angle to the liquid / solid interface.

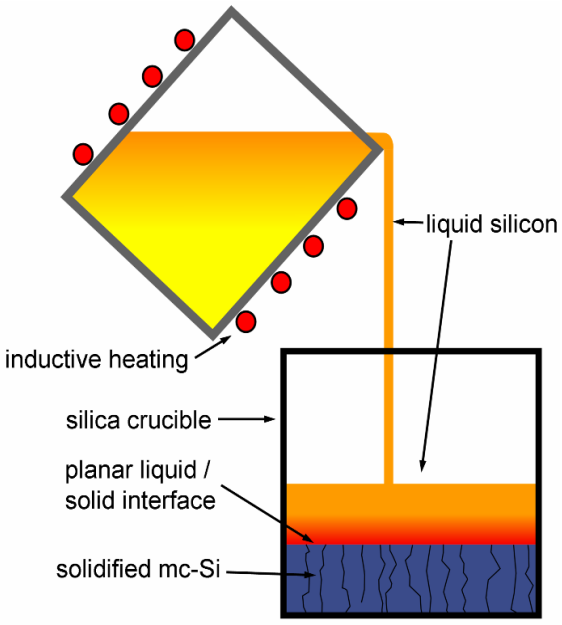

Figure 2.2: Simplified schematic of the block-casting process.

2.2.2 An alternative crystallization technique – Electromagnetic casting

The block-casting of multicrystalline silicon possesses several shortcomings which have been subject to a lot of research efforts. On the one hand, the block-casting is a batch process – one block is crystallized within a piece of equipment at a time, making it relatively slow because preparation and aftertreatment are time-consuming. Secondly, the direct contact between the silicon and the crucible (respectively the SiN lining) allows for indiffusion of impurities, especially Fe and the nitride itself, which impairs the performance of the resulting wafers.

One viable alternative method was developed during the 1990's [21] – the so-called electromagnetic casting of multicrystalline silicon. In *Figure 2.3*, the process is depicted schematically. It makes use of the fact that silicon can be heated via coupling to an external electromagnetic field which is generated with the help of induction coils. The Lorentz force stirs the silicon melt and directs it away from the cold-wall copper crucible. Therefore the melt does not touch the crucible wall.

The silicon then is moved downward on a graphite pedestal, slowly recrystallizing, which is controlled via the afterheaters.

The electromagnetic casting process can in principle be run continuously by feeding the silicon melt with feedstock lumps and pulling the multicrystalline Si from the furnace chamber, cutting the ingot in regular intervals.

Thus, the method produces multicrystalline ingots in a relatively short time. In addition, impurity in-diffusion from the silica crucible is avoided.

The properties of silicon wafers resulting from this alternative crystallization route will be the topic in chapter 5.

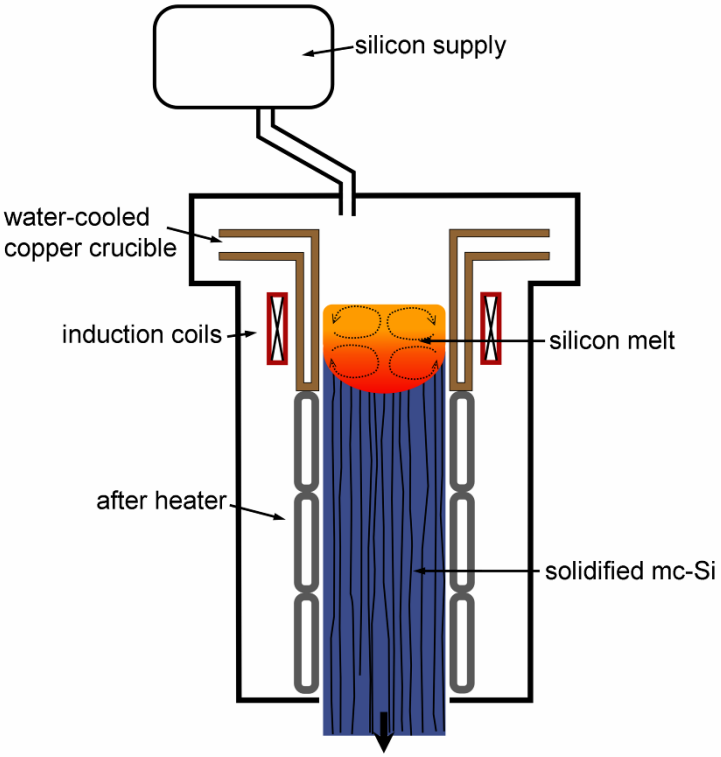

Figure 2.3: Simplified schematic of the electromagnetic casting method (after Kaneko [22]).

2.2.3 Monocrystalline silicon made in the Czochralski method

Crystallization via the Czochralski (Cz) method is the easiest way to obtain monocrystalline silicon ingots with lower crystal defect densities than multicrystalline material.

The Cz-growth makes use of the fact that silicon adatoms tend to be built into the crystal following the given crystal structure. Therefore, the process starts with a monocrystalline silicon seed crystal attached to a rod. It is dipped into the silicon feedstock melt in a silica crucible. Then, the rod is slowly pulled upwards while rotating it at the same time. By controlling the pulling speed, the rotation and the temperature gradients, long monocrystalline silicon ingots can be produced.

A characteristic feature of Cz ingots is the relatively high concentration of incorporated oxygen stemming from the silica crucible. Its implications for the use of UMG-Si feedstock will be discussed in chapter 4.

2.2.4 The solid / liquid segregation effect during solidification

An important property of all unidirectional solidification techniques, be it multi- or monocrystalline processes, is the segregation of impurities between the silicon melt and the solidified fraction. The following compilation is based on reference [23], to which the reader is referred for more details.

Segregation describes the re-distribution of dissolved impurities in a system that consists of two or more phases. The phases can either be different states of the same material, silicon, or different material compositions, such as transition metal silicides and silicon.

The effect of segregation occurs due to the fact that the solubility of trace impurities depends on the material of the matrix, the phase and the temperature. Dissolved impurity atoms can exist in the matrix up to a concentration that corresponds to the equilibrium solubility. When the equilibrium solubility is reached, the matrix is saturated.

When a system of two phases, for example liquid and solid silicon, is allowed to equilibrate, it will minimize its free energy. As a result, a given impurity species will redistribute between the two phases such that the ratio between the concentrations in each phase will correspond to the ratio of its respective equilibrium solubilities.

The ratio between the equilibrium solubilities C_{eq}(el) of element (el) in phases 1 and 2 is called the segregation coefficient k_0:

$$k_{0\,phase1}^{\;phase2}(\mathrm{el}) = \frac{C_{eq}^{phase2}(\mathrm{el})}{C_{eq}^{phase1}(\mathrm{el})} \qquad (2\text{-}4).$$

Most elements are more soluble in liquid silicon than in the Si crystal. During crystallization, the liquid / solid interface moves continuously. Therefore, the silicon melt is increasingly enriched by impurities and the ratio between the concentrations in the solid and liquid phase changes. As a result, with the crystal growing more and more impurities are incorporated into the solidified fraction.

This process is mathematically expressed with the help of Scheil's equation, which describes the impurity concentration of a given impurity in the ingot depending on the solidified fraction f (=1 means the last fraction to solidify) pointing along the direction of the crystallization:

$$C_{solid}(f) = k_{0\;liquid}^{\;solid} C_0 \left[1 - f\right]^{k_{0liquid}^{solid} - 1} \qquad (2\text{-}5).$$

In this equation, $C_{solid}(f)$ is the final impurity concentration at relative ingot height f and C_0 is the initial concentration in the silicon melt.

In the derivation of Scheil's model, following assumptions are made:

i. At the liquid / solid interface, locally equilibrium is reached, allowing for the use of the segregation coefficient.
ii. The impurities do not diffuse within the solidified fraction of the silicon.
iii. The melt is thoroughly stirred; therefore there are no gradients of the impurity concentration in the liquid.

iv. The Scheil equation describes the distribution of each element separately. Impurity atoms do not interfere with each other.

It is clear that the Scheil equation gives only an approximation for the reality with highly idealized assumptions. Therefore, the model was later extended by Burton et al. [24], who describe the segregation more realistically with the help of an effective segregation coefficient $k_{eff\ liquid}^{solid}$, relaxing suppositions (i) – (iii) in the case of monocrystals.

As already mentioned, most elements have a segregation coefficient <1, that is they preferentially stay in the silicon melt during solidification. In *Table 2.2*, the effective segregation coefficients of selected impurities are listed. The values refer to measurements made on monocrystalline silicon.

Table 2.2: List of the effective segregation coefficient of selected impurities in monocrystalline silicon growth. Behind each value, the reference is indicated.

Element	Effective segregation coefficient $k_{eff\ liquid}^{solid}$		Element	Effective segregation coefficient $k_{eff\ liquid}^{solid}$
Al	8.0×10^{-2} [25]		N	7.0×10^{-4} [23]
Au	2.5×10^{-5} [25]		Ni	1.3×10^{-4} [25]
B	8.0×10^{-1} [23]		O	0.25 – 1.4 [23][1]
C	7.0×10^{-2} [23]		P	3.5×10^{-1} [23]
Co	2.0×10^{-5} [25]		Pd	5.0×10^{-5} [25]
Cr	1.1×10^{-5} [25]		Sn	3.2×10^{-2} [25]
Cu	8.0×10^{-4} [25]		Ti	2.0×10^{-6} [25]
Fe	6.4×10^{-6} [25]		W	1.7×10^{-8} [25]
Mn	1.3×10^{-5} [25]		Zr	1.6×10^{-8} [25]
Mo	4.5×10^{-8} [25]			

Since the different crystal structure and crystallization conditions in multicrystalline silicon influences the segregation coefficient, the values shown here have to be revised if mc-Si material is investigated. However, data in literature is scarce; values for various transition metals have been published in references [26-28].

The accuracy of supposition (iv) for Scheil's model has hardly been contested in literature. It will be the topic of chapter 5.2.1.

[1] During solidification, oxygen is dissolved in the silicon melt from the silica crucible, while at the same time volatile SiO evaporates. Therefore, in most cases equilibrium conditions for the oxygen incorporation are never reached, making the effective segregation coefficient difficult to determine. Most publications assume a coefficient ~1.4.

2.3 List of materials used in this thesis

The following table contains a list of all materials used in this thesis aimed to provide an overview. The first column gives the name of the ingot which will be used throughout the text. The second and third column name the growth method (Cz: Czochralski-pulling; b-c: block-casting; EM-c: electromagnetic casting) and the solar cell process run, respectively. The numbers signify which materials were processed in the same run. Results on the different materials are found in the chapters listed in the fourth column. In the last two columns, the main properties and the measurements for which the materials were used are summarized.

Table 2.3: Table of the materials used in this thesis.

Ingot name	Crystal growth	Cell run	Invest. chapter	Characteristics	Used for measurements of
UMG Cz 1	Cz 1	1	4	- Cz from 100% UMG feedstock	- Transition metals in UMG-Si - Compensation - Mobility - Solar cell results
UMG Cz 2	Cz 1	1	4	- Cz blend 50% UMG / 50% virgin	- Compensation - Mobility - Solar cell results
UMG Cz 3	Cz 1	1	4	- Cz from virgin grade feedstock	- Compensation - Mobility - Solar cell results
Comp Cz 1	Cz 2	2	4	- Cz from virgin grade feedstock - weakly compensated with B, P	- Compensation - Mobility
Comp Cz 2	Cz 2	2	4	- Cz from virgin grade feedstock - heavily compensated with B, P	- Compensation - Mobility
UMG mc 1	b-c 1	3	4 & 6.5	- block-cast mc from 100% UMG feedstock	- Transition metals in UMG-Si - Solar cell results - Soft diode breakdown (base doping dependence)
Ref mc 1	b-c 1	3	4 & 6.5	- block-cast from virgin grade feedstock - base resistivity ~0.8 Ωcm	- Transition metals in UMG-Si - Solar cell results - Soft diode breakdown (base doping dependence)

Ingot name	Crystal growth	Cell run	Invest. chapter	Characteristics	Used for measure-ments of
UMG mc 2	b-c 2	--	4	- block-cast mc from 100% UMG feedstock	- Mobility
FZ 1	--	--	4	- p-type FZ wafers with varying base resistivi-ties	- Methods testing - Mobility
Ref mc 2	b-c 3	4	6.5	- block-cast from virgin grade feedstock - base resistivity ~1.2 Ωcm	- Soft diode break-down (impurity de-pendence)
Fe mc	b-c 3	4	5 & 6.5	- block-cast from virgin grade feedstock + 200 ppmw Fe added - base resistivity ~1.2 Ωcm	- Transition metal dis-tribution - Soft diode break-down (impurity de-pendence)
Ni mc	b-c 3	4	5 & 6.5	- block-cast from virgin grade feedstock + 40 ppmw Ni added - base resistivity ~1.2 Ωcm	- Transition metal dis-tribution - Soft diode break-down (impurity de-pendence)
Cr mc	b-c 3	4	5 & 6.5	- block-cast from virgin grade feedstock + 40 ppmw Cr added - base resistivity ~1.2 Ωcm	- Transition metal dis-tribution - Soft diode break-down (impurity de-pendence)
Fe-Cr-Ni mc	b-c 3	4	5 & 6.5	- block-cast from virgin grade feedstock + 200 ppmw Fe + 40 ppmw Ni + 40 ppmw Cr added - base resistivity ~1.2 Ωcm	- Transition metal dis-tribution - Soft diode break-down (impurity de-pendence)
EM-cast mc	EM-c 1	5	5	- electromagnetic cast-ing method from virgin grade feedstock	- Transition metals dep. on dislocation density - Influence P-gettering
Cu mc	b-c 1	3	5	- block-cast from virgin grade feedstock + 20 ppma Cu	- Influence of transi-tion metals on crystal-lization
Fe-Cu mc	b-c 1	3	5	- block-cast from virgin grade feedstock + 20 ppmw Cu + 20 ppma Fe	- Influence of transi-tion metals on crystal-lization

Ingot name	Crystal growth	Cell run	Invest. chapter	Characteristics	Used for measure-ments of
Fe mc 2	b-c 1	3	5	- block-cast from virgin grade feedstock + 20 ppma Fe	- Influence of transition metals on crystallization
Cr mc 2	b-c 1	3	5	- block-cast from virgin grade feedstock + 20 ppma Cr	- Influence of transition metals on crystallization
Dop mc 2	b-c 1	3	6.5	- block-cast from virgin grade feedstock - base resistivity ~0.3 Ωcm	- Soft diode breakdown (base doping dependence)
Dop mc 3	b-c 4	6	6.5	- block-cast from virgin grade feedstock - base resistivity ~0.6 Ωcm	- Soft diode breakdown (base doping dependence)
Dop mc 4	b-c 4	6	6.5	- block-cast from virgin grade feedstock - base resistivity ~1.5 Ωcm	- Soft diode breakdown (base doping dependence)
Dop mc 5	b-c 4	6	6.5	- block-cast from virgin grade feedstock - base resistivity ~2.5 Ωcm	- Soft diode breakdown (base doping dependence)
FZ 2	--	7	6.4	- Direct bonded FZ-wafer - small high-efficiency solar cells	- Early diode breakdown
Ref mc 3	b-c 4	8, 9 & 10	6.5	- Standard material, processed to standard solar cells with different texturizations	- Soft diode breakdown (surface morphology dependence)
Ref mc 4	b-c 5	8, 9 & 10	6.5	- Standard material, processed to standard solar cells with different texturizations	- Soft diode breakdown (surface morphology dependence)
Ref mc 5	b-c 6	8, 9 & 10	6.5	- Standard material, processed to standard solar cells with different texturizations	- Soft diode breakdown (surface morphology dependence)

3 Fundamentals

In this chapter, the fundamental physics of charge carriers in silicon are briefly introduced. For detailed information, the reader is referred to the plentiful treatments in literature, see for example references [29-32] from which the following sections were extracted. In the first section, the carrier distributions in thermodynamic equilibrium are described; the second section covers the generation and recombination processes of charge carriers. In the last section, the carrier redistribution under external influences is discussed.

As a semiconductor, silicon possesses an (indirect) energy band gap between the valence and conduction band of around 1.1 eV. Electrons can be lifted from the valence to the conduction band when they are conveyed the necessary energy via thermal processes, light irradiation or electrical excitation. Since the minimal band gap energy E_G is found between two different electron wave vectors in the energy-band structure (*Figure 3.1*), the electron excitation involves in addition the absorption or emission of phonons.

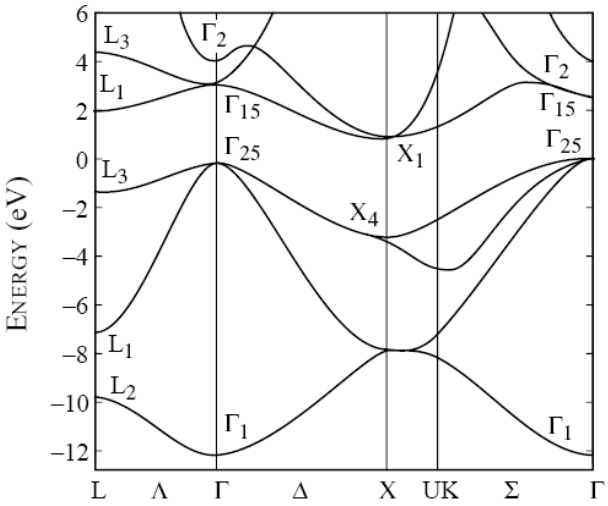

Figure 3.1: Silicon energy-band structure (taken from [33]) over the wave vector into the possible directions of the silicon lattice.

3.1 Silicon in thermodynamic equilibrium

In thermodynamic equilibrium the electron density n_0 in the conduction band can be calculated by integrating the product of the electron density of states *N(E)* and the Fermi-Dirac-distribution of the electrons *f(E)* from the bottom E_C to the top E_{top} of the conduction band:

$$n_0 = \int_{E_C}^{E_{top}} N(E) f(E) dE \qquad (3\text{-}1).$$

The density of states is given for low electron densities and low temperatures as:

$$N(E) = 4\pi\left(\frac{2m_e^*}{h^2}\right)^{3/2}(E - E_C)^{1/2} \tag{3-2}$$

with m_e^* the effective electron mass and h Planck's constant. The energy-dependent Fermi-Dirac-distribution function reads as

$$f(E) = \frac{1}{1 + \exp\left(\frac{E - E_F}{k_B T}\right)} \tag{3-3}.$$

The distribution is mainly characterized by the Fermi energy E_F, with a probability of 50% that an electron possesses an energy of $E=E_F$. k_B stands for Boltzmann's constant and T for the temperature in Kelvin.

In the case that the distance between the conduction band and the Fermi energy level is significantly larger than k_BT, the Fermi-Dirac distribution function can be replaced by Boltzmann's distribution. Then the electron density is calculated as

$$n_0 = N_C \exp\left(\frac{-(E_C - E_F)}{k_B T}\right) \tag{3-4}$$

with an effective density of states N_C

$$N_C = 2\left(\frac{2\pi m_e^* k_B T}{h^2}\right)^{3/2} \approx 3 \times 10^{19}\ \text{cm}^{-3} \tag{3-5}$$

at room temperature [31].

Analogously, the hole density in the valence band p_0 is

$$p_0 = N_V \exp\left(\frac{-(E_F - E_V)}{k_B T}\right) \tag{3-6}$$

with the effective hole density of states

$$N_V = 2\left(\frac{2\pi m_h^* k_B T}{h^2}\right)^{3/2} \approx 1 \times 10^{19}\ \text{cm}^{-3} \tag{3-7}$$

at room temperature [31].

The electron and hole densities in equations (3-4) and (3-6) are also valid in doped silicon. A semiconductor is doped when impurity atoms are incorporated into the crystal that have either one valence electron less (acceptors) or one more (donors) than silicon. In this way, the hole or the electron density, respectively, can be enhanced because dopant atoms are, in first approximation, completely ionized at room temperature [31].

However, the product of electrons and holes n_0p_0 is independent from doping:

$$n_0 p_0 = n_i^2 = N_C N_V \exp\left(\frac{-E_G}{k_B T}\right) \tag{3-8}.$$

Here, n_i is the intrinsic carrier density, which is in the order of $1\text{x}10^{10}$ cm^{-3}.

Typically, the concentration of dopant atoms exceeds the intrinsic carrier density by a few orders of magnitude. Then the hole and electron densities in p-type and n-type silicon can be estimated as

$$p_0 = N_A, \quad n_0 \approx \frac{n_i^2}{N_A} \tag{3-9}$$

and

$$n_0 = N_D, \quad p_0 \approx \frac{n_i^2}{N_D} \tag{3-10},$$

respectively, with N_A the acceptor and N_D the donor concentration.

Since the Fermi energy level describes the occupation probability, it changes with doping concentration. It is calculated for p-type silicon as

$$E_F - E_V = k_B T \ln\left(\frac{N_V}{N_A}\right) \tag{3-11}$$

and for n-type silicon:

$$E_C - E_F = k_B T \ln\left(\frac{N_C}{N_D}\right) \tag{3-12}.$$

3.2 Generation and recombination of charge carriers

When an electron is lifted to the conduction band, at the same time a hole in the valence band is created. In the inverse process, the generated electron-hole pair recombines, and its energy is released. This can happen either via the emission of a photon (radiative recombination) or recombination can take place via defect levels in the forbidden band gap, which is mainly a non-radiative process. At very high carrier densities, Auger processes prevail.

3.2.1 Electron-hole pair generation

The most important process (from the viewpoint of photovoltaics) for the generation of electron-hole pairs is the absorption of photons with energies $\hbar\omega \geq E_G$. When light impinges on the silicon surface, a certain fraction of the light is reflected and the remainder of the photon current J_{ph} traverses the bulk silicon. Due to absorption mainly by valence electrons but also by free carriers especially in the far infrared wavelength range (section 4.2.1), the photon current density decreases following the exponential

$$J_{ph}(z, \hbar\omega) = J_{ph}(z_o, \hbar\omega)\exp(-\alpha(\hbar\omega)(z - z_0)) \tag{3-13}$$

as a function of the semiconductor depth z, z_0 signifying the reference point. The absorption depends on the photon energy and is described by the absorption coefficient $\alpha(\hbar\omega)$. As a rule of thumb, the coefficient increases with increasing photon energy.

When free electron-hole pairs are generated, both the electron and the hole densities increase and the semiconductor leaves the thermodynamic equilibrium. As a result, the Fermi energy E_F loses its meaning; the electron and hole densities have now to be described by the two quasi-Fermi energies $E_{F,e}$ for electrons and $E_{F,h}$ for holes: The equations

$$n = N_C \exp\left(\frac{-\left(E_C - E_{F,e}\right)}{k_B T}\right) \tag{3-14}$$

and

$$p = N_V \exp\left(\frac{-\left(E_{F,h} - E_V\right)}{k_B T}\right) \tag{3-15}$$

replace equations (3-4) and (3-6), respectively. Equation (3-8) becomes

$$np = n_i^2 \exp\left(\frac{E_{F,e} - E_{F,h}}{k_B T}\right) \tag{3-16}.$$

3.2.2 Radiative recombination

The inverse process to the electron-pair production by light is the radiative recombination. In indirect semiconductors such as silicon, radiative recombination is less probable than recombination via defect levels or Auger recombination (see following sections) because it requires interaction with phonons.

The total radiative ecombination rate R_{rad} is proportional to the concentration of free electrons and holes:

$$R_{rad} = B\, n\, p \tag{3-17}$$

where B is a material-related constant, B=3x10^{-15} cm^3/s for silicon [31]. Taking into account the generation rate of free carriers at the same time gives the net recombination rate

$$U_{rad} = B\left(n\, p - n_i^2\right) = B\left((n_0 + p_0)\Delta n + \Delta n^2\right) \tag{3-18}$$

with Δn=Δp=n-n_0 the excess carrier densities of electrons and holes which are approximately equal because charge carriers are produced in pairs.

3.2.3 Recombination via defect levels – Shockley-Read-Hall theory

Impurities and crystallographic defects induce defect levels in the forbidden band gap, characterized by the trap energy E_t. Figure 3.2 gives the trap levels of selected transition metals, being some of the most recombination active impurities in silicon. Extensive information on transition metal properties in silicon is found in Graff [34].

Via the defect levels, electrons and holes recombine in a two- or more-step process which is described by the Shockley-Read-Hall (SRH) theory [35]. In this model, each defect state is either occupied by an electron or by a hole. Recombination occurs when the defect state catches a hole from the valence band in the former or an electron from the conduction band in the latter case; the probabilities of this happening are expressed with the capture cross sections $\sigma_{h,t}$ and $\sigma_{e,t}$, respectively.

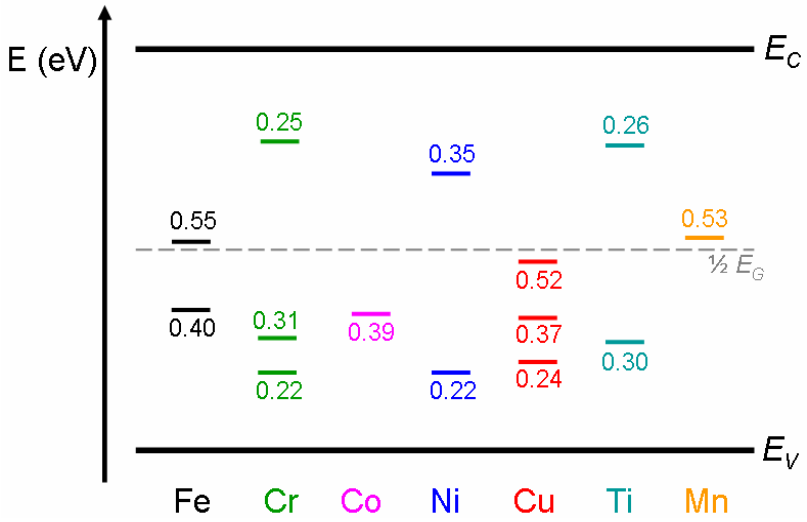

Figure 3.2: Trap levels of selected transition metals. The dashed line shows the center of the bandgap: Traps below ½ E_G give the trap level E_t from the valence band edge, traps above denote the difference to the conduction band edge. Trap levels taken from [36, 37], after [38].

However, the inverse processes – the electron being emitted from the defect level into the conduction band or the hole emitted into the valence band – have to be considered as well. The probability of re-emission increases with the proximity of the defect level to the conduction band or the valence band edge, respectively. Therefore, defect levels close to the center of the band gap generally have the largest impact on the recombination activity.

The evaluation of the above mentioned processes leads to the net SRH recombination rate of the defect characterized by the density of the defect level N_t with trap level E_t and capture cross sections $\sigma_{h,t}$ and $\sigma_{e,t}$:

$$U_{SRH} = \frac{\left(n\,p - n_i^2\right)}{\frac{1}{N_t \sigma_{h,t} v_{th}}\left(n + n_1\right) + \frac{1}{N_t \sigma_{e,t} v_{th}}\left(p + p_1\right)} \qquad (3\text{-}19),$$

with v_{th} the thermal velocity of the free carriers, and n_1 and p_1 are the SRH-density of electrons and holes, respectively:

$$n_1 = N_C \exp\left(\frac{-\left(E_C - E_t\right)}{k_B T}\right) \qquad (3\text{-}20)$$

and

$$p_1 = N_V \exp\left(\frac{-(E_t - E_V)}{k_B T}\right) \quad (3\text{-}21).$$

3.2.4 Auger recombination

Like radiative recombination, the Auger process is innate to semiconductors. Auger recombination describes the energy transfer from a recombining electron-hole pair to a free electron or hole, which then loses its energy to the silicon lattice by thermalization. The net recombination rate is given as

$$U_{Aug} = g_{eeh} C_e \left(n^2 p - n_0^2 p_0\right) + g_{ehh} C_h \left(n p^2 - n_0 p_0^2\right) \quad (3\text{-}22).$$

Here, C_e=2.8x10^{-31} cm^6/s and C_h=9.9x10^{-32} cm^6/s are the Auger coefficients and g_{eeh} and g_{ehh} stand for correction factors due to the Coulombic interaction [39].

3.2.5 Carrier lifetime

The annihilation of electron-hole pairs via the different recombination channels is characterized by the minority carrier lifetime τ_e in p-type (τ_h in n-type) silicon. In this analysis, it is supposed that the injection density is lower than the background doping (e.g. $\Delta n << N_A$ in p-type Si), and thus, the recombination rate is limited by the supply of minority carriers.

The general definition of the minority carrier lifetime reads as

$$\tau_e = \frac{\Delta n}{U} \quad (3\text{-}23)$$

in p-type material; an analogous expression is valid in n-type silicon for τ_h. In the case of a homogeneous carrier distribution, the recombination equals the generation of free charge carriers under steady state conditions. The various contributions through the different recombination channels are accounted for via

$$\frac{1}{\tau_{e,tot}} = \frac{1}{\tau_{e,rad}} + \frac{1}{\tau_{e,SRH}} + \frac{1}{\tau_{e,Aug}} + \frac{1}{\tau_{e,surf}} \ldots \quad (3\text{-}24).$$

Here, $\tau_{e,surf}$ stands for recombination at the sample surface, which can be neglected when the surface is well passivated.

An equivalent measurand is the minority carrier diffusion length L which is suitable to estimate the average distance being covered by the free minority carriers before they recombine, e.g. for electrons in the p-type base, being linked to the carrier lifetime via:

$$L_e = \sqrt{D_e(\mu_{C,e})\tau_e} \quad (3\text{-}25).$$

D_e stands for the diffusion coefficient of electrons, depending on the minority carrier conductivity mobility $\mu_{C,e}$. The latter is discussed in more detail in the following section.

3.3 Charge carrier distribution

The movement of carriers in silicon, which is exploited in the generation of electrical power in photovoltaic devices, is mainly directed by the electric field $\vec{E}$ (drift) and the gradient of the charge carrier density $\vec{\nabla} n$ (diffusion). On their way, the carriers are hampered by collisions with (quasi-)particles expressed with the help of the mobility μ or the diffusion coefficient D. Scattering occurs mainly at ionized dopant atoms, free carriers, impurities or at the silicon lattice, which can happen e.g. by interaction with phonons [29]. The mobility and the diffusion coefficient are associated via Einstein's relation

$$D_i = \frac{k_B T}{q} \mu_{C,i} \tag{3-26}$$

where the subscript i stands for electrons or holes.

3.3.1 Carrier distribution and continuity equations

Since drift and diffusion often occur simultaneously, the net current densities of electrons $\vec{j}_n$ and holes $\vec{j}_p$ are expressed as the sums

$$\vec{J}_n = q\mu_{C,e} n\vec{E} + qD_e \vec{\nabla} n \tag{3-27}$$

and

$$\vec{J}_p = q\mu_{C,h} p\vec{E} - qD_h \vec{\nabla} p \tag{3-28},$$

respectively. As shown by Würfel [31], both drift and diffusion currents can be unified in the gradients of the quasi-Fermi potentials Φ_e and Φ_h, defined by

$$\Phi_i = -\frac{E_{F,i}}{q} \tag{3-29},$$

resulting in the expressions

$$\vec{J}_n = -\sigma_e \mathrm{grad}(\Phi_e) \tag{3-30}$$

and

$$\vec{J}_p = -\sigma_h \mathrm{grad}(\Phi_h) \tag{3-31}$$

where σ_e and σ_h stand for the electron and hole conductivity, respectively:

$$\sigma = \sigma_e + \sigma_h = q\mu_{C,e} n + q\mu_{C,h} p \tag{3-32}.$$

The carrier distribution is then described by the continuity equations, taking into account generation and recombination processes:

$$\frac{\partial n}{\partial t} = \frac{1}{q}\vec{\nabla}\cdot\vec{J}_n - R_n + G_n \qquad (3\text{-}33)$$

and

$$\frac{\partial p}{\partial t} = -\frac{1}{q}\vec{\nabla}\cdot\vec{J}_p - R_p + G_p \qquad (3\text{-}34).$$

In a pn-junction in equilibrium, the current contributions of electrons and holes due to drift and diffusion in conjunction with recombination and generation of electron-hole pairs equilibrate and the electrostatic potential Ψ develops according to Poisson's equation

$$\nabla\left[\varepsilon\nabla(\Psi)\right] = -q\left(p - n + N_D^+ - N_A^-\right) \qquad (3\text{-}35),$$

where N_D^+ and N_A^- are the ionized dopant densities in the space charge region and ε stands for the permittivity of the semiconductor.

3.3.2 Carrier mobility in silicon

While the carrier transport by diffusion or drift in an electric field in a semiconductor is described by the carrier conductivity mobility $\mu_{C,i}$ as defined by equation (3-32), for the movement of carriers in an additional magnetic field as in a Hall experiment [40], the adequate definition of the carrier mobility is given by the Hall mobility $\mu_{H,i}$. It can be used for example to delineate the contributions of minority and majority carrier mobilities on the integral mobility with the help of temperature-dependent Hall measurements.

The conductivity mobility and the Hall mobility are linked via the Hall scattering factor r:

$$\mu_{H,i} = \frac{r}{q\sigma_i N_j} = r\mu_{C,i} \qquad (3\text{-}36),$$

with the subscript i denoting either electrons (e) or holes (h), while the subscript j stands for acceptors (N_A) or donors (N_D), respectively.

The Hall scattering factor contains the different influences of the various scattering mechanisms – e.g. scattering at ionized impurities, lattice scattering or scattering at neutral atoms – compared to the conduction mobility, when the carriers undergo the circular movements in a magnetic field $\vec{B}$. From the experimental parameters of a Hall measurement (with the Hall voltage V_H measured at the sample edges, the current I passing through the sample of thickness d, and the specific material resistivity ρ), the Hall coefficient R_H and the Hall scattering factor are defined as

$$R_H = \frac{V_H d}{\left|\vec{B}\right| I} = \frac{r}{qN_j} \qquad (3\text{-}37),$$

where the Hall mobility can be extracted from

$$\mu_H = \frac{\left|R_H\right|}{\rho} \qquad (3\text{-}38).$$

The scattering mechanisms and therefore the Hall scattering factor depend generally on the carrier energy, the temperature and the strength of the magnetic field.

For details on Hall measurements, please refer to Schroder [40] or similar treatments in literature.

4 Properties of upgraded metallurgical grade silicon

Contrary to standard silicon feedstock purified via the (more or less) standardized Siemens process, the modern refinement routes for upgraded metallurgical grade silicon yield material of highly differing specifications. The UMG-Si properties depend strongly on the raw silica and the purification recipe, which are mostly proprietary processes developed in parallel by many silicon producers (section 2.1.2).

Since the silicon refining in the UMG-Si route is much less elaborate than the Siemens process, the impurity concentration can exceed standard silicon contamination by several orders of magnitude. Two groups of impurities are critical: transition metals, decreasing the minority carrier lifetime, and dopants, because industrial standard processes are in general optimized for a relatively narrow range of base resistivities.

Due to the silicon shortage around the year 2006, the PV industry as well as research institutes around the world have put a lot of effort into the determination of UMG-Si related material and solar cell properties.

A large number of publications have covered the solar cell performance mainly of multicrystalline UMG-Si, the influence of adapted processes – mainly the high-temperature fabrication steps like P-gettering – and UMG-Si related issues like the carrier mobility.

The mc-Si solar cell efficiencies of UMG material reported by various research institutes using industrial-like processing range between 15 - 16%, with best solar cells around 16.3%, which was only about 0.2-0.3% abs. below the reference values for this solar cell technology [41-44]. In a recent study by Junge et al., high-efficiency processing even yielded a performance of 18.4% on the best solar cell made from UMG mc-silicon provided by CaliSolar [45], also being close to the standard reference value of the respective solar cell process. While these results were obtained in small-scale processing, Hoffmann et al. presented a long-term comparison between standard and UMG mc-silicon solar cells (Elkem feedstock) processed in an industrial facility in mass-production with a statistical basis of in total 150,000 solar cells in 2008 [46]. He reported UMG-Si solar cell efficiencies of 15.4%, only about 0.1% abs. lower than the reference. This performance could be raised by 0.4% abs. to an average value of 15.8% in 2010 by optimizing the process in the same industrial process line, with best UMG-Si solar cells having an efficiency of 16.4% [47].

Note that the wafers used in these studies had been fabricated from feedstock resulting from different purification techniques of various silicon feedstock producers. Details on the differences between these materials and standard silicon wafers are not known. However, it is evident that some examples for UMG silicon already compete with traditional Siemens-process based refinements on the solar cell performance level.

Besides the cell performance, the research has focused on the two critical UMG-material issues, namely the impact of transition metals and their behavior during high temperature processing steps and the influence of the high dopant concentrations on the solar cell properties.

It was propagated mainly by Buonassisi and co-workers that metal-rich silicon wafers could benefit from "internal gettering" techniques, thus reducing the total interface between silicon and metal atoms, which would minimize the recombination activity [6]. They suggested that internal gettering could be enhanced by the presence of e.g. Cu being known to readily form co-precipitates with other transition metals [48]. Some implications of this approach will be the topic of the next chapter 5.

The second obvious issue is the relatively high concentration of *both* dopants, boron and phosphorus. Since boron atoms act as acceptors while phosphorus atoms are donors, one dopant type compensates partly for the electrical influence of the other on the resulting free carrier density. This has consequences for the base resistivity distribution [49], the Cz-related boron-oxygen defect which causes light-induced degradation (LID) [50-52] and for the charge carrier mobility [53].

This chapter summarizes the work which has been performed within this thesis to determine the influences of high dopant concentrations on the silicon wafer properties. These studies have been done in collaboration with Juliane Geilker in the frame of her diploma thesis [54], which was supervised by the author of this thesis. In addition, several measurement results by Florian Schindler have been used, whose diploma thesis is currently being supervised by the author.

Cz-grown as well as block-cast upgraded metallurgical grade silicon of three different producers have been investigated. The first Cz-crystal is made of 100% UMG-Si feedstock produced around the year 2008, called "UMG Cz 1". For comparison, a Cz crystal containing a blend of 50% UMG-Si feedstock with virgin grade feedstock ("UMG Cz 2") as well as a 0% reference were pulled, "UMG Cz 3". In order to be able to distinguish the influence of dopant compensation on the properties of UMG-Si from all the other possible material-related impacts (e.g. background contamination), in the frame of the project SolarFocus, two Cz-crystals were grown from virgin grade silicon. Two different concentrations of boron and phosphorus were added to the melt, thus intentionally compensating the dopant influences: "Comp Cz 1" was weakly compensated by adding $[B]=[P]=3x10^{16}$ at/cm^3; "Comp Cz 2" was heavily compensated by doping with $[B]=6x10^{16}$ at/cm^3 and $[P]=9x10^{16}$ at/cm^3.

The investigated multicrystalline UMG silicon blocks were both cast from commercially available UMG-Si feedstock of different origin. One, named "UMG mc 1", was crystallized in the experimental block-casting facility IS30 at SolarWorld in the frame of the joint project SolarFocus in the year 2009. For comparison, in the same facility a reference block – "Ref mc 1" - was cast from high-purity feedstock. The second UMG-Si containing mc-Si ingot "UMG mc 2" was cast in the frame of the project ALBA2 also in the year 2009.

This chapter starts with the determination of the transition metal and the dopant concentrations and focuses on the carrier mobility reduction due to the increased number of scattering centers in UMG-Si. In the second section, the limitations of both material classes are assessed, which covers in particular the boron-related defect in Cz-crystals made from compensated silicon feedstock. At last, the solar cell parameters of exemplary process runs of both material classes are compared to standard feedstock silicon.

4.1 Transition metal concentration

Although already developed 60 years ago, Neutron Activation Analysis (NAA) [55] remains one of the most sensitive techniques for the detection of trace impurities in silicon until now. It is based on the artificial activation of radioactive isotopes of most elements.

For this technique, a small sample – small pieces of silicon or crunched wafers – is placed in the range of a low energy neutron source (thermal neutrons), provided for example by nuclear reactors. When the irradiated neutrons collide with the sample atoms, instable radioactive isotopes form, which decay in average after the element-characteristic half-life in the order of minutes to several hours. In decomposing, the elements emit X-rays of characteristic wavelengths which are detected in usual scintillation detectors and used for the determination of the type and concentration of each element. The detection limit depends mainly on the sample volume and the radiative (wavelength-dependent) background and is in the order of $1x10^{10}$ – $1x10^{12}$ at/cm^3 for most transition metals in silicon.

Note that the NAA technique measures the total impurity content; it is not capable of distinguishing between the dissolved atoms, which are more harmful due to their large effective surface, and the precipitated fractions of the impurity content.

The ingot height-dependent concentration of the transition metals Cu, Fe, Ni, Cr and Co in the Cz-grown ("UMG Cz 1") and block-cast mc ("UMG mc 1") upgraded metallurgical grade silicon crystals are displayed in *Figure 4.1*. For comparison, the detected metal content of the reference mc-Si block is also plotted[2]. Besides the five transition metals, only spurious amounts of Au (in the order of $1x10^9$ at/cm^3) were measured. In addition, the UMG-silicon crystals contain a higher concentration of Ge, which is in the same elemental group as Si, and As, which acts as a donor. However, both impurity densities are not expected to affect the UMG silicon properties.

The NAA reveals that the UMG Cz-crystal mainly contains Cu (~$1x10^{12}$-$1x10^{13}$ at/cm^3), Cr (~$1x10^{12}$-$1x10^{13}$ at/cm^3) and Co (~$1x10^{11}$-$1x10^{12}$ at/cm^3). Fe and Ni are not detected. These values lie in the typical range of Cz-grown crystals made from standard silicon feedstock and generally below the metal profiles of both mc-Si blocks.

Both multicrystalline blocks contain a concentration of around $1x10^{13}$-$1x10^{15}$ at/cm^3 of Fe. The Cu contamination of both blocks is also comparable (~$1x10^{13}$-$5x10^{14}$ at/cm^3) as is the Co content (~$1x10^{11}$-$1x10^{12}$ at/cm^3). While the reference block holds in addition a low concentration of Cr (~$1x10^{11}$ at/cm^3), the UMG-Si block is contaminated with a relatively high concentration of Ni (~$1x10^{14}$-$1x10^{15}$ at/cm^3).

The first conclusion is that the transition metal content of silicon wafers made from upgraded metallurgical grade feedstock material does not differ significantly from current standard mc-Si wafers, keeping in mind that variations due to different production conditions exist for every feedstock material. Referring to literature, a compilation of mc-Si impurity contents of different silicon wafer suppliers are given for example by Istratov et al. [56] and Macdonald et al. [26]. According to these publications, standard mc-Si wafers often contain Fe, Cr and Ni concentrations in the order of $1x10^{14}$-$1x10^{15}$ at/cm^3, resembling the results obtained on our UMG-Si material.

[2] All NAA measurements were performed at Elemental Analysis, Inc. (EAI), USA, commissioned by I. Reis.

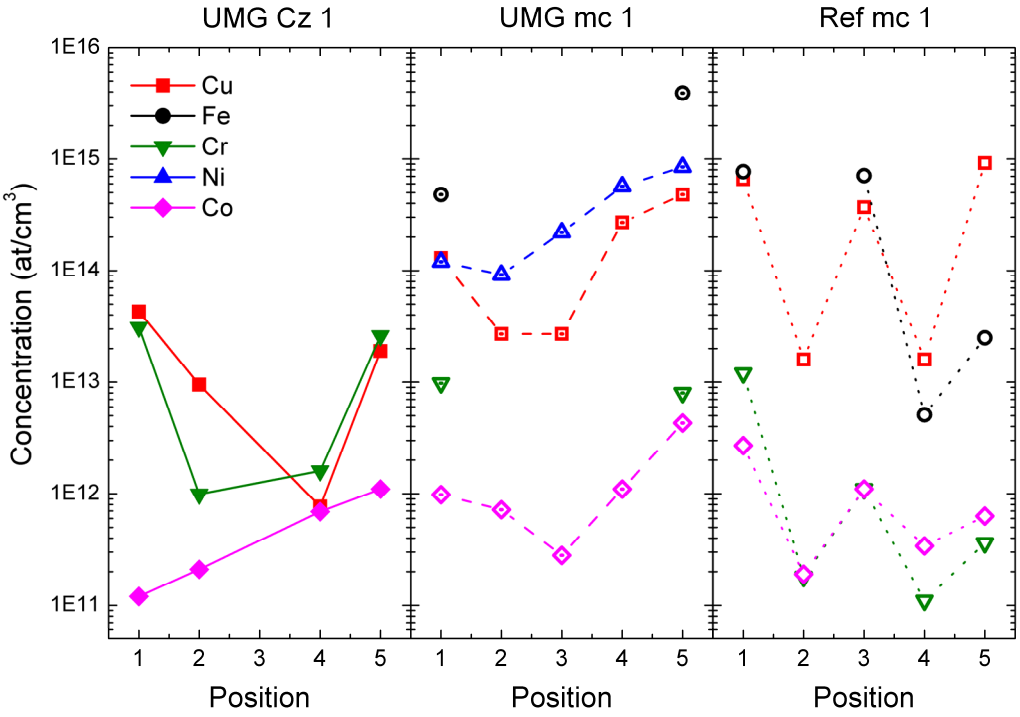

Figure 4.1: Transition metal concentration versus the ingot position (1 = launch of crystallization, 5 = end of crystallization) of Cz-grown (left) [57] and block-cast (middle) UMG silicon, compared to the concentration measured on a block-cast reference ingot (right)[2].

4.2 Dopant concentration

The high concentration of both dopant types, boron and phosphorus, has implications on the base resistivity distribution, on the net doping concentration and the charge carrier mobility. The latter decreases the carrier diffusion length of holes and electrons, which affects the solar cell parameters because the pn-junction collects less charge carriers.

In standard, uncompensated p-type material, the resistivity ρ correlates directly with the acceptor concentration via

$$\rho(N_A) = \frac{1}{q\mu_C(N_A)N_A} \qquad (4\text{-}1),$$

where $\mu_C(N_A)$ stands for the (known) doping-dependent majority carrier mobility. The determination of many other measurands like the minority carrier lifetime is based on the three variables $\rho, \mu_C(N_A)$ and N_A. However, in compensated material these derivations are more complex. The interdependencies are visualized in *Figure 4.2*.

Instead of the acceptor concentration, the electrically active fraction of dopants, the net doping concentration p_0, has to be used:

$$p_0 = N_A - N_D \qquad (4\text{-}2).$$

Although the electrically active fraction is lower than N_A and N_D, both dopants take effect as scattering centers for free holes and electrons. Hence, both the majority and the minority carrier mobility are lower than in uncompensated material of same net doping. Therefore, the mobility model which is used for the evaluation of $\mu_C(N_A)$ in equation (4-1) is not valid any more in compensated material and cannot be used for the determination of the net doping concentration. A different majority carrier mobility model has to be implemented, depending on N_A and N_D [50]:

$$\mu_C(N_A, N_D) = \frac{1}{q\rho|p_0|} \qquad (4\text{-}3).$$

Due to the lack of data on compensated silicon material in literature, the carrier mobilities of compensated Si wafers were investigated and compared to existing mobility models in order to assess their quality.

To do this, measurements of the base resistivity and at least two of the three measurands p_0, N_A and N_D are necessary:

A) The retrieval of the base resistivity can be done e.g. by the four-point-probe technique or via inductive sheet resistance measurement methods [58].

B) The net doping concentration can be measured directly via the CV-method or with the help of a technique which has been newly developed in the frame of this thesis in collaboration with S. Rein and J. Geilker [54, 57]. The so-called FCA-FTIR method is explained in detail in section 4.2.1.

C) For the detection of N_A or N_D, the limits of existing techniques such as NAA, inductively coupled plasma mass spectrometry (ICP-MS), ICP optical emission spectroscopy (ICP-OES), ICP atomic absorption spectroscopy (ICP-AAS), glow-discharge mass spectrometry (GDMS) and secondary ion mass spectrometry (SIMS) are often in the order of 10^{16} at/cm^3, which is also the expected dopant content. Another, more sensitive method would therefore be desirable. Macdonald showed a way to independently determine the boron concentration with the help of the iron-boron pairing time constant τ_{assoc}^{Fe-B} [59] with the detection limit estimated to be reliably below 1x10^{16} at/cm^3 [54]:

$$N_A = M \frac{T}{\tau_{assoc}^{Fe-B}} \exp\left(\frac{0.66\,\mathrm{eV}}{k_B T}\right) \qquad (4\text{-}4).$$

Here, the constant M=5.0x10^5 s/Kcm^3 and T is the sample temperature. Macdonald proved that the iron-boron pairing in p-type compensated material was not altered by the high concentration of phosphorus [59], equation (4-4) therefore remaining valid. The acceptor concentration can thus be measured by the simple means of time and temperature-dependent carrier lifetime techniques such as quasi-steady state photoconductance (QSSPC). Note that the absolute values of the carrier lifetime are not important; therefore the measurement does not have to be corrected for the different mobility in compensated material (section 4.3.1). Neither does the iron concentration matter. The only constraint on the Fe-content is that the FeB-pairs (and the interstitial species Fe_i) must have a significant impact on the minority carrier lifetime, which is true in many cases. Otherwise, the wafers can be intentionally doped with Fe, e.g. by

scratching iron onto the wafer surface and driving the contaminant into the wafer bulk during a high-temperature step.

The feasibility of this approach is shown in the next section with the help of intentionally Fe-contaminated Fz-samples.

Note, however, that this method does not work on n-type compensated silicon as no FeB-pairs are formed.

D) When the net doping concentration p_0 and the acceptor concentration are known, the donor concentration N_D can be calculated with the help of eq. (4-2).

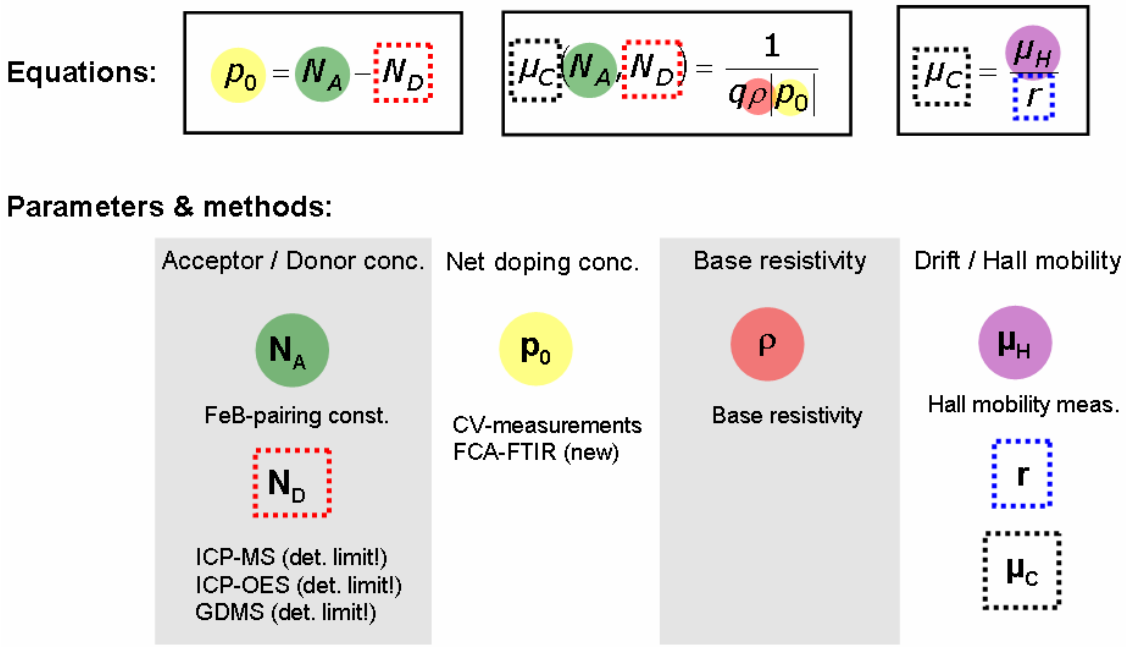

Figure 4.2: Interdependencies between the measurands relevant for the characterization of UMG silicon wafers. The encircled measurands can be directly analyzed with the help of existing techniques. The dotted rectangles identify measurands which have to be determined by a combination of several other values.

By another approach with the same number of measurements, the conductivity mobility can also be determined by Hall mobility measurements μ_H when the Hall factor $r(N_A,N_D)$ is known:

$$\mu_C = \frac{\mu_H}{r(N_A, N_D)} \qquad (4\text{-}5).$$

Conductivity and Hall mobilities of UMG silicon and intentionally compensated Cz-wafers and the deduced Hall factors are presented in section 4.2.4.

4.2.1 Novel determination technique for the net doping concentration: FCA-FTIR

The following novel analysis of the net doping concentration based on Fourier Transform Infrared Spectometry (FTIR) has been developed in collaboration with S. Rein and J.

Geilker and is also described in references [54, 57, 60]. It is especially useful if standard measurements of the ingot under investigation, as is often the case, comprise the characterization of the interstitial oxygen [O_i] and substitutional carbon [C_s] densities with the help of FTIR, because the same set of data can be taken.

In absence of external carrier generation, i.e. in the dark, the net doping p_0 approximately equals the free carrier concentration. Free carriers absorb light having an energy smaller than the bandgap, that is in the far infrared spectral wavelength range. For the free carrier absorption (FCA), the absorption coefficient α_{FC} can be described as a function of p_0, the wavelength λ and the doping-dependent mobility $\mu(N_A,N_D)$ with the following expression [29, 61]:

$$\alpha_{FC}(p_0,\lambda) = c_{FCA}\frac{p_0}{\mu(N_A,N_D)}\lambda^2 \qquad (4\text{-}6).$$

Here, c_{FCA} stands for a constant which is obtained by fitting the equation to literature data on absorbance versus p_0 [62]. Two different fits have been reported with the weighting function putting emphasis either on the lower or on the higher net doping concentrations: at lower net doping concentrations around 10^{16} at/cm^3, c_{FCA} (λ=5 µm) has been determined to 4.17x10^{-12} m^2/Vs on p-type and to 5.63x10^{-12} m^2/Vs on n-type silicon [63]; for higher net doping concentrations >2x10^{17} at/cm^3, c_{FCA} (λ=5 µm) was determined to be 3.8x10^{-12} m^2/Vs on p-type and as 3.1x10^{-12} m^2/Vs on n-type silicon [57].

Replacing the carrier mobility from eq. (4-3) yields:

$$\alpha_{FC}(p_0,\lambda) = c_{FCA}\left(q\rho p_0^2\right)\lambda^2 \qquad (4\text{-}7).$$

The free carrier absorption coefficient α_{FC} increases quadratically with the wavelength λ, therefore the absorption is especially strong in the far infrared wavelength range detected in FTIR measurements.

The transmittance directly obtained with FTIR consists of light that was not reflected (expressed by the wavelength-dependent reflection $R(\lambda)$) or absorbed and reads as [40]:

$$T(p_0,\lambda) = (1-R(\lambda))^2 \exp\left[-(\alpha_{Si}+\alpha_{Def}+\alpha_{FC})d\right] \qquad (4\text{-}8)$$

with d being the sample thickness and α_{Si}, α_{Def} und α_{FC} the wavelength-dependent absorption coefficients of the silicon lattice, of defects and of the free carriers.

The correlation between transmission and absorption leads to the following equation of the absorbance $A(p_0,\lambda)$ of a FTIR measurement:

$$A(p_0,\lambda) := -\log\left[T(p_0,\lambda)\right] = -2\log\left[1-R(p_0,\lambda)\right] + \alpha\log[e]d \qquad (4\text{-}9)$$

with $\alpha = \alpha_{Si} + \alpha_{Def} + \alpha_{FC.}$.

To extract the FCA-based part of the FTIR spectrum, the contributions of the silicon lattice and defects to the absorption α_{Si} and α_{Def} have to be eliminated. This is done by subtracting a thickness-corrected reference spectrum of a FCA-free silicon sample from the

spectrum under investigation, assuming that α_{Si} is the same in both samples and the influence of absorption due to impurities α_{Def} is small:

$$A_{fit} = A_{sample} - A_{ref} \frac{d_{sample}}{d_{ref}} \qquad (4\text{-}10).$$

The reference sample is selected according to the requirement that α_{FC} equals zero, i.e. p_0 is very low.

In the following, it has to be assumed that the wavelength-dependency of the reflectance R of both samples is negligible, which then gives a simple offset C to the spectrum A_{fit}. As a result, the fit function of the FCA-FTIR method has only one unknown parameter p_0:

$$A_{fit}(p_0, \lambda) = C + \underbrace{[c_{FCA} \log(e) q]}_{Const.} [d_{sample}\, \rho_{sample}] p_0^2\, \lambda^2 \qquad (4\text{-}11).$$

Two example measurements are pictured in *Figure 4.3*. The continuous colored lines show the original FTIR spectra of two differently compensated samples (green and blue) and the reference sample (red line). As is the rule for FTIR measurements, all samples had been mechanically polished on both surfaces in order to avoid distortion due to surface effects. For reference, a FZ silicon wafer of high resistivity (15 Ωcm) was taken in order to ensure negligible FCA. The spectra of both compensated samples show a continuous absorbance increase with increasing wavelength due to free carrier absorption as well as two peaks at around 9 µm and 16 µm, which can be attributed to oxygen defects and phonon-phonon interaction.

In the next step, the absorbance data at the defect peaks are eliminated and the reference spectrum is subtracted (dashed lines). The resulting curves can be fitted with the help of equation (4-11) (black lines).

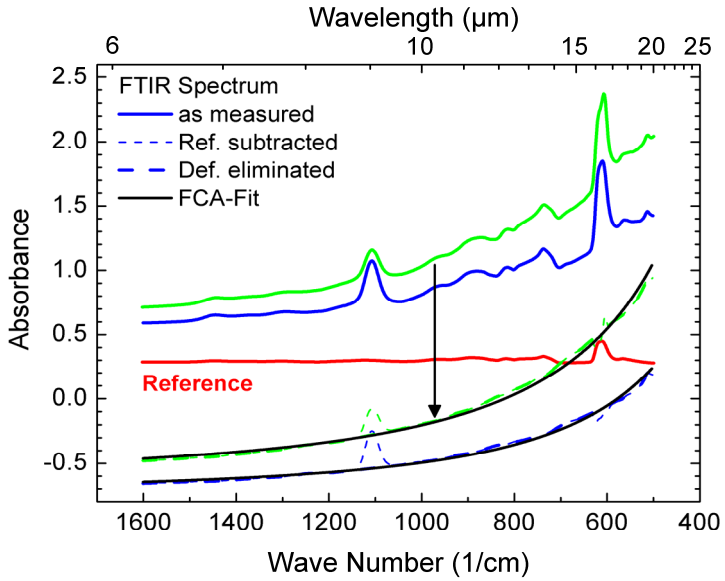

Figure 4.3: Example for the determination of the net doping concentration via FCA-FTIR. After ref. [57].

The accuracy of the FCA-FTIR method for the determination of the net doping concentration as well as the accurateness of the deduction of the acceptor concentration N_A via eq. (4-4) were tested with a set of FZ wafers (d=250 µm) with p-type base resistivities[3] ranging between 0.1 Ωcm and 100 Ωcm. The samples were not compensated, therefore $p_0=N_A$.

As reference method, the doping concentrations of the FZ samples were calculated via eq. (4-1), taking the measured base resistivities and modeling the majority (hole) mobility $\mu_C(N_A)$ according to the generally accepted form published by Caughey and Thomas [64].

In *Figure 4.4*, the p_0-values obtained by using FCA-FTIR are plotted versus the reference calculations. In addition, the acceptor concentration N_A determined via Macdonald's approach (section 4.2.C) on the same material is shown[4]. For base doping concentrations between approx. $1x10^{16}$ at/cm^3 and $3x10^{17}$ at/cm^3, both FCA-FTIR and FeB-pairing measurements are in good or very good accordance with the expected values. As the net doping concentration is expected to lie mainly within this range, both techniques are therefore well suited for our purpose.

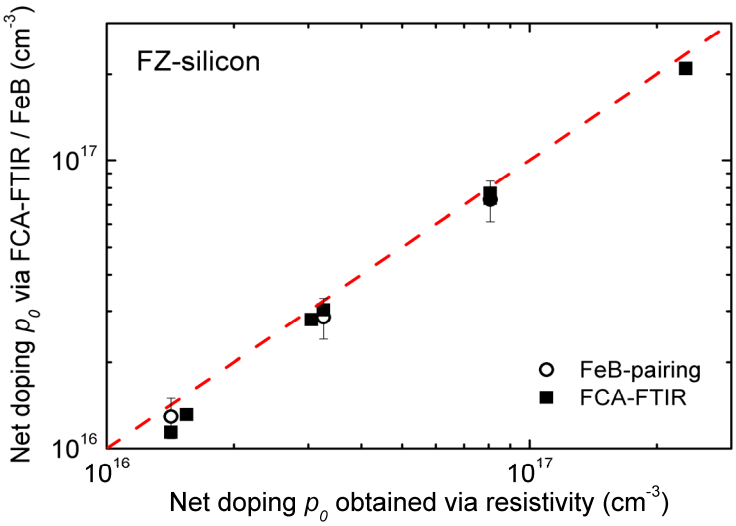

Figure 4.4: Accuracy of FCA-FTIR (closed symbols) and FeB-pairing (open symbols) measurements of the net doping density $p_0=N_A$ versus the calculation of p_0 with the help of equation (4-1). The measurements were performed on p-type FZ wafers of varying base resistivities. The dashed line denotes the bisecting line. After ref.s [54, 60].

However, for higher and / or lower net doping concentrations, the analysis of both measurements becomes tricky. For p-type doping levels significantly above $1x10^{17}$ cm^{-3}, the linearity with p_0 assumed in eq. (4-6) is no longer valid [65]; however, the deviation from linearity for p-type material remains relatively low. In addition, at doping concentrations $>5x10^{17}$ cm^{-3}, the free carrier absorption is very strong, which can lead to the saturation of the FTIR detector. One possible solution of the latter problem is to decrease the thick-

[3] Measurements performed by I. Reis, analyzed by J. Geilker.
[4] Measurements and analsis by J. Geilker.

ness of the samples and thus the absorbance. In addition, the minority carrier lifetime, used in the FeB-pairing method, decreases with increasing doping concentration. In the present case, the carrier lifetime hardly changed during the FeB-pairing for doping concentrations >1x10^{17} cm^{-3}, thus preventing the analysis of the association time constant τ_{assoc}.

At the other end of the doping concentration scale, the free carrier absorption becomes small compared to the corrections subtracted and the fitting procedure yields incorrect values for p_0. This can for example be seen in *Figure 4.4*: For the sample with the lowest doping concentration, which had been calculated to have a boron concentration of 1.42x10^{16} cm^{-3}, FCA-FTIR yielded a value of 1.14x10^{16} cm^{-3} deviating by 20%. Again, this problem can be overcome by adjusting the thickness of the sample; thicker samples allow for measurements of lower net doping concentrations (see section 4.2.3).

At the Fraunhofer ISE, the FTIR spectra can be obtained most rapidly when a special sample geometry is provided. This not always being the case, for some analyses of mc-Si UMG material a CV- setup has been used.

4.2.2 Base resistivity distribution

One of the fundamental wafer specifications is the base resistivity, directly related to the net doping concentration via equation (4-3). For solar cell process purposes, resistivity values typically range between 0.8 – 1.2 Ωcm, though with a relatively wide window regarding normal use in standard processes.

At high net doping concentrations, the minority carrier lifetime suffers due to the proportionality of the SRH mechanism, equation (3-19). At even higher net doping, the Auger limit may be reached.

On the solar cell level, decreased minority carrier lifetime translates into a lower short circuit current because less minority carriers are collected by the pn-junction due to the decreased diffusion length [32]. However, as the saturation current J_0 is inversely proportional to the net doping of emitter and base, it is expected that J_0 decreases in highly doped material, resulting in higher open circuit voltages [32]. These predictions of course always depend on the actual solar cell processes.

In UMG-Si, the simultaneous presence of comparable amounts of boron and phosphorus leads to the problem that the base resistivity / the net doping concentration can vary strongly along the ingot height, an effect brought about by the different segregation coefficients (k_{eff}(B)=0.8, k_{eff}(P)=0.35, *Table 2.2*) during crystallization.

A simulated example is shown in *Figure 4.5*: Starting with equal initial concentrations of [B] and [P] of 1x10^{16} at/cm^3 in the melt, the segregation following equation (2-5) leads at the beginning to a higher boron content [B]>[P]. However, as the crystallization continues, the silicon melt is more enriched by phosphorus atoms than by boron. Therefore, the incorporation of phosphorus even gets ahead at around 85% crystallized ingot height. At this point, the conduction type changes from p- to n-type and the net doping concentration [B]-[P]=p_0=N_A-N_D becomes negative.

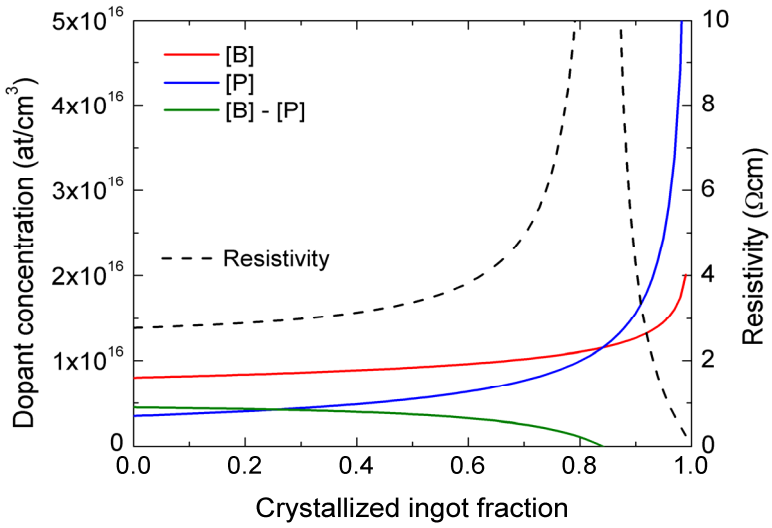

Figure 4.5: Simulated boron and phosphorus concentrations using the Scheil equation (2-5), the net doping concentration and the resulting base resistivity distribution versus crystallized ingot fraction.

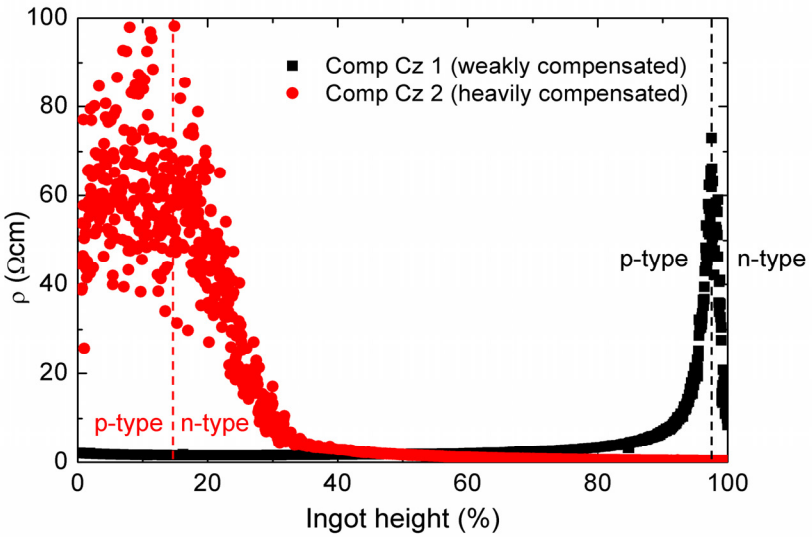

Figure 4.6: Resistivity distribution versus ingot height of the intentionally compensated Cz-grown ingots "Comp Cz 1 and 2"[5].

Following the reciprocal of the net doping p_0, the base resistivity shows a singularity when p_0 approaches zero.

Although solar cell processes in general react relatively benignly to varying base resistivities, they are optimized for p-type conductivity. In the above example, approx. the top 20% of the ingot would have to be discarded.

Therefore, the boron and phosphorus concentrations have to be adjusted for maximum ingot yield, see e.g. Enebakk et al. [66]. Alternatively, it has been proposed to intentionally add a third dopant species such as Ga or As, both possessing lower segregation coef-

ficients and thus counteracting the strong [P]-increase at the end of the crystallization [67-70].

In *Figure 4.6*, the resistivity distributions of both intentionally compensated Cz-grown crystals are shown, exemplifying the impact of similar boron and phosphorus contents[5]. While the weakly compensated ingot "Comp Cz 1" is largely p-type (at 50% ingot height ca. 1.9 Ωcm (p-type)) with the type changeover close to the tail end, the base resisitivity of the heavily compensated crystal "Comp Cz 2" turns to n-type conduction very early during crystallization (at 50% ingot height ca. 1.5 Ωcm (n-type)). The scatter in the data is due to a very inhomogeneous crystallization front, leading to strong lateral variations in the base resistivity at the beginning of solidification.

The UMG-Si ingots investigated in the frame of this thesis show varying base resistivities: The Cz-grown ingots "UMG Cz 1 and 2" have resistivities between 0.5 Ωcm and 0.75 Ωcm without any considerable variation along the ingot[6]. A similar distribution of 0.8 – 1.1 Ωcm was measured on the ingot "UMG mc 2", without any change in the conduction type on the entire height of the ingot. On the other hand, the base resistivity of the multicrystalline UMG-Si block "UMG mc 1" ranges between 0.25 Ωcm at the block bottom and 0.5 Ωcm in the block center, with a distinct resistivity increase at the conduction type changeover around 80% ingot height[7].

4.2.3 Dopant concentration

While the measurement of the base resistivity is simple, some effort is needed for the determination of the doping concentrations p_0, N_A and N_D, which form the basis for many material analyses. In the following, the results obtained on the intentionally compensated Cz ingots and on the UMG-Si blocks are discussed.

Since the FeB-pairing method for the determination of N_A does not work in the n-type parts of compensated ingots, in the case of the reference measurements along the lightly and heavily compensated Cz crystals "Comp Cz 1 and 2", the phosphorus concentration was measured via GDMS by external institutions along the entire length of both ingots, thus ensuring consistent results. Being the heavier of both dopant elements, it is expected that the GDMS-measurement of [P] is more reliable than that of [B]. The consistency of the phosphorus concentration measurements was checked by having the same set of experiments performed also by a second external institute. The results were found to agree within a maximum error of 15% on [P].

[5] Inline base resistivity measurements performed by J. Geilker.
[6] Unfortunately, the ingot tail end had been discarded by the crystal grower shortly after crystallization and was therefore not available for the investigation.
[7] Base resistivities commissioned by the project consortia for the general use in the research projects.

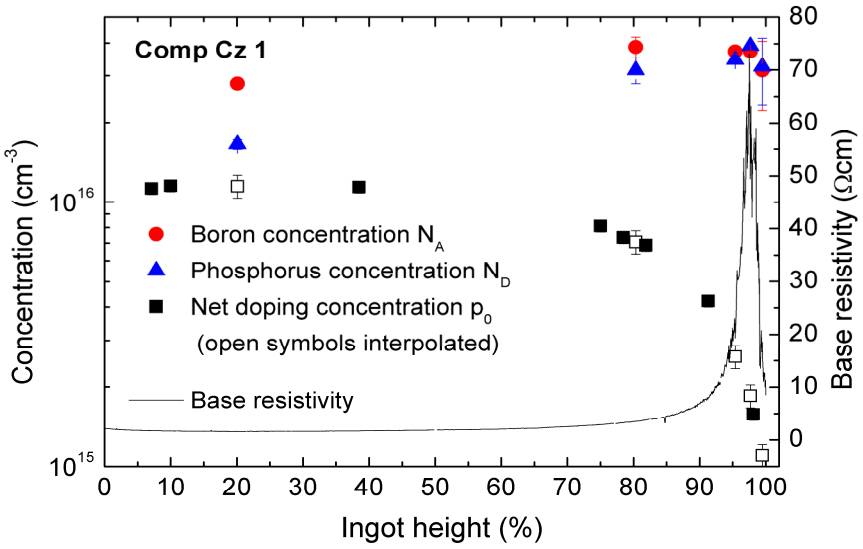

Figure 4.7: Doping concentrations versus ingot height of the weakly compensated ingot "Comp Cz 1". p_0 was measured via FCA-FTIR, N_D was determined with the help of GDMS and N_A was calculated via eq. (4-2). After ref. [60].

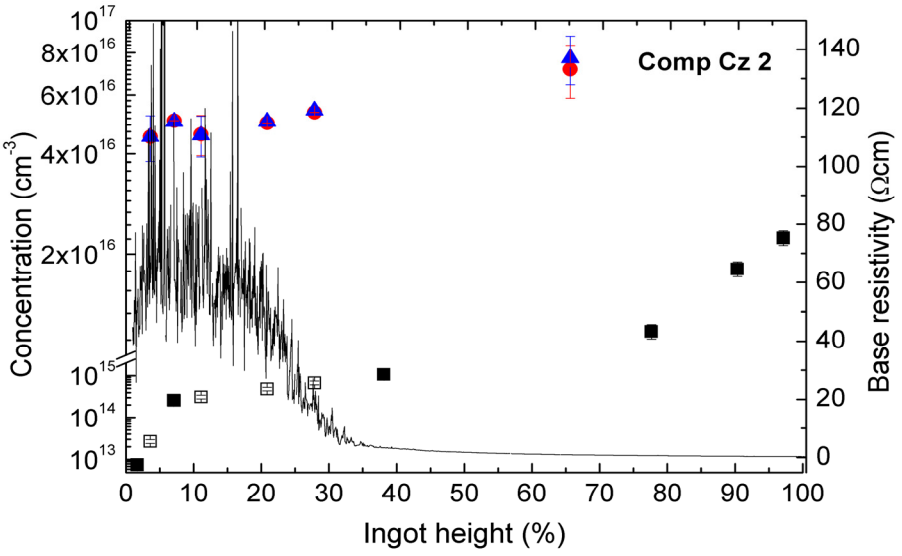

Figure 4.8: Doping concentrations versus ingot height of the heavily compensated ingot "Comp Cz 2". The symbols bear the same meaning as in Figure 4.7. After ref. [60].

The net doping concentration was determined via FCA-FTIR on 1.7-1.9 mm thick samples. Simultaneously, the interstitial oxygen and the substitutional carbon concentration were measured, see section 4.3.3[8]. The data of the net doping concentrations were interpolated in order to estimate p_0 at the position of the GDMS samples; then, the boron concentrations were calculated.

[8] Measurements performed by I. Reis, analyzed by J. Geilker.

The results are shown in *Figure 4.7* for the weakly compensated and in *Figure 4.8* for the heavily compensated ingot.

In both crystals, the decrease of the net doping concentration towards the conductivity type changeover is in good agreement with the measured increase in the base resistivity. In general, the boron and phosphorus concentrations increase as expected with solidified ingot fraction. However, close to the type changeover, the measured values fluctuate, tending to be lower than at lower ingot height.

This is remarkable because one would expect that the determination of the phosphorus concentration via GDMS is independent from the boron concentration. However, when the phosphorus concentration approximately equals the boron concentration, a lower [P]-content is detected. This could be hypothetically explained by the formation of boron-phosphorus pairs which do not break during the measurement. Then, the GDMS-system would detect a molecule possessing the mass of the sum of the boron and phosphorus atoms which would not be identified as such. However, there are only indirect indications in literature supporting the hypothesis of B-P-pairing [43, 50].

The net doping and the dopant concentrations of the 100% UMG-Si containing Cz crystal "UMG Cz 1" and of Cz ingot "UMG Cz 2", which contains a blend of 50% UMG-Si and 50% high-purity silicon (without additional doping) are shown in *Figure 4.9*. The net doping concentration was measured via FCA-FTIR[9] and the boron concentration with the help of FeB-pairing[10]; from both measurements, the phosphorus concentration was computed.

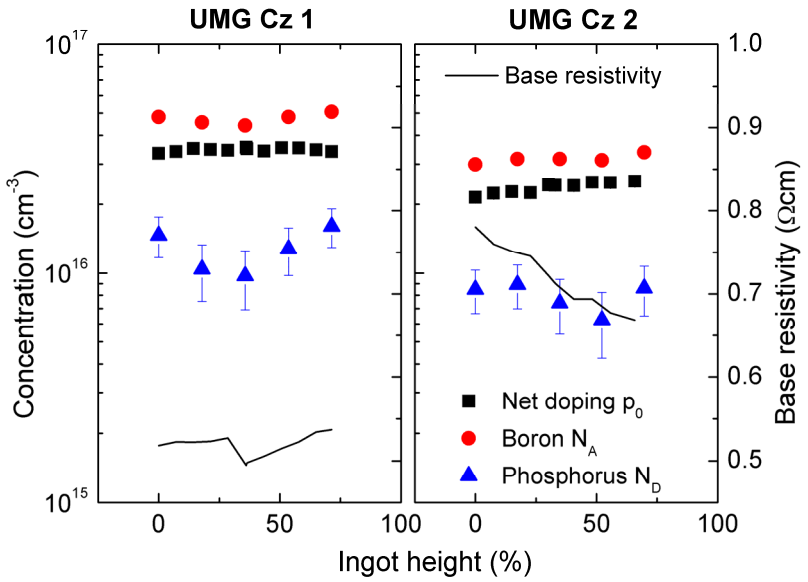

Figure 4.9: Net doping and dopant concentrations and the base resistivity versus ingot height of both UMG-Si containing Cz ingots. After ref. [60].

[9] Measurements by I. Reis, analyzed by J. Geilker.
[10] Measurements and analysis by J. Geilker.

As expected from the base resistivity measurements (black lines), the doping concentrations vary only slightly along the ingot length. While the boron content in the 100% UMG-Si ingot Cz 1 is approximately 4-5x10^{16} at./cm^3, the phosphorus concentration ranges approx. between 9x10^{15} -2x10^{16} at/cm^3. As a result, the net doping concentration is in the range of 3-4x10^{16} cm^{-3}.

The values measured at the UMG-Si blend ingot "UMG Cz 2" validate this assessment. Containing about 50% of undoped virgin grade silicon, the doping concentrations and the resulting net doping concentrations are about half of the amount found in the "UMG Cz 1" ingot.

Assuming that Scheil's model is valid and taking the respective segregation coefficients for boron and phosphorus, the measured dopant distributions in the UMG-Si Cz ingots give a hint at the initial B- and P-concentrations in the UMG silicon feedstock after refinement, but before the final crystallization. The boron concentration thus is evaluated to 5-7x10^{16} at/cm^3; the phosphorus concentration adds up to 2.5-4.5x10^{16} at/cm^3. During solidification, the conductivity type changeover probably occurred at around 95% of the ingot height, which would have been left in the pot scrap after Cz pulling.

Therefore, the observed boron and phosphorus concentrations obviously allow for 100% p-type silicon crystals, with relatively low base resistivities around 0.5 Ωcm.

For the multicrystalline UMG silicon crystal "UMG mc 2", made from 100% UMG-Si feedstock, similar experiments were carried out.

The results are shown in *Figure 4.10*. The net doping concentration was determined via ECV measurements. For the boron content N_A the FeB-pairing method was used[11].

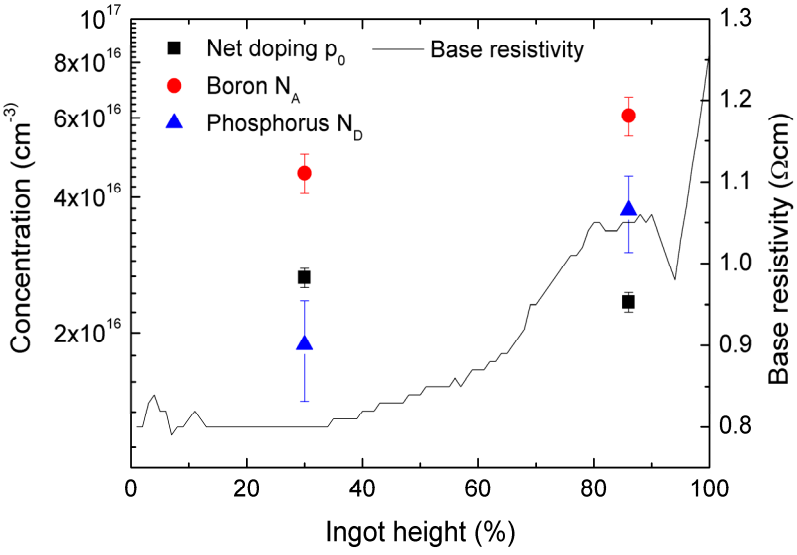

Figure 4.10: Net doping and dopant concentrations and base resistivity versus ingot height of ingot "UMG mc 2".

[11] Measurements performed by F. Schindler.

The boron and phosphorus concentrations are approximately in the same range as in the crystal "UMG Cz 1": While a boron concentration of 4-6x10^{16} at/cm^3 was measured at different ingot heights, the ingot contains about 2-4x10^{16} cm^{-3} phosphorus atoms which is slightly more than in the 100% UMG Cz crystal; in total, the net doping concentration in the mc-UMG-Si ingot ranges between 2-3x10^{16} cm^{-3} in about 90% of the entire ingot.

From these measurements, the following initial boron and phosphorus contents in this silicon feedstock can be deduced: [B]~5.2x10^{16} at/cm^3 and [P]~3x10^{16} at/cm^3, both approximately equal to the concentrations measured in "UMG Cz 1". It follows that the conductivity type changeover should occur at a similar ingot height. Although from the multicrystalline block only a few millimeters had been taken off from the top, the ingot does not contain the type changeover, supporting the result that with these initial boron and phosphorus contents, entirely p-type blocks can be produced from UMG silicon.

In summary, our investigations on UMG silicon have shown that the boron and phosphorus concentrations which are left after current UMG-purification processes, although both being a factor of more than 5 larger compared to standard silicon feedstock, are relatively well suited for solar cell purposes. They are well calibrated [66]: slightly more or less of only one dopant species would result in either a premature type changeover, thus decreasing the ingot yield, or the base resistivity would become intolerably low.

A higher base resistivity and a reliable ingot yield of ~100% can therefore only be obtained when both dopant concentrations are reduced at the same time.

4.2.4 Impact on the majority carrier mobility

Having determined the base resistivity, the net doping p_0, the acceptor and donor concentrations N_A and N_D, we can now evaluate the conductivity mobility as a function of the immobile scattering centers $\mu_C(N_A,N_D)$. The aim is to compare our measured values with the existing mobility models – the model by Caughey and Thomas [64] and by Thurber [71] for noncompensated silicon, and the model published by Klaassen [72] explicitly taking compensation into account – and to assess their quality because a mobility model is needed in several fundamental electrical wafer and solar cell characterization techniques.

In a second step, the Hall mobility $\mu_H(N_A,N_D)$ of the compensated material has been determined in Hall measurements, which differs from μ_C by the Hall scattering factor r. Taking both mobility measurements, the ratio r can be computed. Although the knowledge of the scattering factor is essential for the analysis of Hall measurements, data in literature, particularly on compensated silicon, is scarce. With the theoretical knowledge of r the conductivity mobility could be calculated from Hall measurements if necessary. If the Hall factor proved to be independent from the dopant densities, conductivity mobilities could be directly determined via Hall mobility measurements without having to worry about the analysis of the net doping density.

In order to visualize the difference between the conductivity and the Hall mobility[12], in *Figure 4.11* both measurands obtained on p-type FZ wafers ("FZ 1") are plotted versus

[12] Measurements and analysis by J. Geilker.

the boron concentration. With increasing dopant density, the mobility of the majority carriers (and that of the minority carriers, which is not examined here) decreases due to the scattering at ionized dopants. This tendency is seen by both techniques. However, the Hall mobility is in general lower than the conductivity mobility, described by the Hall factor. The ratio $r=\mu_H/\mu_C$ is plotted in the lower graph. At a boron density of around $1x10^{16}$ at/cm^3, the ratio is about 0.6, increasing to 0.7 at high doping concentrations.

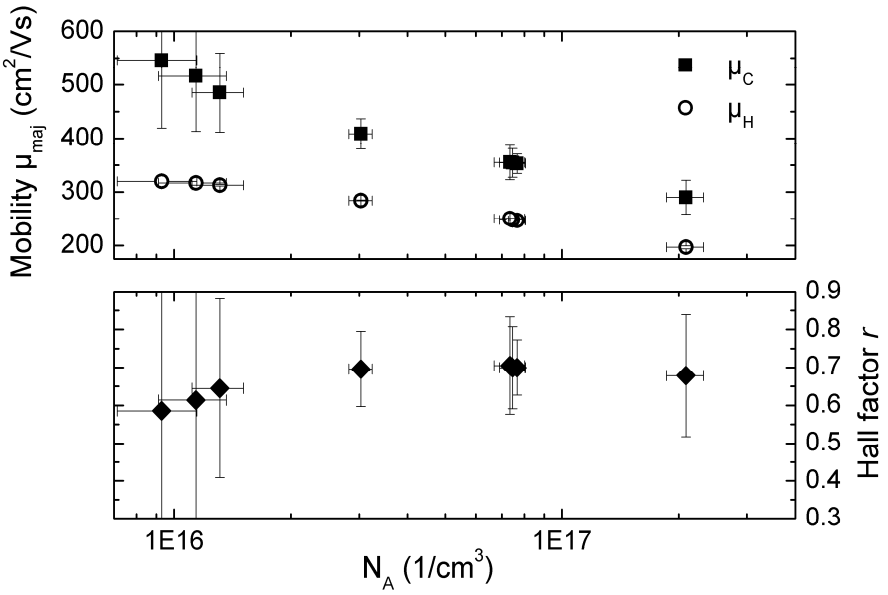

Figure 4.11: Top: Comparison of the conductivity mobility μ_C with the Hall mobility μ_H of the majority carriers (holes) measured on FZ wafers, plotted versus the boron concentration. Bottom: Hall factor r calculated from the above data. After ref. [54].

The graph also illustrates the problem inherent to mobility measurements, complicating the determination of the Hall factor: As explained in section 4.2.1, the accuracy of the determination of the net doping density depends strongly on the sample properties. For example for the FCA-FTIR technique, the measurement sensitivity decreases with decreasing p_0 if no precautions are taken; this leads not only to larger errors in the abscissa, but following eq. (4-3) also to increased errors in the ordinate of the mobility measurements, seen e.g. at $N_A<2x10^{16}$ at/cm^3 in *Figure 4.11*. After error propagation, the accurateness of the Hall factor is acceptable only when the error in both mobility measurements is relatively small (<10%).

It is therefore essential to take great care in the determination of the doping concentrations. Fortunately, the concentrations in UMG-Si samples are usually relatively high, being in a regime where the described techniques are most precise. It was hence possible to assess the Hall and conductivity mobilities of the compensated as well as the UMG-Si samples with relatively good accuracy.

In general, at a given base resistivity, i.e. net doping concentration p_0, the carrier mobilities are lower in compensated materials than in silicon from standard feedstock. This is valid for the conductivity as well as for the Hall mobility, both plotted versus p_0 in *Figure 4.12*. Here, the black symbols represent the reference material and the colored symbols

stand for the compensated wafers. Shown are the results from the UMG-Si Czochralski[13] and multicrystalline wafers[14] as well as the values obtained on the weakly compensated p-type crystal "Comp Cz 1"[13]. Since the resistivity of UMG-Si wafers are aimed at acceptable base resistivities for solar cell processes, these materials contain similar net doping concentrations. For comparison, reference measurements include the FZ wafers with a wide range of base resistivities and one standard reference multicrystalline wafer with a base resistivity of 0.92 Ωcm[14].

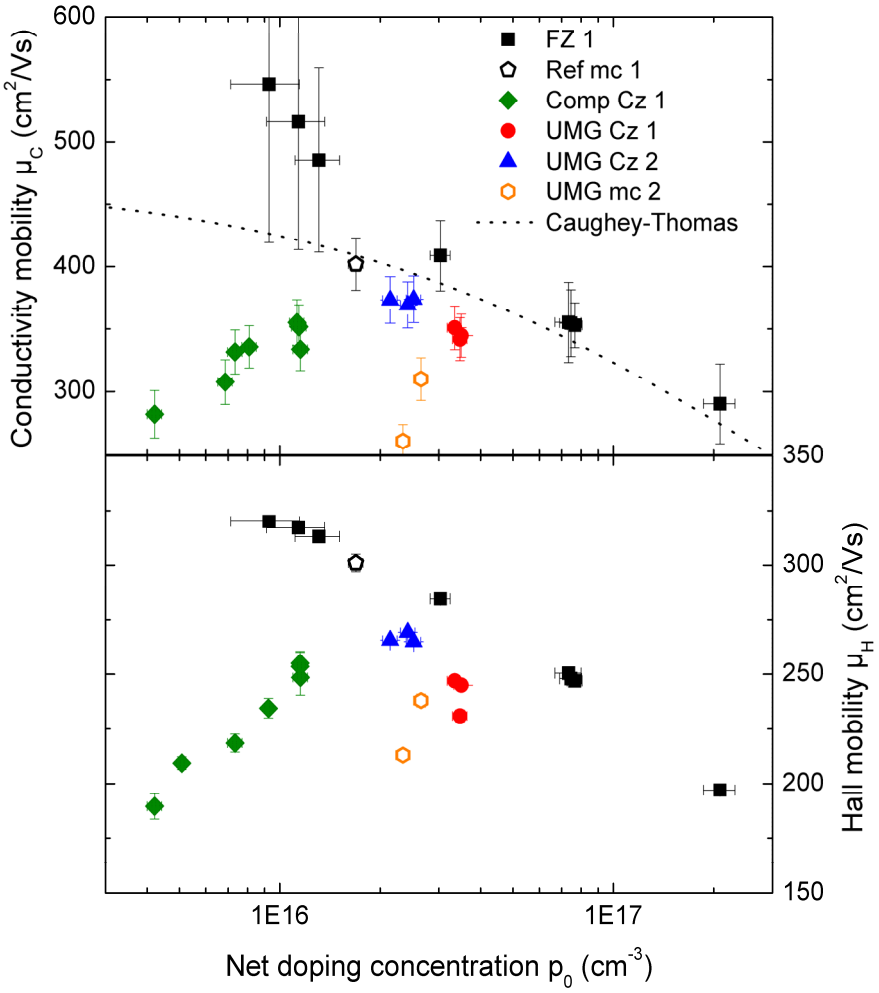

Figure 4.12: Conductivity (top) and Hall (bottom) mobility of the majority carriers (holes) versus the net doping concentration in different materials. The conductivity mobility is compared to the model by Caughey & Thomas [64].

The dotted line shows the calculated μ_C after the model by Caughey and Thomas [64], which is for example implemented in the widely used PC1D simulation tool.

In order to compare the measurements with modeled mobilities, our values for the conductivity mobility are plotted versus the sum of ionized impurity scattering centers, i.e. the ionized doping atoms N_A+N_D in *Figure 4.13*.

[13] Measurements by J. Geilker.
[14] Measurements by F. Schindler.

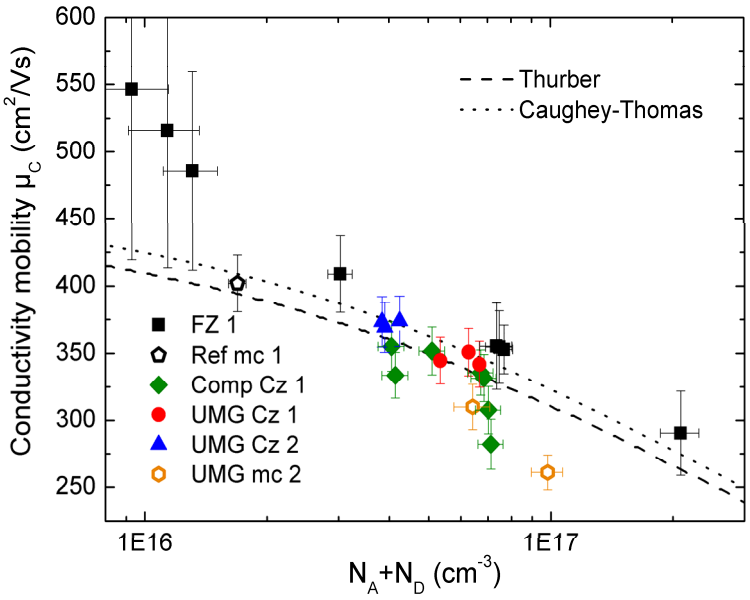

Figure 4.13: Compilation of measured conductivity mobility of the majority carriers (holes) in different materials versus the sum of the boron and phosphorus concentrations. For comparison, the plot contains the mobility calculated according to the models by Thurber [71] and Caughey-Thomas [64].

The lines represent predicted mobilities by the model of Thurber [71] and Caughey & Thomas [64] (dashed and dotted lines, respectively). Both models do not take differences in the scattering cross sections of different dopant species into account.

The models by Thurber and by Caughey & Thomas predict correctly the measured conductivity mobilities of the uncompensated reference wafers within the measurement error. The impact of phosphorus on the mobility of wafers from both UMG-silicon Cz crystals is relatively small; their measured values agree relatively well with both models. For the intentionally compensated samples from ingot "Comp Cz 1", the data is consistent with the modeled mobilities only for low dopant concentrations. With increasing sum of scattering centers N_A+N_D, the measurement yields rapidly decreasing mobility values; this is true for the relatively highly compensated multicrystalline UMG-Si wafer from 86% ingot height, too. These values deviate significantly from both Thurber's as well as Caughey & Thomas' models.

Since for increasing dopant concentrations the traditional models fail, our data is compared to the more realistic approach by Klaassen, who includes a term which takes scattering of free carriers at dopant atoms of both signs into account. In *Figure 4.14*, the conductivity mobility is plotted versus the boron concentration. The influence of the compensation by the different phosphorus concentrations N_D in the various materials were calculated, shown by the continuous lines. According to Klaassen, the decrease of the conductivity mobility compared to uncompensated reference material should be measurable for N_D>1x10^{16} at/cm^3.

Similar to Thurber and Caughey & Thomas, Klaassen's model predicts μ_C correctly for the reference silicon wafers as well as for the lightly compensated samples from the UMG-Si Cz crystals. However, for higher compensation with N_D>2-4x10^{16} at/cm^3, present in the

intentionally compensated Cz crystal as well as in the multicrystalline mc-Si samples, Klaassen overestimates the conductivity mobility by almost 20%.

Due to the indirect nature of the conductivity mobility measurement, it might be suspected at a first glance that the observed divergence for high dopant concentrations comes about by an underestimation of the measurement error. However, Hall measurements, which have been performed with more exactness, show the same unexpectedly low values at high phosphorus concentration.

Therefore, the reason for the divergence between theory and experiment is analyzed in the following in more detail.

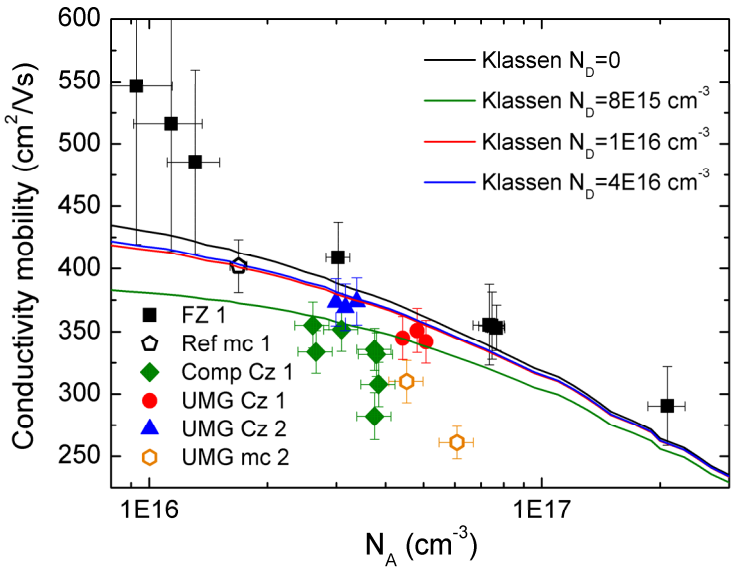

Figure 4.14: Compilation of measured conductivity mobility of the majority carriers (holes) in different materials versus the boron concentration. For comparison, the plot contains the mobility calculated according to the model by Klaassen [72]. The phosphorus concentration N_D was varied according to the minimum (blue line) and maximum (green line) phosphorus content measured on the compensated samples (see preceding sections). Roughly, the colors of the symbols and the simulated N_D values correlate.

The decisive parameter set for the mobility in p-type silicon is not the phosphorus concentration alone. In *Figure 4.15*, the measured conductivity mobility is plotted versus both, the sum of ionized dopant atoms and the net doping concentration: At a given sum of boron and phosphorus atoms, the mobility decreases with increasing N_A+N_D at a given net doping concentration, with the exception for the lowest dopant concentrations around $1x10^{16}$ at/cm^3. Furthermore, it decreases as well with decreasing $N_A-N_D=p_0$. For clarification, an interpolation of our data is shown in *Figure 4.16*.

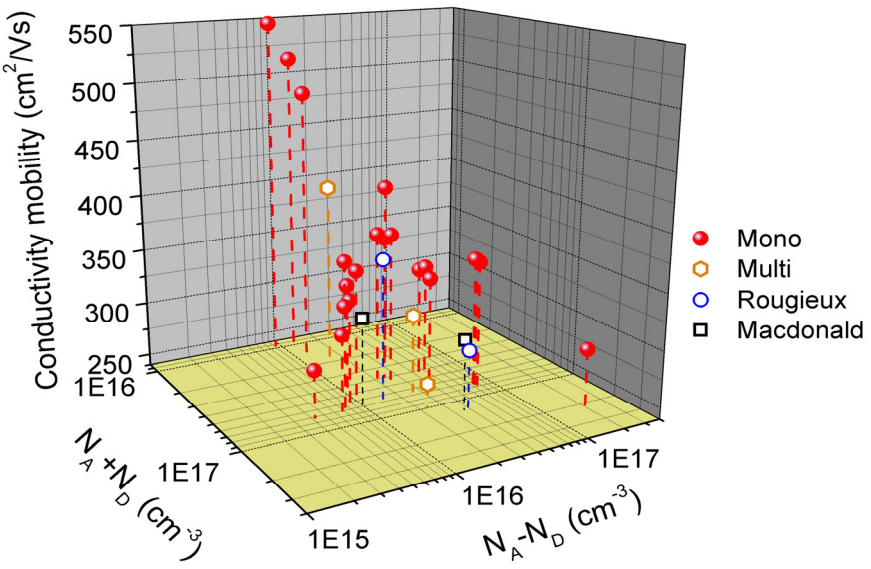

Figure 4.15: Three-dimensional plot of the conductivity mobility versus the sum of both dopant species and the net doping concentration.

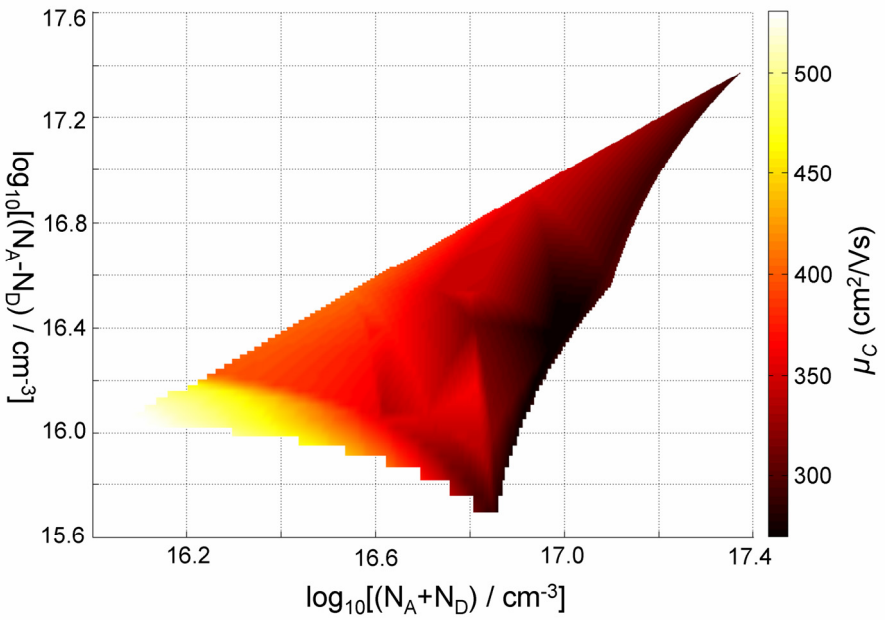

Figure 4.16: Interpolation of the hole conductivity mobilities displayed in Figure 4.15. The values decrease with increasing sum of ionized dopants and with decreasing net doping concentration.

Depending on the actual content of boron and phosphorus atoms in compensated silicon, the influence of either the sum of ionized dopant atoms or of the net doping concentration prevails, determining the conductivity mobility.

To substantiate this result, conductivity mobility measurements on compensated p-type silicon recently performed by other groups are taken for comparison: Macdonald et al. [73] and Rougieux et al. [74] claim that their measured hole mobilities coincide well with Klaassen's model; however, both groups rely on data obtained on only two compensated samples (measurements are contained in *Figure 4.15*). In both cases, the mobility meas-

ured on one sample differs from Klaassen's prediction by more than the measurement uncertainty but follow the same trend as our data.

Our finding is also supported by recent investigations on compensated p-type silicon published by Veirman [75] and by Lim et al. [53]. The latter authors determined the net doping concentration and the conductivity mobility versus the ingot height of a multicrystalline UMG-Si block, comprising a type changeover at around 80% block height. Therefore, some mobility measurements were performed on wafers of very low net doping concentrations. In this region, μ_C decreases strongly: Starting at the bottom of the ingot with a value above 200 cm^2/Vs (which is very low, indicating that both, the boron and the phosphorus concentration – which were not communicated – are very high), the conductivity mobility is reduced to ~100 cm^2/Vs at the type changeover. The decline is not linear; this suggests that it is not only the sum (N_A+N_D), which determines the mobility, but also the net doping concentration, being consistent with our results. Lim et al. attributed this decrease to reduced screening of ionized scatter centers by free charge carriers and fitted the experimental values convincingly to a formula introduced by Brooks and Herring [76] which relates both, the sum of ionized dopant atoms and the net doping concentration to the conductivity mobility via:

$$\mu_{C,maj} = \frac{a_{maj}}{\left(N_A + N_D\right)\left(\ln\left(\frac{b_{maj}}{N_A - N_D}\right)\right)} \qquad (4\text{-}12),$$

with a_{maj} and b_{maj} as free parameters.

Although the use of the Brooks-Herring model points into the right direction, it is impossible to find a parametrization of equation (4-12) which correctly predicts the conductivity mobility of *different* compensated materials as it neglects the varying contributions to the carrier scattering e.g by the silicon lattice and electron-electron / hole-hole interactions provided by the more sophisticated descriptions such as Klaassen's model.

As we want to hold on to this relatively successful model, the question arises: What is the cause for the deviation of the mobility measurements in compensated material compared to Klaassen's description and how can it be overcome?

Screening of ionized impurities by free carriers is integrated into Klaassen's model for all relevant scattering mechanisms: Majority and minority impurity scattering as well as interactions between free carriers. For high free carrier concentrations, the Brooks-Herring formula is used; however, approaching zero free carriers ($N_D \rightarrow N_A = p_0 \rightarrow 0$ in the dark), the collision cross section cannot be computed with the Brooks-Herring model. To resolve this problem, Klaassen describes the scattering at low free carrier densities with the model by Conwell & Weisskopf [77] which converges for zero free carriers.

As a result, Klaassen needs to implement the collision cross sections into the different scattering mechanisms by using a weighted sum of Brooks & Herring as well as Conwell & Weisskopf approaches, leaving four free parameters to be adjusted to experiments. This parametrization needs to balance sensitively between low and high carrier concentrations.

Klaassen proposes a set of parameter values which are fitted to minority and majority mobility data from both p- and n-type silicon as well as from intrinsic pin-structures. It is

this set of parameters which was used for the calculation of the conductivity mobility in *Figure 4.14* and presumably also in the various treatments of compensated silicon in recent literature. However, Klaassen's fit does not include compensated silicon samples; it is quite likely that the balance between the capture cross sections mathematically formulated by Conwell-Weisskopf and Brooks-Herring changes when the amount of ionized atoms increases with N_A+N_D while the free carrier concentration decreases with N_A-N_D.

It seems therefore that the suggested parametrization well suited for measurements on uncompensated wafers is not adequate for increasingly compensated silicon wafers which results in wrong predictions of the conductivity mobility. It follows that an adjustment of the parameters is needed; the necessary conductivity mobility measurements on many differently compensated samples were however beyond the scope of this thesis.

At last, we determined the Hall scatter factor r[15], shown in *Figure 4.17* and *Figure 4.18*, where they are compared to data from Lin et al. [78] and Veirman et al. [75] on uncompensated p-type monocrystalline silicon, and to values on compensated p-type Cz-silicon published by Rougieux et al. [74]. In addition, Lin's theoretical prediction of the dependency on the dopant concentration is shown for comparison.

Our measurements on the non-compensated monocrystalline samples "FZ 1" covering a wide range of boron concentrations of $1x10^{14}$-$1x10^{18}$ at/cm^3 lie between 0.6 and 0.7 and are slightly lower than measurements published by Lin [78] and Veirman [75] on uncompensated p-type silicon while "Ref mc 1" (r=0.75) fits well to these data. However, the experimental error in particular on measurements of the FZ wafers is large and therefore prohibits to draw any conclusions.

Generally, the Hall factor of compensated Cz-wafers tends to be lower than r-values published on uncompensated material and ranges between 0.65-0.75. Plotted versus the sum of ionized dopant atoms in *Figure 4.17*, r seems to decrease with increasing (N_A+N_D) while the graph of the Hall factor versus the net doping concentration in *Figure 4.18* suggests that in compensated material, lower net doping densities lead to lower values for r. These tendencies are supported by measurements from Rougieux et al. [74].

In fact, this behavior of the Hall scatter factor in compensated p-type silicon mirrors the observed extreme decrease of the Hall and the conductivity mobilities at decreasing net doping concentrations and / or for high ionized dopant concentrations. It implicates that the decrease is more pronounced in the conductivity mobility than in the Hall mobility. However, as previously explained, the error on the determination of the Hall factor is relatively large. To gain confidence in this finding, more measurements are necessary.

All mobility and Hall factor measurements presented so far describe the transport of the *majority* carriers in the silicon (in all investigated cases: the holes). Since their concentration exceeds the minority carrier density (the electrons) by several orders of magnitude, the majority carrier properties dominate all the above applied measurements aimed at the retrieval of the mobility.

[15] Analysis of Cz-Si values of r by J. Geilker.

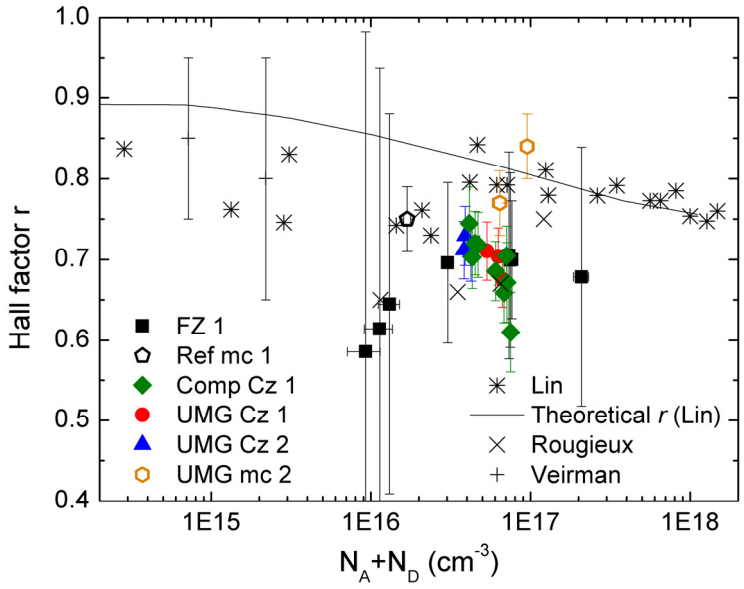

Figure 4.17: Hall factor r versus the sum of boron and phosphorus concentrations. For comparison, Lin's theoretical prediction of the Hall factor is plotted by the continuous line; it fits only for large doping concentrations.

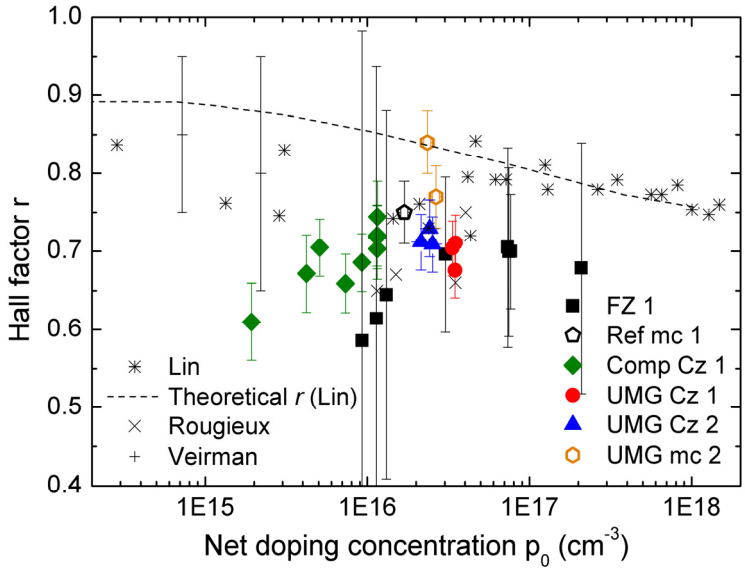

Figure 4.18: Hall factor r versus the net doping concentration.

The minority carrier mobility can be measured either with the help of temperature-dependent Hall measurements, yielding the minority carrier Hall mobility. From this, the minority carrier conductivity mobility may be deduced if the respective Hall factor is known.

Alternatively, an approach published by Sproul et al. [79] directly delivers the mobility-dependent minority carrier diffusion coefficient (eq. (3-26)), e.g. D_e in a p-type sample, by measuring the effective minority carrier lifetime τ_{eff} of wafers with infinitely high carrier recombination at the surface. In that case, the following expression for the minority carrier lifetime applies:

$$\frac{1}{\tau_{eff}} = \frac{1}{\tau_b} + \left(\frac{\pi}{d}\right)^2 D_e \qquad (4\text{-}13).$$

An infinite bulk lifetime τ_b would allow for immediate calculation of $\mu_{C,min}$. As this is seldom the case (especially not for compensated wafers), an alternative analysis can be performed by measuring the effective carrier lifetimes on samples of varying thicknesses d, but taken from the same material; then the slope of τ_{eff} versus $(\pi/d)^2$ yields the diffusion coefficient. However, care has to be taken that all the samples contain the same amount of both dopants, which is true for parallel samples only in a small part of compensated silicon ingots.

Unfortunately, for all the compensated materials investigated in the course of this thesis, no samples of different thicknesses were available. Therefore, in the following section regarding the impact of reduced mobilities on the wafer properties, the prediction of Klaassen's model has been used also for the minority carrier mobility, keeping this description's strengths and weaknesses in mind. Generally, the scattering center-dependent minority carrier mobility in compensated material shows the same trend as the majority carrier mobility [74].

4.3 Assessment of UMG material-related limitations

In this section, the impact of the impurity content on the wafer properties is discussed. Since the transition metal concentration in UMG-Si is not significantly increased, the limitations are mainly imposed by the high [B]- and [P]-concentrations. Hence, this section focuses on the influence of B and P on the minority carrier lifetime / the diffusion length, which is three-fold: (i) The diffusion length (and therefore also τ_{eff}) is modified by the reduced carrier mobility. (ii) The net dopant concentration is part of all recombination mechanisms; in general, a higher net doping leads to higher recombination rates. (iii) Boron forms highly recombination active defect centers with oxygen.

Since the influence of the (net) doping concentration on the recombination mechanisms is treated in literature, it is not regarded in the following.

4.3.1 Correction of the minority carrier lifetime measurements

The different techniques for the determination of the carrier lifetime work on the premise that the carrier mobility is known. In the following, the influence of the carrier mobility on the lifetime measurements is first shown for two exemplary techniques, which are very important in today's material characterization: the quasi-steady state photoconductance (QSSPC) [80] and photoluminescence imaging (PLI) [81].

A) Quasi-steady state photoconductance

During the QSSPC measurements, excess carriers are injected by illuminating the sample with a photo flash providing intensities between 0-500 suns during a controlled intensity decay. The time-dependent light intensity $S_{av}(t)$ is detected with a reference solar cell; at

the same time, the change in the conductivity $\Delta\sigma(t)$ is recorded with the help of an induction-coil.

The analysis of the minority carrier lifetime then consists in the calculation of the averaged excess carrier density $\Delta n_{av}(t)$ in the sample of thickness d via

$$\Delta n_{av}(t) = \frac{\Delta\sigma(t)}{q(\mu_{C,e} + \mu_{C,h})d} \tag{4-14}$$

which corresponds to the definition of the conductivity in equation (3-32). At the same time, the generation $G_{av}(t)$ of carriers is computed to

$$G_{av}(t) = \frac{S_{av}(t) f_{abs} N_{ph}^{1sun}}{d} \tag{4-15},$$

with N_{ph}^{1sun} the photon flux at an intensity of 1 sun and f_{abs} a correction factor which accounts for the fact that not all incident photons are absorbed.

In the mathematically simplest case, the quasi-static analysis of the carrier lifetime reads as

$$\tau_{eff}(t) = \frac{\Delta n_{av}}{G_{av}(t)} \tag{4-16}$$

where the dependency on the carrier mobility is introduced via equation (4-14)[16]. The QSSPC measurement tool implements the mobility model by Dannhäuser and Krausse [83, 84], which describes the mobility as a function of the (uncompensated) doping concentration and the excess carrier density Δn_{av}. During the QSSPC-measurements, the determination of Δn_{av} is repeated, until the excess carrier density and the mobility are consistent in equation (4-14).

As a rule, if during the QSSPC-measurements of compensated silicon samples the lower minority and majority carrier mobilities are not accounted for, the resulting measured lifetimes *underestimate* the real carrier lifetime.

Therefore, the evaluation tool of the QSSPC setup has been adjusted to the use of compensated silicon samples in the following way[17]: Instead of giving the base resistivity as input parameter from which the mobility is calculated, the software asks directly for the sum of the conductivity mobilities ($\mu_{C,e}+\mu_{C,h}$). Lacking alternatives, these mobilities are derived from Klaassen's model for the measured dopant densities N_A and N_D, giving a good description at least for low compensation. In the following, the same iterative procedure as described above determines the excess carrier density.

A comparison of measurements of the uncorrected and corrected effective carrier lifetime is shown in *Figure 4.19*. The uncorrected lifetime values are based on the measured resistivities. The samples were taken from different positions over ingot height of the weakly compensated ingot "Comp Cz 1", hence the net doping concentrations and the conductivity mobilities vary strongly, which is reflected in the lifetime values. The high net doping concentration in the seed end of the crystal leads to very low lifetime due to

[16] In the transient [80] and generalized [82] mode of the QSSPC technique, the influence of the mobility on the carrier lifetime measurements is similar.

[17] Adjustment done by J. Geilker.

the predominant boron-oxygen defect which will be discussed in section 4.3.3. With decreasing p_0 towards the tail end of the ingot, the carrier lifetime increases.

The difference between the mobility models can significantly influence the measurements: At the seed end, the correct lifetime exceeds the uncorrected value by about 10%. As the enhanced dopant densities towards the tail end result in lowered conductivity mobilities, the difference in this ingot part even amounts to more than 30%.

In the following sections, therefore, the lifetime measured via QSSPC on compensated samples is always corrected for the dopant concentration-dependent conductivity mobility.

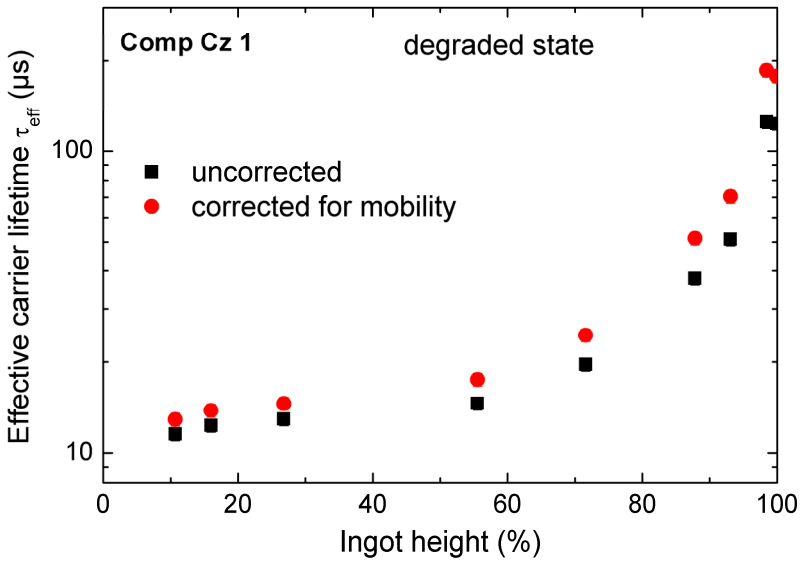

Figure 4.19: Comparison between uncorrected QSSPC-measurements and for mobility corrected values exemplified by samples from ingot "Comp Cz 1" in the degraded state versus ingot height (=varying mobilities). The effective lifetime was evaluated at $\Delta n = 0.1 x p_0$. After ref. [54].

B) Photoluminescence imaging

Photoluminescence imaging makes use of radiative band-to-band recombination described in section 3.2.2. Excess carriers are generated by illumination with a laser. The intensity of the resulting radiative recombination, which is detected by a silicon charge coupled device camera, is proportional to the electron and hole densities. For p-type compensated silicon, the signal depends therefore on the net doping density:

$$\begin{aligned} n &\approx \Delta n \\ p &= p_0 + \Delta n \end{aligned} \qquad (4\text{-}17).$$

From equations (3-17) and (4-17), it follows that the detected intensity per unit volume $S_{PL,dV}$ equates

$$S_{PL,dV} = A_{i,dV} B\left(p_0 \Delta n + \Delta n^2\right) \qquad (4\text{-}18)$$

with $A_{i,dV}$ describing a factor depending on the geometry of the measurement setup. The excess carrier density Δn, which is then used for the calculation of the carrier lifetime according to eq. (4-16), depends on the net doping concentration as

$$\Delta n = -\frac{p_0}{2} + \sqrt{\left(\frac{p_0}{2}\right)^2 + \frac{S_{PL,dV}}{A_{i,dV}B}} \qquad (4\text{-}19).$$

Hence, the measurement of the excess carrier density per se does not depend on the conductivity mobility and can be determined when both N_A and N_D are known.

However, a calibration of the camera signal – corresponding to the determination of the parameter $A_{i,dV}$ – is needed, which may involve the carrier mobility. For example, in reference [85], three approaches are presented:

i. Self-consistent lifetime calibration
   The generation of excess carriers is approximated by measuring the incident photon flux and calculating the absorption via eq. (3-13). In this method, the carrier mobility is not involved.

ii. Calibration by means of comparison with alternative lifetime measurement techniques
   This calibration is probably most commonly used. As reference lifetime measurement, the QSSPC method is often employed. Therefore, the PLI necessitates a correct analysis of the QSSPC lifetime as described in the previous subsection.

iii. Calibration by use of selective filters
   In this method, only selected wavelengths of the entire spectrum of radiative recombination are measured with the help of band-pass filters. By combining two or more images at different wavelengths, the carrier diffusion length can be estimated, which is proportional to the effective carrier lifetime. However, the diffusion length L, eq. (3-25), involves the conductivity mobility, see the following section. Care has hence to be taken when using this calibration.

4.3.2 Impact of reduced conductivity mobility on the effective diffusion length

More important than the minority carrier lifetime from the viewpoint of solar cells is the effective diffusion length L_{eff} under illumination as it is directly related to the collection efficiency of the solar cell's pn-junction and thus to the short circuit current [32]. Often, it is simply calculated from carrier lifetime measurements as the diffusion coefficient of charge carriers in uncompensated material is known.

Equations (3-25) and (3-26) show that the conductivity mobility enters the effective diffusion length determined with the help of the QSSPC technique twice via the diffusion coefficient D_i and the carrier lifetime τ_i:

$$L_{eff,i} = \sqrt{\frac{k_B T}{q}\,\mu_{C,i}\,\frac{\Delta\sigma}{q\left(\mu_{C,i} + \mu_{C,j}\right)d}} \qquad (4\text{-}20),$$

with subscripts i and j standing for electrons and holes.

To illustrate its implications, let's consider the following example: Given are two p-type silicon samples of the same base resistivity, one of which is taken from uncompensated material, the other from compensated silicon. If the uncorrected minority carrier lifetimes are equal, then the effective minority carrier diffusion length in the compensated sample differs from the uncompensated wafer by the factor $\sqrt{\frac{\mu_{C,e,comp}\left(\mu_{C,e,unc}+\mu_{C,h,unc}\right)}{\mu_{C,e,unc}\left(\mu_{C,e,comp}+\mu_{C,h,comp}\right)}}$. Since mobilities in the compensated material are generally lower than in the uncompensated material ($\mu_{C,i/j,comp}<\mu_{C,i/j,unc}$), the effective minority carrier diffusion length estimated from uncorrected QSSPC lifetime measurements on the basis of the known mobility – resistivity relation (e.g. by taking Caughey and Thomas' mobility model) yields a *lower limit* for the real value.

In summary, if the dopant concentrations N_A and N_D from compensated material are unknown, measurands determined by the QSSPC technique with only the base resistivity as input parameter will always give a *lower limit* of the actual value. If the absolute values are not important, then these measurements can give a safe estimate of the material quality without having to correct for the modified conductivity mobility.

4.3.3 Carrier lifetime reduction by light-induced degradation in compensated material

In all p-type Czochralski-grown wafers, light-induced degradation (LID) seriously decreases the minority carrier lifetime [86-89]. In the degraded state, it was shown that the reciprocal carrier lifetime depends linearly on the boron concentration and quadratically on the oxygen content in non-compensated silicon wafers [89, 90]. It is therefore assumed that the recombination active complex consists of a substitutional boron atom B_S and an interstitial oxygen dimer O_{2i} [91][18].

The light-induced degradation can be reversed in an annealing step (250°C for 25 minutes) with a complete recovery of the carrier lifetime [93], which then undergoes the next degradation cycle as soon as it is exposed to light. The recovery can be made permanent by sample annealing under simultaneous illumination [94-96].

With regard to the high dopant levels in UMG silicon, it was suspected that the minority carrier lifetime in Cz-wafers made from UMG silicon suffers from the high boron concentration due to the linear dependency of the Cz-related defect on [B]. However, measurements published by Macdonald et al. [50] suggested that in compensated p-type silicon, only the electrically active fraction of the boron atoms is able to associate with the oxygen dimers, meaning that the Cz-defect concentration depends linearly on the *net* doping concentration p_0.

By extrapolation, this finding also implies that no Cz-defects form in n-type compensated silicon as the electrical activity of boron is overcompensated by phosphorus. However, Schutz-Kuchly et al. [97] observed light-induced degradation also in compensated n-type

[18] Recently, Voronkov et al. [92] argued that it is not the substitutional boron atom B_s which forms a complex with O_{2i}, but rather its interstitial counterpart B_i. However, this is not relevant for the following analysis.

Cz silicon, which they convincingly attributed to the same boron-oxygen complex formation as in p-type wafers.

Note that – disregarding results on uncompensated reference samples – Macdonald et al. based their conclusion essentially on compensated samples of two different doping concentrations (see previous section), while Schutz-Kuchly et al. relied on measurements made on only one compensated wafer.

As these findings are contradictory but important for the future use of UMG silicon feedstock, a more reliable set of data is needed. Therefore, we investigated the Cz-defect formation on a set of samples with largely varying boron and phosphorus compositions resulting in p- and n-type silicon of different compensation ratios.

For this study [98], samples were taken from the following five different ingots:

1. The non-compensated, p-type reference Cz crystal with base resistivity ranging between 1-2 Ωcm, ingot "UMG Cz 3"; here Cz wafers of standard material which served as references for passivation were also included;
2. the Cz crystal which had intentionally been weakly compensated (mostly p-type), ingot "Comp Cz 1" (see Figure 4.7);
3. the Cz crystal which had intentionally been heavily compensated (mostly n-type), ingot "Comp Cz 2" (see Figure 4.8);
4. the compensated p-type Cz ingot made from 100% UMG feedstock material with base resistivities around 0.5-0.55 Ωcm, ingot "UMG Cz 1" and
5. the compensated p-type Cz ingot made from a blend of 50% UMG-Si and 50% virgin grade feedstock with base resistivities ranging from 0.7-0.8 Ωcm (for both UMG-Si Cz-crystals, see Figure 4.9).

Samples were taken from several ingot heights in order to investigate the effect of varying doping concentrations and compensation ratios.

The investigated Cz crystals contain similar interstitial oxygen concentrations, shown in *Figure 4.20* and *Figure 4.21*[19]. The main influence on the Cz-defect density is therefore expected from the different dopant concentrations.

The compensation ratio K_C of the intentionally compensated Cz-ingots depends on the ingot height, with [99]

$$K_C = \frac{N_A + N_D}{N_A - N_D} \qquad (4\text{-}21).$$

For the weakly compensated silicon, compensation ratios between 3 and 150 were found while the heavily compensated ingot featured values mainly between 15 and 200. The two Cz-ingots with UMG silicon feedstock are only lightly compensated; their compensation ratio K_C is below 2.

[19] Measurements performed by I. Reis, analyzed by J. Geilker.

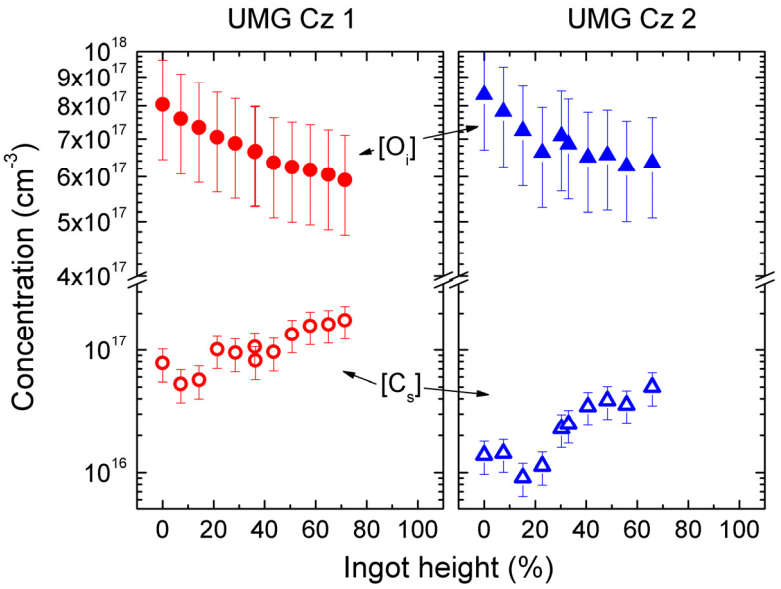

Figure 4.20: Interstitial oxygen (closed symbols) and substitutional carbon (open symbols) concentration measured via FTIR versus ingot height of both UMG-silicon Cz crystals. After [54].

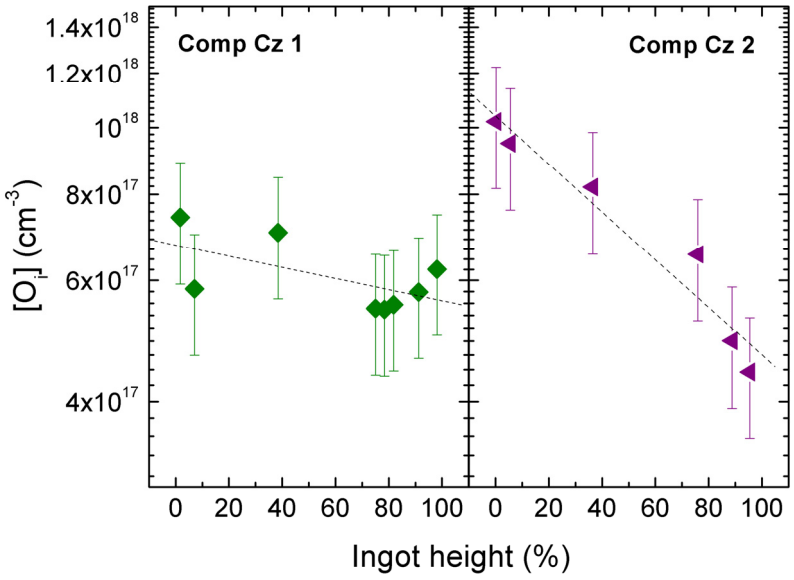

Figure 4.21: Interstitial oxygen concentration versus ingot height of both intentionally compensated silicon Cz crystals. After [54].

For the investigation of the Cz-defect, the surfaces of all samples were passivated on both sides with a high-quality SiN layer after the application of a KOH damage etch and an HNF cleaning step[20].

The light-induced degradation is usually characterized by the normalized defect concentration N_t^* which is linearly proportional to the boron-oxygen complex density. It is calcu-

[20] HNF step by M. Kwiatkowska, SiN passivation done by N. Bayer.

lated from the measurement of the minority carrier lifetimes in the degraded (τ_d) and annealed (τ_0) state by the equation [86, 88]

$$N_t^* = \frac{1}{\tau_d} - \frac{1}{\tau_0} = \left(\frac{1}{\tau_{Cz}} + \frac{1}{\tau_{res}} \right) - \frac{1}{\tau_{res}} = N_t(t) \times f\left(\sigma_{e,t}, \sigma_{h,t}, E_t\right) \qquad (4\text{-}22),$$

where τ_{Cz} stands for the SRH-lifetime of the Cz-defect center with the capture cross sections $\sigma_{e,t}$, $\sigma_{h,t}$ and the trap level energy E_t, while τ_{res} describes the carrier lifetime determined by other recombination channels. The lifetime measurements in degraded and annealed states of all samples were performed with the help of the QSSPC-technique at an injection density of $\Delta n = 0.1 \times p_0$ for each sample which represents the standard condition for determination of the normalized Cz-defect concentration[21]. For the compensated samples, the data was corrected for the lower minority and majority conductivity mobility with the procedure explained in section 4.3.1.

At first the wafers were annealed on a hot plate for 25 minutes at 250 °C to ensure that all boron-oxygen complexes were dissociated. While cooling to room temperature, the samples were stored in the dark before being measured in the annealed state. The samples were then degraded by light soaking for 24 hours with a light intensity of 250 W/m², followed by the measurement in the degraded state.

Lifetime degradation was observed along the entire length of all crystals. Presenting the largest variations in net doping concentration and compensation ratio, the lifetime degradation is exemplified for the weakly and the heavily compensated ingots "Comp Cz 1 and 2" in *Figure 4.22*.

The wafers from the weakly compensated Cz-ingot show the expected behavior [100]: At the seed end, the lifetime degrades strongly from about 135 µs to only 13 µs during light soaking. With increasing ingot height, the lifetimes in the annealed as well as in the degraded state improve due to the increasing compensation of boron by phosphorus. At the tail end (n-type), even the degraded lifetime value exceeds 100 µs.

As a result of the high phosphorus concentration in the heavily compensated Cz-ingot, most wafers taken from this crystal are n-type, allowing for the verification of the observation made by Schutz-Kuchly et al. [97]. *Figure 4.22* (bottom) shows the significant lifetime decrease due to light-induced degradation even at high phosphorus concentrations towards the tail end of the ingot, supporting the published results.

[21] Measurements and analysis of the normalized Cz-defect concentration by J. Geilker.

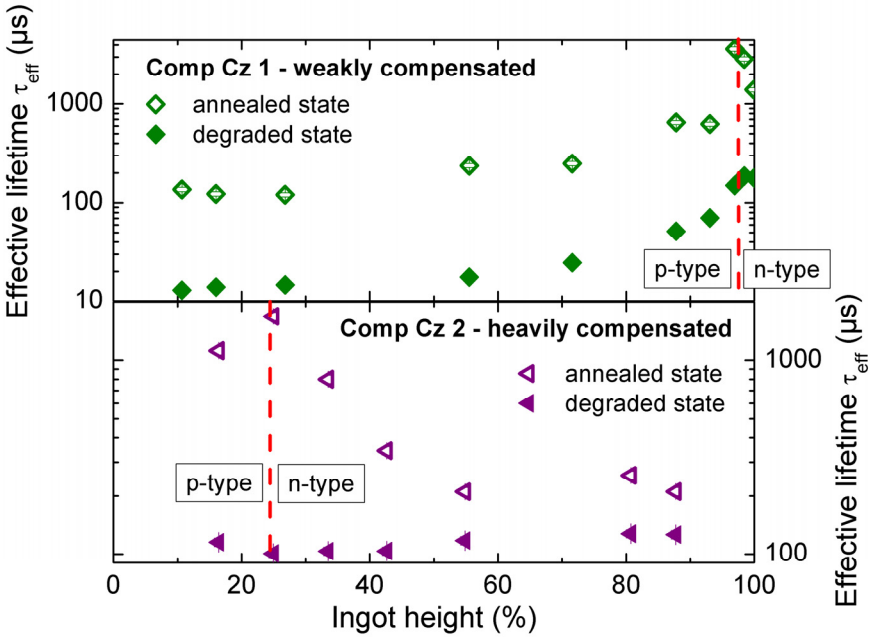

Figure 4.22: Effective minority carrier lifetime in the degraded (closed symbols) and annealed state (open symbols) of both intentionally compensated ingots "Comp Cz 1 and 2" versus the ingot height. The approximate position of the changeover from p- to n-type conductivity is marked by the red dashed lines. After ref. [98].

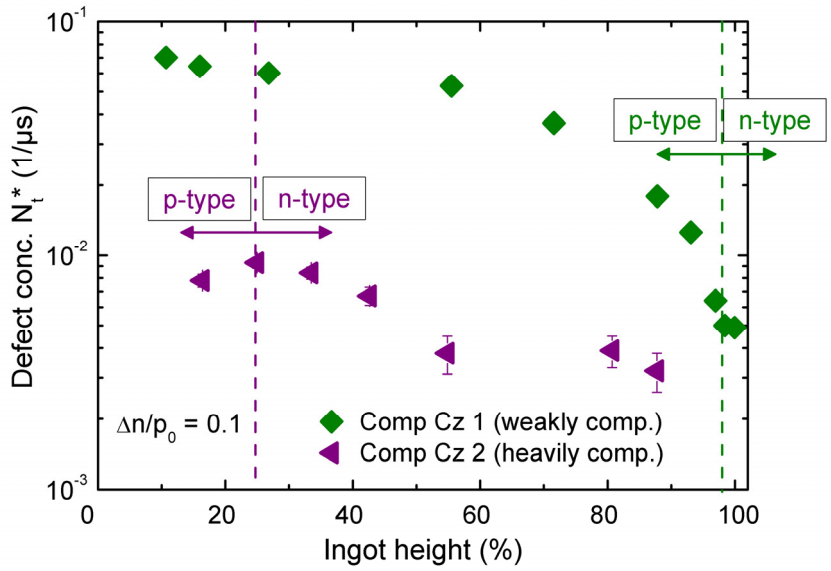

Figure 4.23: Normalized Cz-defect concentration N_t^* versus the ingot height of both intentionally compensated Cz crystals. After ref. [98].

From the above lifetime measurements on the intentionally compensated samples, in *Figure 4.23* the calculated normalized defect concentration N_t^* is plotted versus the ingot height. While the defect concentration decreases continuously from about $8x10^{-2}$ μs^{-1} to below $5x10^{-3}$ μs^{-1} in the weakly compensated crystal, in the heavily compensated ingot, the defect density is around $1x10^{-2}$ μs^{-1} in the seed end dropping to about $3x10^{-3}$ μs^{-1} after the conductivity type changeover. Note that the defect concentration in this part of

the ingot stays at a relatively constant value which implicates that neither the absolute boron and phosphorus concentrations nor the net doping p_0 have a significant influence on N_t^* in the compensated n-type crystal.

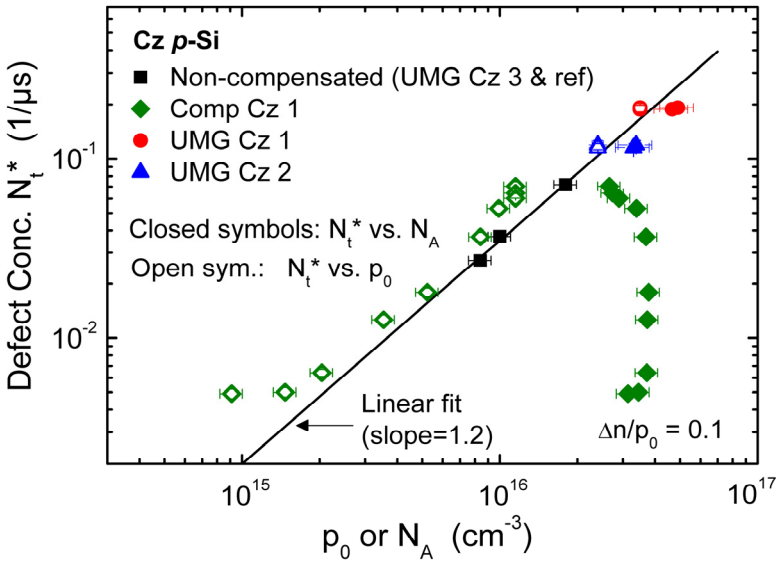

Figure 4.24: Normalized Cz-defect concentration N_t^* versus the boron concentration N_A (closed symbols) and the net doping concentration p_0 (open symbols) of all p-type Cz-samples taken for this study. The linear fit is very similar to the fit obtained on uncompensated boron-doped Cz wafers in literature [90]. After ref. [98].

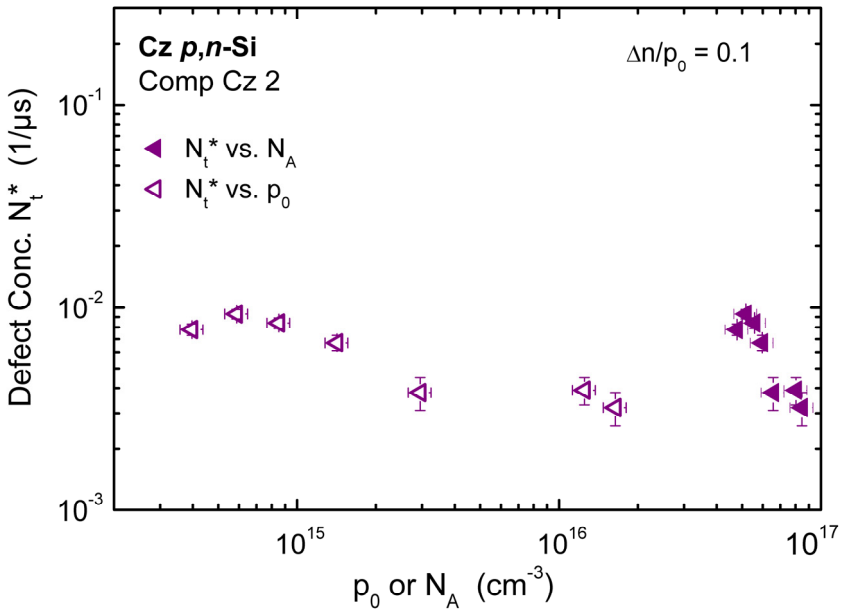

Figure 4.25: Normalized Cz-defect concentration N_t^* versus the boron concentration N_A (closed symbols) and the net doping concentration p_0 (open symbols) of the p- and n-type Cz-samples from the heavily compensated ingot Comp Cz 2. After ref. [98].

According to literature, in non-compensated Cz silicon the normalized defect concentration depends linearly on the boron concentration [90]; for p-type compensated wafers, the defect density is supposed to be a linear function of the net doping concentration p_0.

In order to compare our results to previous publications on the Cz-defect, *Figure 4.24* displays the normalized defect concentration versus the boron concentration N_A and versus the net doping concentration.

The linear fit to the normalized defect concentration of the non-compensated silicon wafers from ingot "UMG Cz 3" (including the reference wafers which have not been discerned from ingot "UMG Cz 3" for reasons of clarity) gives a slope of around 1.2, which is very similar to the characteristic shown on uncompensated boron-doped Cz wafers in literature [90]. Since the phosphorus concentration of the UMG Cz wafers is low, the defect concentrations of ingots "UMG Cz 1 and 2" match the fit to the data obtained on uncompensated material quite well; the coincidence is a little better for N_t^* versus p_0, however the deviation of N_t^* versus N_A from the straight line is not very large. This data therefore supports Macdonald's interpretation.

This finding is strengthened by our measurements of the Cz-defect concentration on the weakly compensated ingot "Comp Cz 1": While the plot $N_t^*(N_A)$ reveals that with approximately the same boron concentration, measured normalized defect densities range between $5\text{x}10^{-3}$ – $7\text{x}10^{-2}$ µs, which is a difference of one order of magnitude, the same data plotted versus the net doping concentration p_0 almost aligns with the linear fit. However, the normalized defect concentrations digress from the line for increasing compensation, that is for decreasing net doping concentrations.

In *Figure 4.25*, the normalized defect concentration of the wafers from the heavily compensated ingot "Comp Cz 2" is shown versus the boron and the net doping concentration. Here, N^*_t-values remain on the same order of magnitude for a wide range of net doping concentrations, showing that the dependency on the phosphorus concentration is very weak. Note that the defect density measured in the n-type wafers from ingot "Comp Cz 2" are similar to the normalized defect concentrations measured close to the conductivity type changeover (p_0<$2\text{x}10^{15}$ cm^{-3}) of the weakly compensated ingot "Comp Cz 1".

Our measurements on the weakly and the heavily compensated Cz silicon crystals prove that the boron-oxygen defect concentration in compensated Cz silicon ingots is not in general a linear function of the net doping concentration as suggested by Macdonald et al. [50, 100], but changes the behavior at increasing compensation ratios: With increasing phosphorus concentration, the normalized defect concentration in the weakly compensated ingot decreases until a minimum value is reached when the conductivity changes from p- to n-type. This minimum value stays then more or less constant in the n-type part as can be seen in the heavily compensated ingot.

Therefore, the normalized defect concentrations of all compensated wafers are plotted in *Figure 4.26* as a function of the absolute value of the compensation ratio, taking into account that R_C is negative for n-type samples. With increasing $|R_C|$, the defect concentration decreases until it reaches the observed minimum value at $R_C \sim 40$.

The data can be fitted to an exponential of the form

$$N_t^*(R_C) = A \exp\left(-\frac{|R_C|}{const}\right) + y_0 \qquad (4\text{-}23).$$

Doing this for the intentionally compensated ingots, we obtain the values A=(108.0±3.0)$\text{x}10^{-3}$ μs^{-1}, for *const*=(5.32±0.17) and for y_0=(5.0±0.1)$\text{x}10^{-3}$ μs^{-1}.

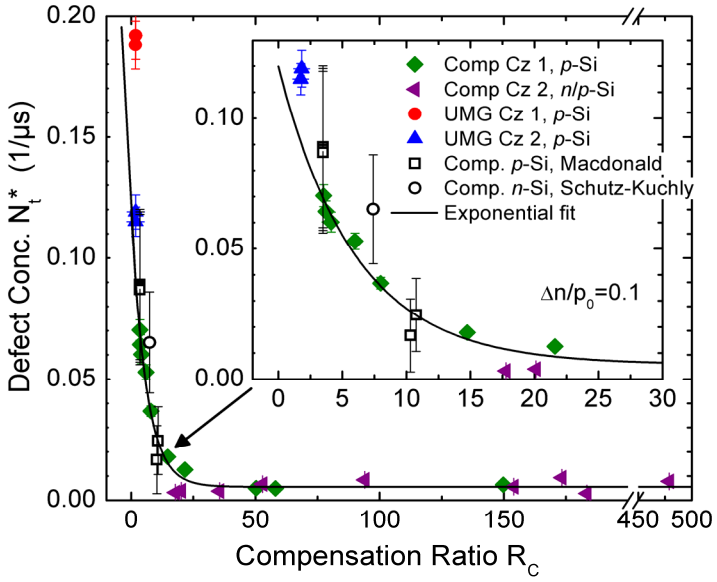

Figure 4.26: Normalized Cz-defect concentration versus the compensation ratio R_C of all compensated samples taken for this study. Note that both p- and n-type Cz-Silicon is included. The data published by Macdonald et al. [50] (p-Si) and by Schutz-Kuchly et al. [97] (n-Si) are shown for comparison. After ref. [98].

The data published by Macdonald et al. as well as by Schutz-Kuchly et al. are also plotted, being in an overall very good agreement. Note that Schutz-Kuchly discussed neither the exact injection density of the lifetime measurements nor the uncertainty on these measurements [97]. For our illustration we assumed an uncertainty of 3 µs on the lifetime values, which is a fair estimation of the measurement error.

However, the defect concentrations of the hardly compensated samples (R_C<2) from both UMG-Si Cz ingots show a deviation from the exponential fit. This is not surprising, as the exponential fails to model the Cz-defect concentration in uncompensated silicon.

In summary, the exponential decrease given by equation (4-23) gives a new description of the normalized defect concentrations in compensated silicon for a wide range of compensation ratios; it presents a link between the contradictory results obtained on p- and n-type compensated silicon as it is, surprisingly, valid for both conductivity types.

Regarding the use of UMG silicon feedstock for the production of monocrystalline wafers, these results indicate that the boron-oxygen complex formation is indeed mainly governed by the net doping concentration. Only for very low p_0-values, the Cz-defect density is higher than expected from the linear dependency. However, in the base resistivity range aimed at the production of solar cells (and which is successfully obtained with current UMG-feedstock fabrication, see section 4.2.2), one can act on the assumption that the UMG-Si Cz wafers will roughly contain the same amount of Cz-defects as standard Cz-wafers with the same base resistivity.

4.4 Solar cells made from UMG silicon in an industrial standard process

Having assessed the main influences on the UMG wafers from mono- and multicrystalline ingots, in the following, representative solar cell results are shown. The intention of this chapter is to highlight the typical properties of the solar cells made from the UMG material presented so far. It is not aimed at an assessment of the efficiency potential of UMG-Si solar cells nor are possibilities for process optimizations discussed, which are the topic of several other works (see e.g. [45]).

4.4.1 Solar cells made from UMG Cz-silicon wafers

For the first batch of UMG silicon solar cells, wafers were taken from five ingot positions distributed from seed to tail end from the crystals "UMG Cz 1" (100% UMG-Si feedstock content) and "UMG Cz 2" (blend of 50% UMG-Si, 50% virgin grade Si). For reference, wafers were taken from ingot "UMG Cz 3" (100% virgin grade Si) as well as highly pure Cz wafers from a different wafer supplier ("ISE Ref").

All wafers were processed in the same run in the PV-TEC laboratory at the Fraunhofer ISE involving the standard process steps in the following order[22]:

- SC1 wafer cleaning
- Alkaline texturization
- Phosphorus emitter diffusion, sheet resistance of 65 Ω/sqr
- Phosphorus silicate glass etch back
- SiN antireflection coating (PECVD)
- Screen printing of the AgAl solder pads on the rear side
- Screen printing of the Al rear side metallization (intended for back surface field-formation)
- Screen printing of the Ag front side metallization
- Fast firing of the metal contacts
- Laser edge isolation
- Degradation of the solar cells by light soaking for at least 15 hrs.

No optimization of the solar cell processing was tackled.

The solar cell results in the degraded state are shown in *Figure 4.27*[23].

We want to focus on the most important findings:

The open circuit voltage V_{OC} gives for all three crystals around 610 mV; the ISE reference shows the relatively low V_{OC} obtained in this solar cell run. Nevertheless, since both the carrier lifetime and the base net doping concentration – which both vary strongly between the three crystals – significantly influence the open circuit voltage, a significant

[22] Industrial solar cell run in the PVTEC was the collaboratory work of several engineers, supervised by G. Emanuel.
[23] Analysis of the solar cell results by G. Emanuel and J. Geilker.

difference in the V_{OC} was initially expected. To identify the origin of this coincidence, the open circuit voltage was calculated as a function of the effective diffusion length (the carrier lifetime) by means of a simple two-diode model with the net doping concentration of the different ingots as input parameter[24] and compared to measurements in *Figure 4.28*.

This simulation approach was by no means intended to yield correct values, as some simplifications like a constant short circuit current for all solar cells were assumed. However, the graph indicates that the reason for the same V_{OC}-level of all materials may lie in the superposition of the counteracting effects of the diffusion length and the base resistivity on the voltage: While with increasing net doping a higher V_{OC} is expected for a given diffusion length, the latter decreases the V_{OC} due to the carrier lifetime-limiting boron-oxygen defect which is linearly proportional to p_0 in this resistivity range.

As the reduced diffusion length affects the collection efficiency of the pn-junction, the short circuit current is significantly lower (~3 mA/cm^2) in the 100% UMG-Si ingot compared to the reference "UMG Cz 3".

This J_{SC}-decrease already accounts for a reduction in the solar cell efficiency of about 1% abs. of ingot "UMG Cz 1". In addition, the solar cells from this crystal suffer from the increased saturation currents J_{rev1} and J_{rev2} which may account for another 1% abs. reduction in the efficiency.

In total, while the reference solar cells show good solar cell efficiencies of around 17%, which is approximately the currently attained efficiency in industry on Cz wafers, the solar cells made from a silicon blend of UMG-Si and highly pure Si ("UMG Cz 2") reach only 16% and the solar cells made entirely from UMG-Si only about 15%. This can mainly be attributed to the Cz-related boron-oxygen defect.

Hence, a reduction of the net doping concentration coming with a lower content of both boron and phosphorus in the UMG silicon feedstock is highly desirable. However, note that due to the rapid technological progress promoted by the feedstock producers, the materials investigated in the course of this thesis are meanwhile outdated. Current feedstock of most manufacturers contains significantly less dopants [101].

[24] Simulations were performed by J. Greulich.

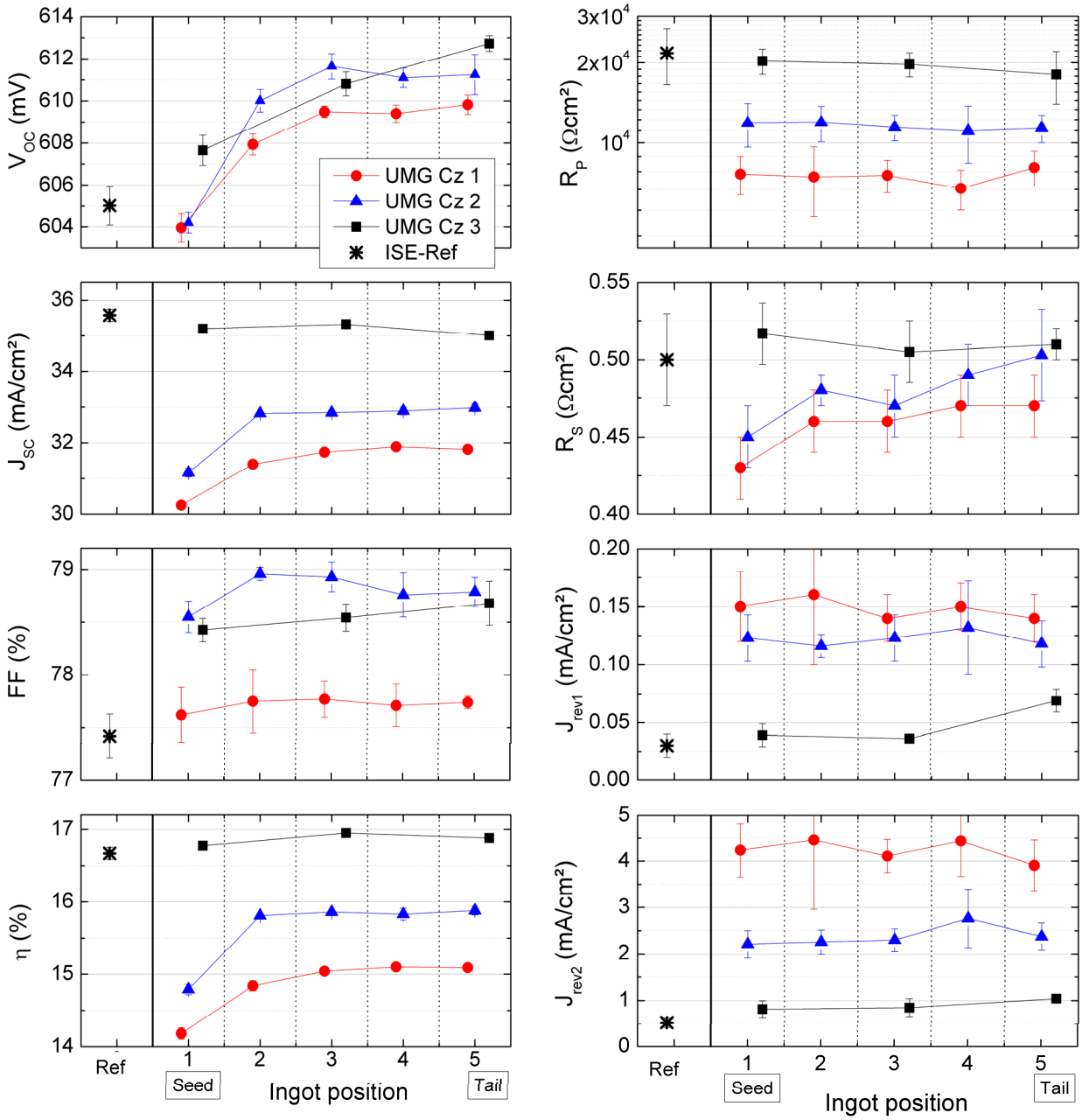

Figure 4.27: Solar cell results in the degraded state of the wafers from the UMG silicon Cz crystals UMG 1 and 2, and the reference ingot "UMG Cz 3" versus ingot position (1=seed end). For comparison, the ISE reference solar cells were made from highly pure standard Cz wafers from a different wafer supplier. After ref. [54].

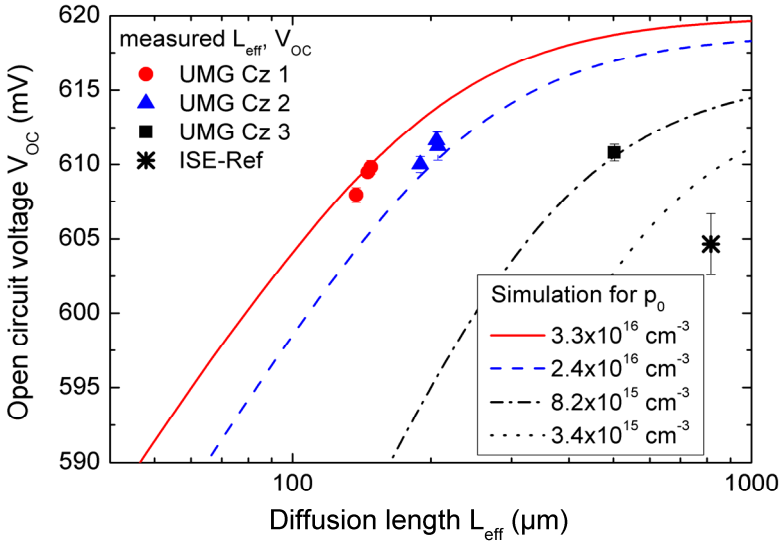

Figure 4.28: Measured open circuit voltage versus the measured diffusion length (calculated from carrier lifetime measurements in the degraded state) of the UMG Cz ingots as well as the reference sample. The lines represent the $V_{OC}(L_{eff})$ relation of various net doping concentrations p_0 simulated by means of a simple two-diode model[24]. The net doping concentrations correspond to the average p_0-values measured on the different crystals.

4.4.2 Solar cells made from UMG mc-silicon wafers

Since multicrystalline silicon generally does not contain similarly high amounts of oxygen, the Cz-defect does not play an important role in most mc-Si wafers.

Therefore, in this section UMG mc-Si solar cells made from ingot "UMG mc 1" are analyzed and compared to reference solar cells made from ingot "Ref mc 1". They were processed in the frame of the project SolarFocus in an standard screen printing process in an industrial facility. The details were not disclosed, but with a high probability they are similar to the process described in the previous subsection.

The results are presented in *Figure 4.29*.

As a consequence of the higher net doping concentration in the UMG silicon wafers, the open circuit voltage of the UMG-Si solar cells exceeds the V_{OC} of the reference solar cells by about 10 mV.

By contrast, the lower SRH-minority carrier lifetime results in a short circuit current which is reduced by approx. 2.5 mA/cm^2, which explains the lower efficiency in the UMG-Si solar cells of about 0.7% absolute.

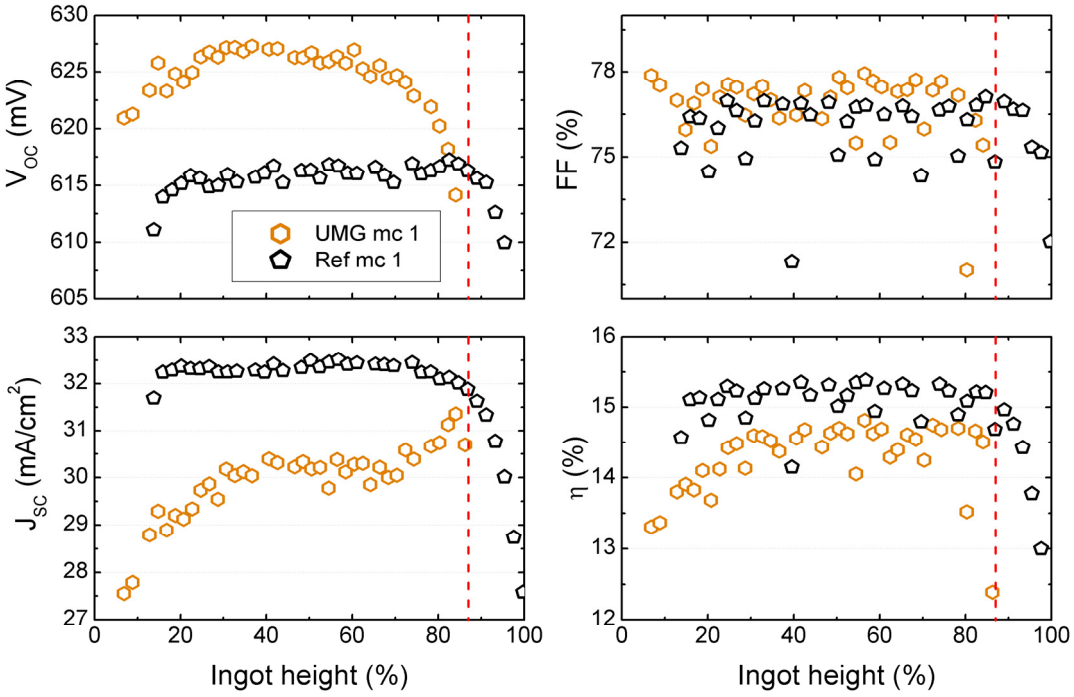

Figure 4.29: Solar cell results obtained on the multicrystalline UMG silicon wafers "UMG mc 1" and on the mc-Si reference wafers "Ref mc 1" versus ingot height. The red dashed line marks the approximate position of the changeover from p- to n-type conductivity in ingot "UMG mc 1"[25].

The impairment of the minority carrier lifetime can be traced back to the metallic impurities which remain in the multicrystalline silicon ingots after solidification. As the comparison with the similarly metal-contaminated mc reference crystal shows, the transition metals by themselves do not have such a deleterious effect; however, in conjunction with a high net doping concentration, the minority carrier lifetime suffers.

While this chapter has centered mostly around the implications of high boron and phosphorus concentrations, the following will focus on the behavior of transition metals during the high-temperature steps in the solar cell process.

[25] Solar cell parameter measurements performed within the industrial facility and provided for the general use of the project consortia.

5 Impurity distribution of transition metals in mc-Si

In the midst of the silicon feedstock shortage around the year 2006, a debate arose which way the silicon production would go in the future, brought about by the rapidly growing demand of the PV industry. In the hunt for optimal solar cell efficiencies in order to save costs, solar cell producers have been calling for increasingly pure silicon wafers at reasonable prices. On the other hand, silicon feedstock makers have been divided: Renowned, large manufacturers have developed increasingly pure "solar grade" materials, while many newcomers have been offering cheap, relatively unclean "UMG" silicon.

Many feedstock makers feared that the pressure they were put under by the solar cell manufacturers and new rivals entering the potentially lucrative market could lead to an expensive, inefficient competition for low-cost production of an increasingly pure material without being sure that the outcome would result in the intended effect of higher efficiencies. What is the tolerable amount of impurities in the silicon feedstock? Which elements are especially detrimental to the solar cell parameters? An answer to these questions has been intensively searched for and has been the topic of numerous workshops, conferences and research projects around the world.

As usual the answer is not a simple one. The impact of some of the most deleterious elements in silicon, the transition metals, on solar cells made from monocrystalline wafers were studied already in the late 1970's by Davis, Rohatgi et al. [37, 102]. However, in the meantime, solar cell processes have evolved to a large degree, involving optimized high-temperature processing and gettering. In addition, it has become clear that metallic impurities in multicrystalline silicon behave differently compared to mono-Si due to the large density of crystallographic defects like grain boundaries and dislocations.

Crystal defects act as traps for diffusing impurities. The idea was put forth to use this effect for "intrinsic gettering" [6, 56]: By adapted high-temperature processes, dissolved metal atoms in the grains are brought to diffuse through the wafer bulk. By chance, they would reach a crystal defect, where they would be caught. With time, many atoms would accumulate, forming impurity clouds around dislocations or metal clusters (precipitates). A beneficial effect on the solar cell parameters is attained when the electrically active effective surface of the impurities can be reduced in this way.

It was noted that some transition metals tend to accumulate together with other elements, forming co-precipitates. This effect was described for example for iron in the presence of copper [103] and nickel, forming complex intermetallic phases consisting of Fe-Cu-Ni [104, 105]. Also, the co-precipitation of copper and nickel was investigated [106]. For the mechanisms involved, a good review is given in [107]. It was suggested that some metal silicides form a liquid eutectic with the surrounding silicon at temperatures around 800-900°C which acts as a gettering sink due to the segregation effect as described in section 2.2.4. [108].

To extend the approach of the intrinsic gettering, it was proposed to use the co-precipitation mechanism for "defect engineering" by intentional addition of metallic impurities to the silicon melt which diffuse and form precipitates easily such as Cu or Ni [48].

While in previous investigations by other groups the focus was set on the basic mechanisms of precipitation, in which metal atoms react to the presence of crystal defects in idealized processes, this chapter draws attention to some of the more practical aspects of defect engineering. The following investigations were mainly performed on wafers from multicrystalline silicon block-cast ingots which had been intentionally contaminated with defined amounts of different transition metals *in the silicon melt*. In addition, for several studies wafers from two blocks produced by the electromagnetic casting method were taken; these blocks were cast from highly pure virgin grade silicon feedstock.

After a short introduction into the properties of impurities in silicon in the first section, indications are presented in the second section that metal atoms do not only passively react to the crystal defects after solidification, but rather interact with each other and the silicon already during crystallization, which has been mostly neglected in previous works. Consequences for the impurity distribution in the mc-ingots and the tolerable metal contents in the melt are discussed. In the third section, the practicability of high-temperature defect engineering is critically reviewed with experiments on wafers from intentionally contaminated mc-Si ingots.

5.1 Impurity properties in silicon

In this section, the kinetic properties of impurities in silicon are introduced which determine the distribution after crystallization and high-temperature processes. It does not give but the most basic information; for more details, the reader is referred to literature, see e.g. the monograph by Graff [34], which has also served as guideline for the following compilation.

5.1.1 Solubility

The solid solubility of impurities in silicon depends strongly on the temperature and follows an Arrhenius law:

$$C_{Me}(T) = C_{0,Me} \exp\left(-\frac{H_{C,Me}}{k_B T}\right) \qquad (5\text{-}1),$$

where $C_{0,Me}$ is a temperature-independent prefactor and $H_{C,Me}$ is the solution enthalpy.

In *Figure 5.1*, the solubility of various transition metals is plotted versus the inverse temperature, measured on monocrystalline silicon.

Roughly, the metals can be categorized according to three groups: Cu and Ni easily dissolve in silicon, with solid solubilities orders of magnitude higher than the other metals. Ti is an example for metals which are hardly found dissolved in silicon due to the very low solubility. Co, Cr and Fe can be dissolved in the silicon bulk in intermediate concentrations.

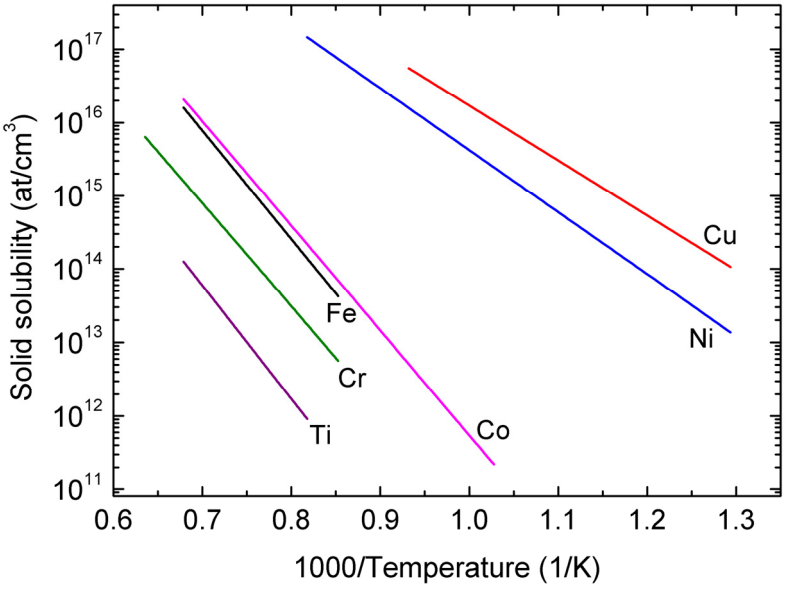

Figure 5.1: Solid solubility of various transition metals versus the inverse temperature in silicon. Values taken from Graff [34].

5.1.2 Diffusivity

Similar to the solubility, the diffusivity can be described by an Arrhenius law

$$D_{Me}(T) = D_{0,Me} \exp\left(-\frac{H_{D,Me}}{k_B T}\right) \tag{5-2}$$

with a temperature-independent prefactor $D_{0,Me}$ and the migration enthalpy $H_{D,Me}$.

For a selection of transition metals, the diffusivity is plotted versus the inverse temperature in *Figure 5.2*.

Again, three groups can be distinguished: The highly soluble elements Cu and Ni diffuse also very fast, as does Co. These metals can be brought to move already at very low temperatures. Fe and Cr belong to the metals which need increased temperatures – for example applied in standard industrial processes – for diffusion. On the other hand, Ti hardly diffuses even at very high temperatures.

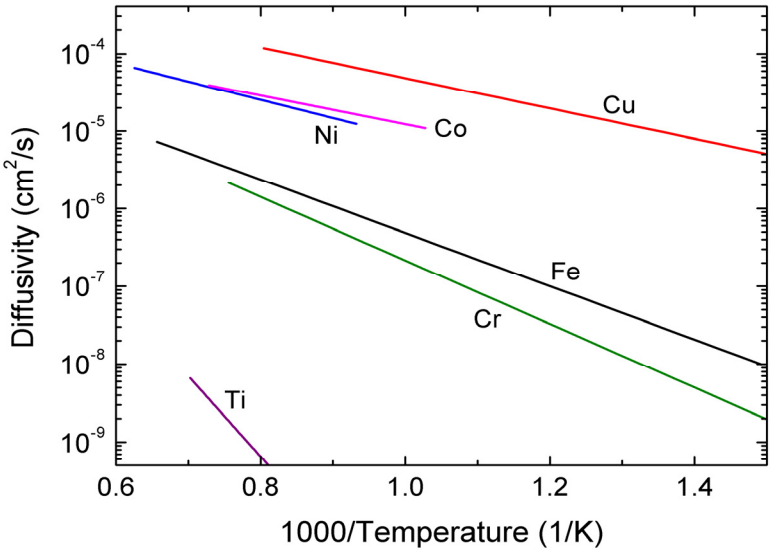

Figure 5.2: Diffusivity of various transition metals versus inverse temperature. Values taken from Graff [34].

5.1.3 Precipitation

Precipitation of impurities in silicon occurs if the free energy of the system consisting of the silicon matrix and the precipitate is lower than the energy of dissolved impurity atoms in the silicon lattice. While some elements, especially Cu and Ni, precipitate without necessitating any inhomogeneities in the silicon lattice (homogeneous nucleation), other impurities, in particular Fe and Cr, form metal clusters only if they come across nucleation sites (heterogeneous nucleation). The latter can consist of crystal defects, grain boundaries and dislocations, or other precipitates.

The precipitation growth and dissolution is thus a complex mechanism depending on the solid solubility of the metal in thermodynamic equilibrium, on the diffusivity which defines the time that atoms need to reach a nucleation site, and on the precipitate size itself due to the energy needed to displace atoms of the host silicon crystal.

Probably the most advanced model for precipitate evolution in silicon is based on the Fokker-Planck mechanism [109]. It describes the density of precipitation sites $F(i,t)$ containing i metal atoms at time t:

$$\frac{\partial F(i,t)}{\partial t} = \frac{\partial}{\partial i}\left(- A(i,t)F(i,t) + B(i,t)\frac{\partial F(i,t)}{\partial i}\right) \qquad (5\text{-}3),$$

with

$$A(i,t) = g(i,t) - d(i,t) \text{ and } B(i,t) = \frac{g(i,t) + d(i,t)}{2} \qquad (5\text{-}4),$$

where $g(i,t)$ and $d(i,t)$ correspond to the growth and dissolution rates of the precipitates, respectively. The growth and dissolution rate depend on the metal diffusivity, D_{Me}, on the local dissolved impurity concentration, C_{Me}, which may exceed the solid solubility in equilibrium, $C^{solid}_{eq,Me}$, on the activation energy E_a constituting an energy barrier to be over-

come during precipitation, and finally on the precipitate size via the average capture radius r_c which is proportional to the number of atoms in the precipitate i:

$$r_c \propto i^{1/2} \tag{5-5},$$

$$g(n,t) = 4\pi r_c D_{Me} C_{Me} \tag{5-6},$$

$$d(n,t) = 4\pi r_c D_{Me} C_{eq,Me}^{solid} \exp\left(\frac{E_a}{k_B T i^{1/2}}\right) \tag{5-7}.$$

Under favorable circumstances, large precipitates continue to grow, while small precipitates are slowly dissolved, thus effectively decreasing the total number of metal clusters and the effective recombination active metal-silicon interface. This process is usually termed "Ostwald ripening".

5.2 Impurity distribution after crystallization

The interaction between impurities in the silicon melt and the crystallization has been topic of several publications, most of which investigate the effect of constitutional supercooling during Cz growth.

Constitutional supercooling can occur when impurities are kept in the silicon melt during solidification due to the segregation mechanism. If the stirring is insufficient, an impurity gradient develops in the melt with the impurity concentration being largest at the solid / liquid interface. When the concentration exceeds a critical level, the freezing point of the silicon-impurity mixture can change towards lower temperatures. Depending on the temperature distribution and gradients which are mostly controlled by the crystallization technique and its parameters, the silicon solidification can occur prematurely, leading to high dislocation and grain boundary densities. In that case, the crystallization velocity and / or the temperature gradients have to be adjusted in order to obtain a good crystal quality. An overview over the mechanism is given in reference [9].

It was shown that in the final Cz-crystal growth of UMG-Si, too, a high transition metal content can lead to "interface breakdown" [110]. Hopkins simplified the description of constitutional supercooling to give an estimation of the critical impurity concentration which leads to breakdown of the crystallization front. He concluded that the only element-specific parameters are the slope of the liquidus curve and the diffusivity in the liquid $D_{Me,L}$; both depend only marginally on the element properties [110]. Therefore, Hopkins expects that interface breakdown during Cz growth is a question of impurity concentration in the melt and less of the impurity species [110]. This statement will be discussed in the following sections under the light of our new results.

Ciszek et al. [111] reported on experiments of mc-Si crystallization via the float zone method which had been intentionally contaminated with iron in the melt. They observed very small grains due to constitutional supercooling only at high Fe concentrations around $1x10^{16}$ at/cm^3.

For block-cast multicrystalline Si, effects of supercooling have been reported in literature e.g. by Gasaparini et al. [112], who investigated the impact of the addition of 5, 100, and 500 ppmw of iron to the silicon melt. They found that the higher the impurity concentration was, the earlier the columnar structure of the mc-Si crystal broke down, resulting in very small grains (diameter ~200 µm) and the formation of large Fe-precipitates. For the most lightly doped ingot, the breakdown occurs at the top of the ingot, which would normally be discarded.

Most recently, Coletti et al. noticed the influence of iron contamination on the crystal structure of block-cast mc-Si [113] by comparing the recombination active crystal defects in L_{eff}-maps at different ingot heights from reference blocks with ingots initially contaminated with 53 ppmw iron in the silicon melt. However, the observed effect was less severe than expected for constitutional supercooling, indicating that the interaction may be based on a different mechanism.

5.2.1 Indications for interaction between high impurity concentration in the silicon melt and the crystallization

In literature, detailed information on the correlation between crystallographic defect density in mc-Si crystals and impurity concentration in the silicon melt has mostly been compiled for the case of iron. In order to extend these investigations, in the following multicrystalline ingots manufactured in the experimental block-casting facility IS30 at the Deutsche Solar which have been processed in different campaigns in the frame of the research cluster SolarFocus are examined qualitatively with regard to the density of recombination active defects in relation to impurity concentration and element versus ingot height.

In particular, this study includes solar cells from the following blocks:

- A reference block made from highly pure virgin grade feedstock, called “Ref mc 1”;
- a block made from virgin grade feedstock, to which 20 ppma (ca. 45 ppmw) Cu had been added to the melt, termed “Cu mc”;
- a block made from virgin grade Si, contaminated with 20 ppma Fe (ca. 40 ppmw), referred to as “Fe mc 2”;
- a block made from virgin grade feedstock, intentionally contaminated with 20 ppma Cu + 20 ppma Fe, called “Fe-Cu mc”; and
- a block made from virgin grade silicon with 20 ppma Cr (ca. 37 ppmw), referred to as “Cr mc 2”.

The crystallization conditions during the solidification of these five blocks were aimed to be practically identical, which allows for drawing direct conclusions on the impurity-related crystallographic defect density. After crystallization, the top 10 – 20 mm were taken off and discarded before wafering, which is the usual procedure. A standard industrial solar cell process, based on screen-printed contacts, was applied in a process line by one of the industry partners, followed by the integral measurement of the solar cell pa-

rameters. All solar cells were then screened by means of electroluminescence imaging[26]; these images were used for the following analysis.

Figure 5.3 exemplarily depicts electroluminescence images of the solar cells taken from four blocks at approximately 80% ingot height. In these measurements, the intensity of the band-to-band radiation is used to identify material-related reductions of the minority carrier diffusion length [114] or process flaws. Electrically active crystallographic defects are marked by dark lines and clusters as a consequence of the high recombination activity of the impurity decoration. At some wafer edges (for example left and right edges in *Figure 5.3* (a)), the images include dark shady areas coming from highly contaminated grains due to impurity indiffusion into the solidified crystal from the crucible. These regions are disregarded in the following because they hold information concerning crystallization–impurity interaction only for the special case of the influence of impurities from the crucible, which is the same in all investigated blocks. In addition, all images in *Figure 5.3* contain dark lines which run parallel to the fingers of the front contacting grid. This intensity reduction is due to the resistive voltage drop along the grid line if one end of the finger is disrupted and has nothing to do with the electrical activity of crystal defects and is therefore disregarded as well.

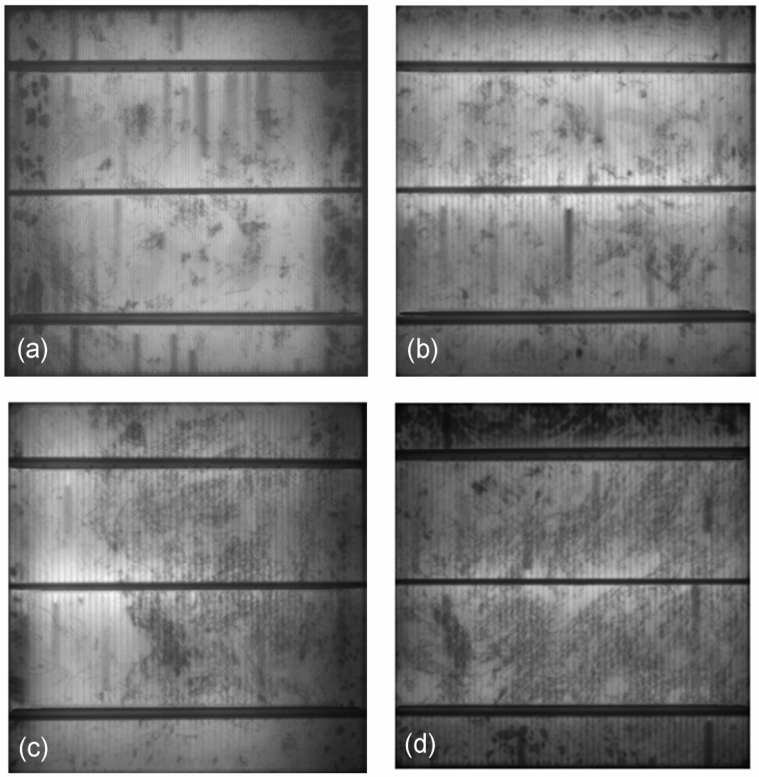

Figure 5.3: Electroluminescence images (performed at ISFH, Hameln) of solar cells taken from 80% ingot height of (a) a virgin grade feedstock reference block ("Ref mc 1"), (b) a block contaminated with 20 ppma Cu ("Cu mc"), (c) a block contaminated with 20 ppma Cu + 20 ppma Fe ("Fe-Cu mc"), and (d) a block contaminated with 20 ppma Cr ("Cr mc 2").

[26] Screening performed at the ISFH, Hameln; images were made accessible to all project partners.

Wafers from the block which was only contaminated with 20 ppma Fe ("Fe mc 2") show an electrically active crystal defect distribution which is very similar to the reference ingot, *Figure 5.3* (a), along the entire ingot length. This indicates that a content of 20 ppma Fe does not affect the crystal quality.

Similarly, 20 ppma of Cu does not significantly affect the mc-Si growth as witnessed by the EL image in *Figure 5.3* (b). However, towards the top of the Cu-contaminated ingot starting at approximately 90% ingot height, individual dot-shaped recombination active defects begin to form. They appear to be independent of crystallographic defects and follow the crystallization front closely. These defects were identified in TEM-measurements as large, veil- or star-shaped Cu clusters of several µm in diameter [115].

While the silicon melt may contain 20 ppma of *either* Fe *or* Cu without changing the crystalline quality, the sum of both (20 ppma Fe + 20 ppma Cu) causes a significantly enhanced appearance of electrically active crystal defects starting at about 60% ingot height (see *Figure 5.3* (c)).

An even larger impact has chromium. In contrast to Fe with otherwise very similar properties, 20 ppma of solely Cr in the silicon melt leads to a very high density of electrically active defects across almost the entire wafer at around 65 – 70 % ingot height, which can be seen in *Figure 5.3* (d). This observation was corroborated by results obtained on a second block of similar composition, not shown here.

Assuming that all dislocations have accumulated enough impurities in order to be recombination active (which is very likely at least in the highly contaminated blocks), these observations suggest that it is the crystal defect density after block-casting of mc-Si blocks which increases if the silicon melt contains a critical amount of metallic contaminants. Moreover, our results also indicate that both the total impurity concentration *and* the impurity species directly influence the crystal quality, which has never been shown before.

Since the latter statement is in contradiction with Hopkins' expectation that the impurity species does not matter for the interaction with the crystal growth process [110] (which he suggested for constitutional supercooling during Cz-crystal pulling) and since the columnar structure of the grains in our investigation is not visibly disturbed, the effect described in this study is probably not a consequence of constitutional supercooling, supporting the statement of Coletti et al. [113]. Therefore, another physical mechanism must play a role.

An indication may be found in the impurity distribution which is influenced by the different growth techniques manifested for example in the different effective segregation coefficients k_{eff} of transition metals in mono- and multicrystalline solidification. In general, the segregation coefficient was shown to be larger in the case of mc-Si growth [28].

This can be explained by a modification of a model published by Macdonald et al. [26], proclaiming a liquid / solid system consisting of three instead of only two phases during solidification: Besides segregation between the solid and the liquid fraction, intrinsic gettering occurs at crystal defects – forming the third phase – in the solid within a very short time, depending on the diffusivity of the metal and on the distance between the

crystallographic defects[27]. Thus, the crystal intragrain regions close to the solid / liquid interface are depleted of metals and – according to the segregation mechanism (section 2.2.4) – absorb additional quantities coming from the silicon melt. The effective solid solubility, taking into account precipitation of the respective metal in silicon, $C_{eq,eff}^{solid}$(Me) would then be a function of the crystal defect density which means that it is generally increased in mc-Si.

The latter supposition was for example proposed by Schön et al. [116] in order to explain the Fe distribution in as-grown silicon wafers over ingot height in numerical simulations. However, its validity has been topic for ongoing discussions in the community. In the following section, the soundness of this assumption will be inspected with the help of experiments.

Coming back to the model, during the intrinsic gettering, the metal atoms form precipitates which most often do not fit to the silicon matrix [107]. As a result, stress is exerted on the silicon lattice, which we can suppose to be enhanced by the different thermal expansion coefficients of the metal clusters and Si and the temperature gradients during the cooling down. Additional dislocations are likely to be punched out, which may pervade the crystal until the solid / liquid interface.

The development of crystal defects, especially dislocations, and hence the incorporation of transition metals could thus be a highly non-linear system, constituting a positive feedback loop. It depends on the elemental properties, most importantly on the temperature-dependent solid solubility and diffusivity in the monocrystal, both of which influence the tendency of an impurity to form precipitates. Furthermore, the misfit and thermal expansion coefficients of the metal silicide and thus the ability of the metal precipitates to provoke increased stress and to punch out dislocations play a role.

Although the solid solubility in mono-Si has been determined only for a limited temperature range, it is safe to assume that the solubility of the different transition metals right after crystallizing (i.e. at ~1400°C) follows the same trend as shown in *Figure 5.1*: Therefore, C_{eq}^{solid} of Cu will exceed the solubility of Fe by approximately two and that of Cr by about three orders of magnitude. As a consequence, for a given impurity concentration in the silicon crystal, Cr will be the first impurity to precipitate during the cool-down provided that the density of nucleation sites is sufficiently high, followed by Fe.

This very simple model could well explain our observations on the blocks intentionally contaminated with either Fe, Cr or Cu. However, for this finding the influence of the different effective segregation coefficients has been neglected so far. With the k_{eff}-values given in *Table 2.2*, the impurity concentration of Fe and Cr in the crystal close to the solid / liquid-interface at a given ingot height is expected to be much lower than that of Cu, neutralizing to a certain extent the effect of the lower solid solubilities. Nevertheless, it has to be kept in mind that these segregation coefficients describe the impurity distribution in *monocrystalline* silicon. Our simple model though assumes that the segregation in *mc-Si* crystallization is strongly modified, therefore the k_{eff} values as shown in *Table 2.2* are not valid in our description and therefore do not allow to draw any conclusions.

[27] Macdonald e.g. estimated that the system of Fe in block-cast mc-Si would equilibrate within 1 second if the dislocation density was in the order of 10^5 cm^{-2}, which is often the case.

Since for this model, the statement that the effective metal solubility in silicon is a function of the crystal defect density is fundamental, a dedicated experiment was performed in order to investigate its validity.

5.2.2 Correlation between metallic impurity distribution and crystal defects

The deteriorating effect of high crystal defect densities has been shown in numerous publications (e.g. [117-119]). These works also conclude that silicon regions with high dislocation densities do not respond as well to gettering as do areas with less crystal defects. This was attributed to metal precipitates located at the defects and acting as practically infinite sources for impurity out-diffusion during the high-temperature solar cell processes. While the qualitative correlation between crystal defect density and the recombination activity before and after gettering has thus often been demonstrated, the extent of the metal concentration increase in the highly dislocated areas has never been investigated.

In order to give an exemplary quantification of the impurity content as a function of crystal defect density, we carried out the following experiment[28]:

Two sets of twenty neighboring wafers (format 156 x 156 mm^2), spanning an ingot length of approximately 8 mm each, were chosen from the center of an electromagnetically cast mc-Si block "EM-cast mc". This specific material has the advantage that the wafers contained one region of low dislocation density and one of relatively high defect density which could be separated from each other with ease. In addition, the negligible contact with the crucible and the continuous electromagnetic stirring guarantee a much higher degree of homogeneous impurity distribution in the melt and in the crystal than can be expected from e.g. standard block-cast multicrystalline material. Further, due to the continuous feeding of the silicon melt, the influence of the segregation on the impurity distribution over ingot height is expected to be smaller compared to other crystallization technologies.

Each set of 20 wafers was cut accordingly, dividing them into a high and a low dislocation density part in all neighboring wafers, resulting in four sets with different crystal defect densities. Small pieces of 20 x 20 mm^2 were taken from each set for the determination of the dislocation densities. Then the remaining samples were chemically cleaned and NAA measurements yielding the total concentration – precipitated as well as dissolved impurities – were performed[29].

The dislocation densities were measured following the standard procedure: One side of each sample was mechanically polished, and then the silicon was Secco-etched for approximately 30 seconds[30], revealing the dislocations and grain boundaries by preferential etching. The etch pits were counted by means of a Zeiss microscope (magnification 50x) and an automated software routine.

---

[28] The following work and analysis were performed in collaboration with S. Rein and I. Reis.
[29] NAA measurements performed at EAI, USA.
[30] Cutting by C. Harmel, polishing by G. Räuber, Secco-etch by M. Kwiatkowska.

The routine sub-divides each image into squares with an edge length of 95 x 95 µm^2 and counts the dislocation etch pits in each square. Dislocation etch pits are automatically separated from other features like grain boundaries and dust particles by pre-defining characteristic geometric factors like diameter, roundness etc. The number of dislocation pits is then averaged over the area of the square and recorded in a table together with the respective geometric location.

For this study, the histograms of the dislocation densities were fitted to Gaussian profiles with very good fit quality. In *Figure 5.4*, the total concentrations of the transition metals of all four sample sets are plotted versus the peak of the Gaussian curves. The correlation between the transition metal concentration and the defect density is evident. Our measurements suggest that the metal concentration increases linearly or even super-linearly with increasing dislocation density. This is true for all metal species within the scatter.

This finding supports the hypthesis stated in the previous section that the effective solubility of the metals $C_{eq,eff}^{solid}(\mathrm{Me})$ is a function of the dislocation density *DL* and may be written as

$$C_{eq,eff}^{solid}(\mathrm{Me}) \propto DL \times C_{eq}^{solid}(\mathrm{Me}) \qquad (5\text{-}8),$$

which has entered in recent simulations of the impurity distribution [116].

The effect of phosphorus gettering on the silicon wafers used for this investigation is shown in section 5.3.3.

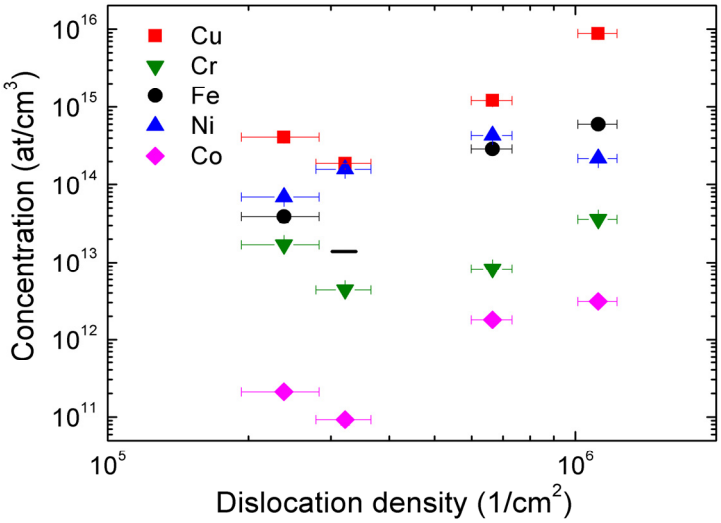

Figure 5.4: Transition metal concentration measured by means of NAA versus the peak of the dislocation density histograms (determined by means of etch pit density). The histograms were fitted to Gaussian profiles (fit quality >0.96), with the standard deviation giving the x-axis error bars. In one case, the Fe concentration was below the Fe-specific detection limit marked by the black line.

5.2.3 Interaction between different transition metals

As neither Cu nor Fe at a concentration of 20 ppma in the silicon melt lead to increased crystal defect densities, how can we explain the high concentration of defects in the block contaminated with the sum of both, depicted in *Figure 5.3* (c)?

In the model described in section 5.2.1, this effect points towards an interaction of both transition metals changing the precipitation behavior during the crystallization.

It has already been mentioned that some metals tend to form co-precipitates, e.g. Fe with Cu and Ni. Firstly, this is because Fe needs a nucleation site as it precipitates only heterogeneously, and secondly, some metals (including Ni) form a liquid eutectic at intermediate temperatures leading to impurity segregation gettering in the silicon bulk [108].

Thus, the composition of the silicon melt contamination has a large influence on the silicon block. To substantiate this statement further, an investigation was launched.

Wafers were taken from the blocks "Fe mc" (intentionally contaminated with 200 ppmw Fe in the melt), "Ni mc" (40 ppmw Ni) and "Fe-Cr-Ni mc" (200 ppmw Fe + 40 ppmw Cr + 40 ppmw Ni) at the same ingot height of 80%. The blocks had been cast at SINTEF, Norway, in the frame of the research project CrystalClear. Several samples of 12 x 12 mm^2 were cut from regions with high crystal defect density, polish-etched and cleaned[31].

Micro-photoluminescence measurements were done on the samples helping to identify highly recombination active grain boundaries[32]. Details on this measurement method can be found in section 6.2.1 and reference [120]. Next, micro-X-ray fluorescence (µ-XRF) scans were carried out at beamline ID22 at the electron synchrotron radiation facility (ESRF) in Grenoble, France, in order to measure the size, spatial distribution and chemical composition of the precipitates present in the different blocks.

The beamline ID22 offers a high photon flux of approx. 10^{12} ph/s in the wavelength range between 6.5-18 keV [121] with a spot size of approx. 1.5 x 3.5 µm. The detection limit of Ni precipitates, described by the precipitate radius, at this beamline is roughly estimated to be around 30-50 nm [121].

µ-XRF scans in areas of 100 x 100 $µm^2$ each were performed around triple points where three highly recombination active grain boundaries meet, thus maximizing the probability of finding precipitates within the scan.

On the samples taken from "Fe mc" and from "Ni mc", twelve scans were run on each, totalling an area of more than 100,000 $µm^2$. Neither on the Fe-contaminated nor on the Ni-contaminated silicon samples, any transition metal precipitate was found within the detection limit. The only clusters consisted of Ca.

However, on the samples taken from the "Fe-Cr-Ni mc"-Si wafer, one or more precipitates were found in 15 of 17 scans. The difference in the precipitation behavior of Fe, Ni and Cr in the investigated blocks is therefore statistically significant.

---

[31] Cutting by C. Harmel, polish etch by M. Kwiatkowska and cleaning by R. Neubauer.
[32] Micro-photoluminescence measurements performed by P. Gundel.

The observed metal clusters can be divided into two groups: (i) Small Ni precipitates, often distributed relatively homogeneously along grain boundaries; (ii) large precipitates consisting mostly of Ni, with trace amounts of Fe and Cr where the Fe signal is always more intensive than the Cr signal. An example of the second type is shown in *Figure 5.5*. These clusters can become as large as several µm in diameter.

Since the wafers were all taken from the same block height, one would expect from Scheil's equation, describing the distribution of the total amount of impurities along the ingot height, that the Fe concentration would be the same in the "Fe mc" wafer as in the "Fe-Cr-Ni mc" samples; an analogous argumentation is valid for the Ni in the "Ni mc" and "Fe-Cr-Ni mc" wafers. However, we infer that this is not the case because we can safely assume that the majority of impurity atoms is concentrated in the very large metal clusters.

This would mean that the assumption of Scheil's model supposing the segregation can be described separately for each element in the silicon melt is not correct (see section 2.2.4). Unfortunately, NAA measurements which could support this conclusion on a sounder statistical basis and which were performed on these blocks in the frame of the CrystalClear project by another institute are not yet available at the time of writing.

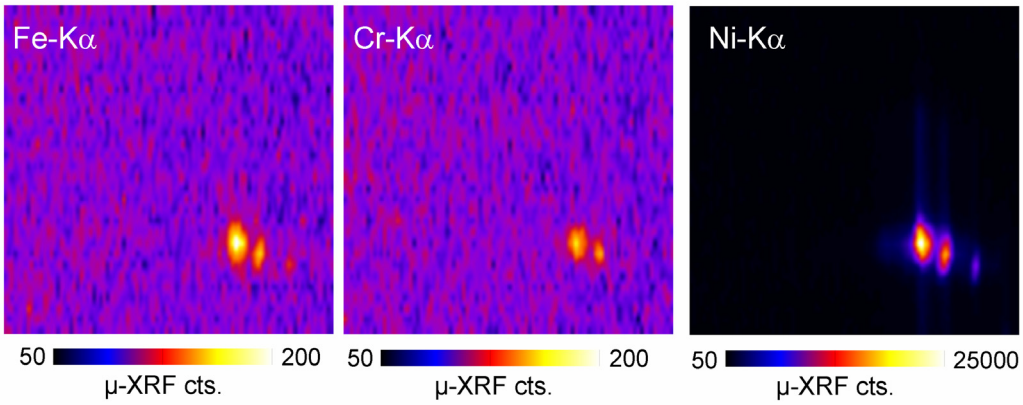

Figure 5.5: Micro-XRF measurements performed at the ESRF Grenoble, ID22, on a wafer from 80% ingot height taken from ingot "Fe-Cr-Ni mc". Note the different scaling of the Ni-Kα line intensity. The side lengths of the scans correspond to 100 µm.

Nevertheless, this investigation suggests that interelemental interactions can change the distribution of the metals probably already during the crystal growth, which has not been previously observed.

5.2.4 Assessment of tolerable impurity and crystal defect concentrations

In literature, the tolerable impurity concentration in the silicon has been assessed by plotting the normalized solar cell efficiency versus the concentration of the various metals, see e.g. [37] for results on monocrystalline and [122] on multicrystalline silicon (*Figure 5.6*). Thus, a direct relation between metal content of the as-grown wafer and the resulting solar cell quality has been established. Based on our observations presented in the previous sections, these relations show only part of the truth because they yield no

information about the metal-crystallization interaction, which is shortly summarized in the following:

During multicrystalline silicon growth, the impurities in the silicon melt interact with the solidification process. This interaction is largely determined by the elemental properties, namely the solid solubility (which is a linear or superlinear function of the dislocation density) and the diffusivity which govern the propensity of an element to form precipitates. Alternatively, metals can interact with each other, increasing the probability of precipitates taking shape, which happens for example when Ni is present. In both cases, the metal clusters form already a short time after the crystallization front has passed. Via the stress put on the silicon lattice, dislocations are generated which can reach the solid / liquid interface fast and increase the crystal defect density. Thus, additional nucleation centers are provided, increasing the likeliness of precipitate formation and the effective solid solubility.

Due to the nonlinear character of the dislocation generation during crystallization of a contaminated silicon melt, an important measurand is the *crystalline quality* as function of the impurity concentration in the melt.

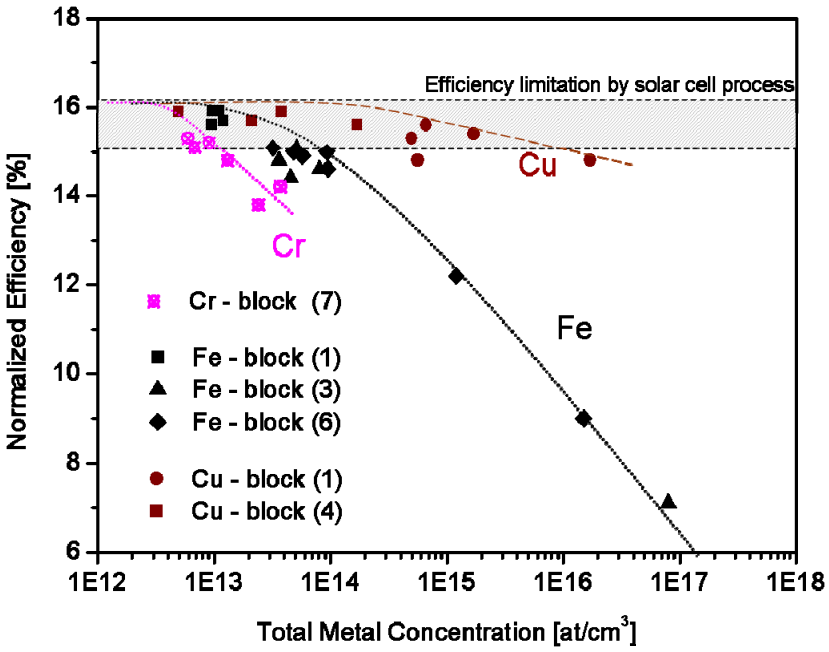

Figure 5.6: Normalized solar cell efficiency (meaning that the influence of the fill factor was taken out of the computation of the efficiency) versus the total metal concentration measured via NAA at the respective ingot height. Taken from Riepe et al. [122]. The solar cell results were obtained on material investigated in this thesis; the correlation with the notation used here is as follows: Cr block (7) – "Cr mc 2"; Fe block (1) and Cu block (1) – "Ref mc 1"; Fe-block (3) – "Fe mc 2"; Fe-block (6) – "Fe-Cu mc"; Cu-block (4) – "Cu mc".

The impact of the crystal defects on the solar cell parameters on the blocks taken in our study is visualized in *Figure 5.7* (for the description of the solar cells, see section 5.2.1). As indicative parameter, the open circuit voltage was chosen, which depends linearly on

the recombination active defect area introduced by the crystal defects according to a study published by Haunschild et al. [123].

By comparison with the reference ("Ref mc 1") and the Fe-contaminated ("Fe mc 2") blocks, the V_{OC}-values in the other transition metal-contaminated ingots are decreased in a larger ingot portion.

The beginning of the crystal defect generation towards the top end – roughly determined with the help of EL measurements – of the two ingots "Fe-Cu mc" and "Cr mc 2" are marked by the dashed black and green line, respectively. Approximately in this ingot region, the open circuit voltage starts to deteriorate, as expected for the relation between recombination active crystal defects, appearing dark in EL measurements, and the V_{OC}. However, this decrease is slow with increasing ingot height at first; only at approximately 90% ingot height, the solar cell performance degrades fast. This is probably due to the final incorporation of the remaining metal impurities from the silicon melt. By contrast, while in a large ingot part the V_{OC} of the Cu contaminated solar cells ("Cu mc") is higher than the reference, it also starts to degrade at approx. 65% ingot height. As soon as the first Cu precipitates are detected as black spots at ca. 90% ingot height, marked by the red dashed line, the open circuit voltage degrades rapidly.

To conclude, for the assessment of the tolerable impurity content in the silicon melt, besides the direct correlation of solar cell efficiency with metal concentration, also the deterioration of the V_{OC} and hence the solar cell efficiency due to increased crystal defect concentrations has to be considered.

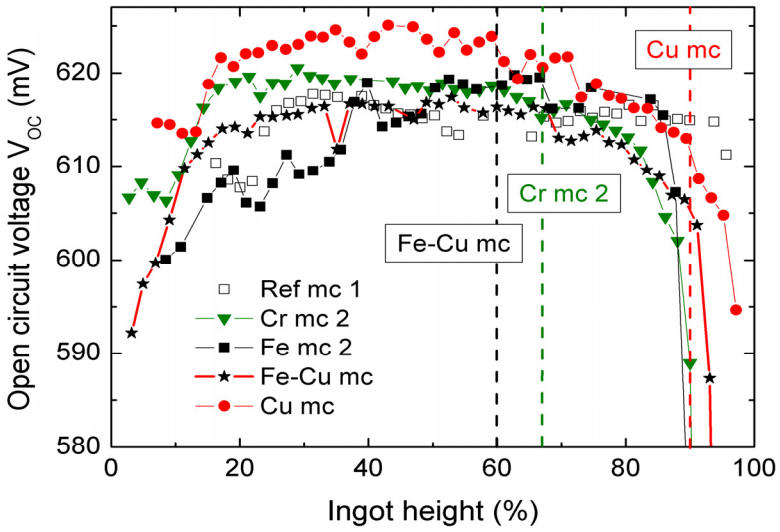

Figure 5.7: Open circuit voltage versus normalized ingot height of the solar cells investigated in section 5.2.1. The colored dashed lines indicate the approximate position where increased crystal defect density is noticed (section 5.2.1).

5.3 Redistribution of metallic impurities during high-temperature processing steps

Having assessed the interaction between metal impurities and crystal defects in general, in the following the impurity reaction to high-temperature steps is investigated. In particular, the concept of "defect engineering" shall be tested from a practical point of view.

In the standard industrial solar cell process, increased temperatures are applied during three processing steps: the phosphorus emitter diffusion, the SiN coating and the contact firing. Since the latter two are either at low temperature (~350°C-550°C) or very short (firing for several seconds), impurity redistribution is mostly determined by the phosphorus diffusion step. Depending on the target sheet resistivity and emitter profile, temperatures in the range of approx. 800°C – 900°C and diffusion times in the order of 30 minutes to an hour are commonly applied. A viable possibility of including defect engineering in current processing schemes would therefore be to apply a low temperature anneal after the P-diffusion or after contact firing at the end of the solar cell process.

Previous publications investigating precipitation mechanisms of transition metals in silicon mainly focused on the resulting impurity configuration of various transition metal elements after different ramping down scenarios [124, 125]. By comparing several Cz or mc wafers which had been intentionally contaminated in a similar way by indiffusion of Fe, Cu or Ni from the wafer surface, for example, it was found that a slow cool after a high temperature step led to larger precipitates than fast ramping down [6]. Applying this knowledge to solar cell processes, Pickett et al. [126] showed an increase of the solar cell efficiency of iron-rich mc-Si at a low temperature anneal of 300-500°C for 30 min. applied after the phosphorus emitter diffusion. Rinio et al. [127] investigated the effect of annealing for 90 min. at temperatures between 300 and 800°C after phosphorus diffusion on the efficiency of standard mc-Si wafers, finding a maximum for an anneal at around 575°C. The corresponding high-resolution light-induced current (LBIC) measurements revealed that during the low temperature treatment, mostly the carrier diffusion length in highly contaminated grains close to the crucible walls was increased. At temperatures above 600°C, the grain boundaries became increasingly recombination active, which was attributed to dissolution of large precipitates followed by a more homogeneous accumulation of the dissolved metal atoms along the grain boundaries without presenting further evidence. The chemical composition of the involved impurities was not investigated.

While in literature on the one hand, detailed information about the precipitation behavior of various transition metals like Fe, Cu and Ni in highly contaminated mc-Si samples obtained in synchrotron measurements is available and on the other hand, the effect of low temperature anneals on standard mc-Si wafers containing trace amounts of all transition metals has been shown in macroscopic investigations, these results have not yet sufficiently elucidated the link between the behavior of different metallic elements and the resulting electrical properties during adapted, realistic processing conditions. In particular, the response of different elemental species to the same processing conditions in multicrystalline material is of high interest, as "intermediate diffusers" such as Fe and Cr will react differently to anneals compared to "fast diffusers" such as Ni.

5.3.1 Response of medium and fast diffusers to adapted high-temperature processes

In the following, some excerpts from the collaboration with Matthias Blazek in the frame of his diploma thesis, supervised by the author, are presented; for more details, the reader is referred to [38].

Intrinsic gettering based on re-precipitation of transition metals is only useful *after* the application of high-temperature steps like emitter diffusion. The driving force of the re-precipitation is the decreasing metal solubility in the silicon bulk with decreasing sample temperature. However, since it takes time for metal clusters to nucleate and grow, the precipitation is only successful if an optimal balance between solid solubility and diffusivity, both determined by the temperature, is reached.

To elucidate the microscopic evolution of the plethora of transition metals which are present in standard mc-Si wafers, we set up two sets of experiments:

In a first approach, the macroscopic influence of differently designed high-temperature steps was investigated on the carrier lifetime of mc-Si wafers which had been intentionally contaminated in the silicon melt with only one element. Thus, the wafer properties were dominated by the behavior of only one metal species; by applying the same processes, the reaction of each metal could be specified.

Secondly, in the next section, the microscopic evolution of individual precipitates during different high-temperature steps is presented by means of synchrotron measurements.

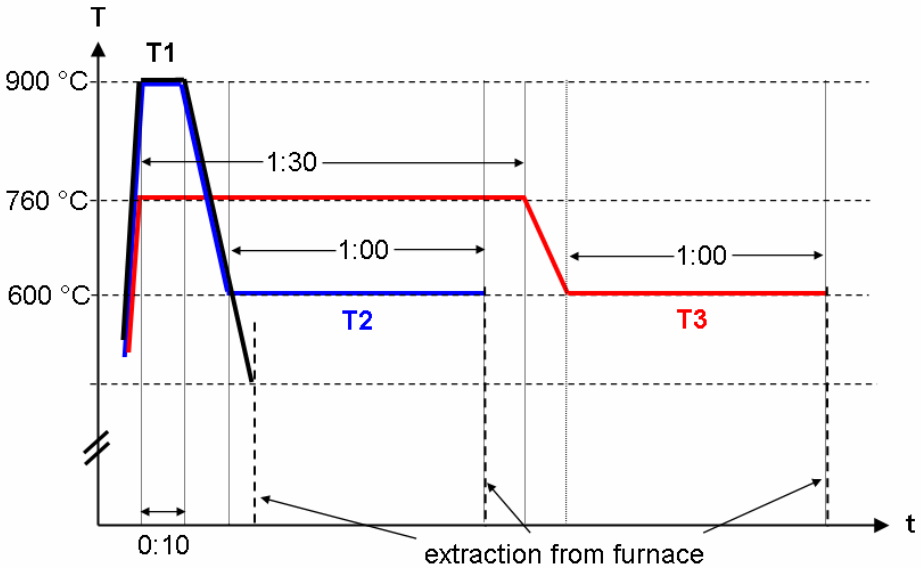

Figure 5.8: Design of the high-temperature processes T1 - T3.

The wafers for the first investigation were neighboring samples taken from the middle of the ingots "Fe mc" (contaminated with 200 ppmw Fe), "Cr mc" (40 ppmw Cr) and "Ni mc" (40 ppmw Ni), all manufactured for the research project CrystalClear at SINTEF, Norway. While Fe and Cr belong to the intermediate diffusers in silicon, Ni diffuses very fast and possesses a high solubility.

At first, the wafers (format 125 x 125 mm^2) were cut into pieces of 50 x 50 mm^2, cleaned and chemically polished[33]. Two samples per ingot were set apart to be used as "as-grown" reference for the following study.

The remainder of the samples was divided into four groups, each of which contained two wafers from each ingot. The first group was phosphorus-diffused at 825°C for 60 min., aiming at a sheet resistivity of 80 Ω/sq. Afterwards, the emitter was etched back[34].

To the other three groups, different high temperature treatments were applied. The temperature-time profiles of these processes T1, T2 and T3 are sketched in *Figure 5.8*. Ramps T1 and T2 started with a high-temperature step at 900°C for 10 min., intended to imitate the contact firing at the end of the solar cell process[35], followed either by a fast ramping down to 550°C and quick extraction from the furnace, or a low-temperature anneal for 90 min. at 600°C and subsequent extraction at the same temperature. While profile T1 imitates standard processes without intrinsic gettering, profile T2 is supposed to show the improvement due to metallic re-precipitation. Alternatively, temperature ramp T3 starts for 60 minutes at 760°C, continued with the low-temperature anneal at 600°C for 90 min. This step is intended to minimize the precipitate dissolution and maximize the intrinsic gettering without losing the capability to permit emitter diffusion. These high-temperature steps were applied to the differently contaminated wafers at the same time under constant Argon flow in a cleanroom tube furnace. Thus, it was ensured that the processing conditions were exactly the same for each group.

After extraction, all samples (including the as-grown wafers and the P-diffused samples) were chemically cleaned and surface passivated with a high quality SiN coating on both sides. The minority carrier lifetime was measured by means of micro-photoconductance decay (μ-PCD) scanning and by QSSPC[36].

The results of the spatially resolved examination via μ-PCD are displayed in *Figure 5.9* and the average values of the QSSPC lifetime of the two simultaneously processed samples from the same ingot are summarized in *Figure 5.10*.

[33] Cutting by M. Schwarzkopf, cleaning, polishing and emitter etch-back by M. Kwiatkowska.
[34] P-diffusion and the high-temperature steps were done with the help of H. Lautenschlager.
[35] The dedicated furnace used for these experiments is not capable of ramping up and down as fast as usual contact firing schemes. Nevertheless, the initial short high temperature successfully dissolves some of the trapped impurities, imitating usual high-temperature steps.
[36] Measurements performed by M. Blazek.

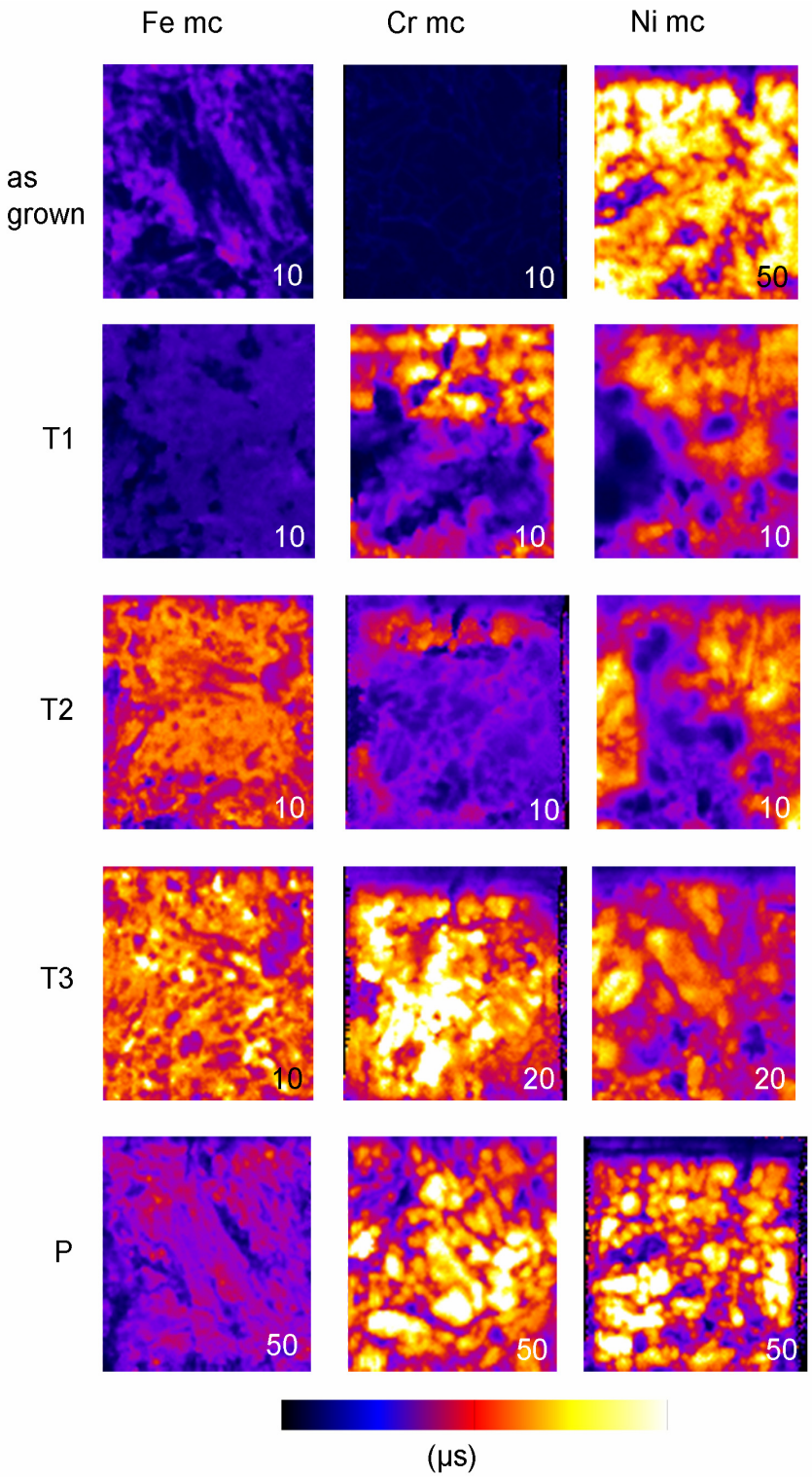

Figure 5.9: Minority carrier lifetime maps obtained with the help of µ-photoconductance decay (µ-PCD) measurements on 50 x 50 mm² samples from ingots "Fe mc", "Cr mc" and "Ni mc". The scaling of each image starts at 0 µs while the maximum value is denoted in the corner at the bottom to the right.

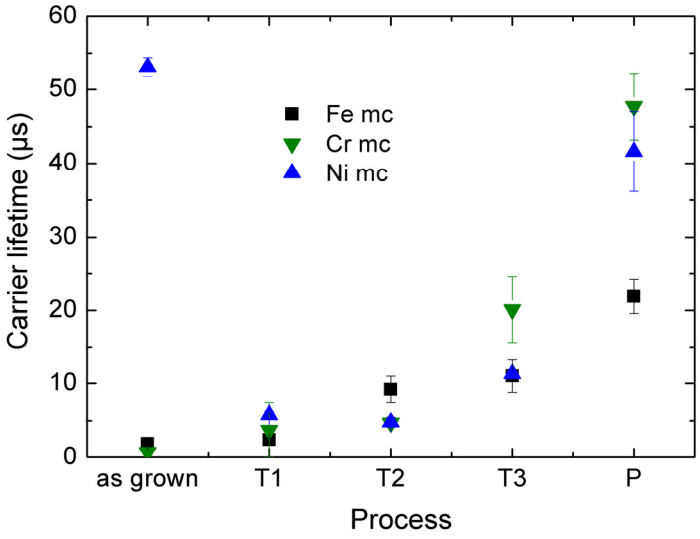

Figure 5.10: Carrier lifetime measured via QSSPC at an injection density of 1x10^{15} cm^{-3} on mc-Si samples taken from the middle of the intentionally contaminated ingots "Fe mc", "Cr mc" and "Ni mc", to which different temperature processes had been applied. For explanation, see text.

The three transition metals exhibit three different responses to our temperature treatments. At the beginning, both the Fe and Cr wafers have very low carrier lifetimes <1 µs, while the Ni contaminated sample shows an extraordinarily high value above 50 µs in spite of the contamination. Again, this finding can be explained by the formation of large Ni precipitates under the optimal conditions (for Ni) during the cool-down after crystallization, for which we also obtained indications in the synchrotron measurements described in section 5.2.1 (see *Figure 5.5*) which had been carried out on samples from the same ingot. On the other hand, our observations suggest that Fe and Cr have not had the chance to accumulate during cool-down, thus being relatively homogeneously distributed. While the Fe-contaminated sample in the as-grown state shows signs of intrinsic gettering (the carrier lifetime at crystal defects is higher than in the grains), the Cr-contaminated sample hardly does. The reason may once more be found in the diffusivity and the solubility of Cr, which are both slightly below the Fe-values, hampering the precipitation process.

After the short application of the 900°C step (profile T1), the picture changes completely: While the Cr-sample experiences a noticeable lifetime enhancement, the carrier lifetime of both Fe and Ni samples suffers due to the significant metal dissolution in the silicon bulk without having the possibility to re-precipitate. In fact, we have made the experience that intrinsic gettering of Cr is not a very delicate process – almost any high temperature leads to a lifetime increase from the admittedly very low initial values in mc-Si material [128].

The low-temperature anneal of the following step T2 at 600°C especially assists in the re-precipitation of Fe, which is in good accordance with results presented in literature [127]. The Cr-wafer also profits from the anneal, while the Ni sample shows a very low lifetime similar to the outcome of ramp T1. This indicates that the Ni out-diffusion during the high

temperature cannot be completely reversed within the low-temperature anneal for 90 minutes.

The temperature profile T3 presents the best option for intrinsic gettering of both Fe and Cr. In addition, the carrier lifetime of the Ni samples is not as deteriorated as after steps T1 and T2. The long, relatively low temperature treatment seems to keep the dissolution of all transition metals at an acceptable level while the subsequent low-temperature anneal leads to intrinsic gettering as intended.

For comparison, the potential of external gettering without making use of precipitation is depicted in the result of the P-diffused wafers. The carrier lifetimes of all wafers doubles that of the best intrinsic gettering step T3. Nevertheless, the success of step T3 especially for the intermediate diffusers Fe and Cr is considerable. Only the re-precipitation of Ni is difficult to enforce which is due to its high solubility in silicon.

To summarize, the three transition metals respond very differently to the high temperature treatment. While the intrinsic gettering of the medium diffusers Fe and Cr can be relatively well controlled with the help of adapted temperature-time profiles, the Ni atoms tend to exhibit a contrary behavior, which would make it difficult to bring about a re-precipitation of all transition metals at the same time (e.g. when a multicrystalline silicon material contained a noticeable amount of each of them).

Therefore, the dissolution and re-precipitation of Ni clusters is examined in more detail in microscopic analyses of individual precipitate evolution with the help of synchrotron measurements in the following section.

5.3.2 Assessment of the Ni atom redistribution during high temperature steps

The silicon samples used in this investigation were taken from 80% ingot height from the multicrystalline "Fe-Cr-Ni" block to which 40 ppmw Ni, 40 ppmw Cr and 200 ppmw Fe had been added to the melt. As shown in section 5.2.1, the Ni atoms are mostly concentrated in large clusters easily detectable by synchrotron measurements. The wafers were first chemically polished and cut into small pieces, 12 x 12 mm^2 in size. Samples containing similar densities of dislocations and grain boundaries were selected and a soft chemical cleaning was applied in order to remove surface contamination which could interfere with the following measurements[37].

X-ray fluorescence (µ-XRF) investigations were performed at beamline "µ-Spot" at the synchrotron BESSY II in Berlin, Germany. The beamline offers a spot size of approx. 3 x 5 $µm^2$ using a capillary optic. Monochromatic X-ray irradiation with energies between 9.4 and 10.0 keV were used with an approximate photon flux in the order of 10^9 ph/sec [121]. We estimate that this setup is able to detect Ni precipitates of 1 µm in diameter or larger. Several samples were scanned over an area of 150 x 150 $µm^2$, again making use of the fact that Ni precipitates preferrably cluster around triple points and along grain boundaries. Therefore, each scan contained several Ni precipitates of varying size. The location of the measurement was documented by taking in-situ microscope images.

[37] Chemical polish and cleaning by R. Neubauer, cutting by M. Schwarzkopf.

Afterwards, the samples were again chemically cleaned and then subjected to one of the following heat treatments in a standard P-diffusion furnace used also for solar cell processing:

A) 750°C for 3 hrs. and extraction at same temperature,

B) 850°C for 3 hrs. and extraction at same temperature

C) 950°C for 3 hrs. followed by a T-ramp down to 850°C and immediate removal from the oven

D) 950°C for 3 hrs. followed by a low temperature anneal at 550°C for 12 hrs.

E) P-diffused with a standard 80 Ω/sqr. emitter at 825°C for 60 min.

Steps A - D were performed under constant Ar flow[38].

The applied temperature ramps are summarized in *Figure 5.11*.

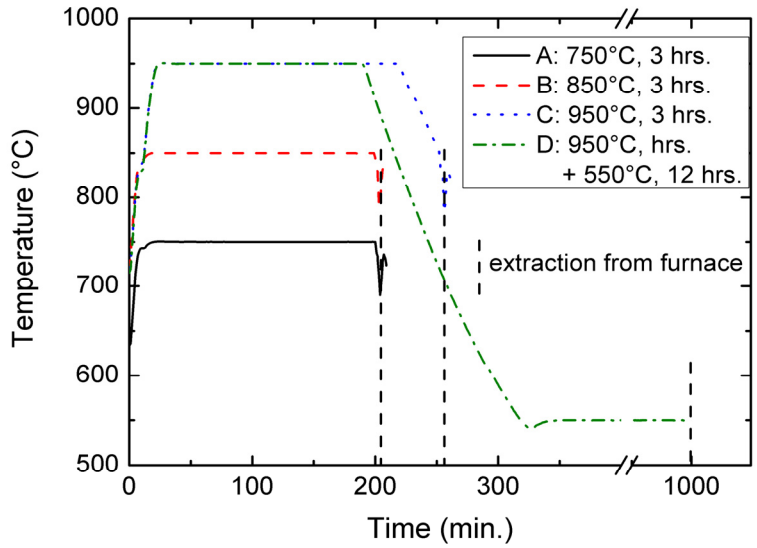

Figure 5.11: Profiles of the high temperature steps A) – D). The black dashed lines denote the moment of sample extraction from the furnace.

In contrast to previous publications [125], our aim was not to extract the samples as quickly as possible from the furnace in order to "freeze in" the impurity distribution at the respective temperature, but to investigate the effect of realistic temperature steps usable in solar cell processing. Therefore, the samples were cooled down by extracting the sample holder slowly from the furnace, the same way one proceeds in standard P-diffusion steps of silicon solar cells. This air cool results in cooling rates of approx. 10-20°C/sec.

After another chemical clean, µ-XRF measurements of all samples were performed at the same positions as the first time. This approach has the advantage that the evolution of *individual* precipitates is documented, which yields more reliable information than drawing conclusions from the statistics of similarly contaminated but in fact different samples.

[38] High-temperature steps done with the help of H. Lautenschlager.

The following analysis is based on the ratio between the counts of the Ni-Kα and the Si-Kα peak measured at every step of the µ-XRF mapping. With this normalization, both the influence of the varying photon flux and of the capillary–sample–detector geometry are taken into account.

The atomic density of Ni in the silicon samples can then be estimated with the help of reference measurements of a homogeneous standard sample with known Ni and Si concentrations. Similar to previous publications [124], in this calculation we can assume for simplicity that the Ni atoms are homogeneously distributed along the depth of the silicon wafer. With µ-XRF measurements of a reference sample, we found that for example a ratio of 10 Ni-Ka cts. / Si-Ka cts. corresponds to approximately $5x10^{12}$ Ni atoms. This approach yields an estimation of the lower concentration limit; depending on the actual location of the precipitates in the wafer bulk, the real concentration may well be larger by up to two orders of magnitude. Since we can assume that the location of the precipitates did not change significantly during the high temperature treatments, the ratio between concentrations measured before and after processing should be independent of the (unknown) distribution along the wafer depth.

As an example, *Figure 5.12* (a) shows the Ni distribution in sample B before the high temperature step. The dashed lines indicate the position of the grain boundary.

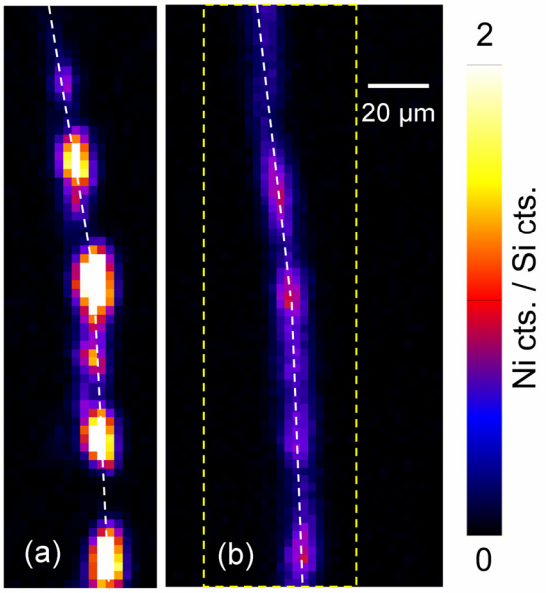

Figure 5.12: The normalized Ni-Kα-line intensity (a) before and (b) after the high-temperature step at 850°C. The dashed white line marks the position of the grain boundary.

The Ni atom distribution in the initial state is mainly determined by the slow cool at the end of the block-cast crystallization with a cooling rate in the order of 1°C/min. Due to the propensity of the system, consisting of Ni atoms dissolved in silicon, to minimize its free energy, precipitates form and Ostwald ripening occurs. As discussed in section 5.1.3, this is driven by the diffusivity and solubility of Ni at the respective temperature when the atoms are given enough time to accumulate. It seems that the cool-down after crystallization provides optimal conditions for the development of very large precipitates along grain boundaries or in their close proximity.

During the high temperature steps which are not followed by a low temperature anneal (samples A – C, E), the solid solubility of Ni in Si is raised to values between 6.5×10^{15} and 1.5×10^{17} at/cm^3 for temperatures between 750°C and 950°C, respectively (section 5.1.1). As a result, the thermodynamic equilibrium between Ni precipitates and the surrounding silicon shifts, and the large Ni clusters are able to partly dissolve. As soon as the samples are cooled down, the Ni atoms again tend to re-precipitate. This time the cool-down is faster than after crystallization, but still slow enough to allow some diffusion through the wafer bulk, especially for the fast-diffusing nickel. In our processes, the impurities therefore cluster at the grain boundaries but the temperature / time does not suffice for Ostwald ripening.

Figure 5.12 (b) shows the Ni distribution of sample B after a temperature step at 850°C for 3 hrs. Compared to the initial condition (a), the Ni count rate at the large precipitates is significantly decreased; during the high temperature step, the clusters have lost about 40 – 80% of their atoms. However, more Ni than before is found along the grain boundary.

A similar redistribution from large clusters towards grain boundaries also happens at the other temperature treatments. The only exception is the result of a low temperature anneal for 12 hrs. at 550°C. *Figure 5.13* shows the difference between the Ni / Si ratio after and before step D: While one precipitate loses about half of its atoms, the others increase in size, gaining about 10 – 80%.

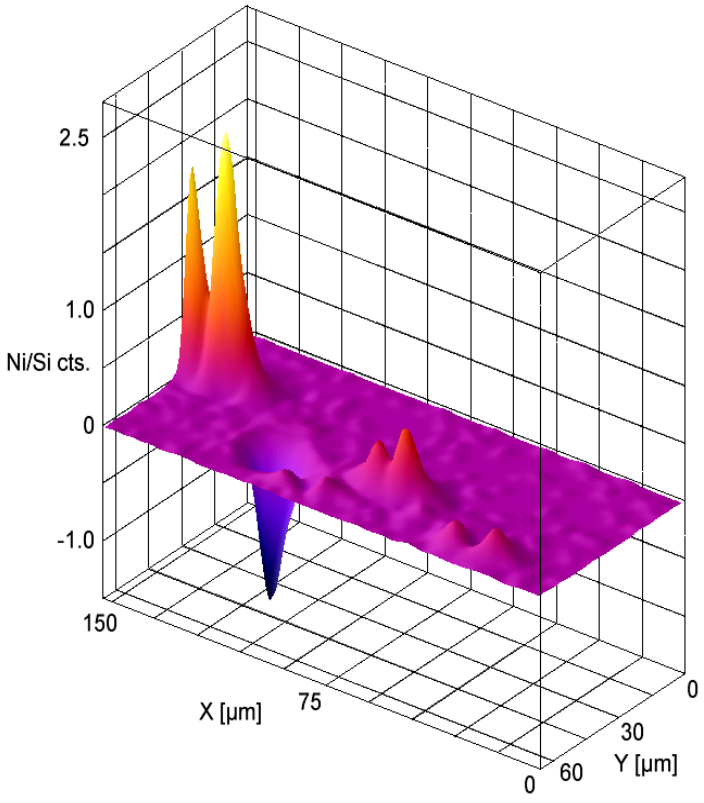

Figure 5.13: Difference between the normalized Ni Kα-line intensity after and before step D (950°C followed by a low-temperature anneal at 550°C). While the cluster in the middle loses atoms, the other large precipitates grow during the annealing.

We conclude that high temperatures above 750°C and the following cool down after extraction from the furnace lead to a homogenization of the impurity distribution along the grain boundaries because the conditions allow for clustering but Ostwald ripening is suppressed. As our measurements show, the ripening occurs at lower temperatures (e.g. around 550°C) during a time span in the order of ten hours.

In order to estimate the precipitate size and the change occurring during the high-temperature steps, in the following we use the integrated ratio of the Ni/Si counts over the area of individual precipitates. This value is directly proportional to the number of Ni atoms as explained above.

In *Figure 5.14* the change in precipitate size on a percentage basis is plotted versus the initial integrated Ni / Si ratio for the high temperature steps A-D. Three different reactions of the Ni precipitates can be discerned: While at high temperatures of 850°C and above without a low temperature anneal (steps B and C), in general the rule holds that the larger the precipitates the more atoms out-diffuse during the process, during step A at 750°C precipitates lose the same relative amount of around 30% regardless of the original size. This result suggests that at higher temperatures, thermal equilibrium is reached during the process time (at 950°C, the outcome of the high temperature step may be determined by the final cool-down to 850°C (see *Figure 5.11*), giving an alternative explanation of the very similar results of steps B and C). By contrast, precipitate dissolution is hampered at 750°C. If a low temperature anneal at 550°C for 12 hours is added, some precipitates grow in size while others diminish. However, no clear correlation between growth rate and precipitate size can be established.

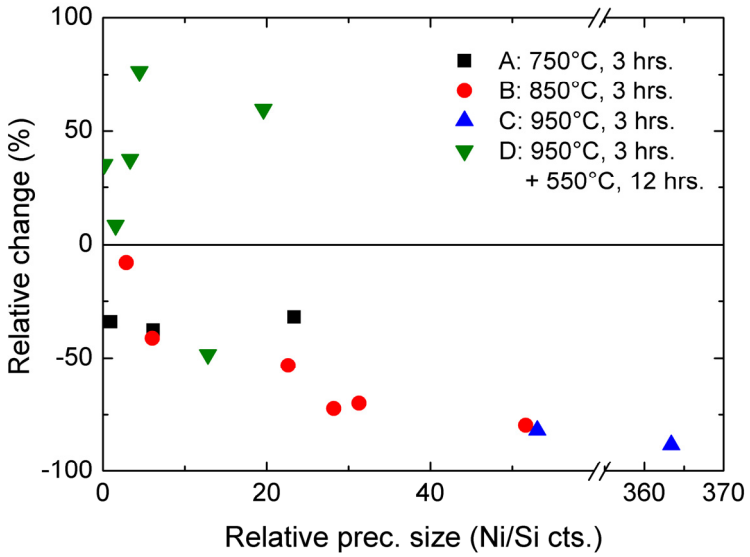

Figure 5.14: Relative change of the normalized precipitate size during the different high-temperature steps.

At this point, it is illustrative to compare our results to the predictions of the precipitation theory according to the Fokker-Planck mechanism described in section 5.1.3:

Both, the generation and the dissolution rate are linked to the precipitate size via the average capture radius of the precipitates, which is proportional to the square root of the number of metal atoms found in the cluster. One would therefore expect that precipitate

ripening is more effective in large precipitates, which does not seem to be the case in our sample. This may indicate that here, geometric conditions have a stronger influence on precipitate ripening than the initial precipitate size.

Further, one would presume that the dissolution – the number of atoms leaving a precipitate – is proportional to the square root of the precipitate size. However, in our measurements of steps B and C, the dissolution depends linearly on the original size, as can be seen in *Figure 5.15*. Taking the detection limit and the spot size of our measurements into account, this finding could be explained by the assumption that our large precipitates do not consist of one homogeneous nickel silicide particle but are rather composed of many small precipitates of similar size that are densely clustered. Precipitates with a small diameter and distances from one precipitate to its neighbor less than the capillary spot size of approx. 3 µm x 5 µm would not be resolved, therefore such a scenario is plausible. At increased temperature, every small precipitate would lose a similar amount of Ni atoms according to the similar size. Then the resulting difference in Ni/Si ratios would reflect the number of small precipitates rather than the influence of the precipitate size on the dissolution behavior. (If the large clusters consisted of several small precipitates, this would also have an influence the growth rate, giving an alternative explanation for our observations at low temperatures.)

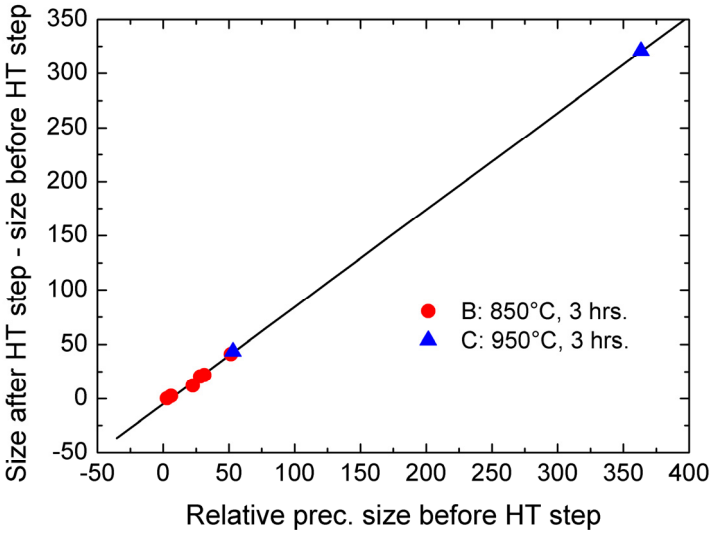

Figure 5.15: Difference of the normalized precipitate sizes after and before the high-temperature steps at 850°C and 950°C versus the initial normalized precipitate size. The black line visualizes the linear relationship of the atom out-diffusion with the precipitate size.

In order to show that our high temperature treatments A – D reflect well the precipitate evolution during a standard high temperature step used in solar cell processing, for comparison sample E was measured before and after a standard emitter diffusion yielding a sheet resistivity of 80 Ω/sqr. In *Figure 5.16*, the difference between the Ni / Si ratio after and before the P-diffusion is shown. The result is very similar to the precipitate redistribution during the high temperature steps B and C: While the large clusters found on both sides of the grain boundary lose a significant number of atoms during the processing (on

average, a reduction by about 95% was observed for each precipitate), afterwards Ni precipitates formed along the grain boundary marked by the black arrows.

To link these microscopic investigations with the macroscopic wafer properties, another piece of the same wafer (format 50 x 50 mm^2) was at first chemically polished, cleaned and passivated with a high-quality SiN layer on both sides. The minority carrier lifetime was characterized quantitatively with the help of QSSPC, while the lateral lifetime distribution was measured by means of micro-photoluminescence mapping. Afterwards, the SiN layer was etched back, the sample was cleaned and then P-diffused in parallel with the small sample used for µ-XRF measurements (step E). After emitter etch-back, the procedure described above was repeated[39].

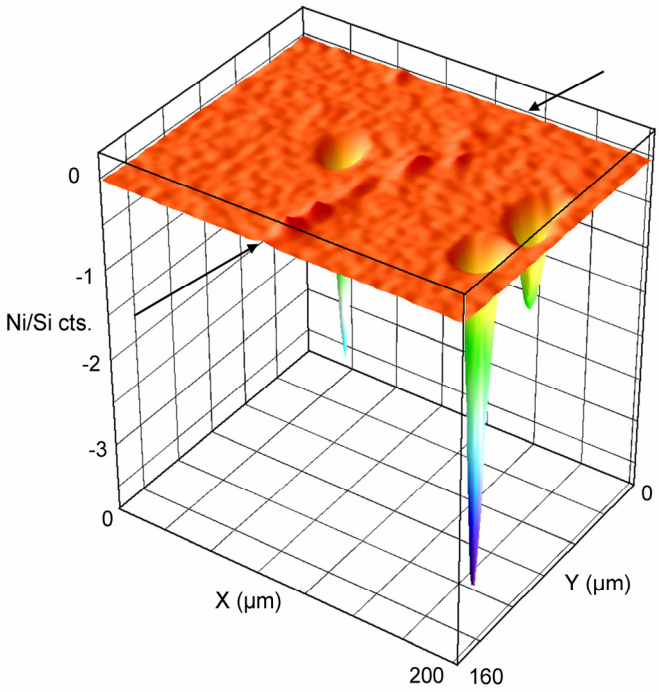

Figure 5.16: Difference between the normalized Ni Kα-line intensity after and before step E (phosphorus emitter diffusion). The arrows mark the position of the grain boundary along which Ni atoms re-precipitate after P-diffusion.

As expected from the high contamination level of the original feedstock material, the carrier lifetime before the P-diffusion is very low with a value of 0.8 µs (QSSPC). The PL mapping reveals that this is due to a very low lifetime within the grains where the metallic impurities are fully dissolved, thus presenting a very large effective recombination surface, see *Figure 5.17* (a). On the other hand, crystal defects, such as grain boundaries and dislocation clusters have served as very efficient precipitation sites, which led to a "denuded zone" with decreased impurity concentration and high carrier lifetime. Having a closer look at the crystal defects, one can see that the recombination activity along the grain boundaries is not homogeneous; parts with relatively low electrical activity are interrupted by several singular clusters with a significantly larger impact on the local carrier lifetime (some examples are marked by arrows). We suppose that these clusters

[39] Chemical treatments done by M. Kwiatkowska, micro-PL mapping performed by P. Gundel.

consist of Ni precipitates; in reference [129], it was proven that the used micro-photoluminescence setup is capable of detecting precipitates of the size which is found in this sample.

After the emitter diffusion, this picture changes completely. The P-gettering removes a large part of the contamination, lifting the carrier lifetime measured via QSSPC to about 6.6 µs. *Figure 5.17* (b) shows that gettering is most effective within the grains (the remaining contrast between the different grains is caused by the crystal orientation-dependent surface emissivity influencing the PL-measurements). On the other hand, by comparison the recombination activity along the grain boundaries and in the dislocation clusters after emitter diffusion appears homogeneously large. Singular cluster can no longer be discerned.

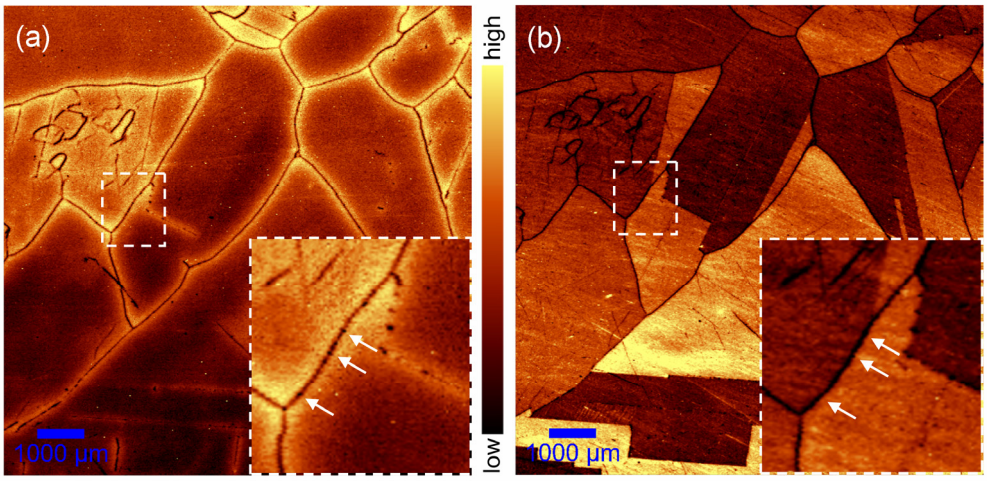

Figure 5.17: Micro-photoluminescence measurements[39] (a) before and (b) after phosphorus emitter diffusion. The insets show a close-up of the region marked by the white dashed rectangles. While the recombination activity along the grain boundaries before the emitter diffusion is inhomogeneous (arrows point at examples for local maxima), after the high-temperature step, the recombination activity appears to be homogeneous.

Therefore we conclude that the Ni re-distribution during the high temperature steps, observed in the µ-XRF measurements, directly translates into a homogenized recombination activity of crystal defects. At least during a phosphorus diffusion, this effect is confined to the grain boundaries and dislocation clusters themselves; within the bulk of the grains, the P-gettering works very effectively.

This result provides the first direct evidence for the validity of the hypothesis formulated by Rinio et al. [127], who attributed an enhancement of the recombination activity of grain boundaries after high-temperature steps to the re-distribution of impurities along the crystal defects.

5.3.3 Crystal defect-dependent response of transition metals on external gettering

In order to be able to design optimal high-temperature processes, it is necessary to take into account the different reactions of transition metals to adapted processing schemes.

As shown in the previous sections, the metals can be divided into three groups: fast diffusing elements (Ni and Cu), medium diffusers (Fe, Cr, etc.) and slow diffusers (Ti, V, etc.). Since the latter hardly respond to any high-temperature processes, only the former two are accounted for in the following.

While phosphorus diffusion gettering during the emitter formation works well for both the fast and the medium diffusers in multicrystalline material with relatively low crystal defect densities (see also section 5.3.1), which has been shown in several publications (see e.g. [130-132]), it has also been supposed that highly dislocated sections of mc-Si wafers cannot be completely gettered as a result of the many metal precipitates acting as impurity sources during the high-temperature step [119, 133, 134]. However, the specific element-related response in these regions has not been clarified so far.

In order to assess the reaction of the different impurities on P-gettering in highly dislocated wafer areas, an analogous experiment to the analysis of the impurity distribution in electromagnetically cast silicon wafers (section 5.2.2) was carried out on the same material:

For the following study, again two sets of 20 neighboring wafers (format 156 x 156 mm^2) were taken from the ingot "EM-cast mc", both sets covering ca. 8 mm of the ingot length subsequent to the ingot position of the samples used for the investigation in section 5.2.2. We assume that the influence of segregation on the local impurity concentration is negligible due to the continuous addition of silicon feedstock to the melt and the considerable length of the EM-mc block. Therefore, we suppose that the initial impurity concentration in both experiments on the EM-cast mc-Si wafers as well as the dislocation densities are comparable.

The wafers were chemically cleaned and then phosphorus-diffused for one hour at 880°C in a standard P-diffusion furnace[40]. Although the chosen temperature exceeds that of a standard emitter diffusion step, the thermal budget exerted on the samples is not considerably different, allowing to relate the following results to standard emitter processes. After diffusion, the emitter was etched back. The wafers were cut similarly to the previous experiment in order to separate the two regions of different crystallinity. After another chemical clean, NAA measurements were performed on the two sets of highly dislocated samples[41].

The most prominent transition metal concentrations after P-gettering are compared to the initial, ungettered impurity contents of the parallel samples in the high dislocation density areas (section 5.2.2) in *Figure 5.18*. In addition, *Figure 5.19* shows the gettered fraction of the different transition metal species, calculated as the difference between the impurity concentration before (UG) and after (G) the gettering, divided by the initial metal content.

[40] These steps were carried out by the PVTEC engineers; the work was performed in collaboration with S. Rein and I. Reis.
[41] NAA measurements performed at EAI (USA).

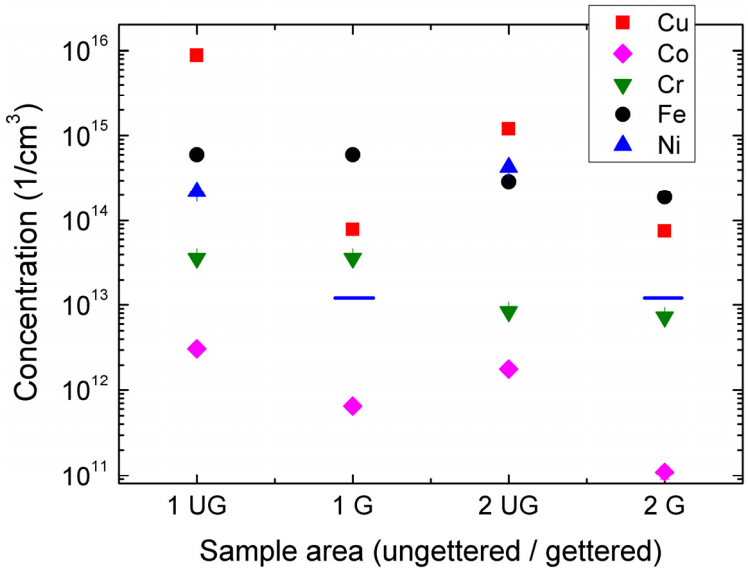

Figure 5.18: Comparison of the transition metal concentrations measured by means of NAA in two highly dislocated regions of the electromagnetically cast ingots before (ungettered, UG) and after (gettered, G) a phosphorus diffusion. The blue lines indicate the Ni-specific detection limit.

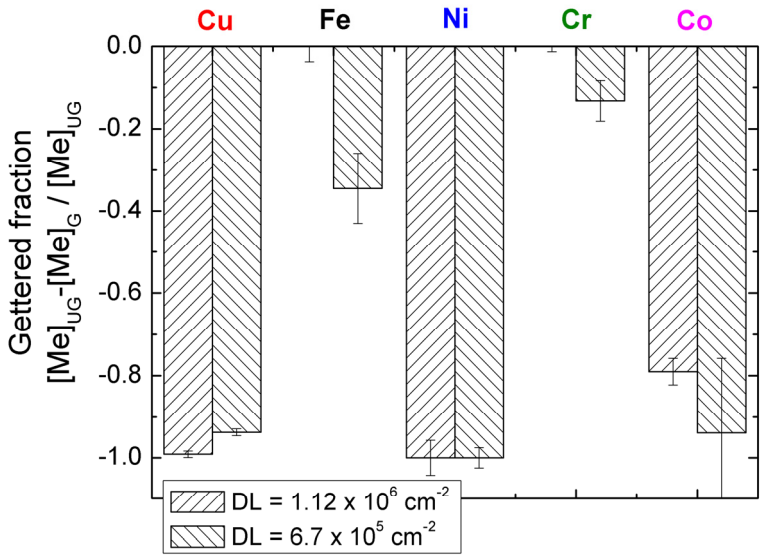

Figure 5.19: Gettered fraction of the transition metals calculated from data plotted in Figure 5.18. Sample area 1 in the latter possesses a dislocation density (DL) of 1.12 x 10^6 cm^{-2}, sample area 2 a DL of 6.7 x 10^5 cm^{-2}.

The results clearly indicate that the two different classes of fast and medium diffusers react entirely differently to the high-temperature gettering processes in high dislocation density areas. While the intermediate diffusers Fe and Cr are not removed from the wafer bulk, the P-gettering decreases the concentration of the fast diffusers Ni and Cu to a large extent by more than one order of magnitude. Although Co possesses the same diffusivity as Ni (*Figure 5.2*), its relative concentration decrease is not as significant, which may be due to the relatively low initial value.

Further, although the difference in dislocation densities between both sets of samples is relatively small (approximately a factor of 2), this divergence already results in a slightly enhanced gettering response of the medium diffusers Fe and Cr in the wafer parts that are less dislocated. It seems therefore that with the chosen gettering recipe, Fe and Cr only react in wafer regions with dislocation densities below 10^6 cm^{-2}.

To summarize the results on P-diffusion gettering, the fast diffusers Ni and Cu can be very effectively removed even from areas with many crystal defects. The remaining high recombination activity and deleterious impact on the solar cell efficiency of these regions can thus be attributed only to the medium and slow diffusers.

5.3.4 Evaluation of the concept of "defect engineering"

Concerning the "defect engineering" making use of the *intrinsic gettering*, we observed a significant minority carrier lifetime increase in mc-Si wafers predominantly contaminated with either Fe or Cr (intermediate diffusers), when low temperature anneals at 600°C for 2 hrs. were added to high-temperature steps (without external gettering sink). If these metals constitute the main impurities in a multicrystalline block, intrinsic gettering may thus be a good way to enhance the solar cell performance.

However, in wafers contaminated with the fast diffusers such as Ni, the carrier lifetime deteriorates during this step due to the large diffusivity and thus to the relative homogeneous distribution of small Ni precipitates after the intrinsic gettering. In order to obtain precipitate ripening, we have seen that long temperature anneals at a slightly lower temperature (550°C) for a relatively long time (~12 hrs.) are useful for this element. As Ni possesses a substantial diffusivity even at room temperature, one might think that Ostwald ripening of Ni precipitates may also occur with time at room temperature without further annealing. However, spatially resolved carrier lifetime measurements of a Ni-contaminated sample six months after the application of a high-temperature step with subsequent low temperature anneal gave no evidence of room-temperature driven intrinsic gettering.

Therefore, to minimize the impact of fast diffusers such as Ni or Cu, an *external gettering* has to be applied, to which both respond very well even in wafer regions of high crystal defect density.

This means that in the solar cell process, the interplay of extrinsic and intrinsic gettering can be optimized for the specific group of intermediate diffusers, since fast diffusers are externally gettered while slow diffusers cannot be mobilized in the interesting temperature and time scale.

As mentioned in the introduction of this chapter, it has been proposed to use the co-precipitation mechanism to improve the intrinsic gettering of medium diffusers like Fe and Cr [48] by intentional addition of Cu or Ni into the silicon melt. It was however seen in experiments within the research project SolarFocus that this approach brings about no improvement of the solar cell parameters. Furthermore, in the course of this thesis we have come to the notion that there are several reasons speaking against this route of defect-engineering:

i. At least in the case of Cu, a contamination of the melt with this metal can lead to increased crystal defect generation which entails the incorporation of a higher amount of all impurities – also the medium diffusers, which were intended to profit from the addition. We can assume that a high concentration of Ni in the melt also leads to increased dislocation densities.

ii. During the P-gettering, Cu and Ni are effectively gettered from all wafer areas. Afterwards, they are not available any more as sinks for intrinsic segregation gettering.

iii. Even if the P-diffusion does not succeed in removing all Cu and Ni atoms, the latter diffuse through the entire wafer bulk and re-precipitate homogeneously everywhere, degrading the electrical wafer properties. For precipitate ripening of these metals, lower temperatures and longer annealing times have to be applied than necessary for the intermediate diffusers, making the process uneconomical.

Hence, it should remain the principal aim to keep the total impurity concentration of all transition metals - but also of other precipitating contaminants such as C, N or O - as low as possible in the silicon melt.

6 Diode breakdown behavior in multicrystalline silicon solar cells

Although today's UMG-Si solar cells perform comparatively well, module manufacturers keep reservations about the use of UMG-Si cells mainly because their long term stability in the module is unknown. Since conventional solar cells have been used in modules for decades, some experience on the change in their behavior over the years has been gained: The materials degrade (including e.g. light-induced degradation due to B-O complexes, deterioration of the metal contacts and worsening of the optical performance of the module) and the solar cells can be subject to extreme conditions such as high reverse biases, which happens for example when one solar cell in a string is shaded [135]. In out-door use, (partial) shading of modules occurs regularly, for example when leaves or snow fall on top of the module or when the module is inappropriately positioned.

By contrast, modern UMG-Si solar cells have entered the market in non-negligible numbers only recently, which is why important information on their every-day performance is still lacking. Some results indicate that although UMG-Si cells show good cell efficiencies, the reverse current at a certain reverse bias is significantly increased compared to conventional solar cells [46].

It is well known that large reverse currents are critical because they can lead to heat development and to the formation of so-called "hot spots". At high temperatures, the sensitive EVA-foil enveloping the solar cells can be destroyed [135]. Possible consequences are: (i) Leakage currents corrode the electrical safety of the module, disallowing their further use, and (ii) whole cell strings can fail, seriously decreasing the module output.

In order to prevent hot spot formation, two actions are usually taken: Solar cells exceeding a critical reverse current at a certain reverse bias (e.g. -3 A at -12 V) are rejected, and in a module, solar cell strings are connected to by-pass diodes. When one solar cell of a string is shaded, the by-pass diode takes on the current generated by the remainder of the cells in that string. However, in that case, the power of these cells is wasted during the shaded period.

Although hot spots can strongly affect the module directly or indirectly via lost solar cell output, surprisingly, manufacturers have long relied on rough integral current-voltage measurements of the solar cells. Generally, however, hot spots are what they are called: highly localized sites of extensive heat generation. Therefore, the most important measurement parameter is the local power dissipation. Small reverse currents can be concentrated within a small spot, leading to large reverse current densities. By contrast, large reverse currents can be widely dispersed over the whole solar cell area, and the reverse current density can be minimal.

In principle, there are two mechanisms which are responsible for increased local reverse currents: ohmic shunts and diode breakdown. While shunts are mostly process-induced, therefore avoidable and independent from the material in use[42], the physical properties of all pn-junctions allow principally for the occurrence of diode breakdown (BD), which is of course also the case for solar cells. The first appearance of diode breakdown (the

[42] Except for shunts due to SiC-/ Si_3N_4-clusters or large metal precipitates occurring sometimes towards the top regions of mc-Si ingots [10].

breakdown voltage) and the reverse current-voltage characteristics are influenced by many properties which will be discussed in the following sections.

Diode breakdown investigations of the principal physical mechanisms were conducted in the 1950's and 60's; they focused mainly on the behavior of planar pn-junctions because of their enormous importance for the integrated-circuits industry. In spite of its importance for modules, relatively little is known about diode breakdown in mc-Si solar cells. Due to the following reasons, mc-Si solar cells behave very differently to simple pn-junctions:

i. The area which is covered by the pn-junction is orders of magnitude larger than in usual semiconductor diodes. Therefore, it is much more probable that the area contains a local defect at an arbitrary site which strongly influences the diode behavior.
ii. Contrary to mono-Si, mc-Si wafers and solar cells possess a significantly higher crystal defect concentration such as grain boundaries and dislocations, which have a large impact on the breakdown behavior.
iii. Even high-purity silicon which is currently used for solar cells contains a significantly larger amount of impurities than the material which is used for the integrated-circuit industry in order to save costs. Metals and oxides, which tend to form precipitates at nucleation sites, can alter the pn-junction properties.
iv. In general, the wafer surfaces of solar cells are textured in order to maximize light capture. Forcibly, the emitter follows the complex surface morphology which leads to strong variations in the electrical field distribution in the space charge region. This directly influences the pn-junction properties.

Until recently, diode breakdown in solar cells has been mostly investigated from a module-centered point of view aiming at an understanding of the relation between the global solar cell reverse characteristics and the module behavior under realistic conditions; see for example [136] and references therein. Alonso-García et al. stated that the global reverse I-V-characteristics strongly differ from solar cell to solar cell, mainly containing the superposition of two effects: a shunt resistance term and a term describing the "multiplication" during diode breakdown, both of which can be incorporated into the common two-diode model ([137] and references therein).

However, detailed analyses of the causes and mechanisms have been scarce. Alonso-Garcia for example named „crystal dislocations or impurities around crystal domains", "cracks", "inaccurate contour etching", "migration of ink metal through the junction during high-temperature firing" and heating under soldered metallic contacts as regions of increased heating under reverse-bias but no further specifications of the mechanisms were presented [136]. In the only microscopic study of hot spots in solar cells, Bishop et al. [138] related sites of "microplasmas" (see next section) to pits in the solar cell surface, occasionally decorated by metals from the front grid contacts. In the light of more recent investigations, Bishop's contribution only focused on one facet of diode breakdown in silicon solar cells. In another paper by Lal et al. [139], a link was presented between low shunt resistance, avalanche multiplication and soft reverse characteristics (see section 6.5.8).

Only recently, different groups have begun to put the influences and mechanisms of hot spot formation and diode breakdown in mc-Si solar cells into order, borne by the wide-

spread use of spatially resolved measurement techniques such as dark lock-in thermography (DLIT) and electroluminescence (EL) imaging.

This chapter aims to clarify the reasons for the large reverse currents observed in UMG-Si solar cells and tries to assess whether these currents can lead to hot spot formation. Due to the insufficient knowledge about BD in mc-Si solar cells in general, in the course of this thesis and in other groups working in parallel, at first the basic properties of diode BD in solar cells have been carefully investigated. Thus for the first time, a relatively clear picture about the different solar cell properties leading to large reverse currents has evolved which are discussed in this chapter.

The chapter starts in section 6.1 with a short review of the classical physical mechanisms of diode breakdown in pn-junctions on which the following analyses are based. The measurement methods which have been useful for the clarification of the diode breakdown behavior in mc-Si are presented in section 6.2 and their different advantages are discussed. A central result of this thesis is the observation and classification of three different breakdown types in usual mc-Si solar cells; their general properties as observed by DLIT measurements and EL imaging are shown in section 6.3. In the following sections 6.4 - 6.6, each breakdown type and the influence of the mc-Si properties on the breakdown behavior is reviewed in more detail, involving a discussion about the physics leading to the specific breakdown type. At last, the dangerousness of each breakdown type is evaluated in section 6.7.

6.1 Classical breakdown mechanisms in silicon pn-junctions

During the first period of the investigation of diode breakdown in silicon pn-junctions in the 1950's, it was found that basically three breakdown mechanisms exist: Avalanche breakdown (also called "impact ionization", abbrev. AB), Zener breakdown (often termed "internal field emission", IFE) and thermal breakdown.

6.1.1 Avalanche breakdown

The following section can only give a brief overview over the physics of avalanche breakdown which are needed for the understanding of the studies performed in this thesis. For details of the avalanche breakdown, the reader may refer to the plentiful literature, see for example [140-147] and references therein.

The schematic in Figure 6.1 depicts the current understanding of the mechanism which leads to avalanche breakdown: In reverse-biased pn-junctions, large electric fields accelerate free carriers in the space charge region. Usually, the movement of the carriers is hampered by collisions with other (quasi-) particles. However, when the electric field is adequately high (in the order of 10^5 V/cm, see [140] for an overview over the results obtained by different groups), the kinetic energy gained by the carriers can suffice to knock valence electrons out of their state and lift them to the conduction band (impact ionization) which in turn may then be accelerated and participate in the multiplication process; this mechanism is called avalanche breakdown.

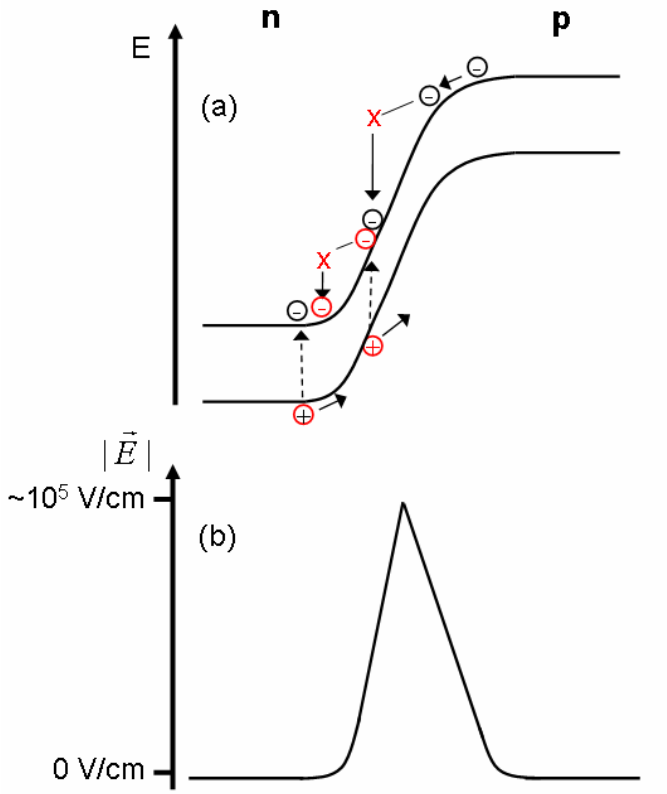

Figure 6.1: Schematic of the avalanche breakdown process. (a) Electrons in the conduction band are accelerated by the large electric fields, depicted in image (b), in the pn-junction in reverse bias. If the kinetic energy is large enough, valence electrons can be knocked out and lifted to the conduction band, taking part in the electron multiplication process.

For the onset of the breakdown, i.e. the breakdown voltage V_B, various definitions exist (in section 6.3, our uses of the term are illustrated). Whatever the definition, in the ideal case of one-sided abrupt junctions the breakdown voltage is proportional to the maximum absolute value squared of the electric field in the space charge region $\left|\vec{E}_m\right|$ and inversally proportional to the doping concentration of the lower doped side of the pn-junction N_{min} in at/cm^3 according to [30]:

$$V_B = \frac{\left|\vec{E}_m\right|^2 \varepsilon}{2qN_{\text{min}}} \qquad (6\text{-}1),$$

with ε the silicon permittivity and q the elementary charge.

Since the carriers are accelerated by the electric field, its maximum value at avalanching conditions is of high interest. Avalanche breakdown does not start at a fixed value of the electric field, but varies depending on the properties of the pn-junction. Sze [30] estimates that $\left|\vec{E}_m\right|$ at breakdown depends on the doping concentration of the lower doped side as

$$\left|\vec{E}_m\right| = \frac{4\times10^5}{1-\frac{1}{3}\log\left(N_{\min}/10^{16}\right)}\ \text{V/cm} \qquad (6\text{-}2),$$

which is plotted in *Figure 6.2* for the case that the base is the lower doped side.

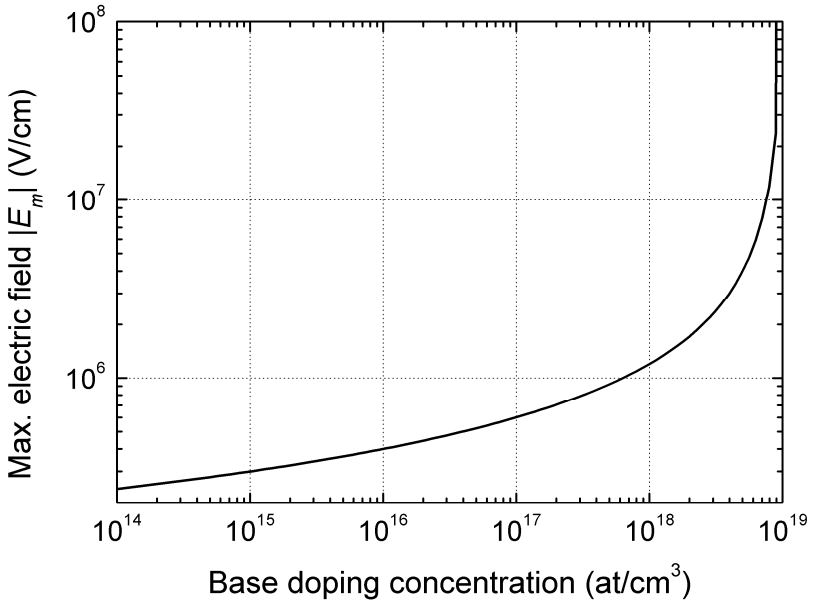

Figure 6.2: Maximum electric field in the space charge region of a one-sided abrupt junction at breakdown versus the background doping concentration in the base according to Sze [30].

Microscopically, the onset of AB, happening in small breakdown sites with a diameter in the order of a few 100 nm to a few µm [141, 148], is often marked by current instabilities which have been described in literature as "microplasma noise" [148]. As comprehensively described by Marinov et al. [149], the current through the microplasma channel is unstable when more carriers are lost due to recombination and / or out-diffusion from the channel than are generated in the multiplication process. In order to sustain avalanche breakdown, each free carrier in the space charge region needs to set at least 2-5 additional carriers free [149]. With increasing reverse bias, more and more carriers gain sufficient kinetic energy to multiply via impact ionization; the avalanche breakdown becomes stable.

As soon as this happens, the many charge carriers flowing through the microplasma channel cause an adjustment (a decrease) of the local electric field. A balance is established between the multiplication of free carriers due to the electric field, the reduction of the electric field due to the avalanche current and the carrier transport away from the microplasma channel limited by the spreading resistance, that is by the doping concentration in the lower doped side $N_{\min}$. In fact, the latter determines the current density J_μ in the microplasma channel [149]:

$$J_\mu = 2qv_sN_{\min} \qquad (6\text{-}3),$$

with v_s the saturation velocity of the free carriers in the semiconductor [30]. Note that J_μ does not depend on the reverse bias or the electric field in the space charge region. A current increase with increasing reverse bias hence means that the cross-sectional area of the microplasma channel increases for which there are also indications in literature (see e.g. [141, 150]).

As the doping concentration in usual pn-junction does barely vary laterally, breakdown happens in many sites at once. Hence, the global current (not the current density) increase is usually large as soon as the breakdown voltage is passed. Therefore, AB is associated with "hard" breakdown characteristics.

Microplasma channels emit bright light in the visible spectral range [148, 151-153]. By carefully comparing the number and size of light-emitting breakdown sites with the global current, it was shown that most if not all of the current is concentrated within the visible breakdown spots [150], each carrying about 100 µA.

The light emitted in the AB sites shows a broad spectral distribution, see *Figure 6.3*. A series of publications has dealt with the underlying physical mechanisms of avalanche breakdown light emission. Various causes for the spectral distribution have been proposed (compilation after Akil et al. [154]):

(i) Interband recombination between hot electrons and holes [152, 155, 156];

(ii) intraband electron transitions (bremsstrahlung radiation from hot electrons scattered by charged coulombic centers) [157-159];

(iii) ionization and indirect interband recombination of electrons and holes under high field conditions [160];

(iv) intraband transitions of hot holes between the light- and the heavy-mass valence bands [161].

In the most recent publication, Akil et al. [154] obtain reasonable fits for observed spectra of different silicon pn-junction devices with a combination of mechanisms (i) - (iii). However, the contributions of the different mechanisms are still topic of ongoing discussions due to the difficulty of experimental verification of existing models.

Disregarding the different possibilities of radiative transition, the most important point consists in the statement that breakdown light emission always involves hot electrons and holes far away from the conduction and valence band edge, respectively. They can be generated either directly by acceleration in a large electric field or indirectly via energy / momentum transfer processes as a secondary effect resulting from large field strengths.

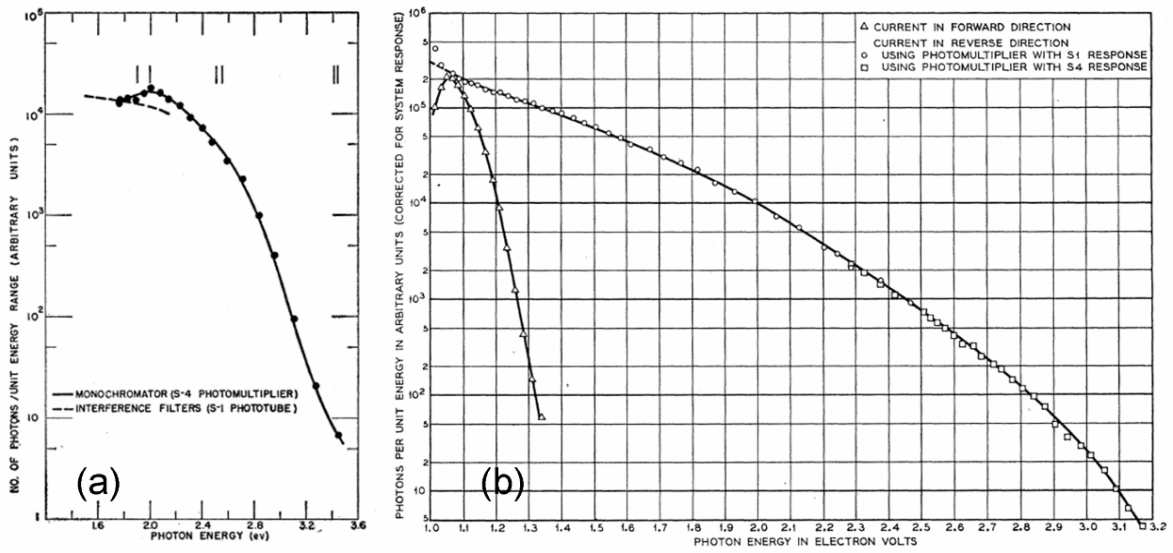

Figure 6.3: Examples for the corrected spectral distribution of avalanche breakdown in different silicon pn-junctions measured by (a) Newman et al. [151] and (b) Chynoweth et al. [152] (open circles).

Highly localized AB, attributed to locally enhanced electric fields, has been ascribed to various inhomogeneities of the pn-junction:

- Chynoweth et al. for example observed that breakdown light emission was centered at dislocations [162, 163].
- Scratches on the surface of the pn-junction also resulted in highly localized AB [152].
- In structurally perfect pn-junctions, Goetzberger et al. noticed light emission along so-called striation rings. They explained this behavior by slight inhomogeneities of the base doping concentration due to the crystallization process [164].
- Kikuchi [165] and Shockley [166] suspected that oxygen precipitates could cause AB due to electric field enhancement which is a result of the different permittivities of Si and SiOx.
- After intentional contamination of silicon pn-junctions with Cu, junction breakdown was observed at singular, highly localized sites [167]. The authors attributed this behavior to metal precipitates in the space charge region without further proof. In their opinion, the reverse I-V characteristics, however, did not fit to AB; therefore, they claimed that internal field emission processes (see next section) were involved.

A singular property of AB, which allows for a distinction between the different breakdown mechanisms, is the negative temperature coefficient (TC) [141], which means that with increasing sample temperature, the breakdown voltage increases. The reason is that at higher temperature, the mean free path of the charge carriers in the space charge region decreases because they encounter more scattering events with phonons.

6.1.2 Internal field emission

Quantum mechanics predicts that the wave-like nature of charge carriers allows for tunneling through potential barriers; the narrower the potential barrier, the more probable

tunneling events become. Therefore, in reverse-biased semiconductors, electrons can tunnel from the valence to the conduction band through the band gap without change in their potential energy if the space charge region of the reversely biased pn-junction is very narrow. This is for example the case if both emitter and base are highly doped, resulting in very high electric fields (in the order of 10^6 V/cm [168]). Analogous to AB, the higher the doping concentration in the lower doped side, the lower the breakdown voltage of the junction. This breakdown mechanism, depicted schematically in Figure 6.4, is called Zener breakdown or internal field emission.

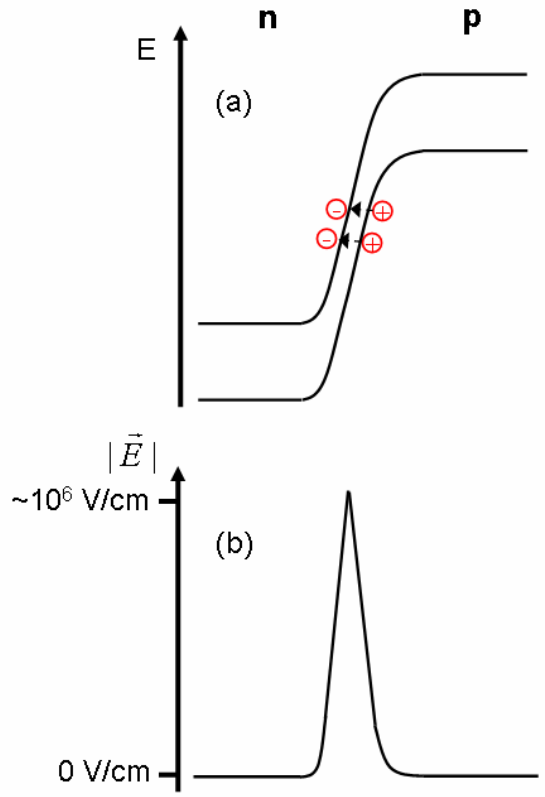

Figure 6.4: Schematic of the internal field emission process. (a) Electrons tunnel from the valence band to the conduction band due to the narrow pn-junction at reverse bias. (b) Due to the strong potential gradient in narrow pn-junctions, the electric field becomes very large even at relatively low reverse bias.

The I-V characteristics of Zener diodes showing internal field emission are usually "soft"; that means that the reverse current increases gently with increasing reverse bias. In general, the breakdown voltage of IFE-diodes is lower than in AB diodes (around -4 to -5 V in silicon [140]).

In one of the first publications about IFE in silicon, Chynoweth et al. reported a faint, uniform visible glow emanated by a large number of small spots from the junction in breakdown. However, light emission due solely to internal field emission processes was never confirmed in any other investigation.

Although the tunneling through the band gap is a non-radiative transition without change in the potential energy, in later stages of the IFE process, almost always avalanche

breakdown occurs. Then, the breakdown sites emit white light similar to microplasma channels.

Since the band gap narrows with increasing sample temperature, the tunneling probability increases which causes a decrease in the breakdown voltage of IFE. Hence, this mechanism is associated with a positive temperature coefficient [140].

6.1.3 Thermal breakdown

High reverse currents, initialized by either one of the latter two classic diode breakdown mechanisms, cause Joule heating. If the breakdown is highly localized and the reverse bias is sufficiently high, the local temperature can allow for thermal generation of free carriers. Eventually, at the turn-over temperature [169, 170], due to large concentrations of free carriers, the semiconductor becomes locally intrinsic and the junction barrier disappears. Then, the high electric fields resulting from the application of high reverse biases are not necessary any more to sustain large local current densities [169].

Since in the following treatments, only the first stages of breakdown in silicon solar cells are investigated, thermal breakdown will be disregarded.

6.2 Measurement methods for the spatially resolved characterization of diode breakdown

Diode breakdown comes along with several physical interactions within the pn-junction, which can be used for the spatially resolved characterization of diode breakdown behavior in solar cells. More specifically, two ramifications are useful:

A) Avalanche breakdown, localized within microplasma channels, emits bright light (section 6.1.1). Internal field emission itself is a non-radiative transition, which, however, is often followed at slightly higher reverse biases by a multiplication process which causes visible light emission.

B) In breakdown sites, a reverse current is transported across the pn-junction. This causes the dissipation of heat due to Joule heating.

6.2.1 Measurements based on an electroluminescence setup

Light in the visible spectral range can be imaged with the help of silicon charge coupled device cameras usually used in electroluminescence (EL) measurement setups. On 156 x 156 mm^2 solar cells for example, a good resolution in the order of 100 µm is obtained which allows e.g. for a good comparison between breakdown sites and sites of increased recombination activity. In the EL setup used at the Fraunhofer ISE, the solar cell is connected to a voltage generator being able to supply up to 20 V via two or three rows of pins brought onto the busbars.

In order to gain more insight into the microscopic reasons for the local breakdown, the spatially resolved determination of the local breakdown voltage is of great interest. Making use of the very short measurement times of the EL setup (in the order of 10 s or less

per image), we achieved local breakdown maps with EL images taken at consecutively increasing reverse voltages. The measurements were fed into an image processing algorithm which recognizes the position of breakdown light emitting sites. For this, an intensity threshold needs to be defined in order to distinguish between breakdown spots and background noise. Breakdown was detected when the intensity was larger than $<I> + 3\sigma$, $<I>$ being the average background noise level of a dark image and σ denoting its standard deviation. Finally, the algorithm assigned to each camera pixel the lowest reverse voltage at which BD light was detected, which corresponds to the definition of the *local* breakdown voltage used in this thesis (formulated in section 6.3.2).

In this approach, the local breakdown voltage is systematically overestimated; this error is the larger the softer the local breakdown characteristic because of the shallow slope. Moreover, due to refraction and reflection at textured surfaces, the spots appear much larger to the EL camera (some hundred µm) than they are in reality (well below 5 µm in diameter, see Figure 6.17), depending on the surface treatment of the wafer. Both error sources should nevertheless allow for comparison of the local breakdown voltage since the same analytic procedure is applied to each measurement.

As a result, breakdown voltage maps of the solar cells were generated. Alternatively, the fraction of the breakdown light emitting area versus the reverse voltage was estimated. This was done by calculating the ratio between the number of camera pixels which show BD light emission according to the above definition and the total pixel number covering the solar cell area.

For high resolution as well as for spectral measurements, a dedicated PL- / EL-measurement tool comprising a confocal microscope was used, equipped with a Si camera for microscopic images. The microscope is coupled via glass fibers and a 600 G/mm grating to a U-VIS spectrometer (Si line camera) for the spectral wavelength range between 400 – 1000 nm or alternatively via a 150 G/mm grating to an IR spectrometer (InGaAs line camera) for the spectral range between 900 – 1500 nm. Charge carriers can be excited by a green laser (532 nm) coupled into the microscope optics, generating photoluminescence. Alternatively, electroluminescence and breakdown light emission are generated by biassing the sample with the help of a voltage generator, allowing for voltages up to 20 V. The sample is held on a high-precision nanometer-resolution scanning table. An overall resolution in the order of 1 µm can be achieved.

With the help of the PL- / EL-measurement tool, the spectra of singular BD light emitting spots can be analyzed. In order to account for the varying sensitivities of the detectors and for the influences of the optical path on the spectrum, the setup is calibrated using a calibration lamp with a known spectrum. For details on the microscope setup, refer to [120].

6.2.2 Measurements based on thermography

The heat generated in breakdown sites due to the reverse current flow can be measured via dark lock-in thermography (DLIT) [171]. It is directly proportional to the power dissipation and thus to the current in the breakdown sites, yielding the relevant information concerning the solar cell operated in a module.

The DLIT images can be calibrated to the local current density [171] according to

$$J_{local} = T_{local} \frac{I_{total}}{\langle T \rangle A} \quad (6\text{-}4),$$

when the total current flowing through the entire solar cell I_{total} is known; A stands for the entire solar cell area and $\langle T \rangle$ is the average temperature signal.

As a result of the direct proportionality, DLIT measurements can be combined in order to yield information about the breakdown type [172]. Most importantly, with the help of the so-called TC-DLIT method, the local temperature coefficient (TC) can be estimated (see sections 6.1.1 and 6.1.2). This is done by combining two measurements which are performed at the same reverse voltage but at two different temperatures. The difference in the measured reverse current directly indicates the TC.

In the DLIT experiments, the sample is mounted to a copper chuck which is thermostat-controlled. The bus-bars are contacted via four pins which are connected to a voltage generator allowing for biases up to 20 V and 20 A. The generated heat is then detected by a stirling-cooled silicon CCD camera sensitive in a wavelength range between 3 and 5 µm.

6.2.3 Comparison of both measurement methods

Both measurement methods, EL as well as DLIT, present different opportunities and drawbacks which have to be kept in mind during the investigation of the reverse bias dependence of mc-Si solar cells:

As breakdown usually happens in small sites with diameters in the order of a few µm, EL imaging-based investigations provide the possibility to correlate breakdown sites with other solar cell-related issues such as recombination activity or dislocation luminescence with a relatively high resolution in the order of 100 µm. In addition, the acquisition time is in the order of only a few seconds.

DLIT is based upon the thermal waves generated by a periodical voltage variation (30 Hz in most cases, yielding a resolution in the order of 1 mm). To obtain high resolution DLIT measurements also in the order of 100 µm, the frequency of the periodical voltage variation has to be increased. This leads to very low signal-to-noise ratios, prolonging the measurement time to several minutes per DLIT image.

At this point, it needs to be said that in both, camera-based EL measurements and DLIT images, each pixel can contain the signal of dozens of breakdown sites, risking to obliterate any properties of singular breakdown channels.

While the light generated in breakdown sites is an indirect consequence of many charge carriers in a large electric field, for which the correlation with the local reverse current is a priori not clear (see section 6.3.2), the heat is directly proportional to the local reverse current. For measurements involving the current density, thus DLIT-related methods should be preferred. However, due to the broken symmetry at the solar cell edge, special care has to be taken when interpreting the DLIT signal in these solar cell regions [171].

During EL investigations, the reverse bias applied to the solar cell is kept constant for a couple of seconds in order to suppress noise. Therefore, depending on the measurement chuck design, the sites of the breakdown are subject to different heating conditions during the DLIT and EL measurements. Whether or not the increased heating in EL measurements has an influence on the breakdown behavior under different reverse biases is difficult to tell. Taking DLIT measurements as reference, supposing that they are less influenced by the reverse current induced heating, no significant impact has been noticed.

6.3 Co-existence of several breakdown types

In the course of this work, it became apparent that multicrystalline silicon solar cells show a much more complex breakdown behavior than small monocrystalline silicon diodes. While in standard diodes, the junction geometry and the doping of the base and the emitter determine the breakdown behavior which is either avalanche breakdown or internal field emission followed by avalanche multiplication (see [30]), in multicrystalline silicon solar cells a multitude of material properties influences the local and global reverse characteristics.

After the observation was published for the first time by the author in 2008 [173, 174] that in usual mc-Si solar cells, three different types of breakdown exist, this finding was later affirmed by other researchers [175-177] with a remarkable similarity between the results. Therefore, the description of the properties of the different types in section 6.3.2 has meanwhile been widely accepted in the community.

At first, this chapter is introduced in section 6.3.1 with the familiar general appearances of global reverse I-V characteristics, as similar measurements are routinely performed on every solar cell in an industrial production line. The relation between the global I-V curve and the local expression will be the topic in section 6.5.7.

6.3.1 Global I-V characteristics

The global reverse I-V curves of mc-Si solar cells vary significantly. In Figure 6.5, examples of the I-V characteristics of six different solar cells are shown[43].

All the global reverse I-V plots have in common that each curve can be divided into two parts: At low reverse bias, the low reverse current flows through what in this context is sometimes termed "pre-" breakdown sites [140]. Beginning with the point of maximum curvature (marked by the red dashed lines), in the following called the *global* breakdown voltage according to one of the possible definitions discussed by Mahadevan [140], a rather steep slope in the I-V-curve is observed with a large current increase with increasing reverse bias. The solar cells differ in their point of maximum curvature – their global breakdown voltage – as well as in the slopes of the pre-breakdown and of the "steep" regions.

[43] IV-measurements by E. Schäffer.

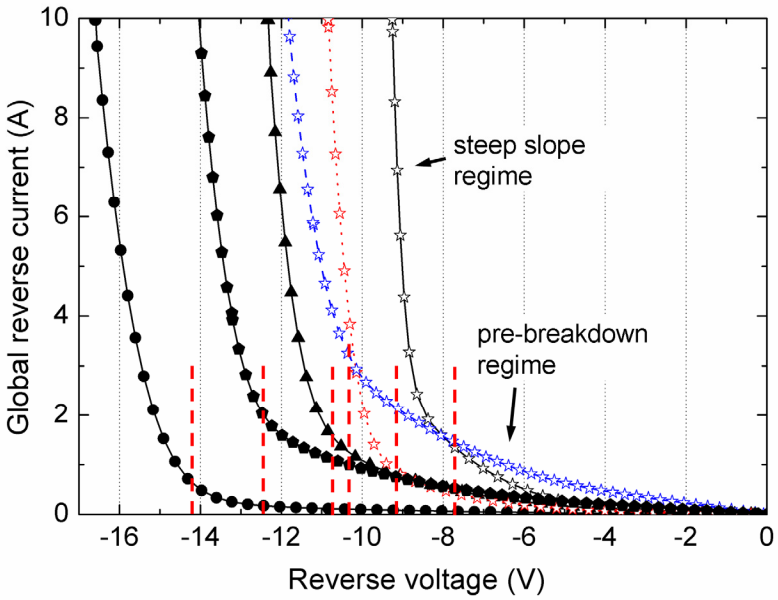

Figure 6.5: Examples for the global reverse I-V characteristics of six different mc-Si solar cells which describe typical features of the reverse behavior of every silicon solar cell [137]. The points of maximum curvature, used as the definition for the global breakdown voltage [140], are indicated by the red dashed lines.

In general, the major threat to solar modules comes from the steep slope regime since there, large reverse currents flow which cause substantial heating of the solar cell. Hence, a low global breakdown voltage suggests that the operation of the solar cell within a module string could be problematic.

However, a significant current at low reverse bias in the pre-breakdown regime could also be dangerous in the case that the current is concentrated within few spots.

Therefore, in the next sections, the local distribution of the reverse current and the correlation with the global reverse I-V characteristics are investigated in detail.

6.3.2 Local reverse characteristics – evidence for several breakdown types

In the following, electroluminescence measurements performed on a standard industrial acidically etched solar cell (156 x 156 mm^2) made from a standard multicrystalline wafer give a typical example of the local breakdown behavior [173]:

Figure 6.6 (a) was measured at 567 mV forward bias. One can clearly distinguish regions with high carrier density, leading to a high EL signal, and areas of the cell which are recombination active. There, the carrier density and thus the junction voltage are lowered, decreasing the EL intensity. These recombination active features have been shown to be primarily due to crystallographic defects like grain boundaries or dislocation networks decorated with impurities, metal-containing precipitates or to highly contaminated grains [114].

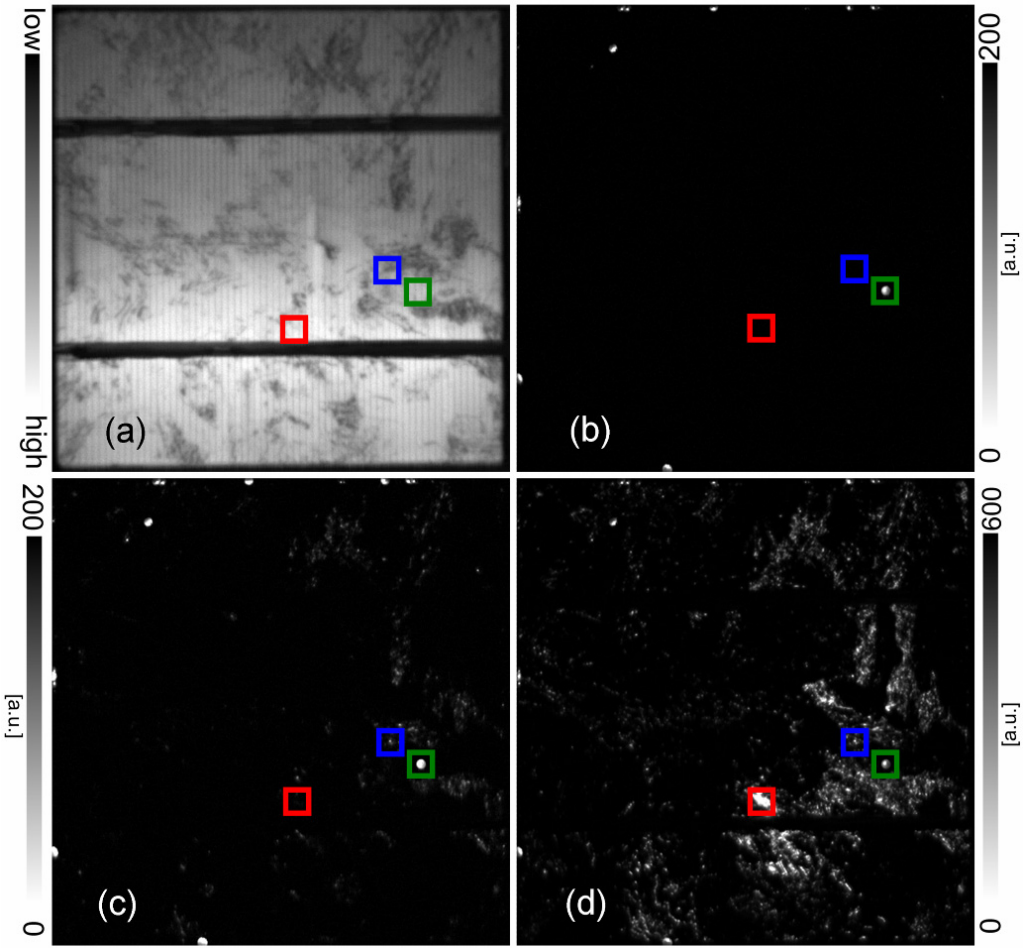

Figure 6.6: EL measurements of a standard industrial mc-Si solar cell, performed (a) at 567 mV in forward bias, showing recombination active areas as dark contrast; (b) at -8.2 V in reverse bias, (c) at -11.9 V and (d) at -14.0 V in reverse bias.

Going from forward to reverse bias, at first some small bright spots start to show up at around -5 V. In Figure 6.6 (b), for example one of these early spots is highlighted by the green rectangle. Most of them are located at the edge and some can be found in the middle of the cell. This onset goes along with noticeable voltage fluctuations typical for microplasmas. Increasing the reverse bias further, the fluctuations disappear and the spots grow brighter, but no new features turn up until around -8.5 V. In this voltage range, the global reverse current flowing through the solar cell grows linearly from 10 to 80 mA. In these measurements, with increasing intensity the dots smear out laterally over a few hundred micrometers. This effect is due to an overflow of the CCD chip of the camera which has to be tolerated in order to make spots of lower breakdown light intensity visible.

At around -8.5V , additional spots start to appear which grow brighter with increasing reverse bias. Figure 6.6 (c) shows an image of the solar cell at a bias of -11.9 V (200 mA reverse current). The brightest dots are those that break down at -5 V, while the dim spots turn up at around -8.5 V (for example the BD site marked by the blue rectangle). Comparing images (a) and (c), the dim spots appear to be restricted to regions with low carrier lifetime.

Then, at -12.5 V, another set of spots emerges in regions with high carrier lifetime. As an example, Figure 6.6 (d) shows an EL image taken at -14 V (1.1 A reverse current), with the red rectangle marking one of the BD sites which are last to break down. These spots grow brighter very quickly with increasing reverse voltage.

Therefore, it is apparent that BD in mc-Si solar cells happens in three different stages which can be distinguished in EL measurements based on the reverse biases at which first breakdown light emission can be detected. In the following, this onset of light emanation will be used as the definition of the *local* breakdown voltage.

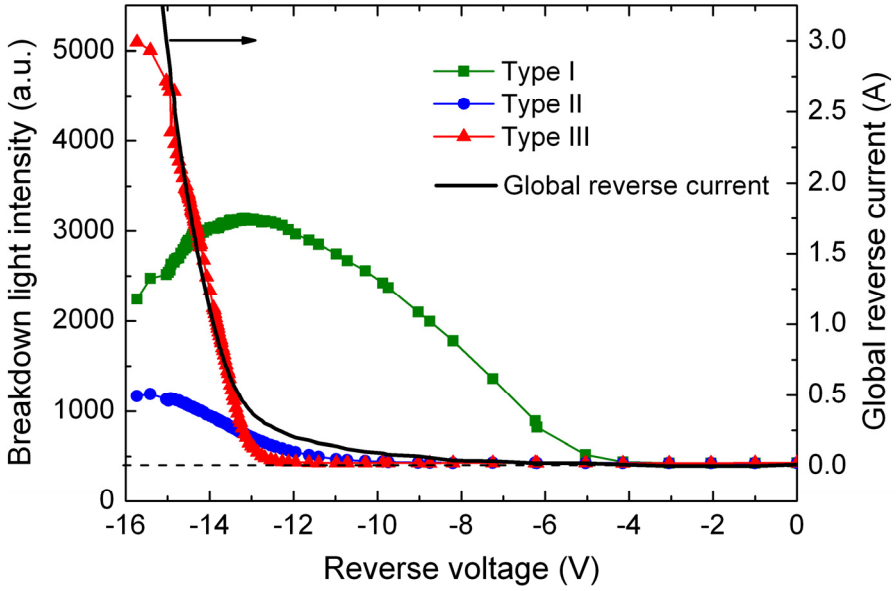

Figure 6.7: Plot of the breakdown light intensity versus reverse bias measured at the center of the colored rectangles in Figure 6.6. The dashed line marks the level of the background of the EL measurement setup. The continuous black curve denotes the global reverse current of the solar cell.

Interestingly, the bias-dependent breakdown light intensity of each stage is also very characteristic. In Figure 6.7, the signal of the breakdown light emission of four typical points, averaged over a cluster of 2x2 pixels which were chosen at the locations denoted by the center of the colored rectangles in Figure 6.6, are plotted versus the reverse bias.

The dashed curve marks the typical background and noise level within grains which show no diode breakdown.

Spots which break down in the *first stage* at very low reverse bias (-5 V or below), which shall be called "early breakdown" or type I in the following, are plotted by the green squares in Figure 6.7. With increasing reverse bias, they soon become very bright and usually dominate the optical image. Very often, we have observed non-monotonic behavior of the bias-dependent breakdown light intensity in the later BD stages[44]. All these dots have in common that at first, they grow in brightness almost linearly with reverse bias until the following stages are reached where an appreciable current starts to flow.

During the following breakdown stage, the breakdown light intensity of the early breakdown spots then stagnates while smearing out of the points can still be observed. When the last breakdown stage is reached, the breakdown light intensity becomes unstable.

Following explanations for these observations are possible:

(i) The onset of additional breakdown sites in the vicinity induces a slight variation in the current transport due to Joule heating of the busbars and the fingers of the front metallization (which connects the breakdown sites under observation) and therefore a change in the series resistance.

(ii) Additional breakdown paths in the vicinity reduce the local voltage available at the spot under consideration.

Breakdown of spots beginning in the *second stage* is signified by an increase in intensity at a reverse bias which is usually larger than the early breakdown but significantly lower than the onset of the last stage. The light emission shows a characteristic similar to a soft breakdown (which usually refers to a moderate reverse current increase with increasing reverse bias, section 6.1.2). Hence it will be termed "soft" breakdown or type II in the following.

The bias-dependent light intensity of breakdown sites of the *third stage* resemble the I-V curve of a hard, avalanche-like breakdown – therefore it will be called "hard" breakdown or type III. The light intensity in these regions grows in brightness quickly. This increase coincides with the abrupt rise in the global reverse current, indicating that both are related.

Although these statements are shown here only for three isolated spots, we infer from numerous observations of breakdown characteristics that every other breakdown site on mc-Si solar cells can be classified according to the above characteristics. This was later verified for example by Bothe et al. [176]. Therefore, reverse bias-dependent EL measurements is one means of categorization of breakdown sites.

It was shown in cooperation with M. Kasemann [175] that in principle, the DLIT signal reflects the same characteristics as the EL behavior. In Figure 6.8, the DLIT intensity is analyzed at the same sites marked by the colored rectangles in Figure 6.6. The signal is averaged over 3 x 3 pixels and divided by the respective reverse voltage; plotted in this way the DLIT intensity is proportional to the local reverse current and to the local heat generation. In *Figure 6.8*, the DLIT signal is compared to the breakdown light intensity.

The light emitted by the type I BD site is very intense while the heat generated in the same site remains comparatively low. This is true for most of the early BD sites with only few exceptions, see section 6.4.

The light intensity of the type II and type III breakdown sites, on the other hand, is roughly proportional to the reverse currents measured by the DLIT setup. As soon as the

[44] Other groups [178] only observed monotonic behavior for this breakdown type. This could be explained by different EL setups which use different designs of the front contacting and measurement chucks. Therefore, voltage distribution and / or heat dissipation via the measurement chuck vary.

breakdown type III sets on, marked by the visible light emission, the reverse current flowing through hard BD sites increases very quickly, dominating the global reverse I-V characteristics in the steep slope regime (see Figure 6.5). However, hard breakdown is process-induced and therefore is not present on every mc-Si solar cell. In that case, the global I-V curve is influenced by other factors, which are investigated in section 6.5.

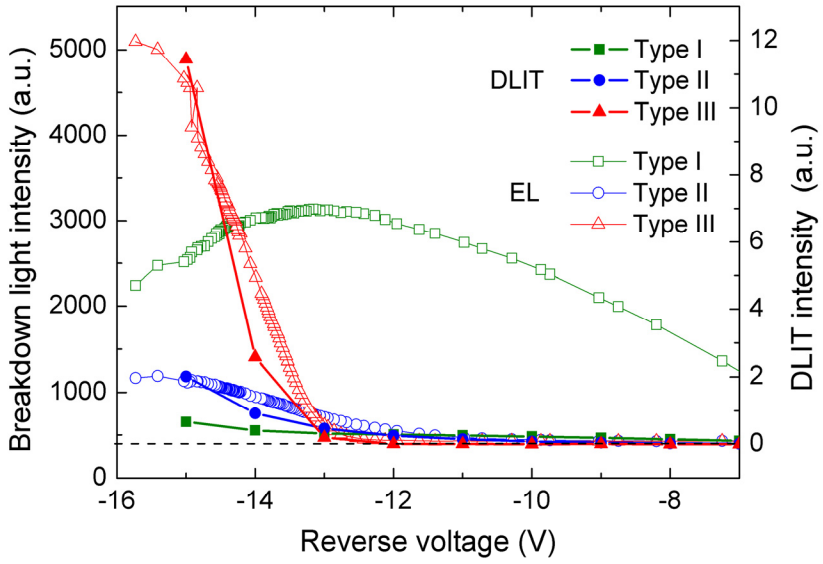

Figure 6.8: Comparison of the breakdown light intensity measured via the EL setup (open symbols) with the DLIT signal divided by the voltage, being proportional to the local reverse current (closed symbols). The dashed line corresponds to the EL camera background noise.

In summary, diode breakdown in mc-Si solar cells happens in three different stages. Each type possesses distinctive properties, indicating that three different underlying causes and mechanisms are responsible for each breakdown stage.

Since diode BD is potentially dangerous for solar modules, it is not only of scientific interest to investigate the physical mechanisms. If the causes are well understood, it may become possible to completely avoid or mitigate the destructiveness of diode BD in silicon solar cells by adapted processing. Therefore in the following sections, the known properties of each BD type are compiled and described in more detail.

6.4 Breakdown type I: Early breakdown

Early breakdown usually happens only in few spots on the surface or at the edges of every solar cell and these spots are always highly localized. Since the concentration of the reverse current in few small areas could lead to large heat development, this breakdown type is of high relevance.

6.4.1 General appearance

In literature [177, 179], reverse current conducting channels with varying properties have all been labeled "early breakdown", having in common the early appearance in a relatively narrow voltage range around -5 V. Exemplified in Figure 6.9, the specifications include:

- Breakdown at the solar cell edge visible only in DLIT. These breakdown sites tend to show a positive temperature coefficient [180]. They are marked by the green circles in Figure 6.9.
- Breakdown at the solar cell edge visible in DLIT and in EL measurements. The emitted light is very bright and can be seen with the naked eye. These breakdown sites tend to show a positive temperature coefficient [180]; they are indicated by the yellow rectangles in Figure 6.9.
- Breakdown on the solar cell surface only visible in DLIT measurements. Slightly negative or zero TC [176, 180]. In Figure 6.9, these spots are marked by the green circles.
- Breakdown on the solar cell surface visible in both, DLIT and EL measurements. Also in this case, breakdown light is very intense. Slightly negative or zero TC [176, 180]. These sites are indicated by the yellow rectangles in Figure 6.9.

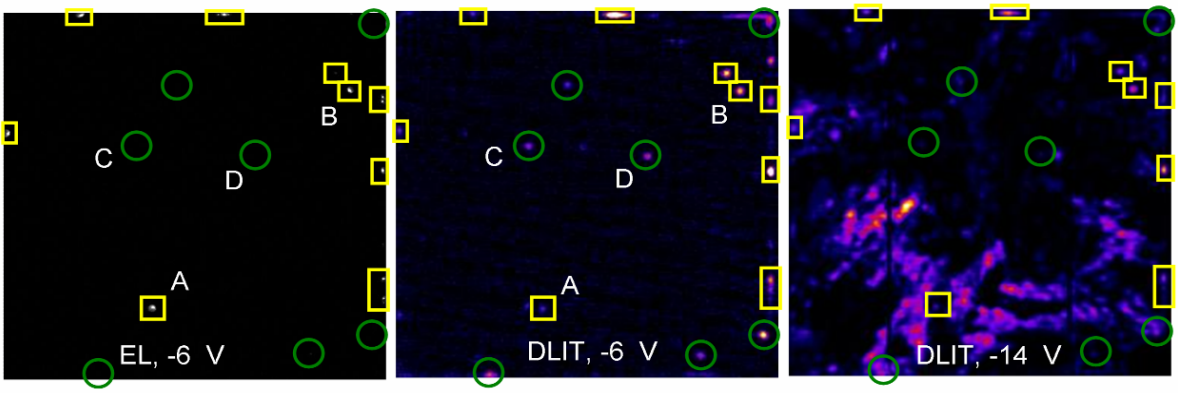

Figure 6.9: Image of the breakdown light emission at -6 V (left) and of the power dissipation at -6 V (middle) and at -14 V (right) of the same solar cell as in Figure 6.6. Yellow rectangles mark early breakdown sites which are visible in EL measurements as well as in DLIT images. Green circles indicate sites of heat generation in reverse bias which do not emit breakdown light.

The difference in the measured temperature coefficients suggests that depending on the location of the BD site at the solar cell edge or in the center, early BD is caused by two different mechanisms. However, in the first case, the measurements of the TC may be influenced by the close proximity to the solar cell edge [171]; therefore this finding needs further investigation.

The second distinction between the various early BD sites is the visible light emission. In Figure 6.10, the DLIT signals of four exemplary sites (A and B showing light emission, C and D not showing light emission) marked in Figure 6.9, are plotted versus the reverse

bias squared. In this plot, the DLIT signal of shunts can be linearly fitted resulting in a straight line crossing the origin (0,0)[181].

Although both type I light emitting sites A and B behave like ohmic shunts at higher reverse voltages, in the beginning their behavior is non-linear. By contrast, the DLIT signals of sites C and D are straight lines and cross the plot origin almost perfectly.

These measurements suggest that regions of heat generation which do not emit light are very weak ohmic shunts, which are not detected in usual shunt imaging measurements due to the very low power dissipation. They should therefore *not* be called early BD sites.

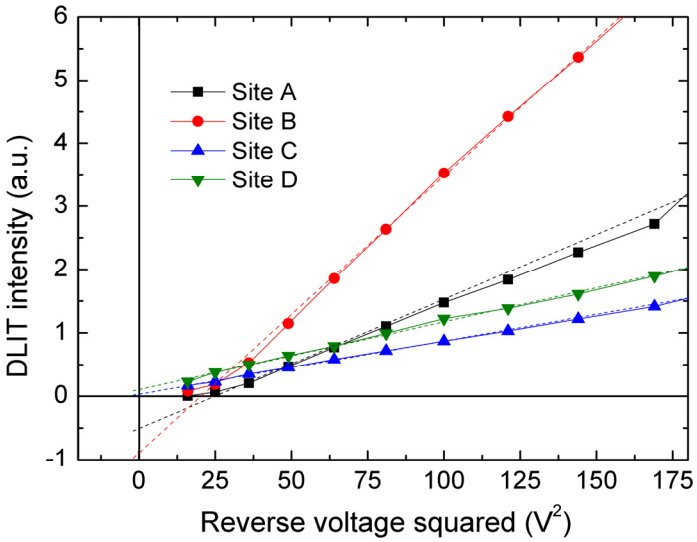

Figure 6.10: Plot of the DLIT intensity measured at sites A – D (see Figure 6.9) versus the reverse voltage squared. While the linear fits (dashed lines) of sites C and D, which both do not show BD light emission, approximately go through the plot origin, sites A and B (both also visible in the reverse bias EL image) show a linear behavior only at increased reverse voltages.

6.4.2 Causes for early breakdown

For the investigation of the cause of early breakdown on different solar cells, microscopic inspections of type I BD sites were performed. In all cases, different surface features were found at the location of the light emission. Four typical examples are shown in *Figure 6.11* and *Figure 6.12*.

Examples 1 and 2 are located on a standard, damage-etched mc-Si solar cell.

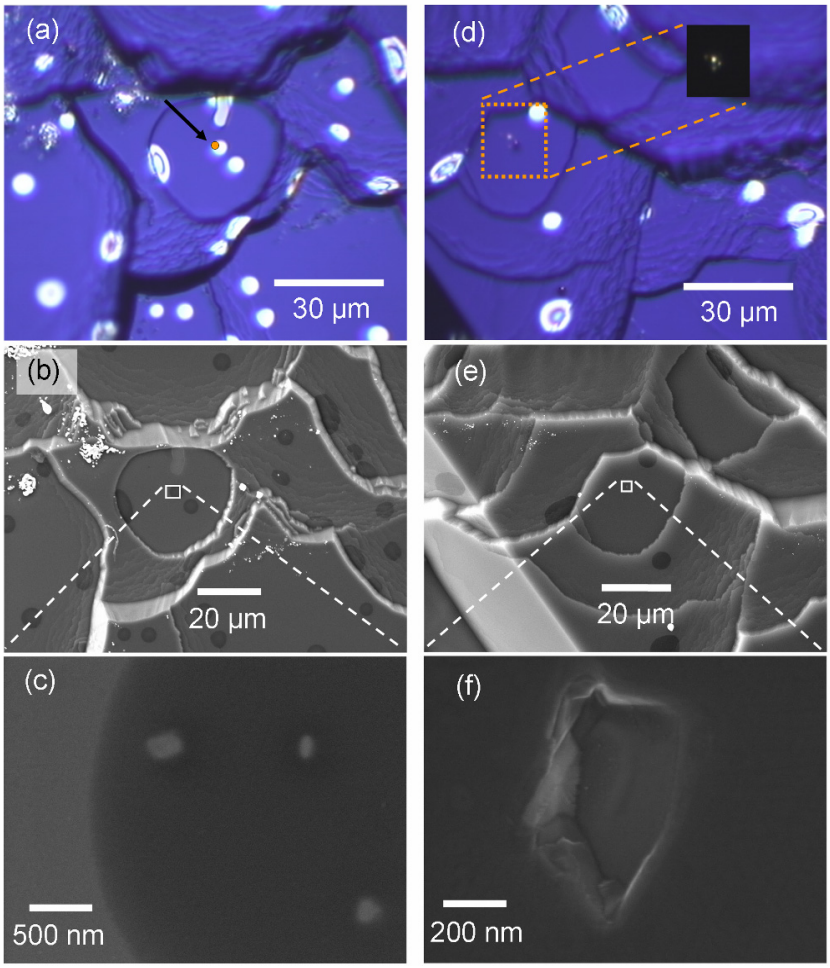

Figure 6.11: Two examples (a)-(c) and (d)-(f) for microscopic investigations of early breakdown sites on a damage-etched standard silicon solar cell. The light emission was localized with the help of a confocal microscope. The breakdown sites are marked by the orange dot in (a) for example 1; BD light of example 2 is seen in the microscope image in the dark (inset of image (d)) of the area marked by the orange rectangle in (d). These sites were investigated with the help of the SEM shown in images (b), (c) and (e), (f), respectively.

At first, the position of the light spot was determined by applying a reverse bias of -10 V to the samples which were placed under the confocal microscope of the PL-/EL-mapping tool. Light was emitted from the spots marked by the orange circles in the microscope image (a). The early breakdown in the second example happens in several tiny spots which can be seen in the inlay of image *Figure 6.11* (d)[45].

High resolution images were then obtained with a SEM, shown in images (b), (c) and (e), (f), respectively. The first example of early breakdown happens at the edge of a surface feature which appears shiny in the optical and dark in the electron microscope image which we attribute to the local absence of the ARC layer. Example 2 appears in a small region where a small dent or crack in the surface can be seen.

[45] Micro-PL/EL measurements performed in collarboration with P. Gundel.

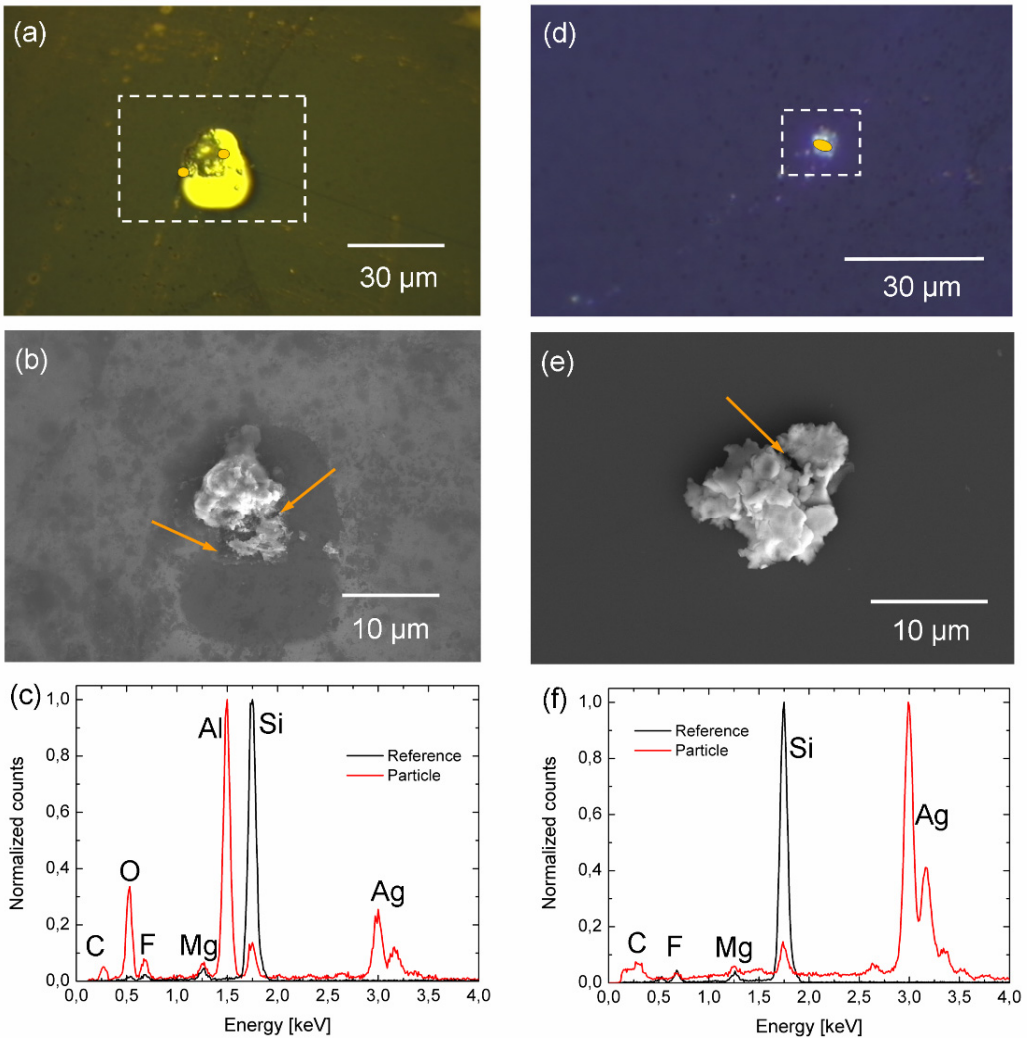

Figure 6.12: Two examples (a)-(c) and (d)-(f) for microscopic investigations of early breakdown sites on a small high efficiency silicon solar cell [129]. The light emission was localized with the help of a confocal microscope. The breakdown sites are marked by the orange dots in (a) and (d) and by the orange arrows in the SEM images (b) and (e). The chemical composition of the particles found at the breakdown sites were investigated with the help of the SEM and EDX, shown in graphs (c) and (f), respectively.

Elemental analysis with the help of EDX revealed no foreign elements at both early breakdown sites within the measurement sensitivity. If any surface contamination like particles of the contact paste were responsible for the breakdown, then they were smaller than a few hundred nanometers in diameter. The nitrogen peak, usually resulting from the SiN surface ARC layer, is significantly decreased in both example sites, indicating that at least the nitride top layer of the solar cell surface is damaged, with the possibility that the underlying thin emitter (thickness about 200 nm) is flawed as well.

The second set of investigations, examples 3 and 4 which are shown in *Figure 6.12*, was performed on 2x2 cm^2-format high-efficiency solar cells made of bonded FZ wafers originally designed for other experiments [129][46]. These solar cells have the advantage that

[46] Solar cells were provided by P. Gundel.

their surface is very smooth, which makes the localization of early breakdown sites simple, at the same time avoiding the other surface-related breakdown type III (section 6.6). The categorization of the breakdown sites was performed with the help of reverse bias-dependent electroluminescence investigations making use of the characteristics described in section 6.3.2. It shows that the classification can in principle be transferred to monocrystalline silicon solar cells.

In examples 3 and 4, early breakdown light emission is detected at the edges of particles which are shown in the SEM images (b) and (e) in *Figure 6.12*. As the EDX spectra show, the specks consist of Al, Ag, C and O in example 3, and of Ag and C in example 4, indicating that breakdown is induced by small paste particles from the rear (ex. 3) and front contacts (ex. 4), respectively, both with diameters in the order of a few µm. Around the paste particles causing early breakdown, round features of a different contrast than the surroundings can be seen (see for example *Figure 6.11* (b) and (c)). This is attributed to the destruction of the ARC due to the paste particles during firing or annealing of the metal contacts. It seems therefore that the paste particles modify the surface and possibly the emitter in the high temperature step.

The latter results have recently been confirmed by another group [182]. They found early breakdown light emission around residues of the Al paste used for the contacting of the rear side of standard industrial silicon solar cells which had obviously been alloyed into the wafer surface.

Similar reasons for breakdown light emission, namely both "pits in the surface, occasionally contaminated with metals (nickel, aluminium, titanium) from the front contacts" were also reported by Bishop [138] to cause hot spots in monocrystalline silicon solar cells, indicating that our findings are correct and that Bishop's study mainly involved type I breakdown sites.

6.4.3 Spectra of light emitted from early breakdown sites

Spectra of the emitted breakdown light were measured at several early breakdown sites with different onset voltages found on small high-efficiency FZ-silicon solar cells [183][47]. Since the solar cell surface of these samples is polished, the influence of the surface morphology on the spectra is minimal.

The results are shown in *Figure 6.13*. In all early BD sites, the light shows a broad spectral distribution ranging from sub-bandgap energies <1.0 eV up to high energies >3.0 eV, very similar to avalanche breakdown spectra published in literature (*Figure 6.3*). For these processes, hot carriers are made responsible [154].

[47] Measurements performed in collaboration with Paul Gundel

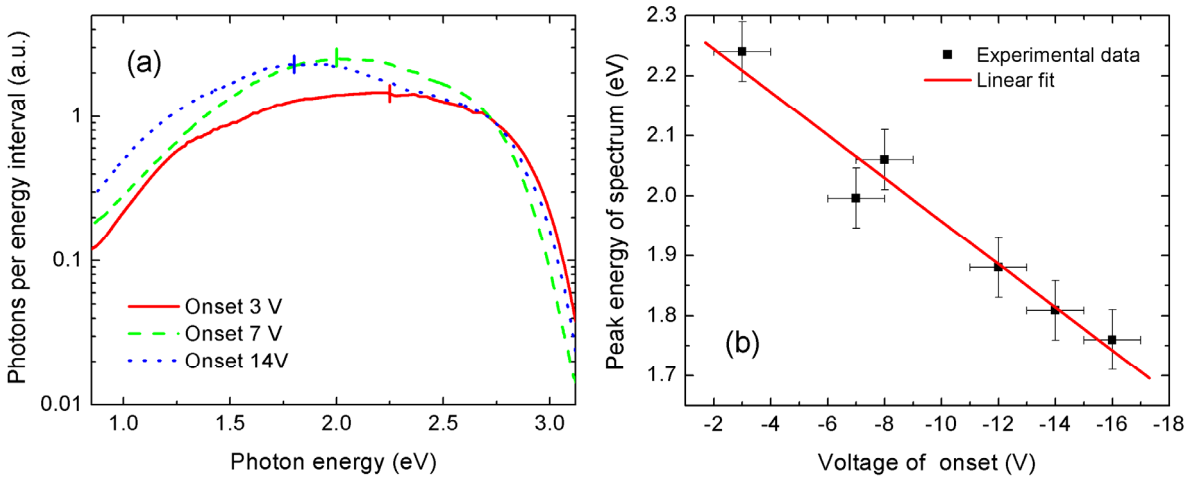

Figure 6.13: (a) Corrected breakdown light emission spectra obtained from early BD sites with different local breakdown voltages. (b) Shift in the peak energy depending on the local breakdown voltage. After ref. [183].

Plotting the peak energy of the spectra versus the onset voltage of the breakdown site shows that the peak energy decreases linearly with increasing breakdown voltage, see *Figure 6.13* (b) [183]. The reason for this behavior is not yet clear and is currently being investigated. It can be excluded that the peak shift is due to reabsorption effects in the silicon resulting from varying breakdown depths because in that case, the shift would point into the opposite direction.

6.4.4 Theoretical considerations on the basic mechanism of early breakdown

The intense white light coming from the BD site implies that hot charge carriers are present (section 6.1.1), necessitating the development of large electric fields at a relatively low reverse bias. A tentative, simple explanation of these findings is summarized in the schematics in *Figure 6.14* and *Figure 6.15*, which show the pn-junction in the presence of a surface scratch damaging the emitter and of an Al paste particle alloyed with the silicon, respectively.

As visualized in the first schematic, let's suppose the surface scratch takes away only a part of the highly n-doped silicon in the emitter, leaving a layer of weakly n-doped silicon. Then, the pn-junction is locally modified: Due to the absence of the highly doped part of the emitter, the charge carriers redistribute in the depletion layer and the space charge region width is increased. Accordingly, the direction of the electric field across the space charge region readjusts to the local variation of charge carriers until equilibrium conditions with the help of equations (3-29) and (3-34). in conjunction with equations (3-27) and (3-28) are attained. In addition, the scratch induces a geometric inhomogeneity into the surface (exemplified by example 2 in *Figure 6.11*), which also enforces the modification of the electric field vectors. This can lead to a high concentration of electric field lines at some points around the scratch, which due to the superposition can add up to a considerable strength. Thus, breakdown can occur at relatively low reverse bias.

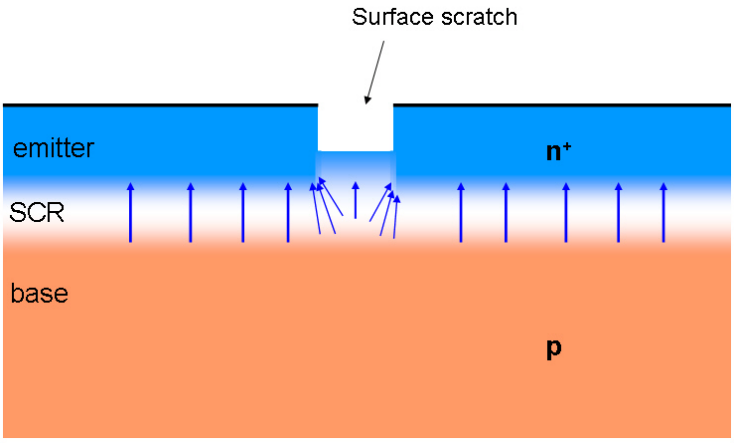

Figure 6.14: Schematic of the pn-junction around a surface scratch which damages the emitter. The red arrows signify the direction of the electric field, their thickness stands for the local field strength.

However, this picture of the physical cause has to be adapted when a paste particle is alloyed into the silicon, see *Figure 6.15*. Part of this concept has already been discussed in [179].

If the particle consists of Al (example 3 in *Figure 6.12*), a p-dopant, it can overcompensate the emitter after the contact firing step because it forms a eutectic with the silicon. This fact is often used in standard industrial screen printing processes. In the case that the particle reaches through the emitter, it can form a direct electric contact with the base (see region 1 in *Figure 6.15*). Then, the region between the Al paste particle and the emitter (region 2) determines the reverse behavior. It does not matter whether the particle forms a Schottky contact with the surrounding n-type silicon or whether a pn-junction develops between the highly p-doped Al:Si-alloy and the emitter: In any case a very narrow space charge region forms, leading to locally large electric fields. In this picture, the similarity of early breakdown and shunts can be explained by different widths of the SCR. If it is very small, charge carriers can easily tunnel through the barrier and effectively, a short (or "shunt") is created between the emitter and the base. On the other hand, if the SCR width is large enough, it may behave like any junction under reverse-bias conditions.

Note that in principle, other metal pastes used for example for the front grid can lead to the same result, because they usually form a Schottky contact with the n-type silicon of the emitter [184] (see section 6.5.8).

In summary, early breakdown is highly localized and emits very bright light. There are strong indications that it originates from dents and cracks in the silicon surface and from paste particles. The causes have in common that they externally modify the solar cell surface and most probably also the emitter.

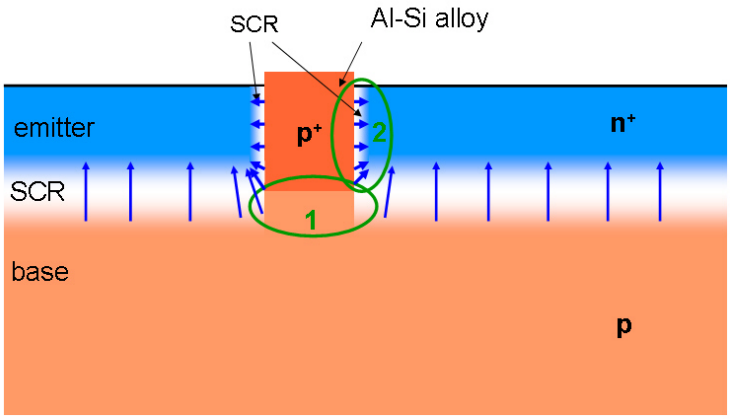

Figure 6.15: Schematic of the pn-junction around an alloyed Al paste particle. The red arrows have the same meaning as in Figure 6.14.

There are two questions that yet remain to be answered in future investigations:

Firstly, it is curious, that the large variety in the possible damages of the surface structure results in relatively uniform breakdown properties. In all the solar cells investigated in this thesis, early breakdown sets in at around -5 V with relatively little variation. Taking into account the wide diversity of possible configurations of the surface, one would expect that the onset happens in a wide range of reverse voltages.

Secondly, contrary to the second and third breakdown types, the light emitted by the early breakdown spots is very intense while the reverse current flowing through the sites is relatively low. This may be related to the fact that early breakdown is induced by damages to the wafer surface. Hence it is possible that early BD occurs directly at the wafer / atmosphere interface without any obstruction in the breakdown light path while soft and hard breakdown happens in the space charge region in the wafer bulk. However, this hypothesis remains to be verified.

6.5 Breakdown type II: Soft breakdown at recombination active defects

The second, soft breakdown type is the only one which is not solar cell process-induced but is inherent to the mc-Si material. As such, the investigation of its properties is of special importance because realistically, it cannot be avoided by optimized processing.

Since the occurrence of type I and type III BD depends on the processing conditions which vary but are essentially the same for standard and UMG-Si wafers, it is likely that increased reverse currents in the latter material are related to the second BD type. Therefore, great importance was attached to the examination of the properties of this breakdown type.

6.5.1 General appearance

Soft breakdown sites correlate macroscopically with recombination active defects which appear dark in forward EL images, see Figure 6.16 (a). As a guide to the eye, type II breakdown regions, which are seen in Figure 6.16 (b), are highlighted by the yellow mask.

On a microscopic scale, soft BD occurs in small spots emitting white light in an area which can be as small as 1 µm in diameter, see Figure 6.17[48]. The correlation with recombination active defects holds also microscopically. This is illustrated in Figure 6.18, showing measurements of a standard industrial mc-Si solar cell which was damage-etched in order to avoid influences of the surface morphology[49].

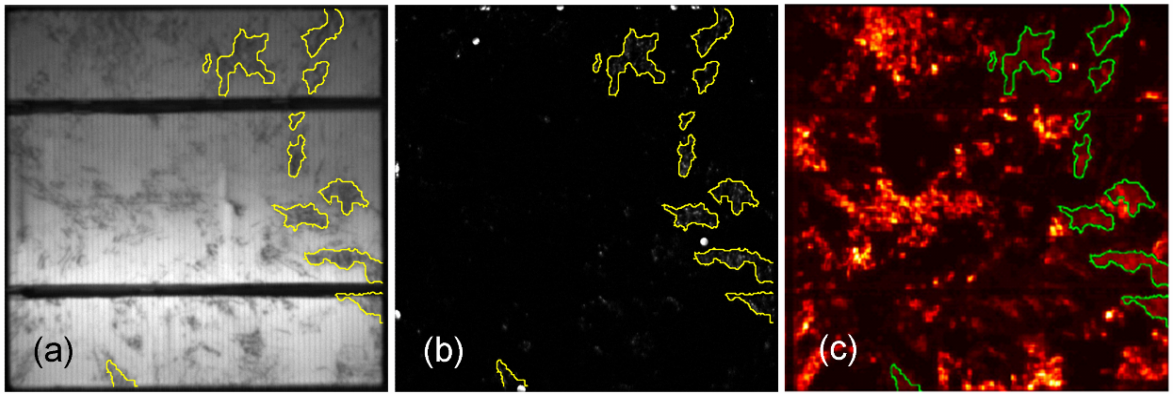

Figure 6.16: (a) EL image at 567 mV forward bias, (b) breakdown light emission at -11.9 V and (c) D-line correlated emission at around 1550 nm at 600 mV forward bias. The yellow and green masks surround the regions which show the strongest soft breakdown light emission.

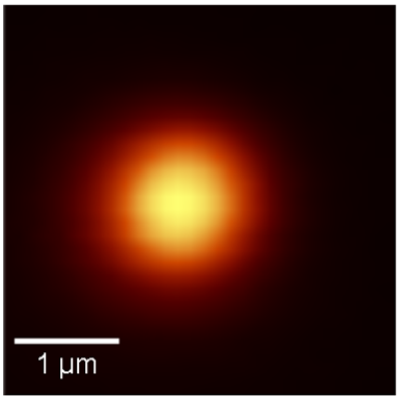

Figure 6.17: High resolution image of the breakdown light emission from a soft breakdown site, obtained with the EL-/PL-mapping tool.

[48] Micro-EL measurement by P. Gundel.
[49] Measurement performed in collaboration with P. Gundel.

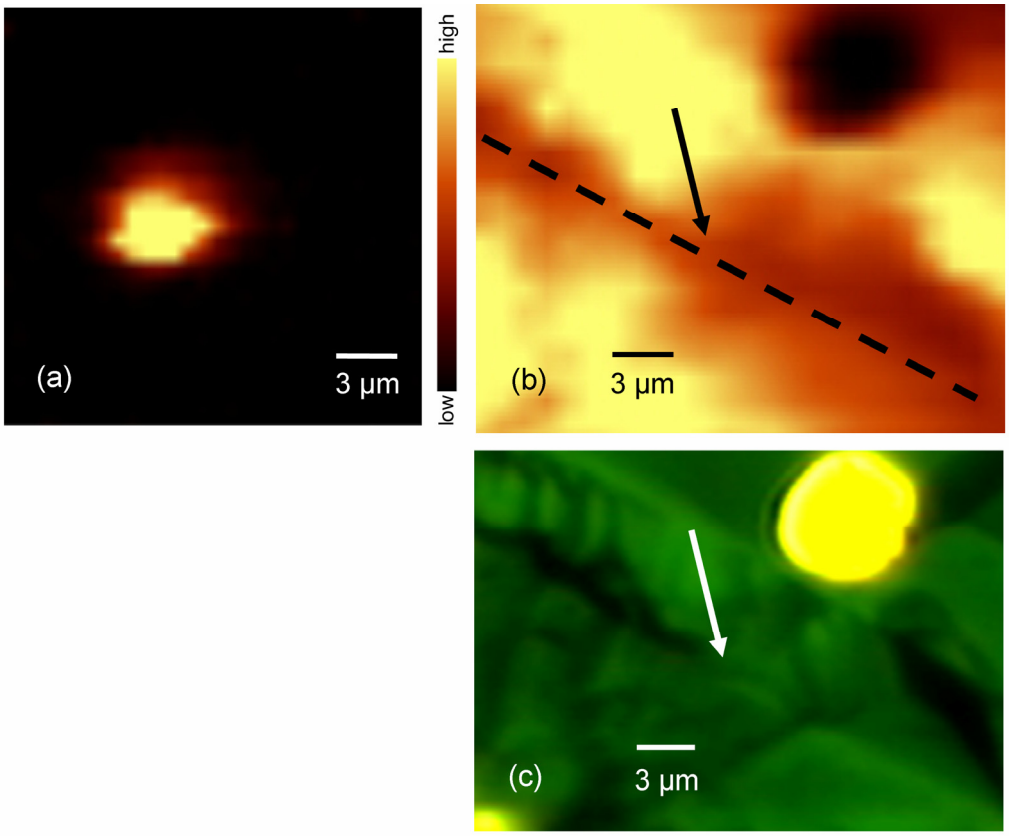

Figure 6.18: Measurements performed with the help of the EL-/PL-mapping measurement setup. (a) Light emission in a soft breakdown site at -14 V. (b) The arrow points at the location of highest breakdown light intensity which is located at a grain boundary, marked by the dashed line in the corresponding PL image of the band-to-band luminescence. The BB-luminescence is decreased due to the recombination activity at the grain boundary. (c) Optical microscope image of the same clipping as in image (b), showing the position of the grain boundary.

It was confirmed with the help of an SEM (SE detector) that the breakdown is not caused by an enhanced electric field at the tip of a deep etching at the grain boundary. Breakdown light comes from a spot approx. 3 µm in diameter, which is exactly located in the highly recombination active part of a grain boundary. Similar measurements reveal that not only grain boundaries but dislocation networks contain soft BD sites at the position of very low PL intensity.

An interesting observation was made by Kasemann et al. [185]: On some mc-Si solar cells, large recombination active areas show only very weak soft breakdown compared to others. For example in Figure 6.16 (a) and (b), soft BD is mainly concentrated in the regions to the right of the image, indicated by the yellow mask, although the recombination activity extends in parts over the whole solar cell area. With the help of an InGaAs CCD camera and by employing a narrow optical band pass filter centered at the spectral wavelength of approx. 1550 nm (0.80 eV) [175], in Figure 6.16 (c) the so-called "dislocation luminescence" is made visible[50]. By comparing the solar cell areas showing weak and

[50] Measurement by M. Kasemann.

strong soft breakdown light emission, one notices that the dislocation luminescence is concentrated only in weakly BD light emitting regions mainly found in the center and the left part of this solar cell. It seems that the defects responsible for 1550-nm radiation suppress soft breakdown.

Luminescence in the spectral region around 1550 nm was first observed by Drozdov et al. [186], who labeled the four different PL lines D1 – D4 in this spectral region. These lines are related to dislocations which decrease the minority carrier density, therefore D-lines are linked to impurity decoration of crystal defects. However, the nature of the impurities is still controversely discussed. There are strong indications that oxygen-related clusters – possibly also containing metals – cause PL lines around 1550 nm [176, 187].

Up to this point, the following picture evolves taking into account the above mentioned observations: Soft BD occurs in tiny spots which are located exactly in recombination active regions, while the opposite is not true: Not all recombination active areas show soft breakdown. In addition, soft BD is suppressed in areas where strong dislocation luminescence is observed.

6.5.2 Cause for soft breakdown

These findings suggest that probably only one specific property of electrically active defects allows for current conducting channels under reverse bias conditions, excluding BD in recombination active defects not meeting the specific property.

A qualitative explanation of some of these observations can be made based on a model that Kveder et al. [188, 189] employed to explain different experimental observations related to recombination at clean and decorated dislocation networks. Following their argumentation, dislocation luminescence is generated by radiative recombination between energy levels (or bands) $E_{DL,C}$ and $E_{DL,V}$ which are highly localized and situated close to the conduction band and the valence band, respectively, both about 0.80 eV apart.

In this picture, strong and weak dislocation luminescence (anti-correlating with the soft breakdown intensity) corresponds to a high and low transition probability between $E_{DL,C}$ and $E_{DL,V}$, respectively. The transition can for example be suppressed in the presence of additional trap levels within the band gap [189].

In literature, non-radiative carrier recombination at crystal defects is therefore attributed to metallic impurities which are either bound to the dislocation core, are stuck at grain boundaries or accumulated in "impurity clouds" around dislocations [190]. In addition, metals tend to form precipitates, see also chapter 5, which also can be highly electrically active [191].

If soft breakdown were caused by an accrual of single metal atoms at dislocation cores or by the surrounding atom clouds, the question arises why the reverse current flows selectively through particular BD channels. One would expect that the atoms are well dispersed along the crystal defects due to simple thermodynamics, thus the differences between the defect configurations should be very small and BD should occur in more sites.

Therefore, it is more likely that soft BD is related to metal precipitates of a sufficient size, since their density is relatively small and each local configuration is unique depending on the impurity element of the cluster, the precipitate size and position relative to the space charge region etc.

While the electrical activity of the system of impurity clouds within the silicon can be described by the Shockley-Read-Hall formula of single energy states around the center of the silicon band gap (see chapter 3.2.3), thus leading to a high recombination activity due to their large total electrically active surface, the system of a metal precipitate in silicon is a completely different issue. As soon as the precipitate contains a critical number of metal atoms, it possesses a metal Fermi energy and its behavior turns metal-like, which has significant implications for the physical properties which are discussed in section 6.5.8.

In literature, breakdown has already been attributed to metal precipitates a long time ago. Goetzberger et al. [167] for example examined the diode behavior of simple silicon pn-junctions, some of which were intentionally contaminated with Cu. The latter tended to show a rather soft reverse I-V characteristic. With the help of a potential mapping technique, they found that the applied reverse voltage was distributed inhomogeneously across the junction. The lowest voltage, signifying the BD site, was concentrated in a small spot which the authors assumed to be a Cu precipitate in the space charge region without providing further proof. In another study by Katz and Cullis [192, 193], the poor reverse characteristics of a silicon p^+n junction was attributed to rod-like $FeSi_2$ precipitates.

To further substantiate the above hypotheses and in order to connect soft breakdown sites with the presence of metal precipitates, the following experiments were carried out [194]:

A damage-etched standard industrial solar cell made from standard feedstock material was characterized via bias-dependent EL measurements. In forward bias, it shows a typical distribution of recombination active regions, while soft BD light emission is detected in reverse bias at many singular spots, correlating to the recombination active defects. Due to the damage etch no hard breakdown (type III) is observed.

For the microscopic investigations, a sample of approx. 10 x 20 mm^2 was cut out containing many soft breakdown sites. Figure 6.19 (a) displays the EL measurement in forward bias (+600 mV) of a part of the sample in which recombination active defects appear as dark regions. At -10 V reverse bias, soft BD light is emitted from the spots marked by the blue circles. Some breakdown sites are located along grain boundaries, which are characterized by dark continuous lines in the EL image, while others are found in areas of rather homogeneously decreased band-to-band luminescence which is typical for high dislocation density regions. Similar regions of breakdown sites correlating with recombination active defects are found in all standard mc-Si solar cells, therefore this sample represents soft breakdown regions well. However, due to the complexity of the microscopic measurements and the restricted experiment time at the synchrotron facility, the following study could be performed only on two exemplary breakdown sites.

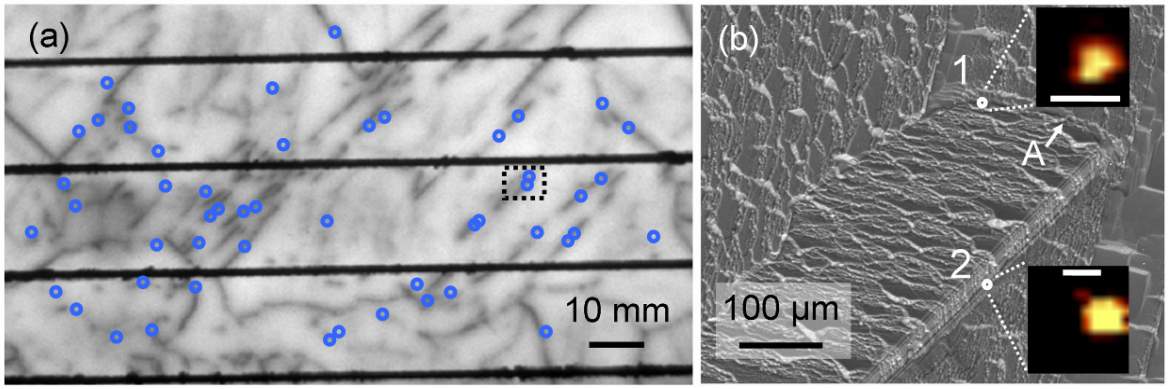

Figure 6.19: (a) Forward EL image (600 mV) of the solar cell piece containing many recombination active defects. Soft BD light emission is detected at the sites marked by the blue circles. (b) SEM image of the grain indicated by the dashed rectangle in (a). BD light emission (see insets; the white bars correspond to 10 µm) is located at the sites 1 and 2 along two grain boundaries.

In order to locate the breakdown sites with a high precision, microscopic investigations were carried out with the EL- / PL-spectroscopy mapping tool[51]. The two breakdown sites found in the macroscopic EL images are located at two different boundaries of one grain (marked by the white circles in the SEM image), see insets in Figure 6.19 (b). Characteristic features of the wafer surface around these coordinates, found in the microscopic images (resolution ~1 µm), are taken as a marker.

Micro-X-ray fluorescence (µ-XRF) measurements of these two breakdown sites were performed at the beamline ID22NI at the European Synchrotron Radiation Facility (ESRF). The nano-imaging stage features a spot size of ca. 100 x 100 nm together with a high photon flux (~10^{12} ph/sec between 6.5 and 18 keV). The combination of small spot size and high photon flux allows for the detection of transition metal precipitates with a diameter in the order of some ten nanometers [121] when the clusters are located within some ten micrometers beneath the wafer surface.

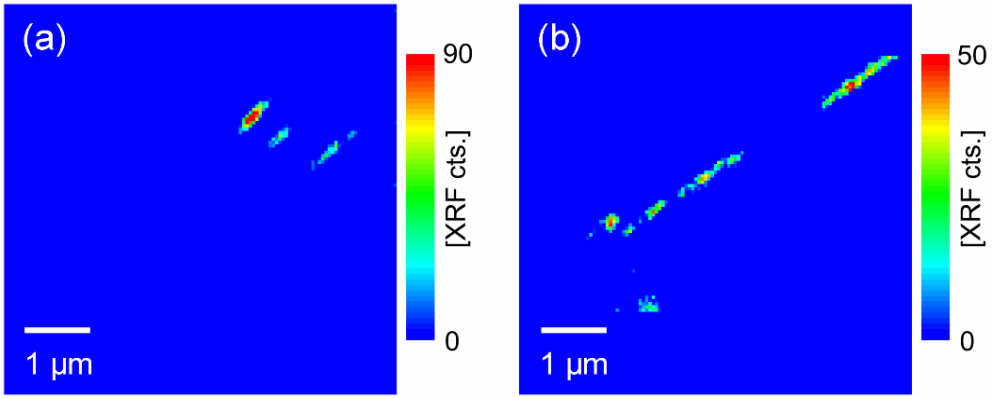

Figure 6.20: Synchrotron µ-XRF measurements (ESRF, ID22NI) of the Fe Kα-line (a) at BD site 1 in Figure 6.19 and (b) at BD site 2.

[51] Measurement performed in collaboration with P. Gundel.

Using the markers determined in the EL maps, the µ-XRF mappings were carried out in an area of 20 x 20 µm^2 centered at the pre-breakdown spots. The results are shown in Figure 6.20.

Iron precipitate colonies are detected at both pre-breakdown sites. They are distributed along single lines which correspond to the grain boundaries. In region 1, also one copper precipitate is found. The distance between this copper cluster, however, and the position of the pre-breakdown is determined to be approx. 5 µm. The location of the iron precipitate colonies, on the other hand, coincides well with the breakdown spots taking into account the limits of the spatial resolution provided by the EL- / PL-mapping tool (1 µm) and the accuracy of the positioning of the X-ray spot on the sample, which is estimated to be around 1 to 2 µm.

In addition, several µ-XRF mappings distant to the pre-breakdown sites along the grain boundary labeled A in Figure 6.19 were performed. However, in spite of the high recombination activity of this grain boundary no other precipitates within the detection limit of around 30 nm in diameter are discovered, underlining the evident concurrence of Fe-containing large clusters and pre-breakdown spots.

This result is further maintained by investigations performed at MPI Halle [195]. By combining high resolution EL microscopy with FIB, TEM and EDX, metal containing precipitates of various chemical compositions were found at type II BD sites. Besides Fe, Cu and Mn oxides were detected.

In summary, there is strong evidence that metal containing precipitates cause soft BD. Since metal precipitates are highly recombination active, the dislocation luminescence is suppressed at soft breakdown sites, explaining previous findings.

6.5.3 Spectra of light emitted from soft breakdown sites

The exemplary spectrum shown in *Figure 6.21* was obtained at the soft breakdown site 1 displayed in *Figure 6.19*[52].

The spectrum is distributed over a broad wavelength range very similar to the spectra of the early breakdown sites (see *Figure 6.13*). Its maximum is found around 750 nm (1.65 eV). Compared to type I spectra, slightly less high energy photons are detected in soft breakdown light. However, this may be attributed to differences in the surface morphology.

In any case, the broad spectral distribution indicates that soft breakdown involves hot carriers pointing towards the existence of high electric fields in the space charge region of soft breakdown sites.

[52] Measurement performed in collaboration with P. Gundel.

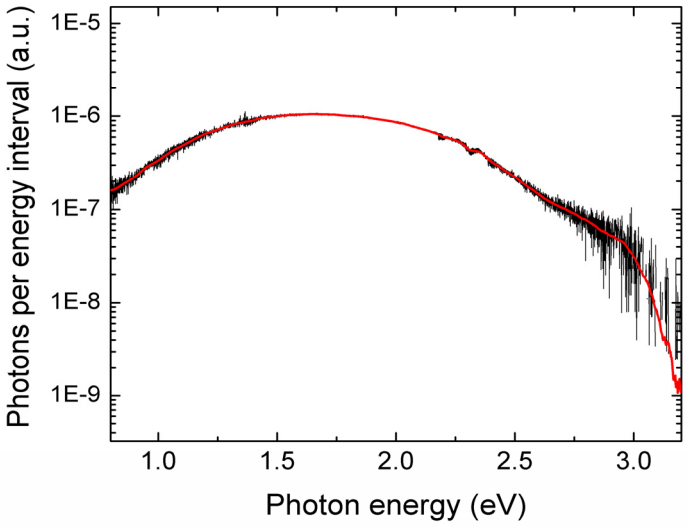

Figure 6.21: Calibrated spectrum obtained on a type II breakdown site[52].

6.5.4 Influence of the impurity concentration

Initially, the investigation of the breakdown behavior of mc-Si solar cells was intended to give an answer to the question what the reasons are for the larger reverse currents in UMG-Si compared to standard material mc-Si solar cells.

Mc-Si wafers differ mainly in their base resistivity, the impurity concentration and distribution, the distribution of crystallographic defects and the surface morphology, which all potentially influence the soft breakdown behavior. One of these contributions has to be responsible for the notably different reverse I-V characteristic of UMG-Si solar cells. Therefore, the influences on the soft BD behavior are demonstrated in detail in the following sections.

Since metal-containing precipitates are very likely responsible for soft breakdown, it is obvious that a varying impurity concentration should have an impact on the soft BD. The impurity concentration and distribution is in general determined by the impurity indiffusion during the crystallization process and the impurity content of the silicon feedstock itself. Both sources are investigated in this section.

Since UMG-Si feedstock is generally considered to be less pure, differences in the impurity content could possibly explain UMG-Si-related increased reverse currents.

In the first investigation [174], wafers from five different mc-Si ingots were taken from different positions distributed over the ingot height and processed to solar cells at the ECN Petten, Netherlands. The ingots were made of high purity solar grade silicon feedstock with transition metals added to the silicon melt. Solar cells from following blocks were taken:

(1) "Ni mc" contaminated with 40 ppmwt of nickel in the melt,

(2) "Fe- Ni- Cr mc" contaminated with a mixture of 40 ppmwt chromium, 200 ppmwt iron and 40 ppmwt nickel,

(3) "Fe mc" contaminated with 200 ppmwt iron and

(4) "Cr mc"contaminated with 40 ppmwt chromium. In addition,

(5) "Ref mc 2", a reference ingot made of high purity solar grade feedstock.

The base resistivity of all ingots was aimed at 1.2 Ωcm [28], with the usual resistivity distribution over ingot height due to the segregation of the boron atoms. After crystallization, ingot cutting and wafer slicing, the wafers were processed in one run in a standard industrial screen printing process including an acidic texturization step. Since all parameters except the contamination were kept constant, differences in the BD behavior of solar cells taken from similar ingot heights should only be due to differences in the impurity content.

The ingot characterization and the solar cell performance are reported in references [196] and [197]. It was verified with the help of Neutron Activation Analysis (NAA) that the ingots were contaminated as intended and impurity segregation towards the top of the ingot took place.

Figure 6.22 shows an example for the measurements taken from blocks 1 to 5. Almost all breakdown sites, represented by the local breakdown voltage map in Figure 6.22 (b), correlate well with the dark areas in the EL image (a). Only a few sites with early breakdown (type I, breakdown voltage >-8V in image (b)) are found on each solar cell. In the limited voltage and current range up to -2 A, hard breakdown can be excluded on the solar cells in this study, based on the analysis of the bias-dependent breakdown light emission. Therefore, the following study involves mainly soft breakdown.

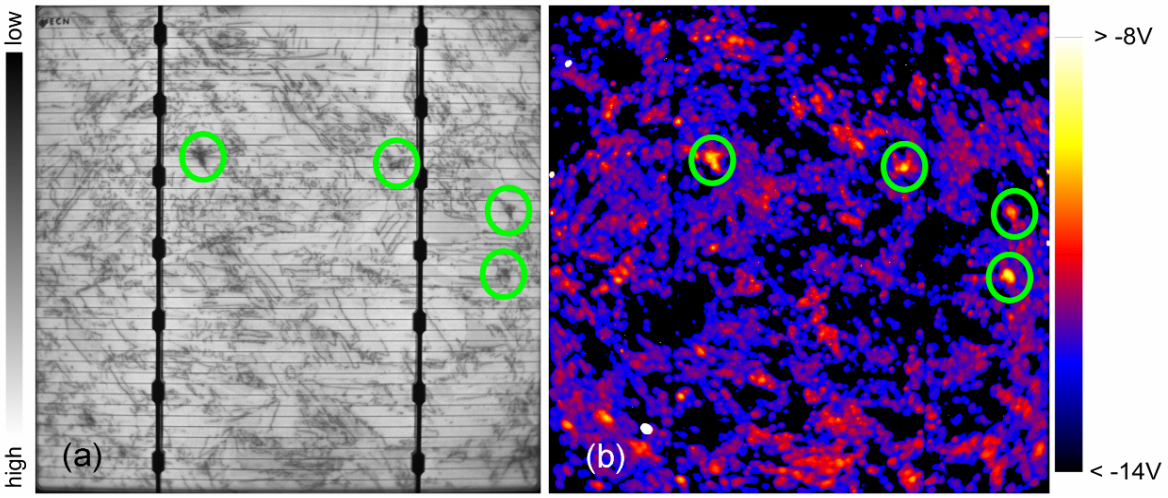

Figure 6.22: (a) EL image in forward bias from the reference solar cell taken from 55% ingot height (Ref mc 2) and (b) corresponding breakdown voltage map. The green circles mark areas with very high recombination activity, which causes a lower soft breakdown voltage than in neighboring regions.

The local breakdown voltage of the breakdown sites related to recombination active defects varies laterally in all mc-Si solar cells. For example in Figure 6.22, some of the first regions that emit visible light at around -8.5 V are indicated by the green circles. In the forward EL image, dense dark clusters can be seen, signifying very high recombination activity. The high electrical activity is associated with a high density of dislocations which

form "nests". By comparison, in this solar cell less distinct recombination active features break down between -10 and -11.5 V which correspond to rather straight, dark lines. They are associated with grain boundaries.

By analyzing the first onset of soft breakdown as well as the variation in local breakdown voltage in the differently contaminated solar cells it becomes apparent that they depend strongly on the contamination level of the silicon wafer. This is illustrated in Figure 6.23, which shows the fraction of the surface area which emits light due to breakdown plotted against the reverse voltage. This is a measure for both, the onset of the soft breakdown in each solar cell and the lateral extension of the breakdown.

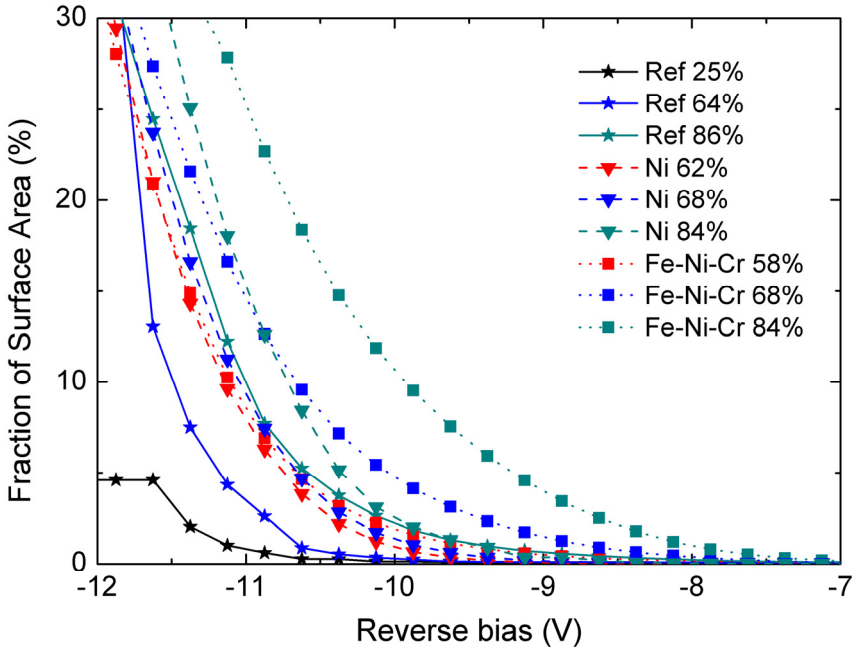

Figure 6.23: Plot of the breakdown light emitting fraction of the surface area of differently contaminated solar cells versus the reverse voltage. "Ref", "Ni" and "Fe-Ni-Cr" refer to block (5), (1) and (2), respectively. The percentage denotes the ingot height from which the wafers were taken (100% = top of the ingot).

Two trends can be observed: Firstly, the more contaminated the ingot, the lower the local breakdown voltage. Secondly, solar cells made of wafers which were taken from close to the top of the ingot possess a lower breakdown voltage than the wafers taken from the bottom or the center of the same ingot.

For example, type II breakdown begins last in the solar cells made of high purity solar grade feedstock without additional contamination, block Ref mc 2. By comparing the solar cells from around 65% of the ingot height of the three different ingots, we find that the difference between the breakdown voltage of the reference block and the Ni contaminated ingot (Ni mc) is about 1 V, while the difference between the reference ingot and the Fe-Ni-Cr ingot (Fe-Ni-Cr mc) is already about 2 V. In this example, the breakdown voltage is decreased by about 20% due to ingot contamination.

An equally strong influence on breakdown voltage comes from the wafer position in the ingot. Solar cells from 25% block height of the reference ingot show first bright spots around -10.0 V, while the topmost (86% ingot height) reference solar cell already starts

to break down below -9.0 V. In the highly contaminated solar cells (Fe-Ni-Cr mc), the onset of breakdown decreases significantly from around -9.0 V (center of the ingot) to around -7.5 V (84% ingot height). Ingot position thus affects all samples regardless of their intentionally added contamination. If the segregation of metal impurities during the crystallization is taken into account, the effect of ingot height on breakdown voltage could be explained by the influence of contamination, too. However, as will be shown in section 6.5.5, the base net doping, which increases with ingot height, has a strong influence as well.

The evaluation of the slopes of the measured curves in Figure 6.23 shows that contamination also affects the lateral breakdown voltage distribution. For the highly contaminated solar cells (Fe-Ni-Cr mc), slowly increasing the reverse bias results in only a gradual increase of the breakdown surface fraction. By contrast, the steep slopes observed for the reference solar cells indicate that here breakdown happens within a rather small voltage range in many spots at once. The correlation between a slow increase in the breakdown surface fraction with reverse bias and the contamination of the solar cell is significant. The implications of this finding are discussed in section 6.5.7.

In addition to the results presented in Figure 6.23, the same measurements were also performed on the ingots contaminated solely with iron and chromium (blocks "Fe mc" and "Cr mc", respectively). Regarding the diode breakdown behavior, no significant difference between the several species of contamination are seen. The fact that impurity atoms are present in a certain concentration seems to suffice for a lower breakdown voltage.

Note that the difference between the soft BD behavior of the various contaminated ingots is relatively small and allows to draw the conclusion only on a statistical basis. This approach may be too rough to discriminate any influences of the different precipitation kinetics of e.g. Ni and Fe / Cr.

In order to substantiate these findings, a laterally varying impurity distribution within the same wafer was examined in a second investigation. For this, solar cells were made in an industrial solar cell process from wafers taken from a block region close to the crucible wall from ingots "Ref mc 1". In order to exclude all influences of the base doping, in this study, it was checked with the help of 4-point-probe measurements that the base resistivity is laterally constant across the entire wafer area [198].

The reduction of the local breakdown voltage due to impurities is observed also in these cells. An example is shown in Figure 6.24 (a). During the cool-down after crystallization, impurities diffuse into the silicon block, contaminating a region limited by the diffusivity of the impurity species (mostly Fe in mc-Si crystallization [199]). This results in the highly recombination active area at the upper wafer edge in the EL image (a).

Since crystal defects act as impurity traps, after solidification (Fe) metal atoms segregate to the grain boundaries and dislocations which results in zones denuded of metallic impurities in the close vicinity of the defects (b). Although the grains themselves are highly recombination active in this region, soft breakdown is restricted to the crystal defects, at which metallic atoms have accumulated (c) and where precipitation has very likely taken place. Here, the high supersaturation of the surrounding grains probably furthered the development of particularly large precipitates, contrasting with the precipitate size in the

wafer center. Within the grains, metallic atoms tend to be in a dissolved state due to a lack of nucleation sites [200].

At the highly contaminated upper wafer edge, breakdown sets in at a significantly lower reverse bias than in the rest of the cell, image (d). In this example, first breakdown light emission at the upper solar cell edge is detected at around -5.2 V, while in the center, soft breakdown happens between -8 to -10 V. Thus, highly contaminated edge zones can lead to a decrease of the local soft breakdown voltage of about 35%.

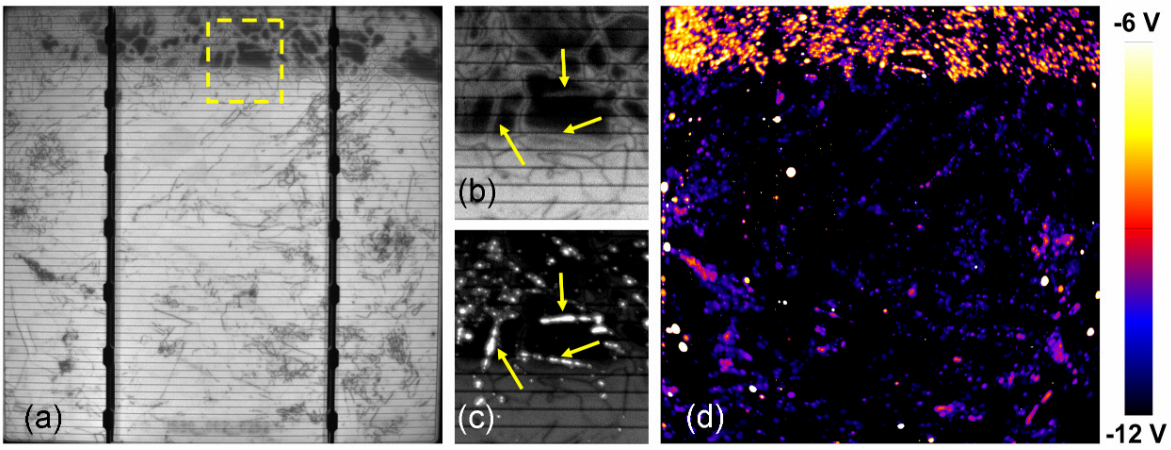

Figure 6.24: (a) Forward EL image of a reference solar cell which is influenced by impurity indiffusion from the crucible wall at the upper wafer edge. (b) Zoom into the region marked by the yellow rectangle in (a), showing denuded zones around grain boundaries and dislocation clusters. (c) Soft breakdown light emission is restricted to the crystal defects at the center of denuded zones. For better orientation, the yellow arrows in image (b) and (c) point exactly at the same positions. (d) In the highly contaminated region at the upper wafer edge, the local soft breakdown voltage is significantly lower than in the other areas.

In summary, relative to the soft breakdown voltage in standard reference material with usual impurity content, a high contamination level can decrease the local breakdown voltage easily by 20 - 35%.

The possible cause of the impurity-induced lowering of the breakdown voltage will be discussed in section 6.5.8.

Besides the metallic impurity concentration, all mc-Si wafers possess varying concentrations of boron and phosphorus acting as dopants. Therefore, the influence of the base net doping is studied in the following section.

6.5.5 Influence of the base net doping

For the *global* breakdown voltage in mc-Si solar cells, the important role of the base resistivity was already pointed out by Wagner et al. [201]. For wafers covering a wide resistivity range of 2.2 to 0.2 Ωcm, a clear correlation between the decrease of resistivity on the one side and the increase of reverse current for typical module operating voltages on the other side was reported. However, the kind of breakdown mechanism responsible for this reverse current increase was not identified in reference [201]. Based on the as-

sumption that in the solar cells taken for the investigation the I-V characteristic was governed by hard breakdown (type III) – as is often the case, see section 6.3 – such a result would be expected.

In order to clarify the impact of the base resistivity of mc-Si wafers on the soft BD behavior, spatially resolved electroluminescence (EL) and dark lock-in thermography (DLIT) measurements are analyzed in the following [198, 202]. The measurements were performed on industrial standard screen printed solar cells (format 15.6 x 15.6 cm^2), which were processed from six different silicon material types[53]. Solar cells from five ingots made from standard pure feedstock with different base resistivities ("Dop mc 1-5") are chosen from different positions over ingot height. In addition, solar cells made from the commercially available UMG silicon ("UMG mc 1") are included in this investigation. An overview over the ingots is given in Table 6.1. The solar cells were processed in two different process lines, both of which yield stable processing conditions. Therefore, all solar cells made in the same process line are comparable to each other.

In order to characterize the diode breakdown under worst case conditions and to establish a link to previous work by Wagner et al. [201], the breakdown light emission as well as the heat distribution at a reverse current of -10 A via EL and DLIT, respectively, is measured and compared to EL measurements under forward bias. The reverse current of 10 A, as expected, is reached at different reverse voltages in each solar cell. A typical example is shown in Figure 6.25. The solar cell is taken from 67% ingot height from ingot "Dop mc 1" (base resistivity: 0.34 Ωcm).

Although in the reverse EL images of all solar cells taken for this investigation, the highest signal always originates from the early breakdown sites (type I), the bright light emission does not translate into an increased heating which would be visible in DLIT measurements in most cases. Hence this breakdown mechanism does not govern the reverse I-V characteristics.

Table 6.1: Overview over the silicon material used in the study of the impact of varying doping concentrations.

Ingot	Solar cell run	Base resistivity [Ωcm]	Approx. global BD voltage [V]	Approx. first soft BD voltage [V]
Dop mc 1	3	0.26 – 0.43	-9.4 to -10.4	-4.5
Dop mc 2	3	0.70 – 0.85	-12.2	-5.5
UMG mc 1	3	0.25 – 1.0	-8.5 to -10.4	-4.0
Dop mc 3	6	0.5 – 0.7	-11.0	-4.5
Dop mc 4	6	1.3 – 1.6	-14.0	-9.0
Dop mc 5	6	~ 2.5	-16.0	-10.0

[53] Solar cells provided by M. Wagner, SolarWorld Innovations, and by research cluster SolarFocus.

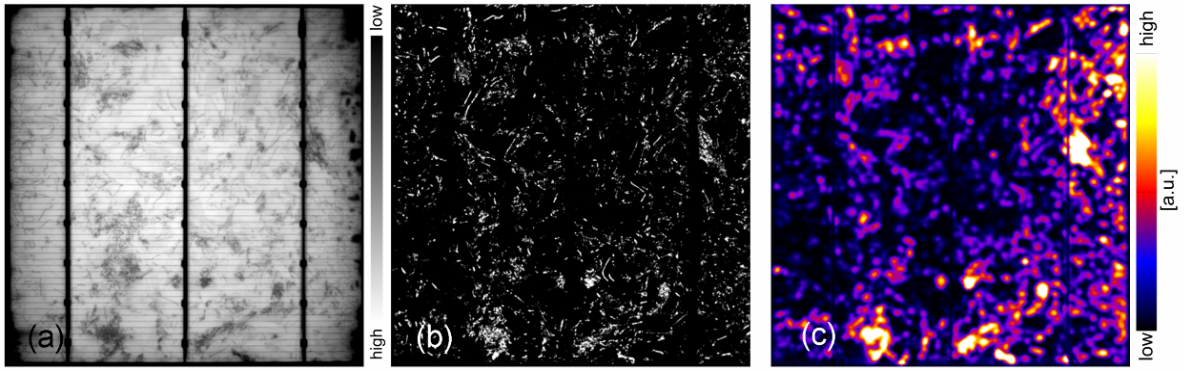

Figure 6.25: The location of recombination active defects, appearing as dark clusters in the EL measurement in forward bias (+ 550 mV) of the solar cell taken from 67% ingot height from ingot Dop mc 1, (a), and the sites of most breakdown light emitting spots measured at -11.14 V (-10 A) (b) coincide. At the same reverse bias, DLIT measurements (c) show the highest signal at the recombination active regions, too. Hence, the breakdown behavior of this solar cell is dominated by soft breakdown at recombination active defects.

Two facts indicate that no hard breakdown occurs in the current-voltage range up to -10 A: (1) Careful analysis of the EL intensity slope, which increases only moderately with reverse bias. Since a pronunciated steep increase in EL intensity is expected in regions of hard breakdown, the observed behavior clearly fits to soft breakdown behavior. (2) By comparing the EL images in reverse, Figure 6.25 (b), and forward bias, Figure 6.25 (a), excluding early breakdown sites, all the remaining breakdown sites can be attributed to recombination active defects clearly visible as dark clusters under forward bias conditions. Since the absence of recombination activity in regions of hard breakdown is striking, this may count as evidence that only soft breakdown attributed to metallic precipitates in the SCR of the pn-junction is observed. Therefore, it can be stated that in none of the solar cells of this investigation hard breakdown sites are observed in the regime up to 10 A, which suggests that an optimal wet chemical texturization had been applied without selectively etching crystal defects, see section 6.6.

Accordingly, the heating, which is the decisive information for solar cells in a module, is also located in these regions with a high density of recombination active defects, as can be seen for example in the DLIT measurement in Figure 6.25 (c). This also proves that if shunts and hard breakdown (type III) are successfully avoided, soft breakdown determines the heat distribution across the solar cell and thus the dangerousness for the solar module.

In Table 6.1, the ranges of the base resistivities of the solar cells taken from the different ingots are related to the roughly determined onset voltage of the very first soft breakdown sites as well as to the approximate global breakdown voltage, averaged over the ingot height. It is obvious that the base resistivity influences both the global as well as the local soft breakdown behavior.

This fact is analyzed in more detail in Figure 6.26 for all solar cells. Depicted are the voltages of maximum curvature of the global reverse characteristics (global breakdown voltage) and of the first appearance of breakdown light at recombination active defects, both plotted over the net doping concentration in the wafer base, analyzed in the same way as

described in section 4.2.3. For comparison, the dashed black line shows the predicted avalanche breakdown voltage of defect-free one-sided abrupt pn-junctions (after Sze [30]).

In general, the very first soft breakdown happens already at a reverse bias 4 – 5 V lower than the global breakdown. It shows the same correlation with the base resistivity as the global breakdown voltage, ranging from approx. -2.25 V for the lowest base resistivity (0.25 Ωcm), to -11.5 V, found on the high resistivity wafers (2.5 Ωcm).

Hence it can be concluded that soft BD shows a similar dependency on the doping concentration in the lower doped side of the pn-junction as both classic breakdown types, avalanche BD and internal field emission. It is possible that the underlying mechanism of soft BD is a modified version of either one of both classic BD types.

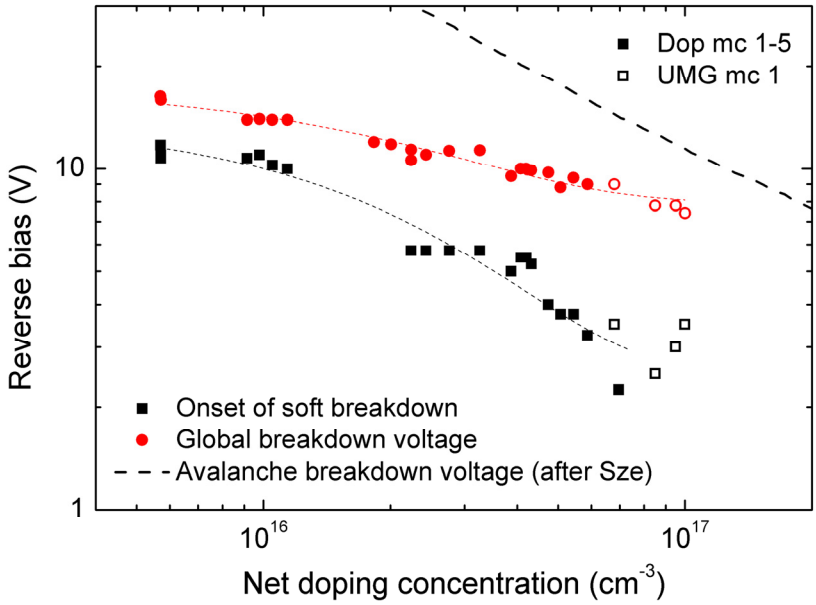

Figure 6.26: Onset of the soft breakdown (black squares) and the global breakdown voltage (red circles) versus the base net doping concentration of all solar cells included in the study. UMG-Si solar cells (open symbols) fit well into the picture. The dashed line only serves as guide to the eye.

Interestingly, the solar cells made of UMG-Si fit well into this picture in the case that the wafers have low p-type resistivity. Therefore, a very important conclusion of this study is that the early increase of the reverse current in UMG-Si solar cells can be mainly attributed to the high net doping concentration, which corresponds to low base resistivity, and only partly to the impurity concent.

The slightly higher scatter in the UMG-Si related data of Figure 6.26 can be explained by laterally inhomogeneous B- and P-concentrations due to a non-horizontal crystallization front which leads to laterally varying local breakdown voltages. This has been observed on p-type UMG-Si wafers from close to the changeover of the conductivity type.

In the worst case, inhomogeneous crystallization of UMG-Si feedstock leads to conductivity type changeover which covers a significant part of the ingot. In this ingot section, each wafer consists of a p- as well as an n-conducting part. Solar cells made of these

wafers still work – although with lower cell efficiencies – because a pn-junction exists in both, the p-type (front-side phosphorus emitter) as well as in the n-type (back-side Al-BSF emitter) part of the wafer. Since the latter junction is not optimal when current industrial cell processes based on screen-printed metal contacts are applied, the reverse characteristics of the n-type parts suffer severely.

In Figure 6.27, an exemplary PL image of a UMG-Si having a p- as well as a n-typ part is shown, taken from 85% ingot height (contrast was artificially enhanced in order to make the PL signal in the n-type part visible). The dark band marked by the dashed white line indicates the local changeover between p- and n-type conductivity, resulting from the locally negligible net doping concentration. The EL image of the solar cell made from this wafer (Figure 6.27 (b)) resembles measurements of good standard reference solar cells which implies that the forward I-V characteristics are satisfactory (the solar cell shown here has a cell efficiency of 12.4%, the major decrease resulting from the low shunt resistance due to the imperfect pn-junction).

DLIT-reverse bias measurements reveal significant heating in the n-type part of the cell, see Figure 6.27 (c). In part of the heated areas, also light, which could be attributed to diode breakdown, is detected, which can be even more intense than the light perceived in early breakdown sites. Whether this is really due to diode breakdown and if so, which breakdown mechanism is at work has still to be clarified.

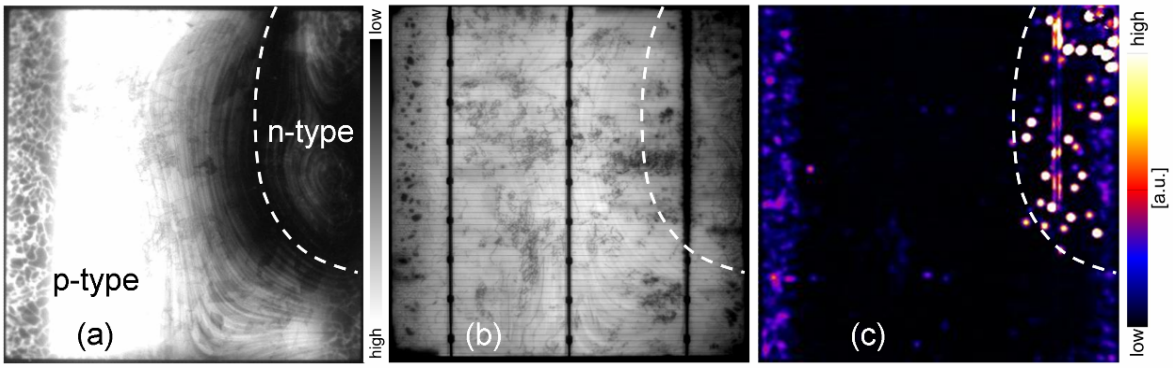

Figure 6.27: (a) PL image of a UMG wafer, featuring a p- and n-type part (contrast enhanced in order to render the n-type part visible). (b) Solar cell made from the same wafer. (c) DLIT image measured at -8 V, showing heat development in the n-type part of the solar cell.

In summary, high reverse currents in solar cells made from UMG-Si feedstock result from relatively high doping concentrations. This leads to

(i) low local soft breakdown voltages due to the low base resistivity and,

(ii) an imperfect pn-junction in the ingot region around the conductivity type changeover if there is a n-type part on the wafer, resulting in a shunted region.

In order to compare the impact of impurity concentration with the influence of the base resistivity, wafers of different base resistivities but all taken from the block region close to the crucible walls are an ideal basis for the analysis. If the crucible material and the crystallization conditions are comparable for the differently doped silicon ingots, we can suppose that the same amount and the same species of impurities have indiffused into

the silicon blocks during the cool down. In addition, their concentration in the block edge region is orders of magnitude higher than any background impurity content of the silicon feedstock, which makes the latter influence negligible. On the other hand, in the wafer center, the recombination activity is determined by the feedstock-induced impurities.

Therefore, in *Figure 6.28*, the EL image in forward bias (a) and the breakdown voltage map (b) of a solar cell taken from 25 % height of an ingot made from the ingot "UMG mc 1" (base resistivity: 0.27 Ωcm) are shown. By comparison, *Figure 6.28* (c) and (d) depict the recombination activity distribution and the corresponding breakdown voltage map of a solar cell from the same ingot height made of 0.8 Ωcm pure feedstock material (ingot "Dop mc 2").

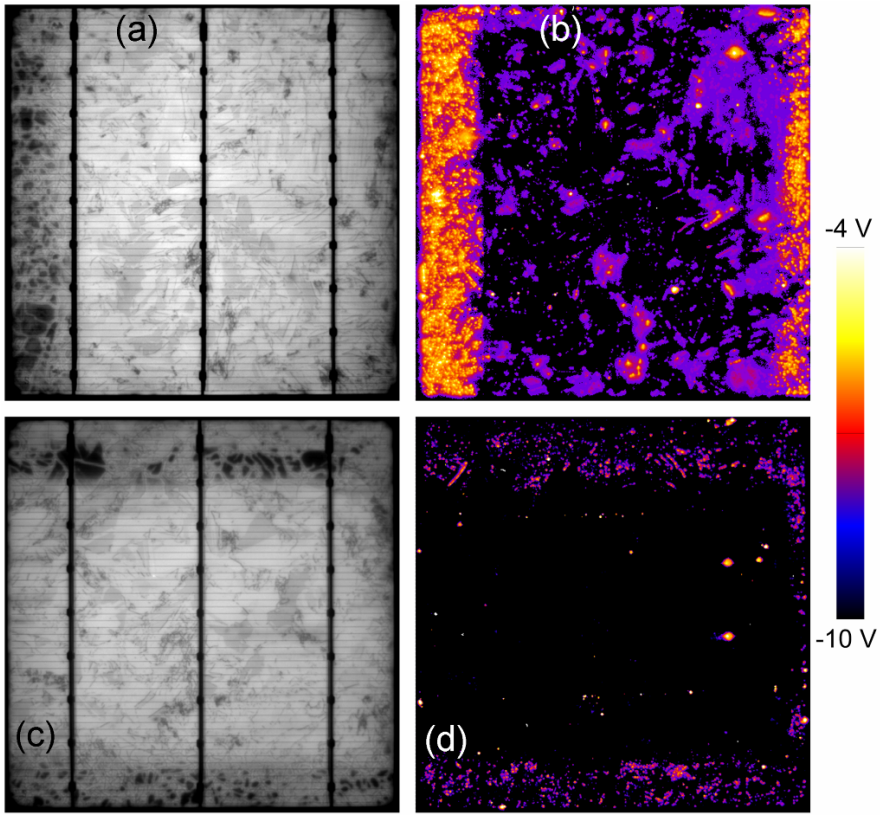

Figure 6.28: (a) and (c) EL images of a solar cell from 25% height of the "UMG mc 1" ingot (0.27 Ωcm) and a standard solar cell taken from 50% height of ingot "Dop mc 2" (0.8 Ωcm), respectively. In both, soft breakdown starts first in the highly recombination active regions at the wafer edges, as seen in the breakdown voltage maps (b) and (d). However, in the standard solar cell, this happens at a reverse voltage about 2-3 V higher than in the UMG-Si cell due to the higher base resistivity.

Both wafers are influenced at the edges by the in-diffusion of impurities from the crucible. These regions are characterized by the dark contrast in the EL measurements due to their high recombination activity. It was checked that the base resistivity did not vary laterally as a hypothetic result of dopant in-diffusion from the crucible wall.

In both solar cells, the highly contaminated regions at the wafer edges are the first areas to break down, at a reverse bias approximately 3 V below the breakdown at the center of the cells where the contamination is less severe (wafer edge: UMG ~ -5 V, Standard

~ -7 V; wafer center: UMG ~ -8 V, Standard > -10 V). Therefore, breakdown at the wafer edge happens at a reverse bias that is about 30-40% lower than the voltage for breakdown at the wafer center which stands for the influence of the varying impurity concentrations. On the other hand, the difference in the base resistivity (base net doping) accounts for a 30% decrease from the 0.8 Ωcm material to the 0.25 Ωcm wafer.

In summary, in this range of impurity and dopant concentrations, both the impurities and the base net doping make up for the same relative impact on the soft breakdown voltage; hence, none of these influences can be neglected in the analyses.

6.5.6 Influence of the surface morphology

Besides inducing hard breakdown at deep etch pits (see section 6.6), the morphology of the wafer surface has also a significant influence on the onset voltage of the soft breakdown.

In order to investigate the dependence of the onset of soft breakdown light emission, the following experiments were carried out in collaboration with Jan Nievendick (details on the process including the texturization recipes and on further results can for example be found in reference [203])[54]:

A set of parallel wafers was taken from the center ingots of three standard multicrystalline blocks ("Ref mc 3-5"), which had been crystallized by different companies. While the impurity concentration and the base doping were comparable, the distribution of crystal defects (dislocations and grain boundaries) and thus the crystalline quality varied.

For the following industrial solar cell process (based on screen-printing metallization), each set of wafers was divided into three groups. After the initial wet chemical wafer cleaning, different wafer surface treatments were applied: while one wafer batch was only damage-etched, two different wet chemical texturization recipes were applied to the two remaining groups.

As a result of the damage etch, surface inhomogeneities were leveled out to a high degree; only along the boundaries between the grains, the crystal orientation-dependent etching rate led to very shallow steps. By contrast, the application of both wet chemical texturization recipes entailed selective etching of crystal defects, in particular deep etch pits at dislocations. The difference between both texturizations lies in their aggressiveness: While one recipe produces very steep etch pits and rough wafer surfaces ("aggressive recipe"), the other generates a more homogeneous morphology with smaller etch pits ("mild recipe").

After the wafer surface treatment, each group of wafers was further processed according to its requirements (i.e. the anti-reflection coating, the firing of the contacts etc. were slightly modified). However, these adjustments are not expected to have an influence on the breakdown characteristics.

Hence, the comparison of the breakdown voltages of the differently texturized parallel wafers, possessing the same impurity concentration, base doping and crystal quality, di-

[54] Solar cells and AFM measurements provided by J. Nievendick.

rectly reveals the influence of the surface morphology. As an example, in *Figure 6.29* (b)-(d), the breakdown voltage maps of the solar cells processed from parallel wafers of material "Ref mc 3" are shown. Distributed over the surface of the damage-etched sample (b) many early breakdown sites can be seen (white and yellow spots), but hardly any soft breakdown sites appear up to a reverse voltage of approx. -13.5 V (compare to forward EL image (a)). In the mildly etched sample (c), the earliest light emission from soft breakdown sites can be detected around -10.0 V, while the deeply etched wafer (d) shows soft diode breakdown already around -9.25 V in the same wafer area marked by the green circles. Taking the damage-etched sample as a reference, the decrease due to the influence of the surface structure thus amounts to 25-30%, which is in the same order of magnitude as the impurity impact and the base doping influence in the relevant parameter range.

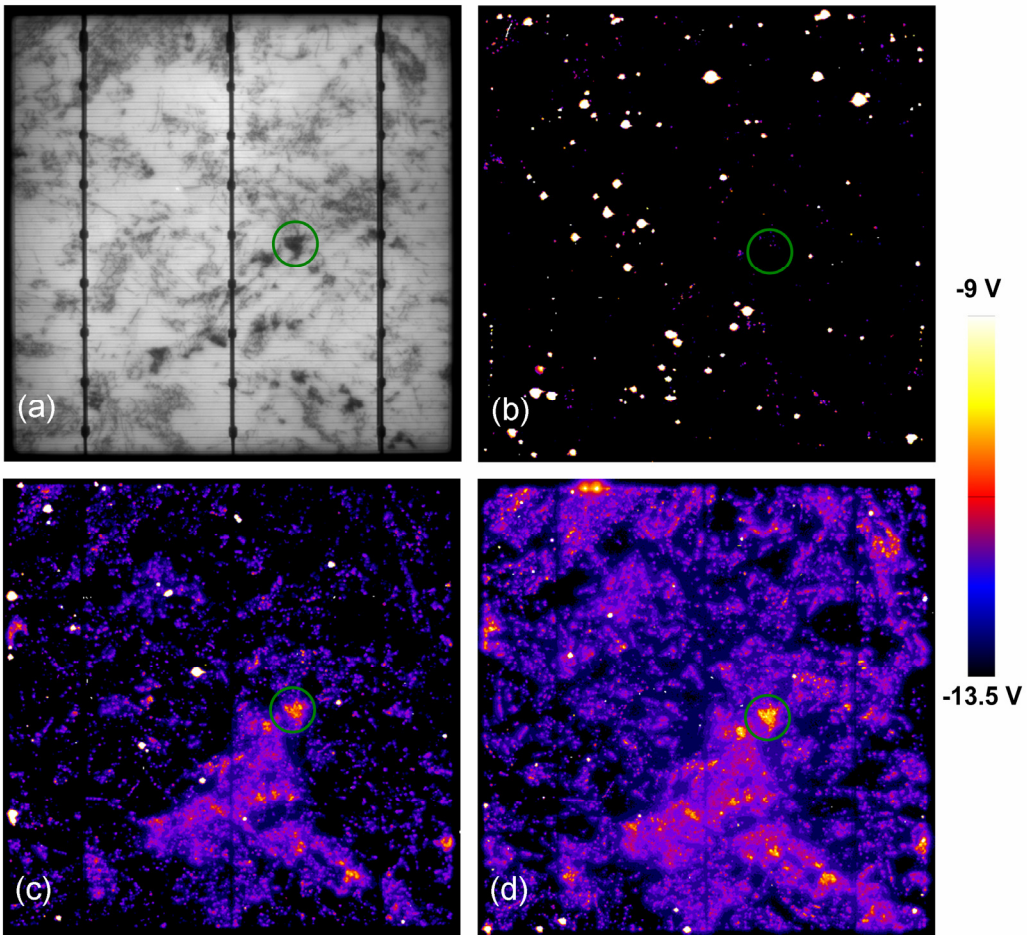

Figure 6.29: Comparison of the breakdown voltage maps of three differently texturized, but parallel solar cells ("Ref mc 3"). (a) Forward EL image (+600 mV); the green circle marks a wafer region with a high concentration of recombination active crystal defects at which the Atomic Force Microscope image depicted in Figure 6.30 was obtained; (b) breakdown voltage map of the damage-etched wafer; (c) breakdown voltage map of a neighboring wafer, textured with the "mild" recipe; (d) breakdown voltage map of a neighboring wafer, textured with the "aggressive" recipe. Note that the same scaling was applied to images (b)-(d).

To quantify this assessment, the height profile of the textured solar cells made from the three standard materials "Ref mc 3-5" in selected regions was measured with the help of Atomic Force Microscopy (AFM)[54]; for example, the highly recombination active region denoted by the green circles in *Figure 6.29* (a)-(d) was chosen. In these areas, the wet chemical texturization etches deep pits where dislocations reach the wafer surface. This is exemplarily imaged in the left part of *Figure 6.30*. Often, the dislocations form lines (small angle grain boundaries) and clusters ("bursts"), in some cases leading to very deep trenches, which can be seen for example in the lower part of the AFM measurement.

The etch pits are often triangularly shaped. In the right graph in *Figure 6.30*, the extraction of the surface morphology parameters which are used in the following, namely the etch pit depth and the depth / width ratio, is exemplified by the blue lines. The depth was determined by measuring the distance between the bottom of the etch pit and the vertical line defined by the lowest point at the rim of the etch pit. This parameter is independent of the pit shape and does not distinguish between different curvatures at the bottom of the etch pit. The diameter at the height of the lowest border identifies the width of the etch pit, from which the depth / width ratio is calculated. This parameter gives an indication for the curvature at the bottom of the etch pit: The larger the ratio, the larger the average curvature.

Both parameters were obtained from several AFM scans (side length of the scans 50 x 50 μm^2) situated at recombination active regions in all three materials in order to increase the statistical significance. After averaging the values from each scan, the etch pit depth and the depth-to-width ratio were correlated to the local soft breakdown voltage measured in the respective region.

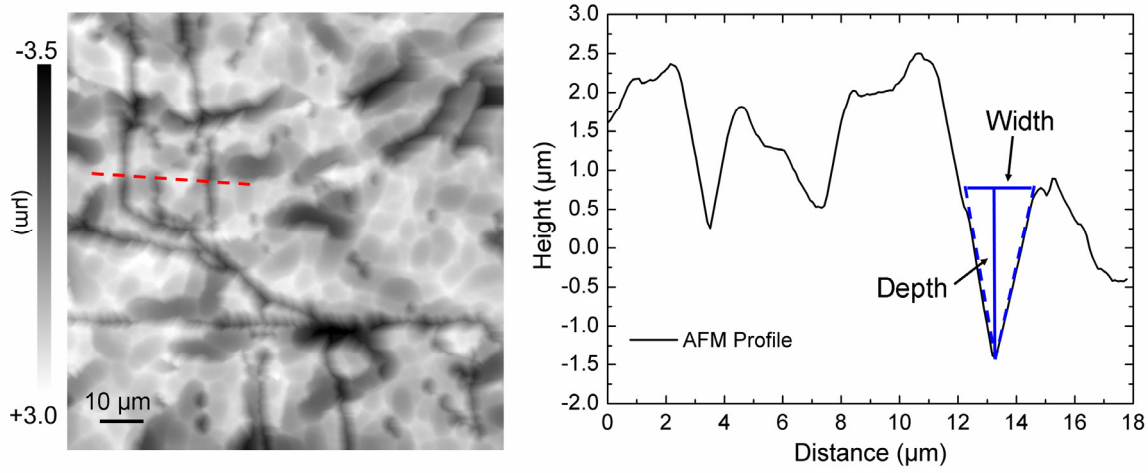

Figure 6.30: Left image: Atomic Force Microscopy (AFM) measurement of the lateral surface height distribution, obtained in the highly recombination active crystal defect region marked by the green circle in Figure 6.29 on the aggressively texturized sample (d). Right graph: Exemplary surface profile extracted along the red dashed line in the AFM image. The etch pit depth is determined by measuring the distance between the bottom of the etch pit and the vertical line defined by the lowest point bordering the etch pit as shown by the blue lines. The diameter of the etch pit at the height of the lowest border identifies the width.

The results are plotted in *Figure 6.31*. The soft breakdown voltage shows a significant correlation with both parameters, suggesting a linear dependence in this parameter range in both cases. However, by extrapolation, on a very smooth surface one would expect a soft breakdown voltage around -11.5 V, which is significantly lower than the real value detected on the damage-etched solar cell (-13.5 V). It seems therefore that the linearity is restricted to etch pits with depth ≥500 nm.

For the occurrence of soft breakdown, high electric fields are necessary (see also section 6.5.8). The influence of the surface on the breakdown may thus be explained by the concentration of the electric field lines due to the curvature in the space charge region at the bottom of the etch pits, which is very similar to the mechanism of the third, hard breakdown type described in section 6.6. However, soft breakdown sets in at a lower reverse voltage than the hard breakdown and shows a different reverse I-V characteristic, suggesting that here, another factor plays a role, which is very likely the presence of metallic precipitates.

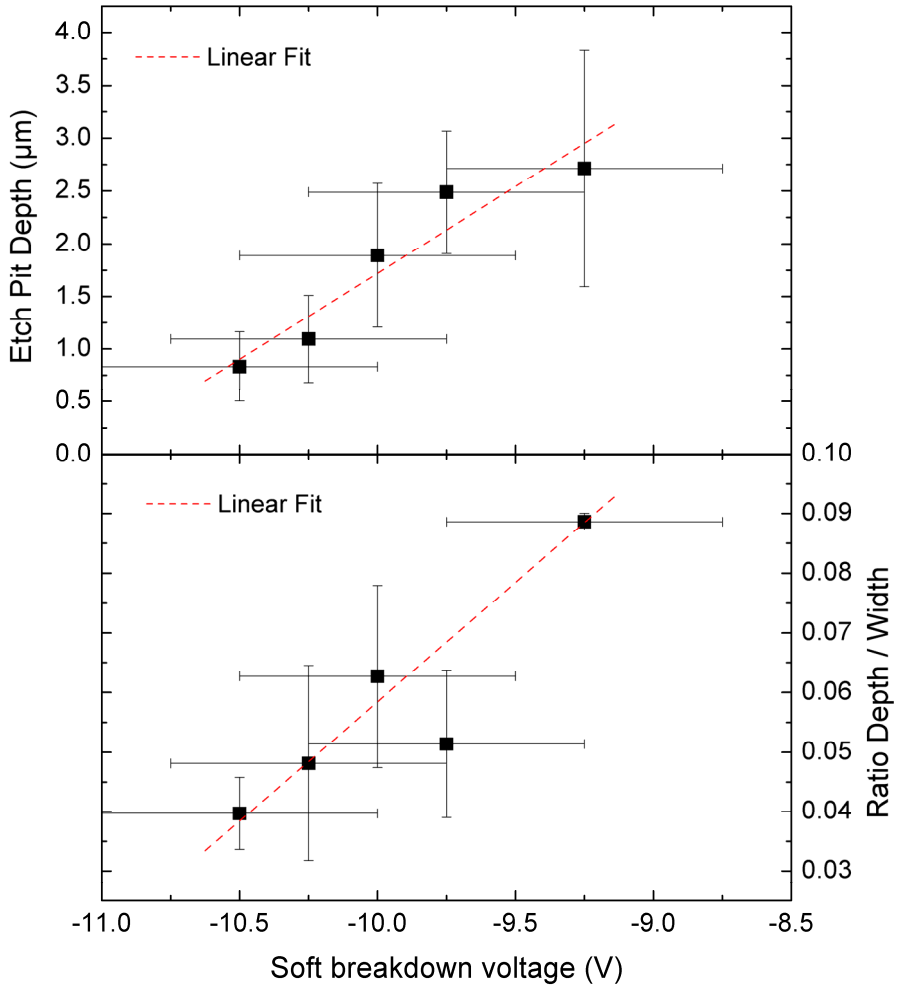

Figure 6.31: Plots of the depth of the etch pits (top) and the ratio between the depth and the width as a measure for the curvature at the tip of the etch pits (bottom) versus the local soft breakdown voltage. The red dashed lines signify linear fits to the experimental data.

6.5.7 Relation between the local soft breakdown and the global reverse I-V characteristics

The global breakdown behavior is determined by the concatenation of the behavior of all local breakdown sites. Hence in the following, the local breakdown from the very first stages of pre-breakdown up to high reverse currents (~ 10 A) is studied with the help of spatially resolved measurements taken over the full solar cell area. The aim is to be able to explain the large variety in the global reverse characteristics as described in section 6.3.1.

In *Figure 6.32* (b), the global reverse I-V characteristics of various solar cells selected from ingots Stand. 2-5 and from the UMG-Si ingot (description see *Table 6.1*) are plotted[55]. All solar cells differ in their global breakdown voltage, that is their point of maximum curvature of the reverse IV-characteristics, depending mainly on the base resistivity of the wafers. While the solar cells taken from ingots Stand. 4 and 5 do not show any early reverse current increase in the pre-breakdown regime (see *Figure 6.5*), a significant current flows through the solar cells from ingot Stand. 2 and 3 and the UMG-Si ingot before the global breakdown voltage is reached.

In the graph *Figure 6.32* (a), for comparison, the fraction of the breakdown light emitting surface is plotted versus the reverse voltage; this fraction corresponds to the percentage of the solar cell area which takes part in the breakdown process. These curves, too, can be divided into two regimes: In the beginning, at low reverse bias, the number of breakdown sites increases rather gently. This is followed by a sudden multiplication of the spots, as soon as a critical reverse voltage is reached. The critical reverse voltage of abrupt increase in BD sites of three examples is marked by the arrows. Note, that in the scale necessary to plot all curves the onset points are not as obvious as from the data values. By comparing graph (a) with the global I-V curve (b), one sees that the rapid BD site multiplication coincides with the global breakdown voltage. The correlation is obvious for the solar cells made from UMG-Si and ingots Stand. 2 and 3; it is not so good for the investigated solar cells from ingots Stand. 4 and 5.

There are two facts to be learned from this comparison: Firstly, in the beginning the total reverse current is determined by the number of breakdown sites, each carrying only a small current. Only later, the exponential behavior of the soft breakdown and hard breakdown sites (if there are any) makes its contribution to the global reverse characterstics[56].

---

[55] Measurement by E. Schäffer.

[56] Recent microscopic investigations of the bias-dependent BD light intensity of single breakdown sites by P. Gundel (Fraunhofer ISE) and by M. Schneemann (FZ Jülich) [179] suggest that the light intensity grows linearly with increasing reverse bias – contrary to the results measured via silicon CCD cameras in usual EL measurements, see Figure 6.7. The macroscopically soft behavior is explained by the close vicinity of many similar breakdown sites, each of which starts to emit light at a different reverse bias, then adding to the macroscopically observed light intensity. Note that the EL silicon CCD camera setup offers a maximal resolution in the order of 100 µm; therefore, one camera pixel may well cover dozens of individual soft breakdown sites.

If the light intensity of one BD site is in fact proportional to the local reverse current flowing through that site, then the above result translates into a linearly increasing reverse current with increasing reverse bias. This would be for example the case if the current is limited by the series resistance due to the transport of carriers toward the breakdown channel. A similar prediction was made in reference [149].

Secondly, one can see that the pre-breakdown regime in the global reverse characteristics is related to the gentle increase of the number of breakdown sites, before a rapid multiplication sets in.

The reason for the moderate amplification of the number of breakdown sites in the pre-breakdown regime is best visualized in the maps of the local breakdown voltage. As an example, the solar cell from the UMG-Si ingot (25% ingot height) is chosen; its reverse bias behavior is plotted in *Figure 6.32* (red stars).

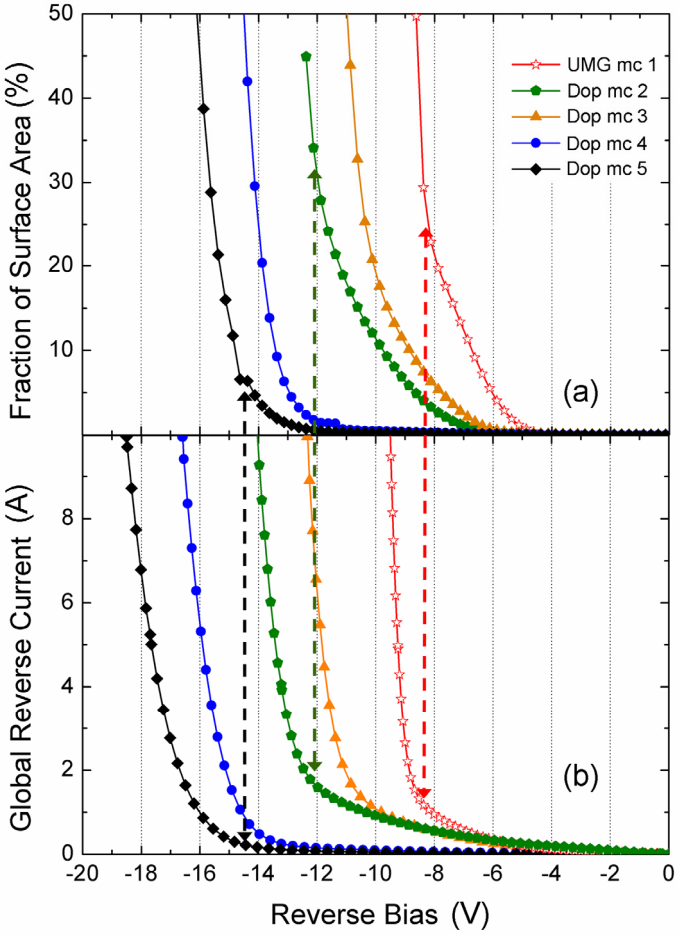

Figure 6.32: Plots of the fraction of the surface area emitting breakdown light (a) and of the global reverse current (b) versus the reverse voltage. Both graphs show measurements of the same selection of different solar cells taken from ingots "Dop mc 2-5" and from the ingot "UMG mc 1" (see Table 6.1), which illustrate the variety of the breakdown behavior. For the explanation of the arrows, please refer to the text.

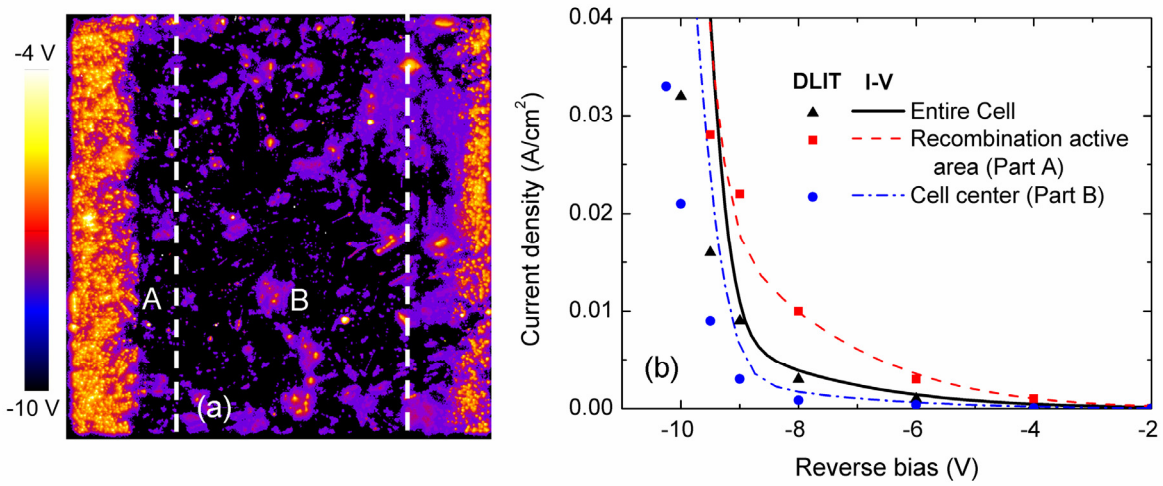

Figure 6.33: (a) Breakdown voltage map of the UMG-Si solar cell taken from 25% ingot height (compare with Figure 6.28) from ingot UMG mc 1. The measurement of the fraction of the light emitting surface area and of the global reverse I-V characteristics of this cell are plotted in Figure 6.32 ("UMG mc 1", red curves). (b) The global reverse I-V characteristics is plotted of the entire cell (black continuous curve) and, after laser cutting along the white dashed lines in (a), of the recombination active area A at the left wafer edge (red dashed curve) and of the cell center B (blue dashed and dotted curve). For comparison, reverse bias dependent DLIT measurements were performed before the cell was cut. The current density was analyzed for the entire solar cell area (black triangles), the recombination active area A (red squares) and the cell center part B (blue circles).

In *Figure 6.33* (a), the breakdown voltage map reveals several groups of breakdown sites, nevertheless all belonging to the soft BD type: At the left and right wafer edges, the local breakdown voltage is decreased as a result of the contamination due to the crucible (see also *Figure 6.28*). Also in the center of the solar cell, there are a few small regions with a lower breakdown voltage due to highly recombination active crystal defects similar to the highlighted features in *Figure 6.22*. All these regions break down between -5 to -8 V (yellow to dark orange in image (a)), which makes them responsible for the slow increase in the pre-breakdown regime.

The second set of breakdown sites appears at around -8 to -8.5V. In image (a), this voltage corresponds to the colors dark red and violet. These sites are mainly found in the solar cell center away from the wafer edges. By comparing the breakdown sites with the forward EL image, *Figure 6.28* (a) and (b), one can see that light is emitted at recombination active defects which are less pronounced. They consist of straight dark lines associated with grain boundaries. In total, there are only very few recombination active defects left which do not break down in the voltage-current range up to -10 A.

Therefore, the relation between the local soft breakdown behavior and the global reverse I-V characteristics is summarized thus: Regions of high contamination and of high recombination activity (which may be due to a certain configuration of crystal defects, especially dislocation clusters, appearing as dark "nests") result in "pre"-breakdown and induce a "soft" global breakdown behavior.

This statement in verified in *Figure 6.33* (b), in which two different bias dependent measurements are plotted. At first, the solar cell was divided into three parts, see image (a): Part A contains mostly the highly contaminated left wafer edge while part B consists of the solar cell center, in which only a few spots break down at a low reverse voltage (part C is disregarded for reasons of lucidity). DLIT measurements were performed and calibrated to current densities which are shown for the entire cell and for part A and B (symbols). Then, the reverse I-V curve of the entire cell was measured before the solar cell was cut along the dashed white lines shown in image (a). Afterwards, the I-V characteristics of parts A and B were reassessed (lines)[57]. Taking into account the different contacting methods of the sample, having different contact resistances, the DLIT and the I-V measurements are in reasonable agreement.

Through the wafer edge (part A), reverse current starts to flow already at a very low bias around -3 to -4 V. The fact that breakdown light is not detected before ca. -5 V is due to the way the detection threshold is set (see section 6.2.1). The I-V characteristics are very soft resembling IFE diodes. On the other hand, the less recombination active cell (part B) center shows a very hard breakdown behavior resembling avalanche breakdown, although breakdown still occurs at recombination active defects.

In fact, the bias-dependent reverse current of the whole, uncut cell matches exactly the sum of the reverse current flowing through the three separate parts A-C.

The analysis shown here yields direct proof that highly recombination active defects soften the I-V characteristics and are responsible for the pre-breakdown in mc-Si solar cells.

6.5.8 Theoretical considerations on the basic mechanism of soft breakdown

The physical mechanism that leads to soft breakdown at electrically active defects has not been clarified so far. A model should be able to give reasonable explanations for the following main properties of these breakdown sites, which have been compiled from the previous sections:

(i) Soft breakdown happens at tiny, individual sites located at recombination active defects.

(ii) There is strong evidence that metal-containing precipitates close to the solar cell surface are responsible.

(iii) The soft breakdown behavior is not influenced by the kind of metallic element in the metal-containing precipitates.

(iv) Statistically, the local breakdown voltage decreases with increasing impurity concentration.

(v) The local breakdown voltage decreases also with increasing base net doping concentration.

(vi) The local breakdown voltage decreases also with increasing solar cell surface roughness.

[57] Cutting by C. Harmel, IV measurements by E. Schäffer.

(vii) The soft breakdown sites emit white light with a broad and relatively smooth spectral distribution peaking at around 1.6 – 2.1 eV. These spectra strongly resemble literature data on avalanche breakdown (see *Figure 6.3*).

(viii) The local temperature coefficient (TC) has values around zero or are slightly negative [176, 180]. More detailed analyses by Kasemann even point towards a more complex behavior, showing a slightly positive TC at room temperature up to around 50°C, which turns into a negative TC at higher temperatures [175].

In literature, there have been cautious speculations about the soft breakdown mechanism. Breitenstein et al. [204], for example, proposed that charge carriers tunnel through the band gap via defect states. If, at very high local defect densities, more than one defect level exists in the band gap, then the tunneling probability should increase which could explain the lowering of the soft breakdown voltage at high impurity concentrations. This mechanism is known as "trap-assisted tunneling" [205].

Later, the same authors revised this model, taking into account the slightly negative TCs which indicate an avalanche multiplication-related breakdown process, and proposed a "trap-assisted avalanche" mechanism [180].

Bothe et al. [176] held "conducting channels extending from the solar cell base region in the p-n junction" responsible which induce defect states in or in the vicinity of the channels. Then, a "multistep field emission" process was proposed to take place. Effectively, this explanation describes the same interrelation between high electric fields under reverse bias and singular defect states within the band gap as trap-assisted tunneling or avalanche.

The idea of the trap-assisted avalanche multi-step mechanism is schematically depicted in *Figure 6.34*. For avalanche multiplication in general, free charge carriers have to be injected into the pn-junction, followed by multiplication via impact ionization. In the classic case, free carriers are generated thermally or by illumination, and after injection achieve impact ionization only if their kinetic energy reaches approx. the band gap energy. In order to sustain a continuous avalanching effect, multiplication must exceed the number of free charge carriers lost due to out-diffusion from the microplasma channel, recombination etc. [149]. If defect states are present in the band gap, charge carriers can use them as intermediate station. Since the barrier between the conduction or valence band and the defect level is relatively small, there is an appreciable probability for tunneling processes which helps to increase the free carrier concentration taking part in the multiplication process. In addition, the energy for the transition between the valence and the conduction band can be given to the carriers in two smaller portions, which decreases the kinetic energy necessary for impact ionization.

These models can well explain the findings (iii)-(vi). As discussed in section 3.2.3, most transition metals possess one or more defect levels at similar energy in the silicon band gap and thus, various metals can lead to similar soft breakdown behavior. With increasing impurity concentration, the density of defect states increases; in case their wave functions overlap, even defect bands can form, which should decrease the soft breakdown voltage. Since it has been shown that both tunneling and avalanche breakdown voltage decrease with increasing base net doping (if the base is the lower doped side), then it is reasonable to assume that the same behavior is found in a combination of both mechanisms. Surface roughnesses probably increase the electric field locally due to the

related curved doping structures, which decreases the breakdown voltage of both IFE and avalanche.

Trap-assisted avalanche may even account for the complex temperature coefficient (viii): At room temperature and slightly above, the breakdown may be limited by the supply of free carriers which take part in the multiplication. In that case, an increasing temperature could augment the supply of free carriers by narrowing the band gap, thus enhancing the tunneling probability and thermal generation of free carriers. This results in a positive TC. At higher temperatures, the beneficial effect may be overcome by the constraints imposed on the multiplication by increased phonon scattering, leading to a negative TC.

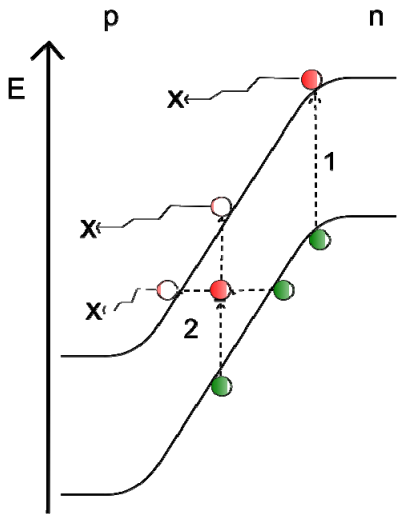

Figure 6.34: Band gap diagram of the trap-assisted avalanche multiplication. While in the classic avalanche process, carriers have to be given the whole band gap energy at once for the transition (1) e.g. of electrons from the valence into the conduction band, whence they can start the avalanche multiplication process, in the presence of one or more defect states in the band gap, the energy to be given for the transition is divided into several parts, making it a multi-step process (2). Thus, tunneling processes are possible and / or charge carriers need to gain less energy in the electric field for impact ionization.

Although several observations can be well explained, the model possesses three weaknesses: Even at high reverse voltages, it is observed that soft breakdown is restricted to individual tiny breakdown sites, all found within recombination active regions, but never covering their entire extent. In other words, soft breakdown always happens at electrically active defects but not all recombination active defects show soft breakdown. As the recombination activity – among other reasons – is mainly attributed to defect levels in the band gap, the question arises why soft breakdown occurs only at some selected spots (i).

Secondly, the broad spectral distribution of the light emitted from soft breakdown sites is very similar to spectra of light coming from avalanching silicon pn-junctions. All theoretical treatments of the emission spectra start from the premise that very high energy carriers are involved, accounting for the high energy end of the wavelength range [154]. The spectral energy maximum depends sensitively on the effective carrier temperature, which is related to the kinetic energy of the free carriers gained in the electric field. If

one assumes that due to the lower kinetic energy needed for impact ionization, the mean kinetic energy of the carriers is lower in a trap-assisted avalanche process than in a classic avalanche multiplication, one would expect a shift of the maximum spectral energy towards the long wavelength end. However, due to the uncertainty of the different contributions to the spectra, this reasoning needs further investigation.

The most important finding, the presence of metal-containing precipitates at soft breakdown sites, is inconsistent with the trap-assisted avalanche model itself. This is because metal-containing clusters behave completely differently than individual metallic impurity atoms. Within the band diagram, metal precipitates cannot be described by discrete defect levels, therefore, we come to the conclusion that the picture shown in *Figure 6.34* has to be discarded and reassessed.

As already mentioned before, as soon as the clusters of metal atoms exceed a certain size, their electric behavior changes from the recombination activity described by individual and discrete defect states towards metal-like, described by a metal-related Fermi-energy $E_{F,m}$. Then, the system of metal cluster and surrounding silicon is expressed with the Schottky contact theory [30]. We will in the following develop a model description based on such a system.

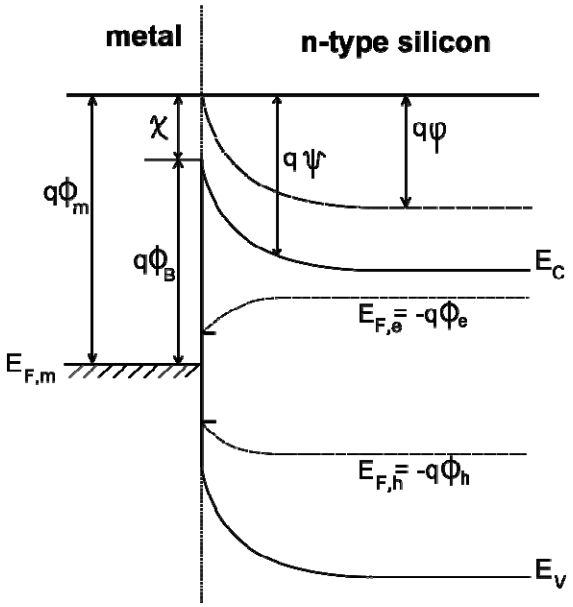

Figure 6.35: Schottky contact between metal and n-type silicon with separated quasi-Fermi levels (non-equilibrium). For explanation, see text. After ref. [206].

Due to the importance of metal-semiconductor contacts for the semiconductor industry, much work has been done on their properties, see e.g. ref. [207]. The theory is reviewed here shortly.

In *Figure 6.35*, the band diagram of an interface between the metal and silicon is shown schematically. The Schottky contact is characterized by a barrier energy $q\Phi_B$, which is the difference between the metal work function $q\Phi_m$ and the semiconductor electron affinity χ [184]. The barrier energy therefore depends on the type of metal or metal silicide, which is in contact with the silicon, and on the doping type. Most transition metal

silicides have a similar barrier height between 0.5 – 0.7 eV with n-type silicon, see *Figure 6.36*.

Without external influences, the system of metal inside the silicon reaches thermodynamic equilibrium. With regard to the band diagram that means that the Fermi-energy in the metal and in the silicon are at the same level, which implies that no net drift and diffusion currents of holes and electrons into the precipitate occur. Therefore, the silicon conduction and valence band bend according to the Schottky barrier height. As a result, while equilibrium is being reached, the precipitate charges with the charge type of the majority carriers; the carriers are distributed at the precipitate surface. On the other side of the Me / Si-interface, a mirror charge develops.

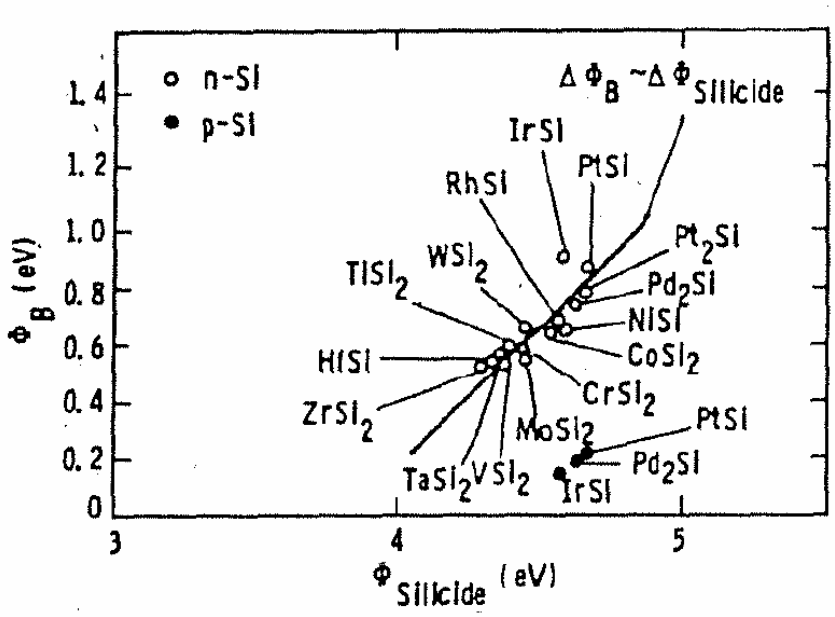

Figure 6.36: Measured barrier height Φ_B between different metal silicides and n- and p-type silicon (taken from Schroder [184]).

When an external bias V_a is applied, the thermodynamic equilibrium is disturbed. Then, the electron and hole concentrations re-distribute, in the silicon expressed by the quasi-Fermi energy levels $E_{F,e}$ and $E_{F,h}$, respectively. In addition, at the Me / Si-interface of the precipitate, a charge current flows which is described by the thermionic emission theory [207].

It is obvious that the large carrier concentrations of opposite sign in the precipitate and in its vicinity induce large electric fields. The question is whether the field strength at its maximum and the field distribution around the metal cluster could account for the observations (i)-(viii). Namely the appearance of white light in the soft breakdown sites (vii) implies that a considerable number of charge carriers flowing through the pn-junction have to be hot, meaning that they are accelerated in large electric fields.

In order to check whether the Schottky contact, which is inherent to metal precipitates in silicon, can account for these electric fields at high reverse bias, numerical simulations have been set up, following closely the approach published by Negoita et al. [206].

Negoita et al. numerically modeled the carrier recombination and generation, the respective carrier densities and potential distributions induced by the internal Schottky junction between a metal silicide precipitate and the silicon in an idealized abrupt pn-junction at low forward and reverse bias. No information on the electric field distribution was given. Since the latter depends sensitively on the static potential distribution, we refined the modeling by employing an error-function emitter diffusion profile in order to account for the pn-junction in a real solar cell.

At first, the case is considered that the precipitate is placed in the space charge region close to the solar cell surface and is relatively small compared to the space charge region width ($2r_{prec} << W$).

In this model, the 3-dimensional problem is solved in two dimensions by using the rotational symmetry in cylindrical coordinates. The geometry is outlined in *Figure 6.37*: A spherical metal precipitate is placed in the space charge region of a simple pn-junction with the axis of symmetry running through the center of the precipitate. The base doping concentration is constant in depth (with z) while the doping of the emitter follows an error function profile starting at the surface of the pn-junction. Both emitter and base are contacted by metallic contacts which are described by the Schottky barrier.

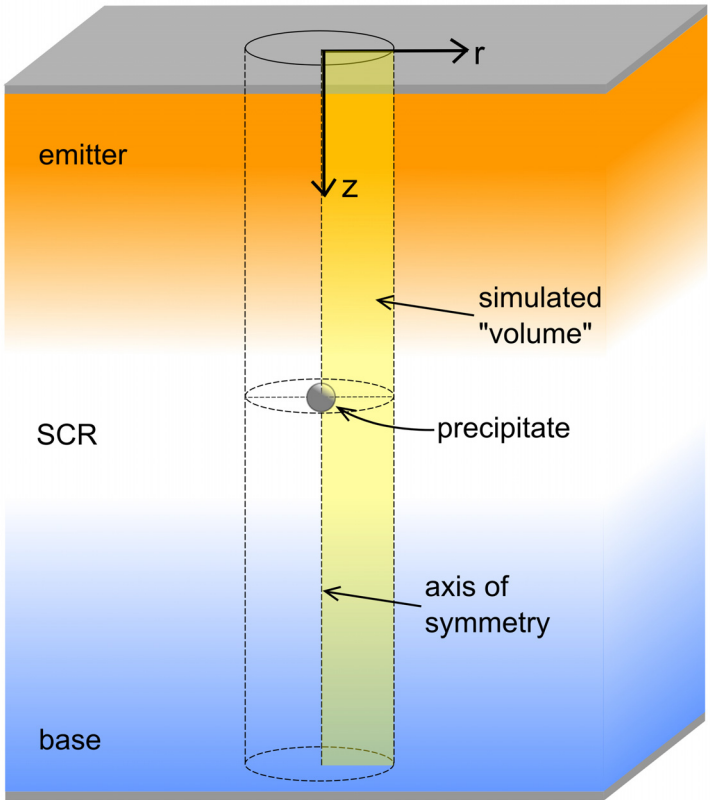

Figure 6.37: Geometry used for the simulation of the precipitate in the pn-junction.

In steady state, the semiconductor is described by the continuity equations for electrons and holes (3-29) and (3-34) with (3-27) and (3-28), by Poisson's equation (3-35) and the Boltzmann approximations for the electron and hole densities (3-4) and (3-5) introduced in chapter 3. For simulation purposes, it is advantageous to perform some variable

transformations using the quasi-Fermi potential introduced in equations (3-29) - (3-31) [206].

$$\nabla\left[\mu_e n \nabla(\Phi_e)\right] - \frac{q(n-n_0)}{\tau_e} = 0 \qquad (6\text{-}5)$$

and

$$\nabla\left[-\mu_h p \nabla(\Phi_h)\right] - \frac{q(p-p_0)}{\tau_h} = 0 \qquad (6\text{-}6)$$

are equivalent to the continuity equations (3-29) and (3-34), with μ_e and μ_h, the electron and hole mobility, respectively, Φ_e and Φ_h the electron and hole quasi-Fermi potentials (see *Figure 6.35*), n_0 and p_0 the equilibrium electron and hole concentrations, and τ_e and τ_h the electron and hole lifetime, respectively.

Poisson's equation in its usual form is used,

$$\nabla\left[\varepsilon \nabla(\Psi)\right] = -q\left(p - n + N_D^+ - N_A^-\right) \qquad (3\text{-}35),$$

with ε the silicon permittivity, Ψ the electrostatic potential and N_D^-, N_A^+ describe the ionized donor and acceptor concentrations, respectively. In this notation, the electron and hole concentrations are written

$$n = n_i \exp\left(\frac{\Psi - \Phi_e}{V_t}\right) \qquad (6\text{-}7)$$

and

$$p = n_i \exp\left(\frac{\Phi_h - \Psi}{V_t}\right) \qquad (6\text{-}8).$$

Here, n_i is the intrinsic carrier concentration and $V_t = k_B T/q$.

Then, the simulation has to determine the three equivalent unknown potentials Φ_e, Φ_h and Ψ, from which all other important parameters – especially the carrier concentrations and the electric field distribution – can be calculated.

According to the thermionic emission theory [207], the metal precipitate is simply described at the Me / Si-interface by the electron and hole flux densities $\left(\vec{j}_e \cdot \vec{s}\right)$ and $\left(\vec{j}_h \cdot \vec{s}\right)$ ($\vec{s}$ stands for the surface normal pointing towards the precipitate), respectively, flowing into the precipitate, coupled with the potential at the precipitate surface. The electron and hole flux densities are given by [206, 207]

$$\vec{j}_e \cdot \vec{s} = \frac{J_{e,sat}}{q}\left\{\exp\left(\frac{-q\Phi_e - E_{F,m}}{k_B T}\right) - 1\right\} \qquad (6\text{-}9),$$

$$\vec{j}_h \cdot \vec{s} = \frac{J_{h,sat}}{q}\left\{\exp\left(\frac{E_{F,m} + q\Phi_h}{k_B T}\right) - 1\right\} \qquad (6\text{-}10)$$

with

$$J_{e,sat} = A_e^* T^2 \exp\left(\frac{-\Phi_B}{V_t}\right) \quad (6\text{-}11),$$

$$J_{h,sat} = A_h^* T^2 \exp\left(-\frac{qE_G - \Phi_B}{V_t}\right) \quad (6\text{-}12).$$

A_e^* and A_h^* stand for the effective electron and hole Richardson constants [207] and E_G denotes the band gap energy.

At the surface of the precipitate, the potential Ψ_S is locally constant. It can be calculated for the case of steady state conditions, which means that the charge in the precipitate does not change any further. Then, the same net electron and hole fluxes have to enter the precipitate (otherwise, the charge distribution would still change and the steady state would not have been reached):

$$\vec{j}_e \cdot \vec{s} = \vec{j}_h \cdot \vec{s} \quad (6\text{-}13).$$

Further, with the help of *Figure 6.35*, the exponents in equations (6-9), and (6-10) can be replaced by the unknown potentials Φ_e, Φ_h and Ψ used in the simulation:

$$\left(-q\Phi_e - E_{F,m}\right)_{\text{int}} = q\Phi_B - \left(q\Psi_S + q\Phi_e\right)_{\text{int}} \quad (6\text{-}14),$$

$$\left(E_{F,m} + q\Phi_h\right)_{\text{int}} = -q\Phi_B + \left(q\Psi_S + q\Phi_h\right)_{\text{int}} \quad (6\text{-}15).$$

With equation (6-13)., making use of (6-9), - (6-12). and (6-14), - (6-15)., the boundary conditions at the Me / Si-interface at the precipitate in steady state can be deduced:

$$\Psi_S = V_t \ln\left\{\frac{J_{e,sat} - J_{h,sat} + \sqrt{\left(J_{e,sat} - J_{h,sat}\right)^2 + 4J_{e,sat}J_{h,sat}\exp\left[\frac{\Phi_h - \Phi_e}{V_t}\right]}}{2J_{e,sat}\frac{n_i}{N_C}\exp\left[\frac{\Phi_B - \Phi_e}{V_t}\right]}\right\} \quad (6\text{-}16)$$

and

$$\vec{j}_e \cdot \vec{s} = \vec{j}_h \cdot \vec{s} = \frac{J_{e,sat}}{q}\left\{\frac{n_i}{N_C}\exp\left[\frac{\Psi_S + \Phi_B - \Phi_e}{V_t}\right] - 1\right\} \quad (6\text{-}17).$$

Last, the metal contacts at the front and the rear of the solar cell have to be implemented to which the external bias V_a is applied. At the p-type back contact, the boundary conditions

$$\Psi_{p-cont.}^{V_a} = \Phi_B - V_t \ln\left(\frac{N_A^-}{n_i}\right) \quad (6\text{-}18)$$

and

$$\Phi_e = \Phi_h = \Phi_B \tag{6-19}$$

are valid, while the n-type front contact is expressed by the equations

$$\Psi_{n-cont.}^{V_a} = \Phi_B - V_a + V_t \ln\left(\frac{N_D^+}{n_i}\right) \tag{6-20}$$

and

$$\Phi_e = \Phi_h = \Phi_B - V_a \tag{6-21}.$$

In this description, the assumption is made that all dopants are ionized which is reasonable at room temperature [31].

Note that the model does not take charge carrier multiplication into account. Therefore, as soon as the critical field strength for avalanching is reached, it is not valid any more as additional processes have to be taken into consideration. However, it is very useful to estimate the order of magnitude of the electric field strength in order to assess whether avalanching may become possible at all at increased reverse biases.

Table 6.2: Parameters used in a first set of simulations.

Parameter	Abbrev.	Value
Temperature	T	300 K
Base doping concentration (p-type)	N_A	4.5 x 10^{15} at./cm^3
Emitter doping concentration (n-type)	N_D	$1e20 * \mathrm{erfc}\left(z/2\sqrt{1e(-13) * 3600}\right)$ at./cm^3
Schottky barrier height between metal and Si (here FeSi)	Φ_B	0.68 eV
Precipitate radius	r_{prec}	20 nm
Position of the precipitate relative to the solar cell surface (z=0 µm)	z_{prec}	1 µm
Minority carrier lifetime	τ_e, τ_h	1.0 x 10^{-8} s
Electron mobility in the emitter and base, respectively	μ_e	1260 / 1310 cm^2/Vs
Hole mobility in the emitter and base, respectively	μ_h	430 / 450 cm^2/Vs
Thickness of the solar cell	d	20 µm
Richardson constant for electrons	A_e^*	118 A/cm^{2}K^2
Richardson constant for holes	A_h^*	59 A/cm^{2}K^2

The parameters used in a first set of simulations are summarized in *Table 6.2*. As a modeling metal, iron silicide (FeSi) was taken which has a Schottky barrier height of 0.68 eV in n-type silicon [206, 208]. As the barrier height of most metal silicides is in a similar range (*Figure 6.36*), this choice describes the general behavior of metal precipitates very well.

With a given set of parameters, the simulation starts at $V_a = 0\text{V}$ external bias. The outcome of this simulation is fed into the solver and a small external reverse bias is applied. Once a solution is reached, the result is taken as initial condition for the next calculation, applying a slightly higher reverse bias. This procedure is repeated until the interesting reverse voltage is attained.

The reason for this iterating method is that the success of the numerical calculations depends sensitively on the initial conditions. In order to obtain stable solutions in the present implementation of the model, the iteration steps have to be very small, in this case in the order of 0.1 V. Unfortunately, calculations of the variables in the interesting reverse voltage range (for soft breakdown up to around -8 V) would take a very long time.

Since it was not possible in the frame of this thesis to perform the numerical analysis up to the interesting reverse voltage range, in a first attempt, the electric field distribution in the pn-junction was calculated with and without the precipitate at low reverse biases up to -2 V. Thus, it was possible to assess the quality of the approach and to estimate the influence of the precipitate on the electric field distribution.

In *Figure 6.38*, the simulated potential distribution from the solar cell surface into the base along the axis of symmetry – which at the same time is the axis along the center of the spherical precipitate – is shown with and without the precipitate. For comparison, the dashed line indicates the emitter doping profile $N_D(z)$. The potential drop across the pn-junction is the built-in voltage $V_{bi} = \Psi_{n-cont.}^{V_a=0V} - \Psi_{p-cont.}^{V_a=0V} = V_t \ln\left(N_A^- N_D^+ / n_i^2\right) \approx 0.95\text{V}$.

The precipitate is positioned approximately at the beginning of the space charge region on the emitter side. In order to meet the boundary requirements (6-16) and (6-17), the potential distribution is strongly bent towards the surface potential at the precipitate surface, which is in the order of the Schottky barrier height slightly modulated by the thermionic emission currents.

The strong potential gradients induce large electric fields, which are plotted in *Figure 6.39* versus the solar cell depth. While the undisturbed pn-junction without precipitate shows the characteristic triangular electric field distribution in the space charge region [30] with a maximum electric field at the "metallurgical junction" [32] in the order of 20 kV/cm, in this configuration, the precipitate is responsible for electric fields as large as $3\text{x}10^5$ V/cm at the very close vicinity to the Me / Si-interface.

With increasing reverse bias, the absolute values of the maximum of the electric field of an undisturbed one-sided abrupt junction should increase approximately as [30]

$$\left|\vec{E}_m\right| = \sqrt{\frac{2q}{\varepsilon}\left(V_{bi} - V_a\right)N_{\min}} \qquad (6\text{-}22).$$

Our simulated values of the maximum electric field in the space charge region of the undisturbed pn-junction without the precipitate are compared to the values predicted by eq.

(6-23) in *Figure 6.40*. The numerical simulations predict the same order of magnitude and the same overall reverse bias dependence as the analytical expression. With the parameter set taken for this study, a breakdown voltage around -88 V would be expected (maximum electric field around 3.5×10^5 V/cm according to eq. (6-2)), see *Figure 6.41*. However, in the voltage range used for the simulation, the calculated values are about 30% lower than the expected values.

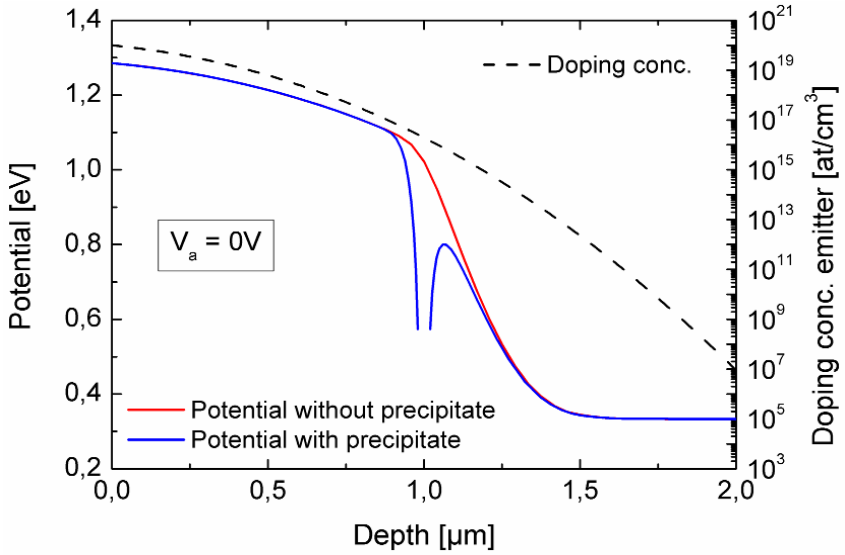

Figure 6.38: Simulated potential distribution along the axis of symmetry (= the center of the precipitate) at 0 V applied bias without (red curve) and with (blue curve) precipitate. The emitter doping profile, starting from the solar cell front surface (z=0 µm), is marked by the dashed line. The simulation parameters are summarized in Table 6.2.

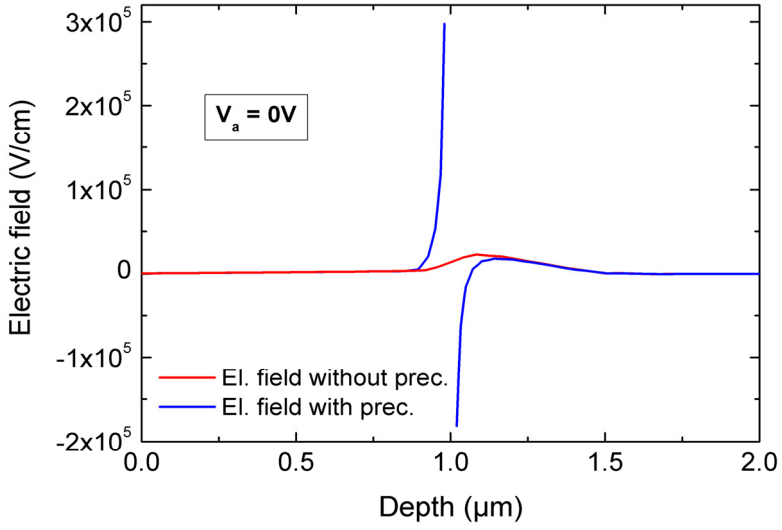

Figure 6.39: Simulated electric field along the axis of symmetry (= the center of the precipitate) at 0 V applied bias without (red curve) and with (blue curve) precipitate. The simulation parameters are summarized in Table 6.2.

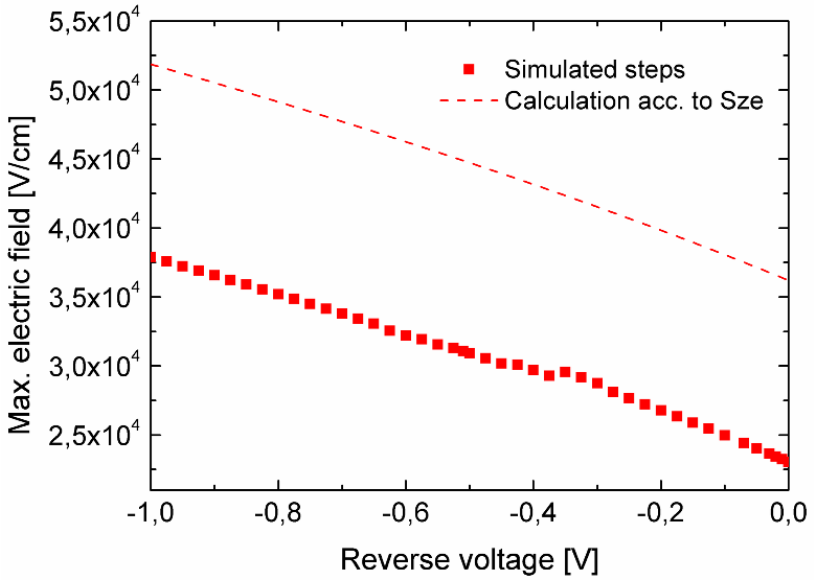

Figure 6.40: Simulated maximum electric field at the metallurgical junction in the undisturbed pn-junction without precipitate (red squares). The absolute value increases with increasing reverse bias. However, the absolute value is lower than the expected values for one-sided abrupt junctions according to equation (6-22).

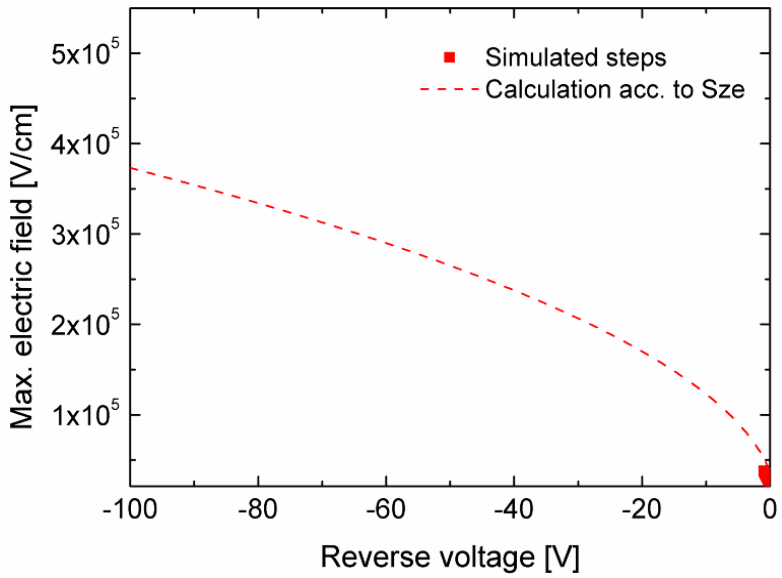

Figure 6.41: Calculated increase of the absolute maximum of the electric field. The critical breakdown field of $3.5x10^5$ V/cm is expected to be reached at around -88 V.

This can be explained by the different doping profiles: While the emitter implemented in the numerical calculations resembles more a diffused profile, eq. (6-22) considers the case of a one-sided abrupt profile. In fact, there are indications in literature [209] that the maximum electric field in real diffused pn-junctions is lower in this voltage range than suggested by the analytical expression.

Therefore, the numerical simulations are able to show the correct tendency of the reverse voltage-dependent electric field distributions. This should allow for an assessment of the role of metal precipitates in the soft breakdown mechanism.

If a metal silicide precipitate is close to the space charge region, the electric field vectors, shown in *Figure 6.42*, always point towards the precipitate surface because it is located in the emitter section of the space charge region and the metal cluster is charged with the majority carriers. Therefore, when free carriers are generated close to the precipitate interface, the electrons are accelerated away from the precipitate. The strongest electric field is found on the emitter side along the axis of symmetry.

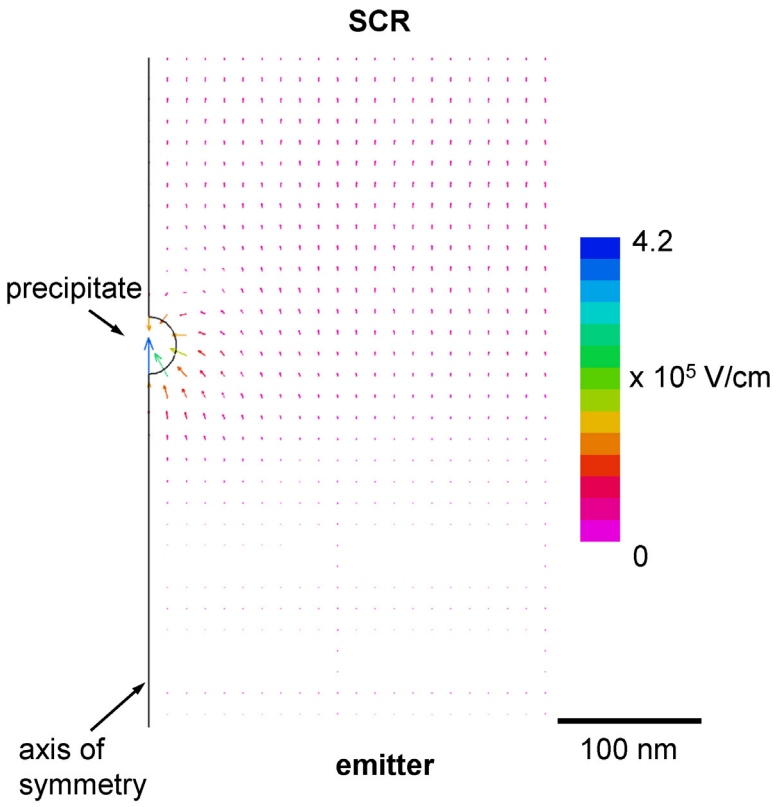

Figure 6.42: Simulated electric field vectors around the precipitate at -2.5 V reverse bias.

Even at no applied reverse bias, the simulated maximum electric field at the precipitate / silicon interface is already in the expected field strength range for avalanche breakdown (compare to *Figure 6.2*). Similar to the maximum electric field in the simple case without precipitate, the electric field strength increases slowly with increasing reverse bias, see *Figure 6.43*. With the parameter set implemented in the simulation, the critical field strength would already be reached between -0.5 to -1.0 V.

It can be stated that metal silicide precipitates can induce very large electric fields in the critical field strength range observed for both avalanche breakdown or IFE even at very low reverse bias. However, breakdown light – indicating hot electrons within the silicon – is emitted (depending on base doping and impurity concentration) at minimum reverse voltages above approx. -2 V (*Figure 6.26* for the case of high base doping and impurity conc.). Therefore, the observed local breakdown voltages are slightly higher than one would expect from the numerical results of the maximum electrical field strength in the case of avalanche.

There are several arguments that could account for the discrepancies between the expected breakdown voltage based on the numerical calculations of the maximum field strength and the observed values:

Firstly, one has to keep in mind that in the numerical simulations, the number of variations which could be investigated were limited due to the needed expense of time. Therefore, only highly idealized configurations were calculated, disregarding the fact that uncertainties are introduced e.g. by the shape of real metal precipitates which probably always deviates from the perfect spherical form.

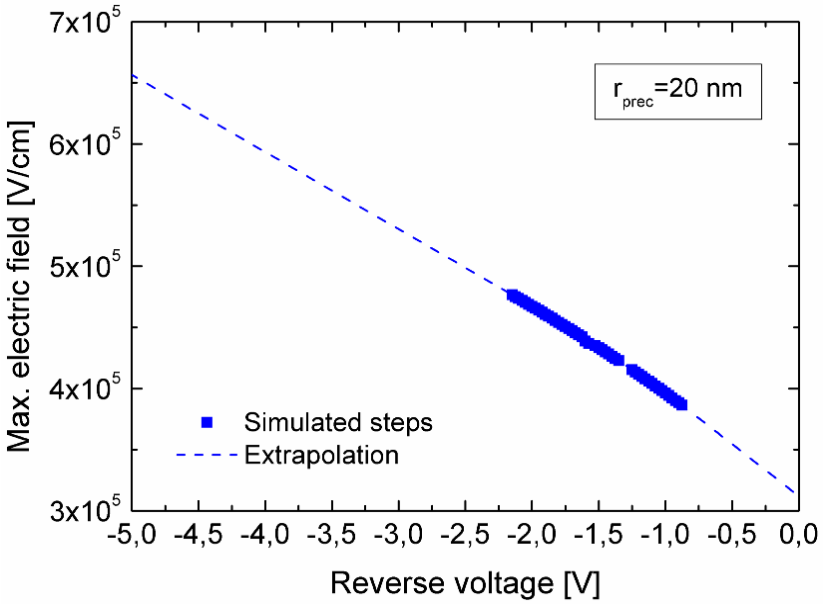

Figure 6.43: Simulated maximum electric field in the presence of a precipitate (blue squares). The maximum is found at the emitter-side of the Me / Si-interface on the axis of symmetry. The absolute value increases with increasing reverse bias.

Secondly, let us assume that avalanche breakdown is indeed initiated on the high-field side by the maximum electrical field strength of a perfectly spherical metal silicide in an otherwise undisturbed pn-junction. The estimations of the critical field strength discussed in [209, 210] are a result of observations and theoretical considerations made on simple, defect-free pn-junctions. For these samples, the microscopic processes leading to stable avalanche breakdown were discussed by Marinov et al. [149]. They argued that, for the stabilization of the local avalanche breakdown within the microplasma channel, relatively complex conditions must be fulfilled. Basically, the carrier multiplication along the microplasma channel must be large enough in order to compensate for losses due to recombination and scattering as well as carrier out-diffusion from the breakdown region (see also section 6.1.1).

The carrier multiplication – the ratio between free charge carriers leaving the avalanche region and the free carriers entering it – depends strongly on the length of the microplasma in which the electric field allows for impact ionization. Therefore, besides the maximum electric field, the electric field distribution along the microplasma channel (i.e. with depth) is of importance.

In the presence of a precipitate, it is fair to assume that the critical field strength needs to be revised. This is because, as the numerical simulation reveals, the electric field is large only in a very thin layer around the precipitate (see *Figure 6.39*). For example with the chosen parameter set (*Table 6.2*), at -2.5 V reverse bias the electric field strength exceeds $1x10^5$ V/cm only in a 20 nm thick layer around the metal silicide cluster. It grows only slowly with increasing reverse bias.

Unfortunately, literature offers only little data on the requirements for sustaining avalanche breakdown besides the maximum electric field or the breakdown voltage depending on doping concentration. Especially the combination of the length of the electric field along the microplasma tube exceeding a certain strength is unknown. Warner [209] published approximations of the average field along the total space charge region width at breakdown. For a depletion layer thickness of 80 nm, he predicts that an average field of ca. $9x10^5$ V/cm is necessary to sustain avalanche breakdown. For larger electric field strengths, in simple pn-junctions tunneling processes start to play a role.

In spite of the scarcity of data, it is clear that the silicon volume in which the breakdown conditions are met is comparatively small. This should shift the critical electric field towards higher values, which could account for our observations.

In addition, the presence of the precipitate itself in the space charge region affects the carrier transport directly and indirectly by inducing stress [120] and by creating crystal defects such as point defects and dislocations [107]. Therefore, scattering events as well as recombination take place more often than in undisturbed pn-junctions, decreasing the mean free path of the charge carriers. Thus, the breakdown voltage should be higher than expected from literature data of critical electric field strengths. The assessment of scattering and charge carrier loss due to the presence of the precipitate was beyond the scope of this study.

As soon as breakdown sets in, the charge carriers and thus the electric fields redistribute [140, 149], modifying the electric field around the precipitate, which could also contribute to the breakdown voltage increase.

Further, it is possible that breakdown is mostly due to tunneling events known as field emission or thermionic field emission by majority carriers from the metal silicide through the Schottky junction into the surrounding silicon [207]. Note that this is not the same process as trap-assisted tunneling. The probability of field emission processes increases with decreasing depletion region width of the internal Schottky junction. Our first numerical simulations suggest that the depletion region width, although usually very small, depends sensitively on the emitter doping profile and the position of the metal precipitate with regard to the pn-junction. However, due to the complexity of the simulations, this could not be investigated further.

In any case, if an IFE process initiates the breakdown, then it must be accompanied by avalanche multiplication because white light is observed coming from hot carriers in silicon.

To summarize, the numerical calculations indicate that metal silicide precipitates are able to induce large electric fields which could initiate breakdown by avalanche multiplication alone or in combination with field emission processes. Thus, observations (i) – (iii) can immediately be explained.

As described in observation (v), the soft breakdown voltage depends on the net doping concentration of the lower doped side, in this case the wafer base. At a first glance, one could be led to think that this is because with a higher doping concentration, the electric field in the space charge region increases. Since the large precipitate-induced electric field depends strongly on the precipitate position in the space charge region and only marginally on the base doping concentration, our simulations cannot explain the experimental results directly. However, Marinov [149] showed that the main influence of the lower doped side of the pn-junction consists in limiting the carrier flow coming towards or leaving the microplasma conducting channel, depending on the charge type. Since the avalanching is only stable when the carrier distributions and thus the electric field vectors are favorable, in steady state, the current density through the impact ionization region must exactly equal the current density flowing through the diffusion region on the lower doped side, which is expressed in eq. (6-3). Therefore, the base doping concentration has a large impact on the local breakdown voltage independent from the actual breakdown cause.

In observation (iv), it was stated that obviously the local soft breakdown voltage decreases with increasing impurity concentration.

Regarding precipitates, higher impurity concentrations in the silicon have two main effects: The number of precipitates is multiplied and the mean precipitate radius increases. While the former is expected to have only an influence on the number and distribution of soft breakdown sites and not on the local breakdown voltage, it is well possible that the latter has an influence on the soft breakdown behavior.

In order to check whether the thermionic emission model is able to explain this observation, the same parameter set, displayed in *Table 6.2*, was used while the precipitate radius r_{prec} was varied between 5 nm and 50 nm. The results are shown for the case of -1 V reverse bias in *Figure 6.44* and *Figure 6.45*. Note that the position of the center of the precipitate with regard to the space charge region was not changed.

The size of the precipitate has several effects, which are linked to each other via the potential Ψ_s at the silicide / silicon interface. The surface potential changes as a result mainly from the difference between the Schottky barrier height and the electron Fermi potential $\left(\Phi_B - \Phi_e\right)$ in the denominator of eq. (6-16) due to the position of the Me / Si interface within the pn-junction. With the present parameters, the surface potential decreases with increasing precipitate radius.

The gradient of the electrostatic field around the precipitate changes together with the surface potential. This leads to large differences in the electric field distribution: While the field strength around the small precipitate (5 nm) is almost twice as high as the electric field around the large precipitate (50 nm), large electric fields are found farther away from the biggest cluster than from the small precipitate. For example, absolute values of the electric field of $>1\text{x}10^5$ V/cm extend into a ca. 10 nm thick layer around the 5 nm precipitate; into a 20 nm thick layer around the 20 nm precipitate; but into a 40 nm thick layer around the largest metal cluster.

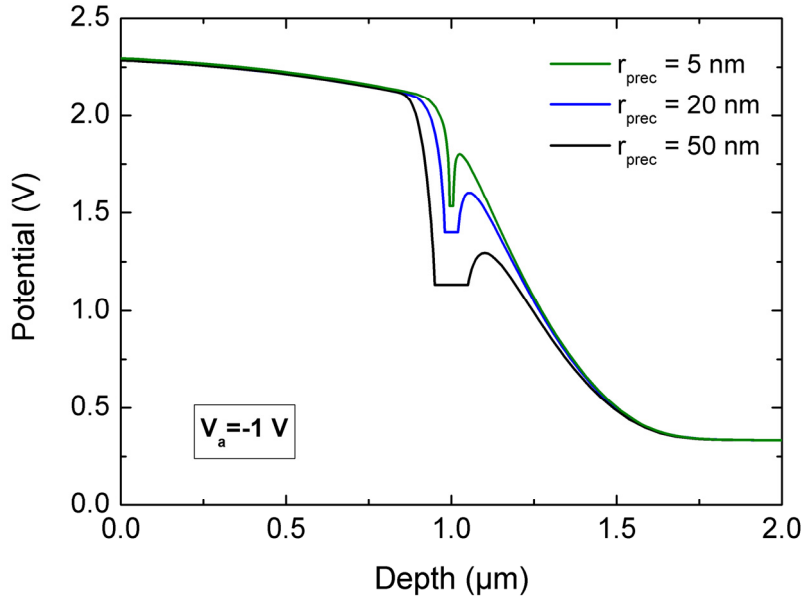

Figure 6.44: Simulated potential distribution along the axis of symmetry; the precipitate radius was varied between 5 and 50 nm.

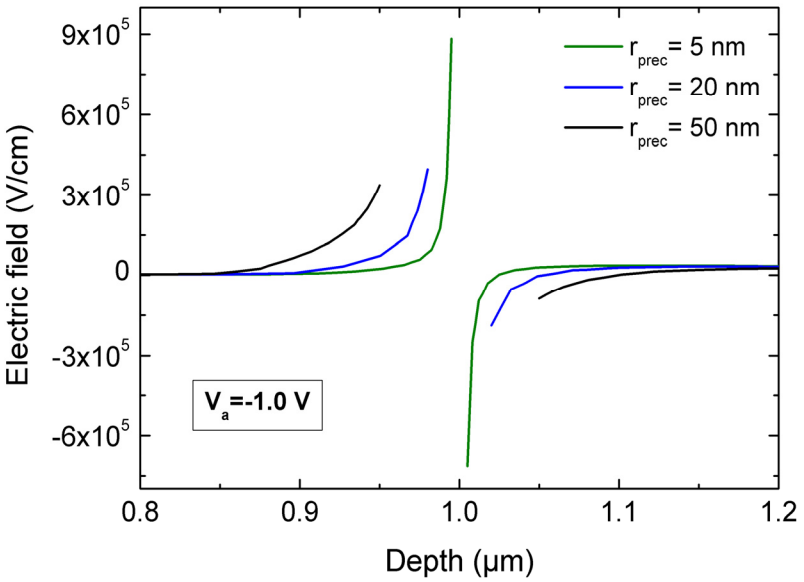

Figure 6.45: Simulated electric field along the axis of symmetry; the precipitate radius was varied between 5 and 50 nm.

Following the argumentation that the carrier multiplication is proportional to the length of the microplasma channel, lower local breakdown voltages in the presence of higher impurity concentrations can therefore be explained by the fact that the volume of high electric fields is larger around larger precipitates, thus sooner meeting the requirements for stable breakdown.

However, with increasing size of the precipitate, i.e. with $2r_{prec} \rightarrow W$, the situation changes, because the precipitate crosses the space charge region width and "sees" both sides of the pn-junction. Lal et al. [139] discussed this case based on a linear or planar defect with dimensions larger than the SCR width, pinning the Fermi level along the de-

fect line, which is for example a precipitate when no external bias is applied. As a result, two Schottky junctions evolve – one in the emitter and one in the base. In steady state, the defect charges at both ends with the respective majority carriers (analogous to small precipitates that charge only with one majority carrier type) and forms a dipole, inducing large electric fields in its vicinity. In this picture, avalanche breakdown can occur either at one end of the precipitate similar to the case of small precipitates discussed above or along the precipitates bridging the SCR if the superposition of the dipole-induced electric field and the field resulting from the pn-junction is high enough for charge carrier multiplication.

In order to compare Lal's model with our simulations, first calculations of very large precipitates crossing the space charge region confirm that the precipitate charges with both kinds of majority carriers at either end of the precipitate. While the electric field vectors point towards the precipitate in the emitter, they now point outwards from the precipitate surface in the solar cell base. The largest electric fields again occur along the axis of symmetry at the points on the precipitate surface reaching farthest into the emitter or the base, respectively. In our simulations, however, the electric dipole does not induce a large electric field along the precipitate within the space charge region.

6.6 Breakdown type III: Hard breakdown due to surface morphology

On mc-Si solar cells, hard breakdown sets in after the early (type I) and soft (type II) breakdown. Analogous to the latter, hard breakdown occurs in many individual, small sites, which can reach a high density in a few areas on the solar cell. Since the current increase with increasing reverse bias is large due to the hard characteristics, the heat generation multiplies fast within a small reverse voltage difference. In combination, the hard I-V curve and the concentration of hard BD sites within small areas make this breakdown type dangerous for solar modules.

A typical example for type III breakdown regions is shown in *Figure 6.46*. This sample was taken from a hard breakdown area, mechanically polished and Secco-etched in order to reveal the crystallographic defects[58].

In hard breakdown regions, a high density of dislocations is found which appear along line-shaped crystal defects that are not recombination active. The line defects run along two preferential directions, shown in *Figure 6.46* (a). The lines are not grain boundaries, which was checked with the help of Electron Back-Scatter Diffraction (EBSD) in an SEM.

As Bauer et al. [211] demonstrated, sometimes the acidic texturization used for mc-Si wafers in standard industrial solar cell processes preferentially etches the dislocations within the observed line-shaped crystal defects similar to the Secco etch. In a next step, the emitter is formed during the phosphorus diffusion step. The emitter follows the textured wafer surface closely. In the tip of the etch pits, the emitter therefore exhibits a strong curvature, leading to the electrostatic tip effect, which enhances the electric field in the space charge region strongly [30]. In fact, Bauer showed that the detected local

[58] Polish by G. Räuber, Secco-etch by M. Kwiatkowska.

breakdown voltage of hard breakdown regions and the curvature observed in TEM measurements of the bottom of the etch pits fit to the expected avalanche breakdown voltage decrease due to the surface morphology published by Sze [30].

In TC-DLIT measurements, Breitenstein et al. [180] consistently showed that the local temperature coefficient of type III breakdown regions is strongly negative. This clearly indicates that the physical mechanism leading to hard breakdown in mc-Si solar cells is the classic avalanche breakdown.

TEM investigations of crystallographic defects revealed that the line defects consist of twin lamellas into which dislocations are incorporated split into two partials with a stacking fault in between. In addition, the dislocations are probably highly decorated by carbon impurities [180].

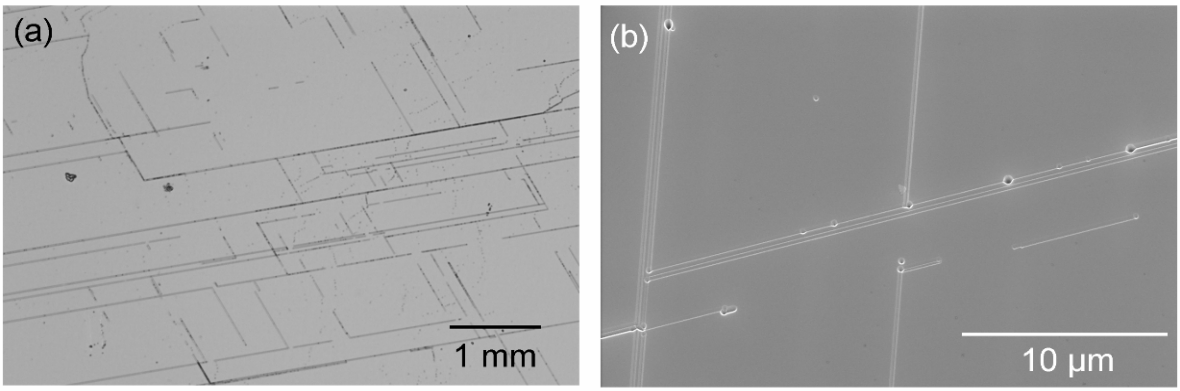

Figure 6.46: (a) Optical microscope image of a representative area where hard breakdown occurs. (b) SEM close-up from the same area, showing the etch pits at dislocations within the line-shaped crystal defects.

6.7 Assessment of the dangerousness of the different breakdown types for the use of mc-Si solar cells in PV solar panels

As mentioned previously, the danger of hot spot development does not result from the global reverse current flowing at a critical reverse bias which can occur within a cell string, but from a high current density, which may come from the confinement of breakdown to a small cell area. Since the properties of the three breakdown types differ, the likeliness that one of them could be responsible for hot spots depends on the breakdown mechanism.

Here, this likeliness – an important information for the solar cell industry – is discussed based on the experiences made during the studies of diode breakdown in mc-Si solar cells. However, stringent tests validating this upshot are still lacking.

I) Early breakdown

While in general, type II and type III breakdown are detected in clusters dispersed over the entire cell area, type I breakdown demonstrates highly localized light emission and heat development, making it potentially dangerous for solar modules. It is likely to occur

in every module because it sets on at very low reverse bias which means that only a few solar cells within a string are needed to generate the necessary breakdown voltage. According to our DLIT measurements, the heat which is developed within the breakdown spots in most cases remains relatively low in the voltage range up to -15 V and therefore it is most often harmless.

However, sometimes (in an estimated 5% of all solar cells) the heat development is large and resembles the power dissipation produced by highly localized shunts although light emission indicates early breakdown. An example is displayed in *Figure 6.47*. The DLIT measurements were performed on a solar cell taken from 75% ingot height from ingot Stand. 3 (see *Table 6.1*) and calibrated to yield the current density. The early breakdown site marked by the white circle is also seen in the reverse EL images; it is therefore clearly a type I breakdown site. Nevertheless, the local power dissipation (*Figure 6.47* (b)) and thus the heat generation in reverse bias are quite large and exceeds that of all other breakdown sites.

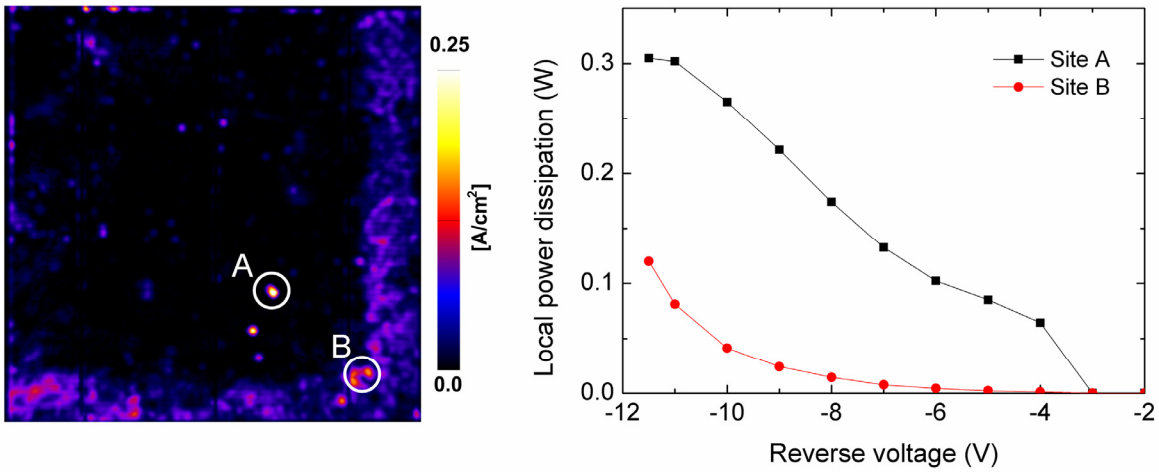

Figure 6.47: Current density image at -11.5 V reverse bias of a standard industrial solar cell. At the bottom and right edge, the wafer is influenced by impurities due to the crucible. The hottest spot on the solar cell is found in site A, which is an early breakdown site. The local power dissipation is plotted versus the reverse voltage in the right graph (black squares). For comparison, the power dissipation through the electrically most active soft breakdown site B is also shown (red circles).

II) Soft breakdown

Breakdown of type II, being related to recombination active defects, is found in all mc-Si solar cells. The local as well as the global breakdown voltage of this type depend strongly on the impurity concentration in the wafer and on the base resistivity. Soft breakdown can set on at voltages as low as -2 V in the extreme case and thus is easily provoked by the voltages produced in a cell string.

The soft reverse characteristic and the spreading of the type II pre-breakdown sites over a large part of the cell area, however, limit the local current density even at relatively high reverse bias. In our experiments, the local power dissipated in soft breakdown sites never exceeded a critical value. Therefore, we expect that the local heat generation due

to this breakdown type probably stays always below the critical threshold within the voltage-current range produced in a standard module.

III) Hard breakdown

Avalanche breakdown (type III) shows a hard I-V characteristic which soon governs the global current-voltage curve (see section 6.3.2). DLIT measurements indicate that this pre-breakdown type leads to large heat development within a small voltage range. In addition, the etched dislocations are often found in clusters. At their centers, high temperatures can occur because lateral heat transport due to the temperature gradient basically takes place only at the edges of the clusters.

The necessary high voltages depend on the surface morphology and the base resistivity; in standard industrial solar cells, type III breakdown starts at around -13 to -14 V. If each solar cell produces about 0.5 V at its maximum power point, then it takes around 25 cells within a cell string to generate the necessary high voltage to initiate hard breakdown. Therefore, it is expected that this breakdown type happens in solar modules only in extreme cases. However, if it occurs then it poses a serious threat to the cell encapsulation.

7 Summary

This thesis considers the use of alternative silicon materials for photovoltaics – often termed "upgraded metallurgical grade" silicon – from different angles and evaluates the risks and implications for the wafer and solar cell properties at selected steps along the entire process chain.

The properties of the alternative, upgraded metallurgical grade silicon materials analyzed in the course of this thesis were governed by the simultaneous presence of boron and phosphorus in high concentrations (in the order of $>2x10^{16}$ at/cm^3) which has fundamental consequences for the base resistivity, the carrier mobility and the light-induced degradation in UMG-Si wafers.

Aiming to compare the experimental data to existing models, the majority carrier conductivity and Hall mobility of UMG-Si and intentionally compensated wafers doped with various B- and P-concentrations was investigated. In compensated silicon, the mobility decreases significantly firstly with growing sum of both dopants (N_A+N_D), hence with increasing density of ionized scattering centers, and secondly with decreasing net doping concentration p_0=(N_A-N_D), attributed to a weakening of the Coulombic screening of ionized atoms. Our measurements suggest that in the commonly accepted model for compensated silicon published by Klaassen, the modified Coulombic screening is not correctly implemented. Hence, Klaassen's model can currently be used safely only in a limited range of N_A- and N_D-values when regarding compensated silicon (e.g. UMG-Si).

A thorough investigation of the light-induced degradation in compensated and UMG Cz-silicon wafers revealed that in general the normalized Cz-defect concentration is a function of the compensation ratio R_C, which surprisingly holds for p- as well as for n-type material. For the special case of UMG-Si wafers with p-type net doping concentrations usually used for solar cells, the Cz-defect density can alternatively be described by a linear dependence on the net doping concentration, supporting results obtained by other groups. Therefore, for oxygen-rich UMG-Si the net doping concentration of the feedstock should be reduced in order to minimize the light-induced degradation. This can only be realized by simultaneously decreasing the B- and P-concentration.

Although the concentration of transition metals in UMG-Si is not as high as previously expected, it has been worthwhile to test the feasibility of the concept of "defect engineering" via intrinsic gettering and co-precipitation (intentional addition of e.g. Cu to the melt). It was shown that an interaction between the total transition metal content in the melt and the crystallization process has a negative impact on the silicon crystal quality, the harmfulness depending on the impurity elements. Moreover, in carefully prepared NAA measurements the total metal concentration was observed to depend (super-) linearly on the dislocation density. Both observations point towards a non-linear crystal defect generation process being started if the metal content in the melt exceeds a critical level, prohibiting the exploitation of co-precipitation.

The optimal design of temperature ramps aimed at intrinsic gettering was demonstrated to depend on the metal species: While intermediate diffusers (Fe, Cr,…) re-precipitate at 600 °C after a high-temperature step (>800 C), the same temperature ramp leads to the dissolution of the large clusters of fast diffusers (Ni,…) being present after mc-Si solidification. Subsequently, the fast diffusers spread along grain boundaries and disloca-

tions, thus presenting a larger recombination active effective surface than before. Our experiments indicate that for intrinsic gettering of fast diffusers like Ni, lower temperatures (around 500°C-550°C) and longer gettering times (12 h) are necessary.

However, in NAA measurements the fast diffusers Ni and Cu, and to some extent also Co, were seen to be easily gettered during P-emitter diffusion even at high initial concentrations from highly dislocated wafer regions. At the same time, P-diffusion gettering of the intermediate diffusers Fe or Cr from high dislocation density areas is not effective, allowing for a significant reduction only in less defected crystal regions.

These results implicate that the interplay of extrinsic and intrinsic gettering can be aimed at and optimized for the specific group of intermediate diffusers, since fast diffusers are externally gettered while slow diffusers cannot be mobilized in the interesting temperature and time scale.

Reports on inferior reverse characteristics of UMG mc-Si solar cells, possibly posing a danger to the solar modules by generating "hot spots", incited detailed investigations of the diode breakdown behavior of mc-Si solar cells in general. In this thesis, it was shown that in these devices breakdown happens in three stages termed "early", "soft" and "hard" breakdown which can be clearly distinguished by their breakdown voltage and reverse I-V characteristics resulting from (at least) three different physical reasons.

All three breakdown types have in common that white light is emitted from the breakdown sites, pointing at the occurrence of "hot" electrons. It can be concluded that electron multiplication due to avalanching is always involved in a way, possibly initiated by tunneling processes at the beginning.

"Early breakdown" sets on at around -4 to -5 V and is presumably induced by surface defects including paste particles from the front as well as from the rear side metallization and small pits in the surface structure. Early breakdown can be explained by a modification of the emitter leading to a local increase of the electric field in the space charge region. Since early breakdown is highly localized and starts at very low reverse voltages, the local heat generation can become large, possibly being harmful to solar modules. However, in most practical cases the heat remains relatively low.

The "soft breakdown" happens exclusively at recombination active crystal defects. XRF-measurements at soft breakdown sites provided strong evidence that it is caused by metal precipitates close to the solar cell surface, i.e. close to or in the space charge region. The onset voltage is influenced by several factors: Both a high impurity concentration and a high base net doping concentration decrease the soft breakdown voltage, as does deep etching of dislocations and grain boundaries during the wet chemical texturization. Depending on the solar cell properties, the onset voltage of soft breakdown can therefore vary between -8 to -14 V. Due to the wide lateral distribution of recombination active defects and the soft reverse I-V characteristics, it is expected that soft breakdown does not pose any danger to solar modules.

To explain the physical mechanism of soft diode breakdown found at the sites of metallic precipitates, a numerical simulation describing the internal Schottky junction between silicide clusters with the surrounding silicon was set up. Under reverse bias in thermodynamic equilibrium, the electric fields around the metal clusters can reach very large val-

ues (>5x10^5 V/cm) which are generally assumed to lead to avalanche electron multiplication.

The “hard breakdown” sets on around -14 to -16 V, happening at deeply etched dislocations at which no recombination active impurities have accumulated. Due to fast increase of the reverse current with increasing reverse voltage, this breakdown type can be detrimental if the necessary high reverse voltage is reached.

Having clarified the physical mechanisms of diode breakdown in mc-Si solar cells in general, the relatively high net doping concentration in the base of UMG-Si solar cells was identified to be the main reason for the large reverse currents at low breakdown voltages. Since thus, the UMG-Si reverse bias behavior can be attributed to the soft breakdown type, we expect that the risk of including UMG-Si solar cells in solar modules is not larger compared to modules consisting of conventional mc-Si cells.

In summary, important properties of UMG-Si wafers (low conductivity mobility and minority carrier lifetime, high Cz-defect concentration as well as relatively high reverse currents) are related to the high concentration of boron and phosphorus. Hence, by further reducing their amount in the silicon feedstock, which is currently being done already quite successfully by several feedstock producers, upgraded metallurgical grade silicon is expected to constitute an interesting, cost-effective alternative to conventional material at present and in the near future. However, as optimizations of the solar cell processes have been yielding significantly increasing efficiencies, in the long term, the fate of UMG-Si will depend firstly on its ability to keep up with future process developments, and secondly on the future trend of silicon feedstock prices.

Bibliography

[1] *Stern Review on the Economics of Climate Change*, Review published by "Government of the United Kingdom", 2006 (URL: http://webarchive.nationalarchives.gov.uk/+/http://www.hm-treasury.gov.uk/stern_review_report.htm, link from 04.10.2010)

[2] *Fourth Assessment Report, AR4*, Report published by "Intergovernmental Panel on Climate Change, IPCC", 2007 (URL: http://www.ipcc.ch/publications_and_data/publications_ipcc_fourth_assessment_report_synthesis_report.htm, link from 04.10.2010)

[3] *Erneuerbare Energien in Zahlen - nationale und internationale Entwicklung*, Brochure published by "Bundesministerium für Umwelt, Naturschutz und Reaktorsicherheit", 2010 (URL: http://www.erneuerbare-energien.de/inhalt/2720/35338/, link from 04.10.2010)

[4] G. del Coso, C. del Canizo, et al., *The impact of silicon feedstock on the PV module cost*, Solar Energy Materials & Solar Cells **94**, 345 (2010).

[5] G. del Coso, C. del Canizo, et al., *Influence of feedstock on c-Si module cost*, in Proceedings of the 24th European Photovoltaic Solar Energy Conference, Hamburg, Germany, (2009),

[6] T. Buonassisi, A. A. Istratov, et al., *Engineering metal-impurity nanodefects for low-cost solar cells*, Nature Materials: Letters **4**, 676 (2005).

[7] M. J. de Wild-Scholten, R. Gløckner, et al., *LCA comparison of the Elkem solar metallurgical route and conventional gas routes to solar silicon*, in Proceedings of the 23rd European Photovoltaic Energy Conference, Valencia, Spain, (2008),

[8] A. Luque and S. S. Hegedus, *Handbook of photovoltaic science and engineering*. (John Wiley & Sons Ltd., Chichester, West Sussex, England, 2004).

[9] W. C. O'Mara, R. B. Herring, et al., *Handbook of semiconductor silicon technology*. (Noyes, New Jersey, 1990).

[10] J. Bauer, O. Breitenstein, et al., *Electronic activity of SiC precipitates in multicrystalline solar silicon*, Physica Status Solidi A **204** (7), 2190 (2007).

[11] A. F. B. Braga, S. P. Moreira, et al., *New processes for the production of solar-grade polycrystalline silicon: A review*, Solar Energy Materials and Solar Cells **92** (4), 418 (2007).

[12] D. Lynch, *Winning the global race for solar silicon*, JOM **61** (11), 41 (2009).

[13] N. Yuge, M. Abe, et al., *Purification of metallurgical-grade silicon up to solar grade*, Progress in Photovoltaics: Research and Applications **9** (3), 203 (2001).

[14] G. Halvorsen, *Method for production of pure silicon*, U.S. Patent No. 4539194 (1985).

[15] C. Alemany, C. Trassy, et al., *Refining of metallurgical-grade silicon by inductive plasma*, Solar Energy Materials and Solar Cells **72** (1-4), 41 (2002).

[16] J. C. S. Pires, J. Otubo, et al., *The purification of metallurgical grade silicon by electron beam melting*, Journal of Materials Processing Technology **169** (1), 16 (2005).

[17] H. C. Theuerer, *Removal of boron from silicon by hydrogen water vapor treatment*, J. Metals **8**, 1316 (1956).

[18] E. Enebakk, M. G. Tranell, et al., *A calcium-based slag for treatment of molten silicon*, Patent No. WO/2003/097528 (2003).

[19] H. Aasen, *Elkem Solar - status and future outlook*, in Proceedings of the 6th Solar Silicon Conference, Munich, Germany, (2008),

[20] J. M. Kim and Y. K. Kim, *Growth and characterization of 240 kg multicrystalline silicon ingot grown by directional solidification*, Solar Energy Materials and Solar Cells **81** (2), 217 (2004).

[21] K. Kaneko, *Silicon electromagnetic casting apparatus and method for operating said apparatus*, Patent No. WO/2007/020706 (2007).

[22] K. Kaneko, K. Nakagawa, et al., *Recent status on electromagnetic casting*, in Proceedings of the 16th Workshop on Crystalline Silicon Solar Cells & Modules: Materials and Processes, Denver, CO, USA, (2006), page 2.

[23] R. Hull, *Properties of crystalline silicon*. (INSPEC, The Institution of Electrical Engineers, London, UK, 1999).

[24] J. A. Burton, R. C. Prim, et al., *The distribution of solute in crystals grown from the melt*, Journal of Chemical Physics **21**, 1987 (1953).

[25] R. H. Hopkins, J. R. Davis, et al., *Fifth quarterly report, ERDA/JPL (USA)*, no. 954331/77 (1976).

[26] D. Macdonald, A. Cuevas, et al., *Transition-metal profiles in a multicrystalline silicon ingot*, Journal of Applied Physics **97**, 33523 (2005).

[27] R. Kvande, L. J. Geerligs, et al., *Distribution of iron in multicrystalline silicon ingots*, Journal of Applied Physics **104** (6), 064905 (2008).

[28] G. Coletti, P. C. P. Bronsveld, et al., *Impact of iron, nickel and chromium in feedstock on multicrystalline silicon solar cell properties*, in Proceedings of the 19th Workshop on Crystalline Silicon Solar Cells & Modules: Materials and Processes, Vail, CO, USA, (2009),

[29] R. A. Smith, *Semiconductors*, 2nd edition ed. (Cambridge University Press, Cambridge, 1978).

[30] S. M. Sze, *Physics of Semiconductor Devices*, 2nd ed. (John Wiley & Sons, New York, 1981).

[31] P. Würfel, *Physics of Solar Cells - From principles to new concepts*. (Wiley-Vch Verlag GmbH & Co KgaA, Weinheim, 2005).

[32] M. A. Green, *Solar cells: operating principles, technology and system applications*. (The University of New South Wales, Kensington, 1998).

[33] J. Singh, *Physics of semiconductors and their heterostructures*. (McGraw-Hill, Inc., 1993).

[34] K. Graff, *Metal Impurities in Silicon-Device Fabrication*, 2nd ed. (Springer, Berlin, 2000).

[35] S. Rein, *Lifetime spectroscopy: a method of defect characterization in silicon for photovoltaic applications*. (Springer, Berlin, 2005).

[36] S. M. Sze and J. C. Irvin, *Resistivity, mobility and impurity levels in GaAs, Ge, and Si at 300°K*, Solid State Electronics **11**, 599 (1968).

[37] J. R. Davis, Jr., A. Rohatgi, et al., *Impurities in silicon solar cells*, IEEE Transactions on Electron Devices **ED-27** (4), 677 (1980).

[38] M. Blazek, *Quantitative Bestimmung des Getterverhaltens von Übergangsmetallen im Solarzellenprozess*, Diploma thesis, University of Freiburg, 2009.

[39] A. Hangleiter and R. Häcker, *Enhancement of band-to-band Auger recombination by electron-hole correlations*, Physical Review Letters **65** (2), 215 (1990).

[40] D. K. Schroder, *Semiconductor Material and Device Characterization*. (John Wiley & Sons, New York, 1990).

[41] K. Peter, R. Kopecek, et al., *Analysis of multicrystalline solar cells from solar grade silicon feedstock*, in Proceedings of the Proceedings of the 31st IEEE Photovoltaic Specialists Conference, Orlando, Florida, USA, (2005), page 927.

[42] A. Halm, J. Jourdan, et al., *Large area industrial solar cells on low cost 100% mc-SoG Si substrates: efficiencies exceeding 16%*, in Proceedings of the 35th IEEE Photovoltaic Specialists Conference, Honolulu, HI, USA, (2010),

[43] K. Peter, R. Kopecek, et al., *Multicrystalline solar grade silicon solar cells*, in Proceedings of the 35th IEEE Photovoltaic Specialists Conference, Honolulu, HI, USA, (2010),

[44] D. Kohler, D. Kiliani, et al., *Comparison of UMG materials: Are ingot height independent solar cell efficiencies possible?*, in Proceedings of the 25th European Photovoltaic Solar Energy Conference, Valencia, Spain, (2010),

[45] J. Junge, J. Ebser, et al., *Evaluating the efficiency limits of low cost mc-Si materials using advanced solar cell processes*, in Proceedings of the 25th European Photovoltaic Solar Energy Conference, Valencia, Spain, (2010),

[46] V. Hoffmann, K. Petter, et al., *First results on industrialization of Elkem solar silicon at Pillar JSC and Q-Cells*, in Proceedings of the 23rd European Photovoltaic Solar Energy Conference, Valencia, Spain, (2008), page 1117.

[47] K. Petter, Y. Ludwig, et al., *Latest results on production of solar cells using UMG-Si feedstock*, in Proceedings of the 25th European Photovoltaic Solar Energy Conference, Valencia, Spain, (2010),

[48] A. Buonassisi, M. Heuer, et al., *Internal gettering by metal alloy clusters*, U.S. Patent No. 2006/0289091 (2006).

[49] A. Cuevas, *The paradox of compensated silicon*, in Proceedings of the IUMRS-ICEM Conference on Optoelectronic and Microelectronic Materials and Devices, Sydney, Australia, (2008),

[50] D. Macdonald, F. Rougieux, et al., *Light-induced boron-oxygen defect generation in compensated p-type czochralski silicon*, Journal of Applied Physics **105** (9), 093704 (2009).

[51] B. Lim, A. Liu, et al., *Impact of dopant compensation on the deactivation of boron-oxygen recombination centers in crystalline silicon*, Applied Physics Letters **95**, 232109 (2009).

[52] S. Dubois, N. Enjalbert, et al., *Slow down of the light-induced degradation in compensated solar-grade multicrystalline silicon*, Applied Physics Letters **93** (10), 103510 (2008).

[53] B. Lim, M. Wolf, et al., *Carrier mobilities in multicrystalline silicon wafers made from UMG-Si*, Physica Status Solidi A, submitted (2010).

[54] J. Geilker, *Cz-Silicium aus kompensiertem umg-Feedstock: Materialeigenschaften, Eignung für die Solarzellenfertigung und Möglichkeiten der Qualitätskontrolle*, Diploma thesis, University of Freiburg, Germany, 2010.

[55] Z. B. Alfassi, *Instrumental multi-element chemical analysis*. (Kluwer Academic Publishers, Dordrecht, the Netherlands, 1998).

[56] A. A. Istratov, T. Buonassisi, et al., *Control of metal impurities in "dirty" multicrystalline silicon for solar cells*, Materials Science and Engineering B **134**, 282 (2006).

[57] S. Rein, W. Kwapil, et al., *Impact of compensated solar-grade silicon on Czochralski silicon wafers and solar cells*, in Proceedings of the 24th European Photovoltaic Solar Energy Conference, Hamburg, Germany, (2009), page 1140.

[58] M. Spitz, U. Belledin, et al., *Fast inductive inline measurement of the emitter sheet resistance in industrial solar cell fabrication*, in Proceedings of the 22nd European Photovoltaic Solar Energy Conference, Milan, Italy, (2007), page 47.

[59] D. Macdonald, A. Cuevas, et al., *Measuring dopant concentrations in compensated p-type crystalline silicon via iron-acceptor pairing*, Applied Physics Letters **92**, 202119 (2008).

[60] J. Geilker, W. Kwapil, et al., *Doping concentration and mobility in compensated material: comparison of different determination methods*, in Proceedings of the 25th European Photovoltaic Solar Energy Conference, Valencia, Spain, (2010),

[61] P. A. J. Schumann and R. P. Phillips, *Comparison of classical approximations to free carrier absorption in semiconductors*, Solid-State Electronics **10**, 943 (1967).

[62] P. A. Schumann, Jr., W. A. Keenan, et al., *Silicon optical constants in the infrared*, Journal of the Electrochemical Society: Solid State Science **118** (1), 145 (1971).

[63] J. Isenberg, *Neue Infrarotmesstechniken der Photovoltaik*, Dissertation, University of Universität Konstanz, 2003.

[64] D. M. Caughey and R. E. Thomas, *Carrier mobilities in silicon empirically related to doping and field*, Proceedings of the IEEE **55** (12), 2192 (1967).

[65] J. Isenberg and W. Warta, *Free carrier absorption in heavily doped silicon layers*, Applied Physics Letters **84** (13), 2265 (2004).

[66] E. Enebakk, A. K. Soiland, et al., *Dopant specification of compensated silicon for solar cells of equal efficiency and yield as standard solar cells*, in Proceedings of the 3rd International Workshop on Crystalline Silicon Solar Cells, Trondheim, Norway, (2009),

[67] C. Bucher, D. L. Meier, et al., *Method for utilizing heavily doped silicon feedstock to produce substrates for photovoltaic applications by dopant compensation during crystal growth*, Patent No. WO/2008/112598 (2008).

[68] J. Kraiem, R. Einhaus, et al., *Doping engineering as a method to increase the performance of purified MG silicon during ingot crystallisation*, in Proceedings of the 34th IEEE Photovoltaic Specialists Conference, Philadelphia, PA, USA, (2009),

[69] A. Cuevas, J. Tan, et al., *Method to control the resistivity of silicon ingots*, (2009).

[70] K. Arafune, *Control of resistivity variation in polycrystalline silicon ingots by multiple doping*, in Proceedings of the 19th Workshop on Crystalline Silicon Solar Cells & Modules: Materials and Processes, Vail, CO, USA, (2009), page 70.

[71] W. R. Thurber, R. L. Mattis, et al., *Resistivity-dopant density relationship for boron-doped silicon*, Journal of the Electrochemical Society **127** (10), 2291 (1980).

[72] D. B. M. Klaassen, *A unified mobility model for device simulation. I. Model equations and concentration dependence*, Solid-State Electronics **35** (7), 953 (1992).

[73] D. Macdonald and A. Cuevas, *Carrier recombination and transport in compensated silicon, and prospects for "compensation engineering"*, in Proceedings of the 19th Workshop on Crystalline Silicon Solar Cells & Modules: Materials and Processes, Vail, CO, USA, (2009),

[74] F. E. Rougieux, D. Macdonald, et al., *Electron and hole mobility reduction and Hall factor in phosphorus-compensated p-type silicon*, Journal of Applied Physics **108** (1), 013706 (2010).

[75] J. Veirman, S. Dubois, et al., *Hall mobility reduction in single-crystalline silicon gradually compensated by thermal donors activation*, Solid-State Electronics **54**, 671 (2010).

[76] H. Brooks, in *Advances in Electronics and Electron Physics*, edited by L. Martin. (Academic Press Inc., New York, 1955).

[77] E. Conwell and V. F. Weisskopf, *Theory of impurity scattering in semiconductors*, Physical Review **77** (3), 388 (1950).

[78] J. F. Lin, S. S. Li, et al., *Theoretical analysis of hall factor and Hall mobility in p-type silicon*, Solid-State Electronics **24** (9), 827 (1981).

[79] A. B. Sproul, M. A. Green, et al., *Accurate determination of minority carrier- and lattice scattering-mobility in silicon from photoconductance decay*, Journal of Applied Physics **72** (9), 4161 (1992).

[80] R. A. Sinton and A. Cuevas, *Contactless determination of current-voltage characteristics and minority-carrier lifetimes in semiconductors from quasi-steady-state photoconductance data*, Applied Physics Letters **69** (17), 2510 (1996).

[81] T. Trupke, R. A. Bardos, et al., *Photoluminescence imaging of silicon wafers*, Applied Physics Letters **89** (4), 44107 (2006).

[82] H. Nagel, C. Berge, et al., *Generalized analysis of quasi-steady-state and quasi-transient measurements of carrier lifetimes in semiconductors*, Journal of Applied Physics **86** (11), 6218 (1999).

[83] F. Dannhäuser, J. Krausse, et al., *Zum Einfluss von Temperaturprozessen auf Widerstandsschwankungen in Siliziumeinkristallen (The influence of heat treatment on the resistivity profile of silicon single crystals -I)*, Solid-State Electronics **15** (12), 1383 (1972).

[84] J. Krausse, *Die Abhängigkeit der Trägerbeweglichkeit in Silizium von der Konzentration der freien Ladungsträger - II (The dependence of carrier mobility in Si of the concentration of free charge carriers -II)*, Solid-State Electronics **15**, 1377 (1972).

[85] M. Schubert, *Detektion von infraroter Strahlung zur Beurteilung der Materialqualität von Solar-Silizium*, PhD thesis, University of Konstanz, 2008.

[86] S. W. Glunz, S. Rein, et al., *On the degradation of Cz-silicon solar cells*, in Proceedings of the Proceedings of the 2nd World Conference on Photovoltaic Energy Conversion, Vienna, Austria, (1998), page 1343.

[87] S. W. Glunz, S. Rein, et al., *Comparison of boron- and gallium-doped p-type Czochralski silicon for photovoltaic application*, Progress in Photovoltaics: Research and Applications **7** (6), 463 (1999).

[88] S. Rein, P. Lichtner, et al., *Advanced lifetime spectroscopy: Unambiguous determination of the electronic properties of the metastable defect in boron-doped Cz-Si*, in Proceedings of the Proceedings of the 3rd World Conference on Photovoltaic Energy Conversion, Osaka, Japan, (2003), page 1057.

[89] K. Bothe, J. Schmidt, et al., *Comprehensive analysis of the impact of boron and oxygen on the metastable defect in CZ silicon*, in Proceedings of the Proceedings of the 3rd World Conference on Photovoltaic Energy Conversion, Osaka, Japan, (2003), page 1077.

[90] S. Rein, S. Diez, et al., *Quantitative correlation of the metastable defect in Cz-silicon with different impurities*, in Proceedings of the Proceedings of the 3rd World Conference on Photovoltaic Energy Conversion, Osaka, Japan, (2003), page 1048.

[91] J. Schmidt and K. Bothe, *Structure and transformation of the metastable boron- and oxygen-related defect center in crystalline silicon*, Physical Review B (Condensed Matter) **69**, 0241071 (2004).

[92] V. V. Voronkov and R. Falster, *Latent compexes of interstitial boron and oxygen dimers as a reason for degradation of silicon-based solar cells*, Journal of Applied Physics **107**, 053509 (2010).

[93] H. Fischer and W. Pschunder, *Investigation of photon and thermal induced changes in silicon solar cells*, in Proceedings of the Proceedings of the 10th IEEE Photovoltaic Specialists Conference, Palo Alto, California, USA, (1973), page 404.

[94] B. Lim, S. Hermann, et al., *Permanent deactivation of the boron-oxygen recombination center in silicon solar cells*, in Proceedings of the Proceedings of the 23rd European Photovoltaic Solar Energy Conference, Valencia, Spain, (2008), page 1018.

[95] A. Herguth, G. Schubert, et al., *A new approach to prevent the negative impact of the metastable defect in boron doped cz silicon solar cells*, in Proceedings of the Proceedings of the 4th World Conference on Photovoltaic Energy Conversion, Waikoloa, Hawaii, USA, (2006), page 940.

[96] A. Herguth, G. Schubert, et al., *Avoiding boron-oxygen related degradation in highly boron doped cz silicon*, in Proceedings of the Proceedings of the 21st European Photovoltaic Solar Energy Conference, Dresden, Germany, (2006), page 530.

[97] T. Schutz-Kuchly, J. Veirman, et al., *Light-induced-degradation effects in boron-phosphorous compensated n-type czochralski silicon*, Applied Physics Letters **96**, 1 (2010).

[98] J. Geilker, W. Kwapil, et al., *Light-induced degradation in compensated p- and n-type Czochralski silicon wafers*, Journal of Applied Physics, under review (2010).

[99] J. Libal, S. Novaglia, et al., *Effect of compensation and metallic impurities on the electrical properties of Cz-grown solar grade silicon*, Journal of Applied Physics **104**, 1045071 (2008).

[100]D. Macdonald, A. Liu, et al., *Boron-oxygen defects in compensated p-type czochralski silicon*, in Proceedings of the Proceedings of the 24th European Photovoltaic Solar Energy Conference, Hamburg, Germany, (2009), page 877.

[101]A. K. Soiland (personal communication), (2010).

[102]J. R. Davis, A. Rohatgi, et al., *Characterization of the effects of metallic impurities on silicon solar cell performance*, Proceedings of the 13th IEEE Photovoltaic Specialists Conference, 490 (1978).

[103]T. Buonassisi, M. A. Marcus, et al., *Analysis of copper-rich precipitates in silicon: Chemical state, gettering, and impact on multicrystalline silicon solar cell material*, Journal of Applied Physics **97** (063503), 1 (2005).

[104]M. Heuer, T. Buonassisi, et al., *Complex intermetallic phase in multicrystalline silicon doped with transition metals*, Physical Review B **73** (235204), 1 (2006).

[105]M. Heuer, T. Buonassisi, et al., *Transition metal interaction and Ni-Fe-Cu-Si phases in silicon*, Journal of Applied Physics **101** (12), 123510 (2007).

[106]C. Rudolf, P. Saring, et al., *Co-precipitation of copper and nickel in crystalline silicon*, Materials Science and Engineering B **159-160**, 365 (2009).

[107]M. Seibt, R. Khalil, et al., *Electronic states at dislocations and metal silicide precipitates in crystalline silicon and their role in solar cell materials*, Applied Physics A (Materials Science Processing) **96** (1), 235 (2009).

[108]T. Buonassisi, M. Heuer, et al., *Transition metal co-precipitation mechanisms in silicon*, Acta Materialia **55**, 6119 (2007).

[109]A. Haarahiltunen, H. Väinölä, et al., *Modeling of heterogeneous precipitation of iron in silicon*, Applied Physics Letters **87** (151908), 151908/1 (2005).

[110]R. H. Hopkins, R. G. Seidensticker, et al., *Crystal growth considerations in the use of "solar grade" silicon*, Journal of Crystal Growth **42**, 493 (1977).

[111]T. F. Ciszek, T. H. Wang, et al., *Properties of iron-doped multicrystalline silicon grown by the float-zone technique*, in Proceedings of the IEEE Photovoltaic Specialists Conference, Washington, D.C., USA, (1996), page 737.

[112]M. Gasaparini and F. Rota, *Crystal growth techniques and segregation effects in solar grade silicon*, Materials Chemistry and Physics **9** (1-3), 79 (1983).

[113]G. Coletti, R. Kvande, et al., *Effect of iron in silicon feedstock on p- and n-type multicrystalline silicon solar cells*, Journal of Applied Physics **104** (10), 104913 (2008).

[114]T. Fuyuki, H. Kondo, et al., *Photographic surveying of minority carrier diffusion length in polycrystalline silicon solar cells by electroluminescence*, Applied Physics Letters **86** (26), 262108 (2005).

[115]J. Bauer (personal communication), (2010).

[116]J. Schön, H. Habenicht, et al., *Simulation of Fe distribution after crystallization of multicrystalline silicon*, Solid State Phenomena **156-158**, 223 (2010).

[117]J. Bailey, S. A. McHugo, et al., *Efficiency-limiting defects in silicon solar cell material*, Journal of Electronic Materials **25** (9), 1417 (1996).

[118]S. A. McHugo, H. Hieslmair, et al., *Gettering of metallic impurities in photovoltaic silicon*, Applied Physics A (Materials Science Processing) **A64** (2), 127 (1997).

[119]D. Macdonald, A. Cuevas, et al., *Response to phosphorus gettering of different regions of cast multicrystalline silicon ingots*, Solid State Electronics **43** (3), 575 (1999).

[120]P. Gundel, M. C. Schubert, et al., *Simultaneous stress and defect luminescence study on silicon*, Physica Status Solidi A **207** (2), 436 (2009).

[121]W. Seifert, O. F. Vyvenko, et al., *Synchrotron microscopy and spectroscopy for analysis of crystal defects in silicon*, Physica Status Solidi C **6** (3), 765 (2009).

[122]S. Riepe, I. Reis, et al., *Research on efficiency limiting defects and defect engineering in Si solar cells - results of the German research cluster SolarFocus*, Physica Status Solidi, to be published (2010).

[123]J. Haunschild, M. Glatthaar, et al., *Quality control of as-cut multicrystalline silicon wafers using photoluminescence imaging for solar cell production*, Solar Energy Materials & Solar Cells, in print (2010).

[124]S. A. McHugo, A. Mohammed, et al., *Copper precipitates in silicon: precipitation, dissolution, and chemical state*, Journal of Applied Physics **91** (10), 6396 (2002).

[125]T. Buonassisi, A. A. Istratov, et al., *Impact of metal silicide precipitate dissolution during rapid thermal processing of multicrystalline silicon solar cells*, Applied Physics Letters **87** (121918), 121918 (2005).

[126]M. D. Pickett and T. Buonassisi, *Iron point defect reduction in multicrystalline silicon solar cells*, Applied Physics Letters **92** (122103) (2008).

[127]M. Rinio, A. Yodyunyong, et al., *Improvement of multicrystalline silicon solar cells by a low temperature anneal after emitter diffusion*, Progress in Photovoltaics: Research and Applications, DOI: 10.002/pip.1002 (2010).

[128]H. Habenicht (personal communication), (2010).

[129]P. Gundel, M. C. Schubert, et al., *Micro-photoluminescence spectroscopy on metal precipitates in silicon*, Physica Status Solidi RRL **3** (7-8), 230 (2009).

[130]A. Bentzen and A. Holt, *Overview of phosphorus diffusion and gettering in multicrystalline silicon*, Mater. Sci. Eng. B **159-160**, 228 (2008).

[131]J. Tan, A. Cuevas, et al., *On the electronic improvement of multi-crystalline silicon via gettering and hydrogenation*, Progr. Photovolt. **16** (2), 129 (2007).

[132]P. Manshanden and L. J. Geerligs, *Improved phosphorous getterin of multicrystalline silicon*, Solar Energy Materials & Solar Cells **90** (7-8), 998 (2006).

[133]M. Kittler and W. Seifert, *Estimation of the upper limit of the minority-carrier diffusion length in multicrystalline silicon: Limitation of the action of gettering and passivation on dislocations*, Solid State Phenomena **95-96**, 197 (2004).

[134]A. Bentzen, A. Holt, et al., *Gettering of transition metal impurities during phosphorus emitter diffusion in multicrystalline silicon solar cell processing*, Journal of Applied Physics **99**, 093509 (2006).

[135]M. Danner and K. Bucher, *Reverse characteristics of commercial silicon solar cells - impact on hot spot temperatures and module integrity*, in Proceedings of the 26th IEEE Photovoltaics Specialists Conference, Anaheim, CA, USA, (1997),

[136]M. C. Alonso-García, W. Herrmann, et al., *Thermal and electrical effects caused by outdoor hot-spot testing in associations of photovoltaic cells*, Progress in Photovoltaics: Research and Applications **11**, 293 (2003).

[137]M. C. Alonso-García and J. M. Ruíz, *Analysis and modelling the reverse characteristic of photovoltaic cells*, Solar Energy Materials & Solar Cells **90**, 1105 (2006).

[138]J. W. Bishop, *Microplasma breakdown and hot-spots in silicon solar cells*, Solar Cells **26** (4), 335 (1989).

[139]R. Lal and R. Sharan, *Shunt resistance and soft reverse characteristics of silicon diffused-junction solar cells*, Solid-State Electronics **29** (10), 1015 (1986).

[140]S. Mahadevan, S. M. Hardas, et al., *Electrical breakdown in semiconductors*, Physica Status Solidi A **8**, 335 (1971).

[141]W. Mönch, *On the physics of avalanche breakdown in semiconductors*, Phys. stat. sol. **36** (9), 9 (1969).

[142]A. G. Chynoweth, *Ionization rates for electrons and holes in silicon*, Physical Review **109** (5), 1537 (1958).

[143]R. L. Batdorf, A. G. Chynoweth, et al., *Uniform Silicon p-n junctions. I. Broad area breakdown*, Journal of Applied Physics **31** (7), 1153 (1960).

[144]K. G. McKay, *Avalanche breakdown in silicon*, Physical Review **94** (4), 877 (1953).

[145]D. J. Robbins, *Aspects of the theory of impact ionization in semiconductors (I)*, Physica Status Solidi B **97**, 9 (1980).

[146]D. J. Robbins, *Aspects of the theory of impact ionization in semiconductors (II)*, Physica Status Solidi B **97**, 387 (1980).

[147]D. J. Robbins, *Aspects of the theory of impact ionization in semiconductors (III)*, Physica Status Solidi B **98**, 11 (1980).

[148]D. J. Rose, *Microplasmas in silicon*, Physical Review **105** (2), 413 (1957).

[149]O. Marinov, M. J. Deen, et al., *Theory of microplasma fluctuations and noise in silicon diode in avalanche breakdown*, Journal of Applied Physics **101**, 064515 (2007).

[150]A. G. Chynoweth and K. G. McKay, *Light emission and noise studies of individual microplasmas in silicon p-n junctions*, Journal of Applied Physics **30** (11), 1811 (1959).

[151]R. Newman, *Visible light from a silicon p-n junction*, Physical Review **100** (2), 700 (1955).

[152]A. G. Chynoweth and K. G. McKay, *Photon emission from avalanche breakdown in silicon*, Physical Review **102** (2), 369 (1956).

[153]J. Tauc, *Electron impact ionization in semiconductors*, Journal of Physics and Chemistry of Solids **8**, 219 (1959).

[154]N. Akil, S. E. Kerns, et al., *A multimechanism model for photon generation by silicon junctions in avalanche breakdown*, IEEE Transactions on Electron Devices **46** (5), 1022 (1999).

[155]L. W. Davies and A. R. Storm, *Recombination radiation from silicon under strong-field conditions*, Physical Review **121** (2), 381 (1961).

[156]P. A. Wolff, *Theory of electron multiplication in silicon and germanium*, Physical Review **95** (6), 1415 (1954).

[157]J. Shewchun and L. Y. Wei, *Mechanism for reverse-biased breakdown radiation in p-n junctions*, Solid-State Electronics **8** (5), 485 (1965).

[158]T. Figielski and A. Torum, *On the origin of light emitted from reverse biased p-n junctions*, in Proceedings of the 6th International Conference of Physics in Semiconductors, (1962), page 863.

[159]A. Toriumi, M. Yoshimi, et al., *A study of photon emission from n-channel MOSFET's*, IEEE Transactions on Electron Devices **34**, 1501 (1987).

[160]D. K. Gautam, W. S. Khokle, et al., *Photon emission from reverse-biased silicon P-N junction*, Solid-State Electronics **31** (2), 219 (1988).

[161]W. Haecker, *Infrared radiation from breakdown plasmas in Si, GaSb, and Ge: Evidence for direct free hole radiation*, Physica Status Solidi A **25**, 301 (1974).

[162]A. G. Chynoweth and G. L. Pearson, *Effect of disolations on breakdown in silicon p-n junctions*, Journal of Applied Physics **29** (7), 1103 (1958).

[163]A. Goetzberger and C. Stephens, *Voltage dependence of microplasma density in p-n junctions in silicon*, Journal of Applied Physics **32** (12), 2646 (1961).

[164]A. Goetzberger, B. McDonald, et al., *Avalanche effects in silicon p-n junctions. II. Structurally perfect junctions*, Journal of Applied Physics **34** (6), 1591 (1963).

[165]M. Kikuchi and K. Tachikawa, *Visible light emission and microplasma phenomena in silicon p-n junction, I.*, Journal of the Physical Society of Japan **15**, 835 (1960).

[166]W. Shockley, *Problems related to p-n junctions in silicon*, Solid State Electronics **2** (1), 35 (1961).

[167]A. Goetzberger and W. Shockley, *Metal precipitates in silicon p-n junctions*, Journal of Applied Physics **31** (10), 1821 (1960).

[168]A. G. Chynoweth and K. G. McKay, *Internal field emission in silicon p-n junctions*, Physical Review **106** (3), 418 (1957).

[169]B. S. Khurana, T. Sugano, et al., *Thermal breakdown in silicon p-n junction devices*, IEEE Transactions on Electron Devices **13** (11), 763 (1966).

[170]J. Tauc and A. Abrahám, *Thermal breakdown in silicon p-n junctions*, Physical Review **108** (4), 936 (1957).

[171]O. Breitenstein and M. Langenkamp, *Lock-in Thermography - Basics and Use for Functional Diagnostics of Electronic Components*. (Springer Verlag, Berlin/Heidelberg, 2003).

[172]O. Breitenstein, J. Bauer, et al., *Imaging physical parameters of pre-breakdown sites by lock-in thermography techniques*, Progress in Photovoltaics: Research and Applications **16**, 679 (2008).

[173]W. Kwapil, M. Kasemann, et al., *Investigations on the pre-breakdown of multicrystalline silicon solar cells*, in Proceedings of the 23rd European Photovoltaic Solar Energy Conference, Valencia, Spain, (2008), page 1797.

[174]W. Kwapil, M. Kasemann, et al., *Diode breakdown related to recombination active defects in block-cast multicrystalline silicon solar cells*, Journal of Applied Physics **106** (6), 063530 (2009).

[175]M. Kasemann, *What photons tell us about solar cells*, PhD thesis, University of Freiburg, 2010.

[176]K. Bothe, K. Ramspeck, et al., *Luminescence emission from forward- and reverse-biased multicrystalline silicon solar cells*, Journal of Applied Physics **106** (10), 104510 (2009).

[177]J.-M. Wagner, J. Bauer, et al., *Classification of pre-breakdown phenomena in multicrystalline silicon solar cells*, in Proceedings of the 24th European Photovoltaic Solar Energy Conference, Hamburg, Germany, (2009), page 925.

[178]K. Bothe (personal communication), (2009).

[179]O. Breitenstein, J. Bauer, et al., *Understanding junction breakdown in multicrystalline solar cells*, in Proceedings of the 20th Workshop on Crystalline Silicon Solar Cells & Modules: Materials and Processes, Breckenridge, CO, USA, (2010),

[180]O. Breitenstein, J. Bauer, et al., *Defect-induced breakdown in multicrystalline silicon solar cells*, Transactions on Electron Devices **to be published** (2010).

[181]B. Walter, *Quantitative Analyse ortsaufgelöster Lock-In-Thermographie-Messungen zur Charaktersierung von Solarzellen*, Diploma thesis, University of Karlsruhe, 2008.

[182]D. Lausch, K. Petter, et al., *Identification of pre-breakdown mechanism of silicon solar cells at low reverse voltages*, Applied Physics Letters **97** (7), 073506 (2010).

[183]P. Gundel, W. Kwapil, et al., *Spectroscopic investigation of breakdown sites in silicon solar cells*, to be published (2010).

[184]D. K. Schroder and D. L. Meier, *Solar cell contact resistance - a review*, IEEE Transactions on Electron Devices **ED-31** (5), 637 (1984).

[185]M. Kasemann, W. Kwapil, et al., *Spatially resolved silicon solar cell characterization using infrared imaging methods*, in Proceedings of the 33rd IEEE Photovoltaic Specialists Conference, San Diego, USA, (2008),

[186]M. A. Drozdov, A. A. Patrin, et al., *Recombination radiation on dislocations in silicon*, Journal of Experimental and Theoretical Physics Letters **23** (11), 597 (1976).

[187]M. Inoue, H. Sugimoto, et al., *Microscopic and spectroscopic mapping of dislocation-related photoluminescence in multicrystalline silicon wafers*, Journal of Materials Science: Materials in Electronics **19** (Supplement 1), 132 (2008).

[188]V. V. Kveder, E. A. Steinman, et al., *Dislocation-related electroluminescence at room temperature in plastically deformed silicon*, Physical Review B **51** (16), 10520 (1995).

[189]V. Kveder, M. Kittler, et al., *Recombination activity of contaminated dislocations in silicon: A model describing electron-beam induced current contrast behavior*, Physical Review B **63**, 115208 (2001).

[190]K. Knobloch, M. Kittler, et al., *Influence of contamination on the dislocation-related deep level C1 line observed in deep-level-transient spectroscopy of n-type silicon: A comparison with the technique of electron-beam-induced current*, Journal of Applied Physics **93**, 1069 (2002).

[191]S. A. McHugo, A. C. Thompson, et al., *Direct correlation of transition metal impurities and minority carrier recombination in multicrystalline silicon*, Applied Physics Letters **72** (26), 3482 (1998).

[192]L. E. Katz, *Relationship between process-induced defects and soft p-n junctions in silicon devices*, Journal of the Electrochemical Society **121** (7), 969 (1974).

[193]A. G. Cullis and L. E. Katz, *Electron microscope study of electrically active impurity precipitate defects in silicon*, Philosophical Magazine **30** (6), 1419 (1974).

[194]W. Kwapil, P. Gundel, et al., *Observation of metal precipitates at prebreakdown sites in multicrystalline silicon solar cells*, Applied Physics Letters **95** (23), 232113 (2009).

[195]O. Breitenstein (personal communication), (2009).

[196]G. Coletti, P. Bronsveld, et al., *Impact of transition metals in feedstock on multicrystalline silicon solar cell properties*, in Proceedings of the 18th International Photovoltaic Science and Engineering Conference, Kolkata, India, (2009),

[197]G. Coletti, P. C. P. Bronsveld, et al., *Impact of iron, nickel and chromium in feedstock on multicrystalline silicon solar cell properties*, in Proceedings of the Proceedings of the 24th European Photovoltaic Solar Energy Conference, Hamburg, Germany, (2009), page 1011.

[198]W. Kwapil, M. Wagner, et al., *Cause of increased currents under reverse-bias conditions of upgraded metallurgical grade multicrystalline silicon solar cells*, in Proceedings of the 35th IEEE Photovoltaics Specialists Conference, Honolulu, HI, USA, (2010),

[199]T. Naerland, L. Arnberg, et al., *Origin of the low carrier lifetime edge zone in multicrystalline PV silicon*, Progress in Photovoltaics: Research and Applications **17** (5), 289 (2009).

[200]A. Haarahiltunen, H. Väinölä, et al., *Experimental and theoretical study of heterogeneous iron precipitation in silicon*, Journal of Applied Physics **101**, 043507 (2007).

[201]M. Wagner, B. Gründig-Wendrock, et al., *Shunts, Diode Breakdown and High Reverse Currents in Multicrystalline Silicon Solar Cells*, in Proceedings of the 24th European Photovoltaic Solar Energy Conference, Hamburg, Germany, (2009),

[202]W. Kwapil, M. Wagner, et al., *High net doping concentration responsible for critical diode breakdown behavior of upgraded metallurgical grade multicrystalline silicon solar cells*, Journal of Applied Physics **108** (2), 023708 (2010).

[203]J. Nievendick, M. Demant, et al., *Appearance of rift structures created by acidic texturization and their impact on solar cell efficiency*, in Proceedings of the 35th IEEE Photovoltaic Specialists Conference, Honolulu, HI, USA, (2010),

[204]O. Breitenstein, J. Bauer, et al., *Defect induced non-ideal dark I-V characteristics of solar cells*, Superlattices and Microstructures **45** (4-5), 182 (2008).

[205]A. Schenk and U. Krumbein, *Coupled defect-level recombination: Theory and application to anomalous diode characteristics*, Journal of Applied Physics **78** (5), 3185 (1995).

[206]M. D. Negoita and T. Y. Tan, *Metallic precipitate contribution to generation and recombination currents in p-n junction devices due to the Schottky effect*, Journal of Applied Physics **94** (8), 5064 (2003).

[207]E. H. Rhoderick and R. H. Williams, *Metal-semiconductor contacts*. (Oxford University Press, London, 1988).

[208]P. S. Plekhanov and T. Y. Tan, *Schottky effect model of electrical activity of metallic precipitates in silicon*, Applied Physics Letters **76** (25), 3777 (2000).

[209]R. M. Warner Jr., *Avalanche breakdown in silicon diffused junctions*, Solid-State Electronics **15**, 1303 (1972).

[210]S. M. Sze and G. Gibbons, *Avalanche breakdown voltages of abrupts and linearly graded p-n junctions in Ge, Si, GaAs, and GaP*, Applied Physics Letters **8** (5), 111 (1966).

[211]J. Bauer, J.-M. Wagner, et al., *Hot spots in multicrystalline silicon solar cells: avalanche breakdown due to etch pits*, Physica Status Solidi RRL **3** (2), 40 (2009).

List of Publications

First Author in Reviewed Journals:

- W. Kwapil, M. Wagner, M.C. Schubert, and W. Warta, *High net doping concentration responsible for critical diode breakdown behavior of upgraded metallurgical grade multicrystalline silicon solar cells*, Journal of Applied Physics **108** (2), 023708 (2010).
- W. Kwapil, P. Gundel, M. C. Schubert, F. D. Heinz, W. Warta, E. R. Weber, and A. Goetzberger, G. Martinez-Criado, *Observation of metal precipitates at pre-breakdown sites in multicrystalline silicon solar cells*, Applied Physics Letters **95**, 232113 (2009).
- W. Kwapil, M. Kasemann, P. Gundel, M. C. Schubert, W. Warta, P. Bronsveld and G. Coletti, *Diode breakdown related to recombination active defects in block-cast multicrystalline silicon solar cells*, Journal of Applied Physics **106** (6), 063530 (2009).

Co-Author in Reviewed Journals:

- O. Breitenstein, J. Bauer, J.-M. Wagner, N. Zakharov, H. Blumtritt, A. Lotnyk, M. Kasemann, W. Kwapil, and W. Warta, *Defect-induced breakdown in multicrystalline silicon solar cells*, IEEE Transactions on Electron Devices, **57** (9), 2227 (2010)
- M.C. Schubert, W. Kwapil, J. Schön, H. Habenicht, M. Kasemann, P. Gundel, M. Blazek, W. Warta, *Analysis of performance limiting material properties of multicrystalline silicon*, Solar Energy Materials & Solar Cells", DOI: 10.1016/j.solmat.2010.04.010, (2010)
- M. C. Schubert, J. Schön, P. Gundel, H. Habenicht, W. Kwapil, and W. Warta, *Imaging of Metal Impurities in Silicon by Luminescence Spectroscopy and Synchrotron Techniques*, Journal of Electronic Materials, DOI: 10.1007/s11664-010-1114-7, (2010)
- F. Clement, M. Menkoe, D. Erath, T. Kubera, R. Hoenig, W. Kwapil, W. Wolke, D. Biro, R. Preu, *High throughput via-metallization technique for multi-crystalline metal wrap through (MWT) silicon solar cells exceeding 16% efficiency*, Solar Energy Materials & Solar Cells **94**, 51 (2010)
- P. Gundel, G. Martinez-Criado, M. C. Schubert, J. Angel Sans, W. Kwapil, W. Warta, and E. R. Weber, *X-ray excited optical luminescence from crystalline silicon*, Phys. Status Solidi RRL, **3** (7-8), 275 (2009)
- P. Gundel, M. C. Schubert, W. Kwapil, J. Schön, M. Reiche, H. Savin, M. Yli-Koski, J. Angel Sans, G. Martinez-Criado, W. Seifert, W. Warta and E. R. Weber, *Micro-photoluminescence spectroscopy on metal precipitates in silicon*, Phys. Status Solidi RRL, 1-3 (2009)
- M. Kasemann, B. Walter, C. Meinhardt, J. Ebser, W. Kwapil, W. Warta, *Emissivity-corrected power loss calibration for lock-in thermography measurements on silicon solar cells*, Journal of Applied Physics **103**, 113503 (2008)
- M. Kasemann, D. Grote, B. Walter, W. Kwapil, T. Trupke, Y. Augarten, R.A. Bardos, E. Pink, M. D. Abbott and W. Warta, *Luminescence imaging for the detection of shunts on silicon solar cells*, Progress in Photovoltaics **16** (4), 297 (2008).

- S. Riepe, I. E. Reis, W. Kwapil, W. Koch, J. Schön, H. Behnken, J. Bauer, D. Kreßner-Kiel, W. Seifert, and M. Seibt, *Research on efficiency limiting defects and defect engineering in silicon solar cells – results of the German research cluster SolarFocus*, Physica Status Solidi, accepted (2010)
- J. Geilker, W. Kwapil, and S. Rein, *Light-induced degradation in compensated p- and n-type Czochralski silicon wafers*, Journal of Applied Physics, under review, (2010)
- P. Gundel, W. Kwapil, M. C. Schubert, H. Seifert, and W. Warta, *Approach to the physical origin of breakdown in silicon solar cells by optical spectroscopy*, Journal of Applied Physics, under review, (2010)
- P. Gundel, M. C. Schubert, F. D. Heinz, W. Kwapil, W. Warta, G. Martinez-Criado, M. Reiche, E. R. Weber, *Impact of stress on the recombination at metal precipitates in silicon*, Journal of Applied Physics, under review (2010)
- O. Breitenstein, J. Bauer, K. Bothe, W. Kwapil, D. Lausch, U. Rau, J. Schmidt, M. Schneemann, M. C. Schubert, J.-M. Wagner, and W. Warta, *Understanding junction breakdown in multicrystalline solar cells*, Journal of Applied Physics, Applied Physics Reviews, under review (2010)

Talks at Conferences and Workshops:

- W. Kwapil, M. Wagner, M. C. Schubert, and W. Warta, *Cause of increased currents under reverse-bias conditions of upgraded metallurgical grade multicrystalline silicon solar cells*, presented at the 35th IEEE Photovoltaic Specialists Conference, Honolulu, HI, USA (2010)
- W. Kwapil, M. Kasemann, P. Gundel, M. C. Schubert, W. Warta, O. Breitenstein, J. Bauer, A. Lotnyk, J.-M. Wagner, P. C. P. Bronsveld, G. Coletti, *Physical mechanisms of breakdown in multicrystalline silicon solar cells*, Plenary talk presented at the 24th European Photovoltaic Solar Energy Conference, Hamburg, Germany, 2009
- W. Kwapil, M. Kasemann, W. Warta, *Durchbrüche – Physik und Materialeinflüsse*, Silicon Forest Workshop, Falkau, Germany, 2009
- W. Kwapil, M. Blazek, J. Schön, H. Habenicht and W. Warta, *Al segregation gettering on intentionally contaminated wafers*, presented at the Workshop Feedstock Specifications, Amsterdam, The Netherlands, 2008

Further Contributions to Conferences:

- W. Kwapil, M. Kasemann, J. Giesecke, B. Michl and W. Warta, *Investigations on the pre-breakdown of multicrystalline silicon solar cells*, Proceedings of the 23rd European Photovoltaic Solar Energy Conference, Valencia, Spain, 2008
- W. Kwapil, M. Kasemann, J. Ebser, S. Rein and W. Warta, *Application of illuminated lock-in thermography to industrial silicon solar cells*, Proceedings of the 22nd European Photovoltaic Solar Energy Conference, Milan, Italy, 2007
- F. Boldt, J. Hampel, Y. Wencel, W. Kwapil, J. Geilker, F. Fertig, S. Rein, and S. Reber, *Effect of segregation during crystallization of highly impure upgraded metallurgical*

silicon, presented at the 25th European Photovoltaic Solar Energy Conference, Valencia, Spain (2010)

- M. C. Schubert, M. Rüdiger, B. Michl, F. Schindler, W. Kwapil, J. Giesecke, M. Hermle, W. Warta, R. Ferre, R. Wade, K. Petter, *The role of material quality in EWT and standard solar cells on multicrystalline standard and UMG silicon material*, presented at the 25th European Photovoltaic Solar Energy Conference, Valencia, Spain (2010)
- F. Schindler, J. Geilker, W. Kwapil, J. Giesecke, M. C. Schubert, and W. Warta, *Conducitiviy mobility and Hall mobility in compensated multicrystalline silicon*, presented at the 25th European Photovoltaic Solar Energy Conference, Valencia, Spain (2010)
- J. Geilker, W. Kwapil, I. Reis, and S. Rein, *Doping concentration and mobility in compensated material: Comparison of difference determination methods*, presented at the 25th European Photovoltaic Solar Energy Conference, Valencia, Spain (2010)
- S. Rein, J. Geilker, W. Kwapil, G. Emanuel, I. Reis, A.-K. Soiland, S. Grandum, and R. Tronstad, *Cz-silicon wafers and solar cells from compensated solar-grade silicon feedstock: potential and challenges*, presented at the 25th European Photovoltaic Solar Energy Conference, Valencia, Spain (2010)
- O. Breitenstein, J. Bauer, K. Bothe, W. Kwapil, D. Lausch, U. Rau, J. Schmidt, M. Schneemann, M. C. Schubert, J.-N. Wagner, and W. Warta, *Understanding juncion breakdown in multicrystalline solar cells*, 20th Workshop on Crystalline Silicon Solar Cells & Modules: Materials and Processes, Breckenridge, CO, USA (2010)
- S. Rein, W. Kwapil, J. Geilker, G. Emanuel, M. Spitz, I. Reis, A. Weil, D. Biro, M. Glatthaar, A.-K. Soiland, E. Enebakk, and R. Tronstad, *Impact of compensated solar-grade silicon on Czochralski silicon wafers and solar cells*, Proceedings of the 24th European Photovoltaic Solar Energy Conference, Hamburg, Germany, 2009
- M. Blazek, W. Kwapil, J. Schön, and W. Warta, *Gettering variation and lifetime characterization on intentionally iron, nickel and chromium contaminated multicrystalline silicon wafers*, Proceedings of the 24th European Photovoltaic Solar Energy Conference, Hamburg, Germany, 2009
- J. Haunschild, M. Glatthaar, W. Kwapil and S. Rein, *Comparing luminescence imaging with illuminated lock-in thermography and carrier density imaging inspection of silicon solar cells*, Proceedings of the 24th European Photovoltaic Solar Energy Conference, Hamburg, Germany, 2009
- O. Breitenstein, J. Bauer, J.-M. Wagner, H. Blumtritt, A. Lotnyk, M. Kasemann, W. Kwapil, and W. Warta, *Physical mechanisms of breakdown in multicrystalline silicon solar cells*, Proceeding of the 34th IEEE Photovoltaic Specialists Conference, Philadelphia, USA, 2009
- B. Walter, M. Kasemann, D. Grote, J. Ebser, W. Kwapil, and W. Warta, *Verification of power loss mechanisms contributing to the illuminated lock-in thermography (ILIT) signal*, Proceedings of the 23rd European Photovoltaic Solar Energy Conference, Valencia, Spain, 2008
- M. Kasemann, W. Kwapil, B. Walter, J. Giesecke, B. Michl, M. The, J.-M. Wagner, J. Bauer, A. Schütt, J. Carstensen, H. Kampwerth, P. Gundel, M. C. Schubert, R. A. Bardos, H. Föll, H. Nagel, P. Würfel, T. Trupke, O. Breitenstein, W. Warta, and S. W. Glunz, *Progress in silicon solar cell characterization with infrared imaging methods*,

Proceedings of the 23rd European Photovoltaic Solar Energy Conference, Valencia, Spain, 2008

- M. Blazek, W. Kwapil, J. Schön, and W. Warta, *Gettering efficiency of backside aluminium layer and Al-Si-eutectic*, Proceedings of the 23rd European Photovoltaic Solar Energy Conference, Valencia, Spain, 2008
- M. Kasemann, W. Kwapil, M. C. Schubert, H. Habenicht, B. Walter, M. The, S. Kontermann, S. Rein, O. Breitenstein, J. Bauer, A. Lotnyk, B. Michl, H. Nagel, A. Schütt, J. Carstensen, H. Föll, T. Trupke, Y. Augarten, H. Kampwerth, R. A. Bardos, S. Pingel, J. Berghold, W. Warta and S. W. Glunz, *Spatially resolved silicon solar cell characterization using infrared imaging methods*, Proceedings of the 33rd IEEE Photovoltaic Specialists Conference, San Diego, USA, 2008
- F. Clement, M. Lutsch, T. Kubera, M. Kasemann, W. Kwapil, C. Harmel, N. Mingirulli, D. Erath, H. Wirth, D. Biro and R. Preu, *Processing and comprehensive characterization of screen-printed mc-Si metal wrap through (MWT) solar cells*, Proceedings of the 22nd European Photovoltaic Solar Energy Conference, Milan, Italy, 2007

Danksagung

An dieser Stelle möchte ich meinen herzlichen Dank aussprechen an alle, die zum Entstehen dieser Dissertation beigetragen haben. Die folgende Liste kann erzwungenermaßen nur unvollständig sein:

Mein Dank gilt

Herrn **Prof. Dr. Gerhard Willeke** für die Vergabe und Betreuung dieser Arbeit,

Herrn **Prof. Dr. Thomas Dekorsy** für die Übernahme des Zweitreferats,

Herrn **Dr. Wilhelm Warta** für die Betreuung und Unterstützung, für motivierende Diskussionen unter Einbringung inspirierender Blickwinkel,

Herrn **Dr. Martin Schubert** für die Unterstützung und das stets offene Ohr bei allen Fragen,

Herrn **Dr. Stefan Rein** für die fruchtbare Zusammenarbeit im Bereich der Materialcharakterisierung bis (ganz selten) spät in die Nacht,

meinen Diplomanden **Matthias Blazek**, **Juliane Geilker** und **Florian Schindler** für die Zusammenarbeit in stets freundschaftlicher Atmosphäre,

Herrn **Dr. Martin Kasemann** für die Inspirationen, die im wahrsten Sinne des Wortes zum „Durchbruch" geführt haben,

Paul Gundel für die intensive Zusammenarbeit bei der Suche nach den Durchbruchstellen und für die vielen lustigen Nachtschichten am ESRF und am BESSY,

Jonas Schön und **Holger Habenicht** für interessante Diskussionen und so manche abendliche Aktivität,

„meiner Büroecke" – **Dr. Florian Clement**, **Gernot Emanuel**, **Juliane Geilker**, **Dr. Daniel Biro** und **Fabian Fertig** stellvertretend für alle wechselnden Besetzungen – für die sehr gute Arbeitsatmosphäre und die freundschaftlichen Unterhaltungen,

Frau **Dr. Gema Martinez-Criado**, den Herren **Dr. Juan Angel-Sans** und **Dr. Ivo Zizak** für die große Hilfe am ESRF und BESSY, manchmal sogar nachts um halb drei,

Herrn **Dr. Otwin Breitenstein**, **Dr. Jan-Martin Wagner**, **Dr. Jan Bauer**, **Dominik Lausch**, **Dr. Karsten Bothe** und allen anderen Beteiligten für den intensiven, offenen Austausch über die Arbeiten und Ergebnisse zum Diodendurchbruch,

stellvertretend geht mein Dank an **Harald Lautenschlager**, **Toni Leimenstoll**, **Elisabeth Schäffer**, **Christian Harmel**, **Martin Schwarzkopf**, **Rainer Neubauer**, **Udo Belledin**, **Mira Kwiatkowska**, **Johannes Giesecke**, **Jonas Haunschild, Dr. Markus Glatthaar** für die Hilfe bei Prozessierung und Charakterisierung.

Vielen Dank an meinen Vater **Konstantin Kwapil** für die Durchsicht des Manuskripts.